Comptes Rendus
de l'Académie des sciences

1873-7234 (electronic)

Mécanique

Thematic issue / *Numéro thématique*
Advances in finite fracture mechanics : a tribute to Dominique Leguillon's scientific achievements /
Progrès récents en mécanique finie de la rupture : un hommage à l'œuvre scientifique de Dominique Leguillon

Coordinated by / *Coordonné par*
Jean-Baptiste Leblond

Académie des sciences - Paris

ACADÉMIE DES SCIENCES
INSTITUT DE FRANCE

CENTRE MERSENNE

Comptes Rendus
Mécanique

Objective of the journal

Comptes Rendus Mécanique is an international peer-reviewed electronic journal, covering all areas of mechanics and engineering science.
It publishes original research articles, review articles, historical perspectives, pedagogical texts or conference proceedings, of unlimited length, in English or in French and in as flexible a format as necessary (figures, associated data, etc.).
Comptes Rendus Mécanique has been published since 2020 with the centre Mersenne pour l'édition scientifique ouverte (Mersenne Center for open scientific publishing), according to a virtuous Diamond Open Access policy, free for authors (no author processing charges nor publishing fees) as well as for readers (immediate and permanent open access).

About the journal

All journal's information, including the text of published articles, which is fully open access, is available from the journal website at https://comptes-rendus.academie-sciences.fr/mecanique/.

Author enquiries

For enquiries relating to the submission of articles, please visit this journal's homepage at https://comptes-rendus.academie-sciences.fr/mecanique/.

Contact

Académie des sciences
23, quai de Conti, 75006 Paris, France
Tel: (+33) (0)1 44 41 43 72
cr-mecanique@academie-sciences.fr

To cite this issue:
Leblond Jean-Baptiste (ed). Advances in finite fracture mechanics : a tribute to Dominique Leguillon's scientific achievements. Comptes Rendus Mécanique, 2025. https://doi.org/10.5802/crmeca.sp.2.

ACADÉMIE DES SCIENCES
INSTITUT DE FRANCE

Comptes Rendus. Mécanique
2025, Vol. 353, p. 1127-1128
https://doi.org/10.5802/crmeca.329

Foreword / *Avant-propos*

Recent advances in finite fracture mechanics—a tribute to Dominique Leguillon's scientific achievements

Progrès récents en mécanique finie de la rupture — un hommage à l'œuvre scientifique de Dominique Leguillon

Jean-Baptiste Leblond

E-mail: jbl@lmm.jussieu.fr

On the scene of contemporaneous French fracture mechanics, Dominique Leguillon stands as a singular and most remarkable character. Indeed, after the completion of his PhD thesis undertaken and pursued at the Laboratoire de Modélisation en Mécanique of Université Pierre et Marie Curie (Paris VI) (now part of Sorbonne Université), he was appointed as Ingénieur de Recherches in the CNRS (Centre National de la Recherche Scientifique). His already heavy task, which he managed to perform alone, consisted in the organization and maintenance of the ensemble and network of computers of the Laboratoire de Modélisation en Mécanique. But he would not limit his activities to such aspects and undertook scientific cooperations with various researchers, and notably our illustrious colleague Evariste Sanchez-Palencia. With him, he dedicated numerous and fruitful efforts to various important issues in mechanics of deformable solids, such as periodic homogenization, matched asymptotic expansions, and occurrence of singularities. The popularity and impact of these studies allowed him to successfully apply for a post of Directeur de Recherches at the CNRS. This highly improbable passage from a position of engineer in charge of computers to one of researcher is exceptional enough in the CNRS to deserve a very special mention.

But it was in the 2000's that Dominique's career and scientific reputation really started to take off. In order to explain the nature of his essential contribution, it is first necessary to provide some elements of context.

The aim of the classical theory of fracture mechanics is to study and predict propagation of cracks in materials. It is of utmost practical importance, and serves as a basis to avoid crack-induced failure of various mechanical objects and structures. But in spite of its very numerous and important successes, it is still prone to notable shortcomings. For instance, it permits to predict crack propagation from some small pre-existing crack, but not in a sound structure devoid of any pre-crack. Even more critically, it fails to predict crack initiation from a notch root, in spite of the frequent occurrence of such a situation, notably in welded joints.

The essential contribution of Dominique, which no longer owed anything to anyone else, was to overcome these limitations by proposing an extended theory, nowadays known as "finite fracture mechanics". This new approach of this type of problems requires the definition of some

"double" or "coupled" criterion, involving two necessary conditions for crack propagation, one on the opening stress before propagation, the other on the energy-release-rate. The new theory is termed *finite* fracture mechanics because it does not split crack propagation into infinitesimal steps, each governed by the double criterion, but into steps that may be finite, over some distance determined by the criterion.

Dominique's proposal immediately drew attention from numerous researchers in the field at various places in the world, and met with very important success; experimenters active in France, Europe, Israël and the USA, embarked on the experimental verification of this proposal and its practical applications. Dominique collaborated with them and accompanied them in his typically friendly way, thus weaving a large web of international cooperations.

These features permit to state that Dominique's new theory of finite fracture mechanics stands as one of the major additions brought to fracture mechanics in the last few decades.

Having retired, Dominique changed almost nothing in his working habits, and went on coming to his research institution every day, pursuing the development of his ideas with his colleagues and friends. However, having reached the age of 75 in full command of his intellectual means, and although nothing permitted to foresee such an event, Dominique suddenly succumbed to a heart attack while he was walking in the street. He leaves an immense emptiness behind him, but also appealing scientific perspectives, because his ideas, being so simple, elegant and straightforwardly applicable to problems of both scientific and technical nature, can still motivate numerous and importants developments; so true it is that fracture mechanics cannot possibly be content with predicting and depicting the propagation of cracks while forgetting about their initiation.

For those who had the privilege of knowing Dominique, he will remain an exceptional colleague and friend. The aim of this special issue of *Comptes-Rendus Mécanique* dedicated to him is to fittingly honor his memory, by showing how his ideas still give rise and stimulate diverse and interesting works.

Jean-Baptiste Leblond
Emeritus Professor
Sorbonne Université
Member of the French Academy of Sciences
France
jbl@lmm.jussieu.fr

ACADÉMIE DES SCIENCES
INSTITUT DE FRANCE

Comptes Rendus. Mécanique
2025, Vol. 353, p. 359-377
https://doi.org/10.5802/crmeca.286

Research article / *Article de recherche*

Mechanisms of transverse cracking induced by adjacent ply matrix cracks in composite laminates

Mécanismes de fissuration transverse induits par des fissures matricielles dans des plis adjacents de stratifiés composites

Nicolas Carrère [a], Aurélien Doitrand [*,b], Mathilde Conan [a] and Eric Martin [c]

[a] ENSTA Bretagne, CNRS, IRDL, UMR 6027, F-29806 Brest, France

[b] Université Lyon, INSA-Lyon, UCBL, CNRS, MATEIS, UMR5510, F-69621 Villeurbanne, France

[c] Bordeaux-INP, Univ. Bordeaux, F-33400 Talence, France

E-mails: nicolas.carrere@ensta-bretagne.fr (N. Carrère), aurelien.doitrand@insa-lyon.fr (A. Doitrand), mathilde.conan@ensta-bretagne.org (M. Conan), eric.martin@enseirb-matmeca.fr (E. Martin)

Abstract. Cracking in composite laminates containing θ-plies adjacent to 90° plies is studied experimentally and numerically using the coupled criterion and finite element calculations. Different damage mechanisms are considered, namely transverse cracking in 90°, cracking in θ-plies, or debonding between adjacent misoriented plies. The influence of the stacking sequence on the damage mechanism sequence is investigated. Experimental observations of the composite edge under tensile loading evidence θ-ply cracking (i) at an imposed strain level much larger than first transverse cracking in 90° ply for a sufficiently large orientation mismatch between adjacent plies or (ii) at a similar imposed strain level if the mismatch angle between two adjacent plies is small. The latter phenomenon may be mitigated by the presence of a 0° ply between the 90° and the θ-plies.

These conclusions are supported by numerical simulation of the experimentally observed damage mechanisms, evidencing a change in the damage mechanism sequence depending on the θ-ply misorientation. The numerical simulations also highlight that debonding between adjacent plies may occur as it becomes more favorable that adjacent ply crack re-initiation for sufficiently large adjacent ply mismatch angle.

Résumé. La fissuration dans les stratifiés composites, contenant des plis orientés à θ° de la direction de chargement adjacents à des plis à 90°, est étudiée expérimentalement et numériquement à l'aide du critère couplé et de calculs par éléments finis. Différents mécanismes d'endommagement sont pris en compte : la fissuration transverse dans le pli à 90°, la fissuration dans les plis à θ°, ou la décohésion entre des plis adjacents d'orientation différente. L'influence de la séquence d'empilement sur la séquence des mécanismes d'endommagement est analysée. Les observations expérimentales effectuées sur des stratifiés sollicités en traction mettent en évidence une fissuration dans les plis à θ : (i) à un niveau de déformation imposé beaucoup plus élevé que celui de la première fissuration transverse dans les plis à 90° pour une désorientation suffisamment grand entre les plis adjacents, ou (ii) à un niveau de déformation imposé similaire si l'angle de

* Corresponding author

désorientation entre deux plis adjacents est faible. Ce dernier phénomène peut être atténué par la présence d'un pli à 0° entre le pli à 90° et les plis à θ.

Ces conclusions sont appuyées par des simulations numériques des mécanismes d'endommagement observés expérimentalement, mettant en évidence un changement dans la séquence des mécanismes en fonction de l'angle de désorientation des plis à θ. Les simulations numériques montrent également que la décohésion entre plis adjacents peut se produire et devenir plus favorable que le ré-amorçage des fissures dans les plis adjacents lorsque l'angle de désorientation entre ces plis est suffisamment grand.

Keywords. Finite fracture mechanics, Coupled criterion, Laminates, Crack re-initiation.

Mots-clés. Mécanique de la rupture incrémentale, Critère couplé, Stratifiés, Ré-amorçage de fissures.

Manuscript received 15 November 2024, revised and accepted 15 January 2025.

1. Introduction

The growing utilization of composite materials in sectors demanding both performance and safety is often guided by principles derived from lessons learned. In specific industries, such as aeronautics, these principles have been formalized into comprehensive best practice guidelines outlined in the Military Handbook [1]. This document outlines, among other aspects, the draping recommendations that must be complied with when defining the lay-up of a laminated composite structure. Among the draping recommendations details, we can mention for example:

(1) Homogeneous stacking sequence are recommended for strength controlled designs. The handbook reminds that *the interlaminar stress distributions are affected, around the periphery of holes, by the variation of ply orientations relative to a tangent to the edge. Since it is difficult to optimize for a single lay-up in this case, the best solution is to make the stacking sequence as homogeneous as possible.*
(2) Since transverse strength is highly dependent on ply thickness, it is strongly recommended to *minimize the grouping of plies with identical orientations*,
(3) The mismatch in Poisson's ratio between adjacent plies, caused by the anisotropy of the ply properties and the difference in orientation between them, can generate out-of-plane stresses at the interface of adjacent plies near the edges of a laminate. It is thus recommended to perform analyses *to predict free edge stresses and delamination strain levels.*
(4) It is recommanded that the laminate has at least four distinct ply angles (e.g., 0°, $\pm\theta$°, 90°) with a minimum of 10% of the plies oriented at each angle.

These recommendations are partly based on experimental observations. Among numerous examples, and without claiming to be exhaustive, we can highlight a few studies that illustrate the aforementioned recommendations. Regarding recommendation #2, the pioneering work published in [2] demonstrated that thickness has a significant influence on the apparent strength of the ply. The impact of blocked versus dispersed plies on strength (recommendation #1) has been illustrated, for example, in unnotched specimens [3] and in open-hole specimens [4]. Delamination initiated from the edge and the effect of the stacking sequence (recommendation #3) have been studied in [5]. Finally, regarding the recommendation #4, the use of 0°, ±45°, 90° plies is a well-established practice driven by the need to balance stiffness, strength, processability, and damage tolerance. These orientations offer a versatile and practical solution for a wide range of engineering applications. It is essential to remember that the recommendations provided in this handbook serve solely as guidelines that should be verified based on the materials used and further assessed in relation to new-generation materials and manufacturing processes. Considering the high cost of testing and the numerous optimization possibilities [6], using models to estimate the influence of stacking on the laminate's strength is crucial.

Various models with differing levels of complexity have been proposed in the literature to achieve this goal. Classical Laminate Theory (CLT) is a simple and widely used model for rapidly designing laminated composite structures [7, 8]. Based on the elastic properties of the individual laminae, the stacking sequence, and the applied loading, this model enables the determination of the laminate's overall elastic properties and the stress distribution within each ply, while accounting for the effects of potential ply failure [9]. However, due to its inherent assumptions, this theory cannot account for the effects of discrete ply failure on adjacent plies or the potential delamination between two plies, whether caused by edge effects or induced by transverse failure. To effectively describe some of these mechanisms, it is essential to capture the discrete nature of the damage, such as transverse crack and delamination [10], particularly in terms of how a ply failure affects the neighboring plies [11, 12]. This approach holds significant potential for accurately describing the phenomena observed experimentally; however, it relies on sophisticated finite element models combined with highly non-linear material behaviors. Consequently, this often results in high computational costs, limiting the applicability of these methods for parametric studies or optimization.

The coupled criterion (CC), introduced by Leguillon in [13, 14], provides an efficient approach to address this challenge while preserving a discrete representation of the damage. It requires only a few elastic calculations to compute the stress field in the plane of the potential crack and the energy released by the crack initiation. It has been applied on composite materials in order to study several of the aforementioned issues [15]. The CC was used to study crack initiation in open hole composite plates [16–19] or in fastened joints composites [20] (recommendation #1 underlined at the beginning of this introduction and taken from the Military Handbook). Regarding composite laminates, the focus was mainly made on transverse cracking in 90° plies (i.e. when the loading direction is perpendicular to the fiber direction) and the effect of the number of grouped plies on the apparent strength (recommandation #2). This topic was studied in 2D [14, 21–23] or 3D [24, 25], also considering manufacturing thermal residual stresses [26, 27]. The CC has also been employed to investigate the onset of free-edge delamination in angle-ply laminates [28] (recommendation #3). Additionally, it has been applied to examine other types of composites. For instance, the CC has been utilized to study 3D transverse cracking and debonding in polymer matrix and glass fiber plain weave composites [29, 30], as well as 2D damage initiation and propagation in a ceramic matrix woven composite [31]. Furthermore, the failure mechanisms at the microscopic scale have been explored, including the debonding of a particle [32, 33] and the fiber-matrix interface [34–38] as well as the influence of the distance and angle between two neighbor fibers on interface debonding initiation [39].

A main difficulty in applying the CC in a 3D problem is determining the shape of the potential crack surface within a 3D geometry. A first way to implement the CC in 3D consists in assuming a crack path and applying stress and energy criteria corresponding to increasingly large cracks following this path. This strategy was adopted to study transverse cracking in laminates based on rectangular crack shapes [24, 26, 40] as well as partially elliptical crack shapes to simulate crack initiation at a V-notch [41–43], tunneling crack in layered ceramics [44] or free edge delamination in angle ply laminates [45]. Parameterized crack shapes may not be the optimal crack shapes, i.e. the ones for which the initiation loading is the minimum. A tentative to get crack shapes closer to the optimal ones consists in defining the crack fronts based on the stress isocontours [46–48]. This approach yields crack shapes that are similar to those observed experimentally in some configurations [49, 50] and enables the possible initiation crack shapes to be described by a single parameter, i.e. the crack surface or equivalently, the associated stress isocontour level. It results in an efficient way to avoid testing all possible crack shapes and was implemented for various 3D configurations [51–54].

It has been shown here that the CC is a pertinent tool to be used during an optimization process taking into account the recommendation of the Military Handbook. Current manufacturing methods, such as automated fiber placement, due to their precision and the intricate deposition paths they facilitate, should pave the way for increasingly complex and optimized stacking sequence such as Bouligand laminates which exhibits lower damage than classical laminates [55]. However, due to the lack of data, the absence of design rules, and conservatism arising from traditional practices, many industries continue to rely solely on 0°, ±45°, and 90° plies. Indeed, the use of varied ply orientations can lead to more complex damage scenarios. Literature has shown that the stacking sequence can significantly affect both the onset and progression of damage, not only in the initially failed ply but also in adjacent plies [56, 57].

The objective of this work is to study crack initiation in θ-plies that are adjacent to a 90° ply in a composite laminate. Experiments carried out on laminates having both 90° and θ°-plies are first presented in Section 2. The aim of this section is to highlight the effect of different parameters (ply thicknesses, angle differences between 90° and θ°-plies on the threshold for the initiation of transverse cracks in each ply. The finite element model and the CC procedure are described in Section 3. Section 4 focuses on evaluating different damage mechanisms such as crack initiation in (i) 90° ply and (ii) θ-ply, as well as (iii) debonding (delamination) between 90° ply and θ-ply. A qualitative comparison to the damage mechanisms observed experimentally is finally provided.

2. Experiments

The laminates under investigation were manufactured from Hexcel ply prepreg with AS4 carbon fibers and 8552 matrix. The panels were fabricated using a press machine, following the pressure and temperature cycles recommended by the prepreg manufacturer. One ply thickness corresponds to $t_{\text{ply}} = 150$ µm. The aim of this section is to highlight the influence of various parameters on the strain threshold for transverse crack initiation in the plies. To achieve this, different layups and stacking sequences were investigated:

- $[30_2/90_2/-30_2/0]_s$ is the base line (see Figure 1). It is expected that the 90° plies will crack first, and that any transverse cracking in the 30° plies will occur only at a loading level approaching failure.
- The $[70_2/90_2/-70_2/0]_s$ layup is designed to investigate whether a crack initiated in a misaligned ply can reinitiate cracking in an adjacent ply. It is important to note that, in this case, the doubled-thickness −70° plies are embedded within the laminate, while the other doubled-thickness 70° plies are located on the outer surface. As shown in [58], the position of the ply within the laminate (whether embedded or on the outer surface) influences the in-situ strength.
- The $[70_2/0/90_2/0/-70_2]_s$ layup is used to investigate the confinement effect of a highly oriented ply (0° in this case) on crack reinitiation. In this case, the outer plies are doubled-thickness 70° plies, while the ply located in the laminate's symmetry plane is a quadrupled-thickness −70° ply.
- The $[70_4/90_4/-70_4/0]_s$ layup is used to study the effect of ply thickness on crack reinitiation.

The specimen surfaces, where cracks are observed, are polished using silicon carbide paper with grit sizes ranging from P80 to P4000. A thin layer of white paint is then applied to these surfaces using a Posc® marker pen (Uni Mitsubishi Pencil). This thin layer of white paint facilitates crack detection, as cracks appear black against the white background. During the test, the gauge length is monitored using a high-resolution camera (4504 × 4504 pixels, with a 50 mm lens). Particular attention has been paid to the lighting to ensure that the light exposure is as even

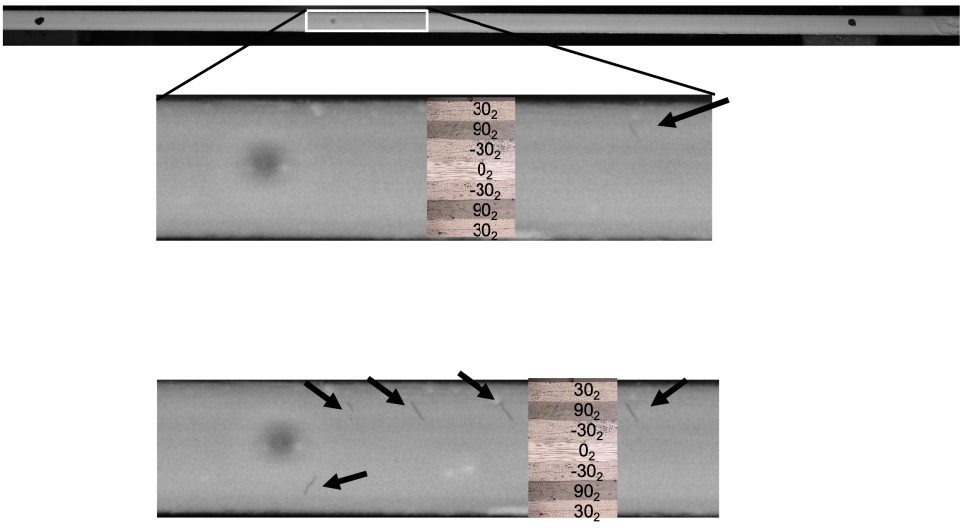

Figure 1. Location of the first cracks in the $[30_2/90_2/-30_2/0]_s$ laminate under two levels of external loading. A representative cross-sectional image has been included to indicate the ply locations (not visible due to the white paint layer). The arrows highlight the crack locations in the 90° plies.

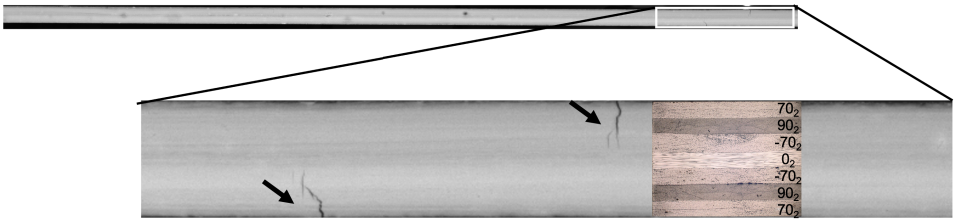

Figure 2. Location of the first cracks in the $[70_2/90_2/-70_2/0]_s$ laminate. A representative cross-sectional image has been included to indicate the ply locations (not visible due to the white paint layer). The arrows highlight the crack locations in the plies.

as possible and remains constant throughout the test. The aim is to detect the crack initiation in each ply and its location. The evolution in the number of cracks during testing falls outside the scope of this study.

The results obtained in the base line are shown in Figure 1. The first crack is initiated in the 90_2 plies. The number of cracks in these plies increases until final failure occurs, driven by delamination (between the 90° plies and the ±30° plies) and fiber failure in the 0° plies.

If the ±30 plies are replaced by ±70 plies, ($[70_2/90_2/-70_2/0]_s$) the scenario changes significantly. The initial failures occur simultaneously in all off-axis plies, namely the outer 70° plies, the 90° plies, and the −70° plies (see Figure 2). It is important to note that cracks in adjacent plies are interconnected, suggesting that a crack initiated in one ply may lead to the initiation of a crack in an adjacent ply.

When the 0° plies are placed between the 90° plies and the ±70° plies (as in the $[70_2/0/90_2/0/-70_2]_s$ laminate), transverse cracks initiate in the ±70° plies (Figure 3a). The locations of cracks in the outer doubled-thickness 70° plies differ significantly from those in the quadrupled-thickness −70° ply. The first cracks in the 90° plies initiate at a slightly higher

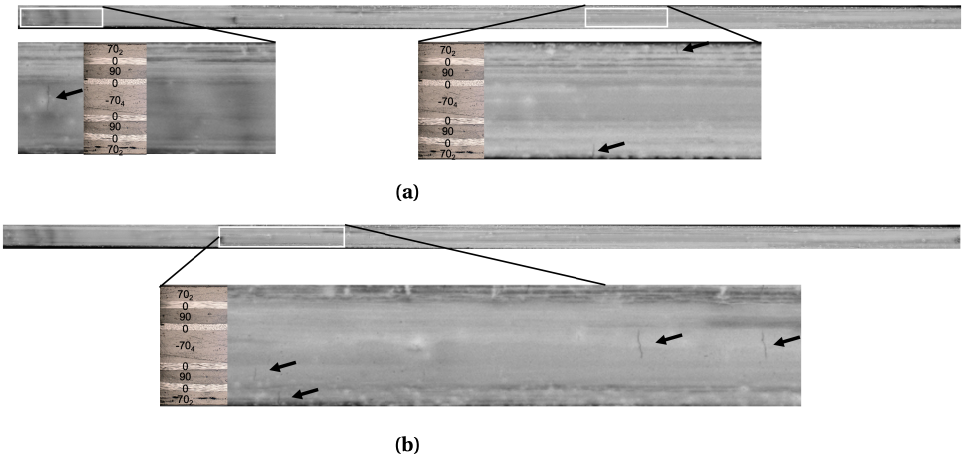

Figure 3. Location of the cracks in the $[70_2/0/90_2/0/-70_2]_s$ laminate. (a) Initial cracks in the ±70° plies and (b) first crack in the 90° ply, occurring at a higher load. A representative cross-sectional image indicates ply locations (not visible due to the white paint layer). The arrows highlight crack locations within the plies.

applied load (see Figure 3b). The crack locations in the plies appear random, with no observable connection between cracks in different plies.

To conclude this experimental section, it is important to note that, on the one hand, when the angular difference between two adjacent plies is large, a matrix crack in the more misaligned ply does not initiate a crack in the adjacent ply, as in the baseline case $[30_2/90_2/-30_2/0]_s$. On the other hand, when the mismatch angle between two adjacent plies is small, a crack in one ply can initiate interconnected cracks in the adjacent plies, as observed in the $[70_n/90_n/-70_n/0]_s$ laminate with $n = 2$ or 4, a phenomenon not predicted by classical design approaches. A single ply with a large mismatch angle (in this case, the 0° ply between the ±70° and 90° plies) could prevent this phenomenon. Another notable result concerns the effect of ply thickness: in the $[70_2/0/90_2/0/-70_2]_s$ laminate, the first matrix cracks appear in the outer doubled-thickness 70° plies and the quadrupled-thickness −70° ply, rather than in the doubled-thickness 90° ply, which would be expected to fail first according to a simple failure criterion. The various observed mechanisms will be examined in the following sections using the CC.

3. Fracture modeling and simulation

3.1. *The coupled criterion*

The CC states that crack initiation occurs if the two following conditions are met:

- The incremental energy release rate ($\mathscr{G}_{inc}$), i.e. the ratio between the elastic strain energy release ($-\Delta W_{el}(S) = W_{el}(0) - W_{el}(S)$) due to the initiation of a crack and its surface (S) must be larger than the material critical energy release rate $\mathscr{G}_c$: $\mathscr{G}_{inc} \geq \mathscr{G}_c$
- The stress over the whole crack path prior to initiation must be sufficiently large. In homogeneous isotropic materials, it reverts to comparing the opening stress to the tensile strength. However, in anisotropic materials such as composite laminates, or for interfaces subjected to mixed mode loadings, a criterion combining the opening (σ_{nn}) and shear (σ_{nt}) stress components and the corresponding strengths can be used. For a lamina under tensile loading, the transverse crack initiation criterion can be described

using a Hashin-based failure criterion: $f(\underline{\sigma}, Y_t, S_c) = \sqrt{(\sigma_{nn}/Y_t)^2 + (\sigma_{nt}/S_c)^2} \geq 1$ where σ_{nn} and σ_{nt} represent the transverse and shear components of the stress tensor in the ply coordinate system. The parameters Y_t and S_c denote the transverse tensile strength and the shear strength, respectively.

Under linear elasticity and small deformation assumptions, the stress components are proportional to the applied strain (denoted ε_0) and the energy is proportional to the square applied strain. These conditions write:

$$\begin{cases} \sigma_{eq} = \sqrt{(\sigma_{nn})^2 + \left(\dfrac{\sigma_{nt}}{\alpha}\right)^2} = \xi(S)\varepsilon_0 \geq \sigma_c \\ \mathscr{G}_{inc} = A(S)\varepsilon_0^2 \geqslant \mathscr{G}_c \end{cases} \tag{1}$$

where $\alpha = S_c/Y_t$, $\sigma_c = Y_t$ and ξ and A are functions depending on the geometry and material properties. Note that in the following, we study configurations in which the stress field in the ply is either uniform (Sections 4.1 and 4.2) or present a gradient (Section 4.4) The strain that must be prescribed in order to fulfill either the stress or the energy conditions can be calculated from Equation (1):

$$\begin{cases} \varepsilon_0^{\text{stress}}(S) = \dfrac{\sigma_c}{\xi(S)} \\ \varepsilon_0^{\text{energy}}(S) = \sqrt{\dfrac{\mathscr{G}_c}{A(S)}} \end{cases} \tag{2}$$

For a given crack surface S, the strain that must be prescribed in order to fulfill Equation (1) is the maximum between $\varepsilon_0^{\text{stress}}(S)$ and $\varepsilon_0^{\text{energy}}(S)$. The applied strain at initiation ε_c is thus determined for the crack surface S_c that minimizes the applied strain:

$$\begin{cases} \varepsilon_c = \min\limits_S(\max(\varepsilon_0^{\text{stress}}(S), \varepsilon_0^{\text{energy}}(S))) \\ S_c = \arg\min\limits_S(\max(\varepsilon_0^{\text{stress}}(S), \varepsilon_0^{\text{energy}}(S))) \end{cases} \tag{3}$$

3.2. *Finite element model of laminates*

The configuration under investigation is $[0_n/-\theta_n/\theta_n/90_n]_s$, except in Section 4.4 where $[-\theta_n/\theta_n/0_n/90_n]_s$ stacking is studied to highlight the influence of the presence of a 0° ply in between 90° and θ° plies. Even if the stacking sequences studied numerically slightly differ from the tested ones, they allow assessing the different damage mechanisms observed experimentally. The FE models presented in the following are set-up using Abaqus™ Standard. Due to the loading and geometry symmetry, only half the laminate thickness is modeled. The thickness of n plies is denoted t, so that $t = nt_{ply}$. It means that when studying θ-ply crack initiation, one crack is present in the n θ-plies (thickness t) in the FE model, which actually represents the simultaneous cracking of the two sets of n θ-plies by symmetry. In addition, when studying 90° ply crack initiation, one crack is present in the n 90° plies (thickness t) in the FE model, which actually represents cracking in a set of $2n$ 90° consecutive plies by symmetry since the 90° ply lies on the symmetry plane. Crack opening for all the studied mechanisms (transverse cracking in a 90° ply, in θ-ply or debonding) are simulated by doubling the nodes along the corresponding surface. The ply angle refers to the angle formed between the loading direction and the fiber orientation within the ply. Since crack paths are oriented by the microstructure, they are likely to follow the fiber direction therefore cracks in θ-ply form a θ angle with respect to the loading direction. The material orientation of each ply is assigned and the same ply properties are defined in the corresponding ply local axis system. The transversely isotropic ply properties are $E_L = 127$ GPa, $E_T = 9.2$ GPa, $\nu_{LT} = 0.302$, $\nu_{TT} = 0.4$, $G_{LT} = 4.8$ GPa [27, 59], where the index L denotes the longitudinal fiber direction and T the direction perpendicular to the fibers in the ply plane. The ply

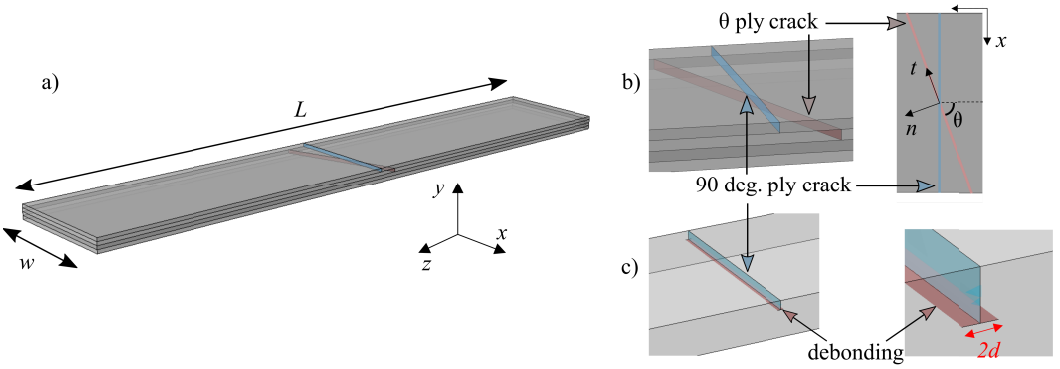

Figure 4. Geometry and dimensions of (a) the tested specimens and of two possible mechanisms occurring after transverse crack initiation in a 90° ply: (b) cracking in θ-ply or (c) debonding between 90° and θ-ply. The loading direction is along $\vec{z}$.

transverse tensile and shear strengths are respectively $Y_t = 63.9$ MPa and $S_c = 91$ MPa, the ply critical energy release rate is 248 J/m^2 [27], which corresponds to transverse crack propagation under opening mode. Boundary conditions are set-up as imposed displacement on the specimen faces along the tensile loading direction (z in the Figure 4). Due to the symmetry of the laminate, only half of the layup is modeled, with symmetric boundary conditions applied along the plane $(O\vec{x},\vec{z})$. The meshes are made of 10-nodes quadratic tetrahedrons, the mesh size being refined in the vicinity of the crack or debonding locations, resulting in meshes with around 250,000 nodes. The mesh size is chosen so that a finer mesh provides a similar initiation loading.

3.3. *Transverse crack initiation*

The main difference between 2D and 3D simulation of transverse crack initiation in laminates arises from the fact that the stress field is not perfectly homogeneous in the whole ply but only in the ply center, the stress increasing closer to the ply free edge. Nevertheless, it was shown by Garcia et al. [24] that the 2D or the 3D applications of the CC for transverse crack initiation leads to similar initiation strain, especially for plies thinner than the Irwin's length $\ell_{\text{mat}} = E_T \mathcal{G}_c/\sigma_c^2$. The differences slightly increase with increasing ply thickness, they however remain smaller than 10%. Therefore, in this case it is possible to simplify the 3D application of the CC for transverse crack initiation by neglecting the stress variation near the 90° ply free edge and considering a constant homogeneous stress within the ply. Under this assumption, Equation (3) reduces to:

$$\varepsilon_c = \max(\varepsilon_0^{\text{stress}}(S_{90}), \varepsilon_0^{\text{energy}}(S_{90})) = \max\left(\frac{\sigma_c}{\xi_{90}(S_{90})}, \sqrt{\frac{\mathcal{G}_c}{A_{90}(S_{90})}}\right) \tag{4}$$

where $S_{90} = w t_{90}$ is the surface of the crack crossing the whole ply. The functions $\xi_{90}(S_{90})$ and $A_{90}(S_{90})$ (corresponding to the functions ξ and A involved in Equation (2) in the case of transverse cracking) are computed from two FE calculations, one before crack opening that enables the calculation of the stress condition (and thus $\xi_{90}(S_{90})$) and the elastic strain energy before initiation, then crack surface nodes are unbuttoned to calculate the elastic strain energy release due to crack initiation and to deduce $A_{90}(S_{90})$. Transverse crack initiation loading is finally calculated from Equation (4).

3.4. *Debonding*

A possible damage mechanism occurring after transverse crack initiation is debonding between the 90° and θ-ply. This occurs because of the presence of a transverse crack in the 90° ply induces a stress singularity at the interface between both plies. It can be noted that under in-plane tensile loading, the interface is parallel to the loading direction thus debonding is not likely to occur without the presence of a crack in a surrounding ply. For the sake of simplicity, we assume that symmetric debonding occurs ahead of the transverse crack and along the whole ply width. This assumption allows us to describe the inter-ply debonding by only one parameter, namely the debonding length $2d$, the corresponding debonding surface being calculated as $S_{\mathrm{d}} = 2d\,w$, where w is the sample width. Thus, the CC for debonding length calculation can be applied following the reasoning described in Section 3.1. We make the hypothesis that the same material strength and fracture toughness as for transverse crack can be used in the case of debonding. This is justified by the fact that both mechanisms involve matrix cracking and fibre-matrix debonding at the microscopic scale. The function ξ_{d} and A_{d} (corresponding to the functions ξ and A involved in Equation (2) in the case of inter-ply debonding) are computed based on FE calculations for several debonding lengths. Since debonding occurs after transverse crack initiation, two possible cases may arise:

- If both the stress and the energy criteria are fulfilled for the loading corresponding to 90° ply transverse crack initiation, thus debonding is likely to occur instantaneously after transverse crack initiation.
- Otherwise, no debonding is observed when the transverse crack initiates so that the loading must be increased in order to initiate a debonding ahead of the transverse crack, the imposed debonding initiation strain can be calculated from Equation (3).

3.5. *Re-initiation in θ-ply*

Another possible damage mechanism occurring after transverse crack initiation is cracking in the θ-ply (Figure 2). In next section we study different scenarii, namely crack initiation in θ-ply alone, simultaneous crack initiation in 90° and θ-ply, or crack initiation in 90° followed by crack re-initiation mechanism in θ ply. For crack initiation in θ-ply alone, the exact same approach as for 90° ply crack initiation presented in Section 3.3 is adopted. For simultaneous crack initiation in 90° and θ-ply, a similar formulation as in Section 3.3 is adopted, except that the elastic strain energy release is calculated for a total crack surface which is the sum of both 90° and θ ply cracks.

The main difference in the CC implementation compared to the two previous scenarii arises for crack re-initiation in θ-ply. This is mainly due to the fact that the presence of a transverse crack in the 90° ply induces a stress singularity at the crack tip, i.e. at the interface between 90° and θ-ply, which results in a heterogeneous stress field in θ-ply. Therefore, the CC can be applied to assess crack re-initiation in θ-ply after the nucleation of a first transverse crack in the 90° ply. The stress heterogeneity in the θ-ply prevents us to adopt a simplified application of the CC and 3D crack initiation has to be studied. The critical step in the 3D CC application concerns the definition of the possible initiation crack shapes. We follow the approach proposed in [47–50, 52] to define the possible crack shapes based on the stress criterion isocontours (Figure 5). The main interest of this method is the definition of a unique relation between the stress level and the crack surface. Besides, for a given crack size, the stress criterion is strictly fulfilled since the crack shape is defined from the stress criterion isocontour. The corresponding crack surface is calculated based on the face area of the FE mesh elements attached to the crack. For a given configuration including a θ-ply, the functions ξ_θ and A_θ (corresponding to the functions ξ and A involved in Equation (2) in the case of crack re-initiation in θ-ply after a first transverse crack initiation in the

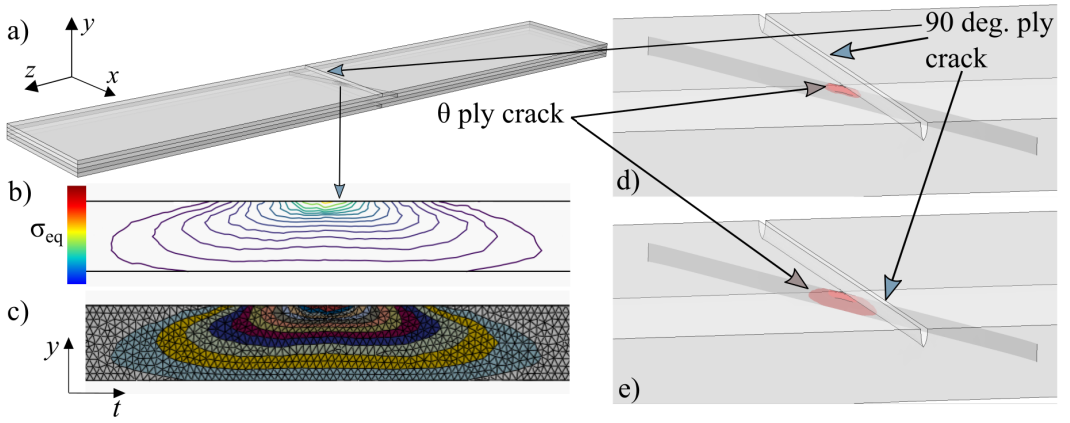

Figure 5. (a) Geometry including both 90° and θ-ply cracks. (b) Stress criterion isovalues in θ-ply after 90° ply crack initiation and (c) corresponding mesh including the stress criterion isocontour based possible crack shapes, (d)–(e) crack visualization in θ-ply.

90° ply) are computed by successively unbuttoning the crack nodes corresponding to decreasing stress isovalues or equivalently increasing crack surfaces. The re-initiation crack surface and imposed strain are finally determined by solving Equation (3). In the sequel, the numerical results corresponding to the different damage mechanisms are presented.

4. Results

We recall that the configuration under investigation is $[0_n/-\theta_n/\theta_n/90_n]_s$, except in Section 4.4 where $[-\theta_n/\theta_n/0_n/90_n]_s$ stacking is studied to highlight the influence of the presence of a 0° ply in between 90° and θ° plies.

4.1. *Crack initiation in 90° or θ ° ply*

We first study transverse crack initiation in 90° or θ° ply. The CC enables the calculation of the strain that must be imposed in order to fulfill the stress criterion, the energy criterion, or both (Figure 6a). Crack initiation in a thick enough ($t > 0.6$ mm) 90° ply is controlled by the stress criterion. Indeed, a thick ply stores a sufficient amount of elastic energy that could be used to form a crack for imposed strain smaller than the imposed strain required to fulfill the stress criterion. Therefore, crack initiation occurs as soon as the stress criterion is fulfilled. This is not the case for a thin ply, for which not enough energy is available to create the crack when the stress criterion is fulfilled. Therefore, it results in a larger crack initiation imposed strain which corresponds to the strain required to fulfill the energy criterion. Figure 6b shows the 90° crack initiation imposed strain for several θ-ply configurations. The larger the disorientation between the 90° ply and the θ-ply, the larger the initiation imposed strain, even if the difference remains smaller than 10% for the studied configurations.

First crack initiation in a θ-ply is also studied and the variation of the initiation strain as a function the ply thickness is shown in Figure 6c. Whatever the ply orientation, the transition between energy-driven and stress-driven crack initiation is observed depending on the ply thickness. For a given ply thickness, the larger the ply misorientation, the larger the imposed strain at initiation. It can be concluded that if the θ-ply is not located at the specimen surface, 90° ply crack initiation is likely to be the first observed damage mechanism. In case the θ-ply

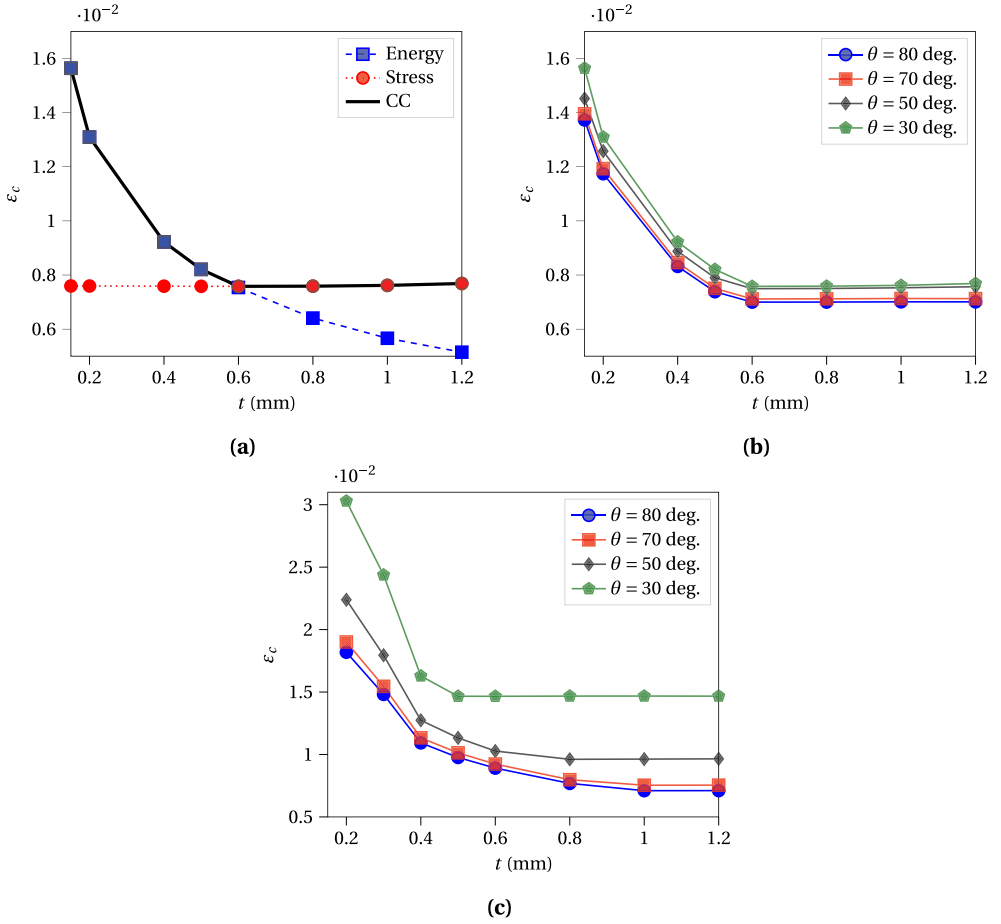

Figure 6. (a) Imposed strain to fulfill the stress (circles, dotted line), the energy (squares, dashed line) or both (solid line) criteria corresponding to 90° ply crack initiation as a function of the ply thickness for $\theta = 30°$ ply orientation. (b) Imposed strain at 90° ply crack initiation as a function of the ply thickness for several θ-ply orientations of the adjacent ply. (c) Imposed strain at θ-ply crack initiation as a function of the ply thickness for several θ-ply orientations.

is located at the specimen surface, crack initiation in θ-ply may be more favorable than crack initiation in inner 90° depending on the ply thickness, as shown in Section 2.

For plies thicker than 0.6 mm, the stress criterion is fulfilled in the 90° ply at the crack initiation imposed strain, however it is not fulfilled in θ-ply because of the ply disorientation with respect to the loading direction. However, for plies thinner than 0.6 mm, crack initiation is driven by the energy criterion which means that the imposed strain may be large enough so that the stress criterion is fulfilled not only for the 90° ply but also for the θ-ply. Thus, another cracking mechanism could be envisioned, namely simultaneous crack initiation in both 90° ply and θ-ply.

4.2. *Simultaneous crack initiation in 90° ply and θ-ply*

The CC is applied in order to determine if simultaneous 90° ply and θ-ply crack initiation may occur instead of 90° ply crack initiation only for thin plies. Figure 7 shows the corresponding

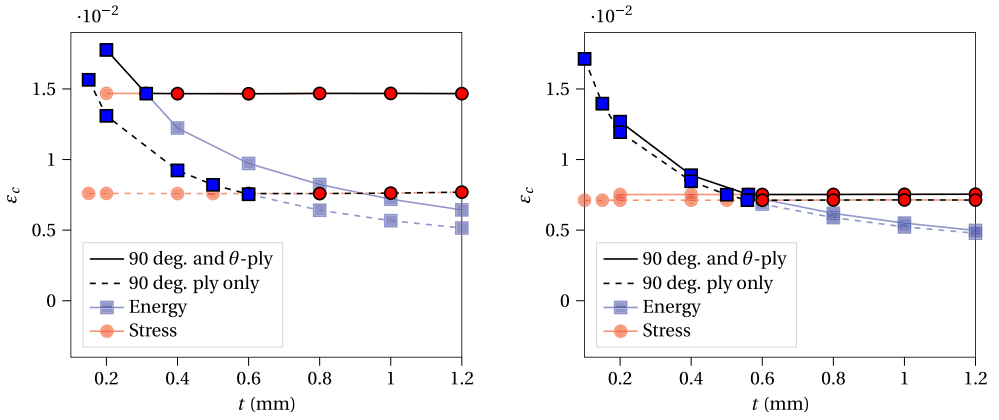

Figure 7. Imposed strain to fulfill the stress (circles), the energy (squares) or both criteria corresponding to either 90° ply crack initiation (dashed line) or simultaneous 90° and θ-ply crack initiation (solid line) as a function of the ply thickness for (a) $\theta = 30°$ and (b) $\theta = 70°$.

imposed strain to fulfill the stress criterion, the energy criterion or both for configurations with 30° or 70° θ-ply.

The imposed strain required for crack initiation in thick plies is larger for simultaneous crack initiation than for 90° ply crack initiation only, thus resulting in a larger initiation imposed strain. Whatever the ply thickness and orientation, the imposed strain to fulfill the energy criterion is smaller for 90° ply crack initiation only than for simultaneous initiation. Therefore, simultaneous crack initiation in both plies is not likely to occur, the mechanism of crack re-initiation in θ-ply after first crack initiation in the 90° ply is therefore selected in the sequel.

4.3. *Debonding ahead of a 90°-ply crack*

Debonding at the interface between the 90° ply and the θ-ply is not likely to occur before any intra-ply cracking because the stress criterion is not fulfilled since the interface between both plies is parallel to the loading direction. However, the presence of a transverse crack in the 90° ply induces a stress singularity at the ply interface and thus enables a possible debonding between plies. The CC is applied in order to evaluate if debonding is likely to occur just after 90°, as depicted in Figure 4c. ply crack initiation or if a larger imposed strain is required. Two configurations arise leading either to a possible debonding or not. If the imposed strain is large enough so that there exists at least a debonding surface for which both criteria are fulfilled, a possible debonding may be observed as a consequence of transverse crack initiation and it occurs at the same imposed strain. Otherwise, if both criteria are not fulfilled for any debonding surface, debonding ahead of the transverse crack is not expected without imposed strain increase. The CC enables the calculation of the imposed strain required to initiate a debonding, its variation as a function of the ply thickness is shown in Figure 8 together with transverse crack initiation strain for $\theta = 50°$ and $\theta = 70°$ ply orientations.

For the studied configurations, debonding is not likely to occur just after transverse crack initiation except for the largest ply thicknesses θ-ply orientation close enough to 90°. Otherwise, the imposed strain must be increased in order to promote debonding ahead of the transverse crack.

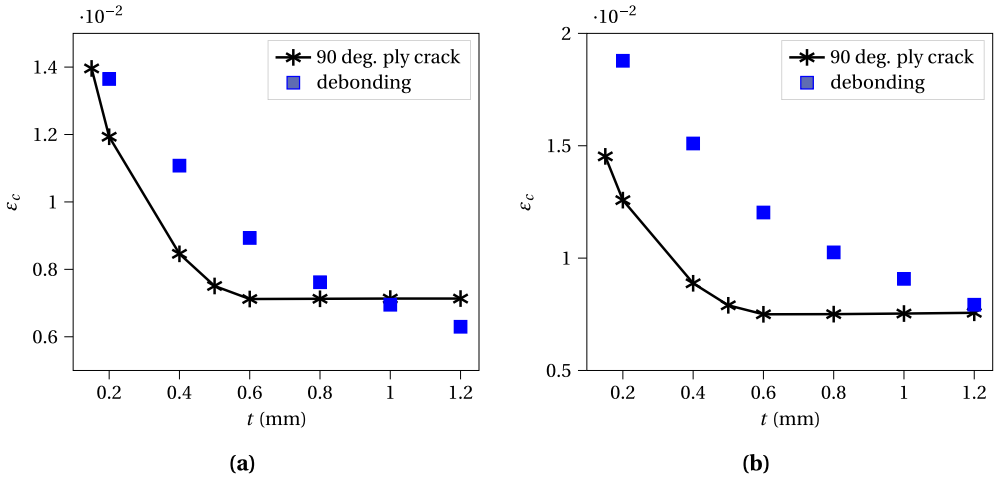

Figure 8. Imposed strain at debonding ahead of a transverse crack for (a) $\theta = 70°$ and $\theta = 50°$ ply orientations.

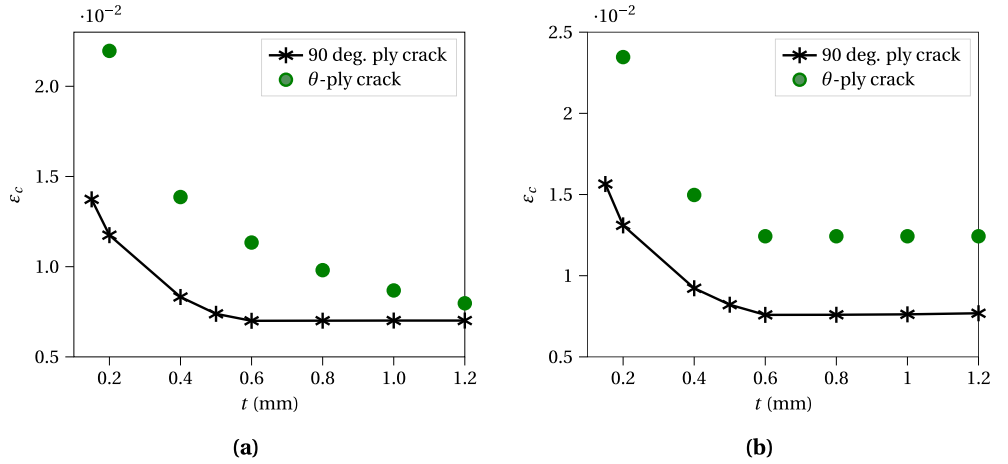

Figure 9. Imposed strain at crack re-initiation in θ-ply after the first crack initiation in the 90° ply as a function of the ply thickness for (a) $\theta = 80°$. (b) $\theta = 50°$ in case the θ-ply and the 90° ply are separated by a 0° ply.

4.4. *θ-ply crack re-initiation*

We first study the case for which the 90° ply and the θ-ply are separated by a 0° ply. The first damage mechanism is transverse crack initiation in the 90° ply. Similarly to previous analysis, simultaneous crack initiation in 90° ply and θ-ply is not likely to occur because it is energetically less favorable. Contrary to the configuration for which the 90° ply and the θ-ply are adjacent, crack initiation in the 90° ply does not induce any stress concentration in θ-ply. Therefore, crack re-initiation in the θ° ply may occur if both the stress and the energy criteria are fulfilled, i.e. for a larger imposed strain than the one corresponding to 90° ply crack initiation (Figure 9). If the 90° ply and the θ-ply are separated by a 0° ply, crack re-initiation is thus not likely to be observed immediately after the first crack initiation whatever the ply thickness or θ-ply orientation.

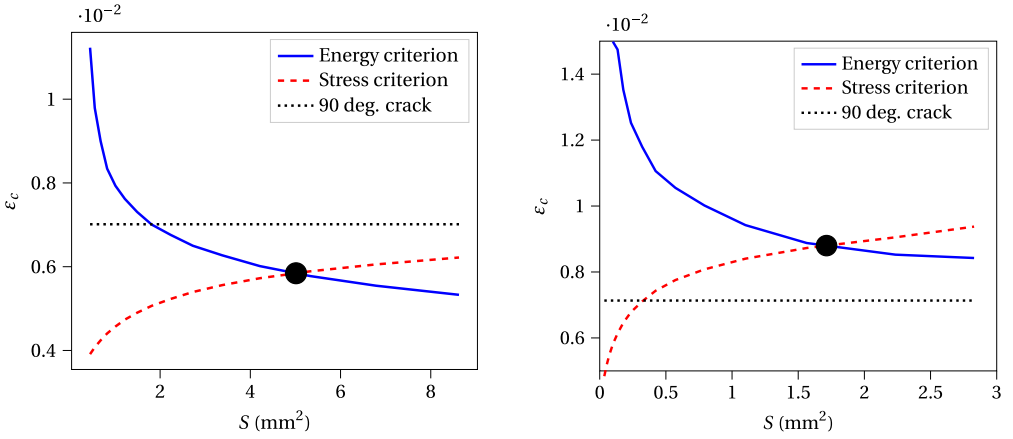

Figure 10. Imposed strain that must be prescribed in order to fulfill stress (dashed line) and energy (solid line) criteria and corresponding minimum imposed strain and crack surface for which both criteria are fulfilled (circle) for $t = 1$ mm ply thickness and (a) $\theta = 80°$ or (b) $\theta = 50°$.

We now study the configuration for which the 90° ply and the θ-ply are adjacent. A first crack initiation in the 90° ply induces a stress singularity at the crack tip located at the interface between both plies and thus a stress gradient in the θ-ply (Figure 5) which may promote θ-ply crack re-initiation. We use the term of re-initiation because we concluded previously that θ-ply crack initiation cannot occur simutaneously or before 90° ply crack initiation. Therefore, this mechanism is a consequence of a first crack initiation in the 90° ply which induces the stress singularity necessary to further enable a possible crack re-initiation. The stress and the energy criterion can be implemented in order to determine θ-ply re-initiation imposed strain as well as crack surface (Figure 10). If there exists a crack surface for which both criteria are fulfilled at the imposed strain corresponding to a first crack initiation in the 90° ply (Figure 10a), crack initiation immediately following 90° ply crack initiation is likely to occur. From an experimental point of view, it is difficult to detect both mechanisms separately since they are expected to occur sequentially in a short time interval. However, it is possible to observe whether a crack nucleated or not in θ-ply just after 90° crack initiation.

If fulfilling both criteria requires an imposed strain larger than the imposed strain at 90° ply crack initiation (Figure 10b), crack re-initiation in θ-ply is not likely to occur immediately after 90° ply initiation but requires an increase in the imposed strain. From an experimental point of view, it means that single crack initiation in the 90° ply is likely to be observed before θ-ply crack re-initiation for a larger imposed strain.

In both cases, it can be noted that the incremental energy release rate (and thus the differential energy release rate $\mathcal{G}$) is an increasing function of the crack surface. Therefore, as soon as crack initiation occurs, unstable crack propagation is likely to occur ($\mathcal{G} \geqslant \mathcal{G}_c$ and $\mathrm{d}\mathcal{G}/\mathrm{d}S \geqslant 0$). It means that without any increase in the imposed strain, the initiated crack will instantaneously grow through the entire ply. Therefore, the crack is expected to be observed experimentally on the specimen surface.

Figure 11 shows the imposed strain at θ-ply crack re-initiation as a function of the ply thickness and orientation. The imposed strain at crack re-initiation decreases with increasing ply thickness or decreasing ply disorientation (difference between 90° and the ply orientation θ).

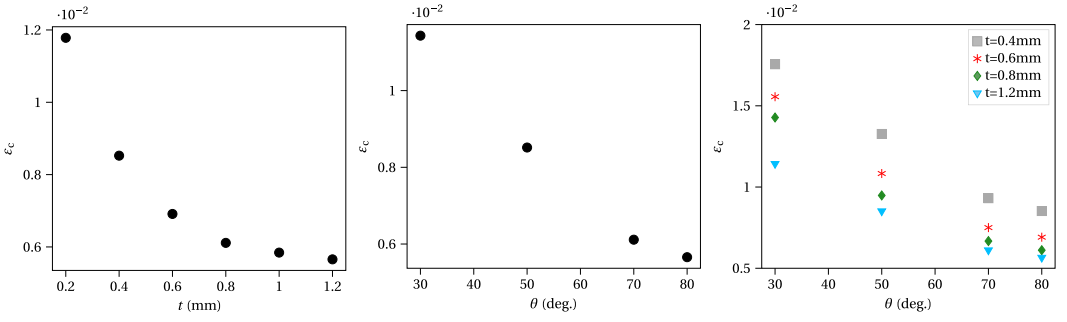

Figure 11. Imposed strain at θ-ply crack re-initiation as a function of (a) the ply thickness for $\theta = 70°$ and of the ply angle for (b) $t = 1.2$ mm or (c) for several ply thicknesses.

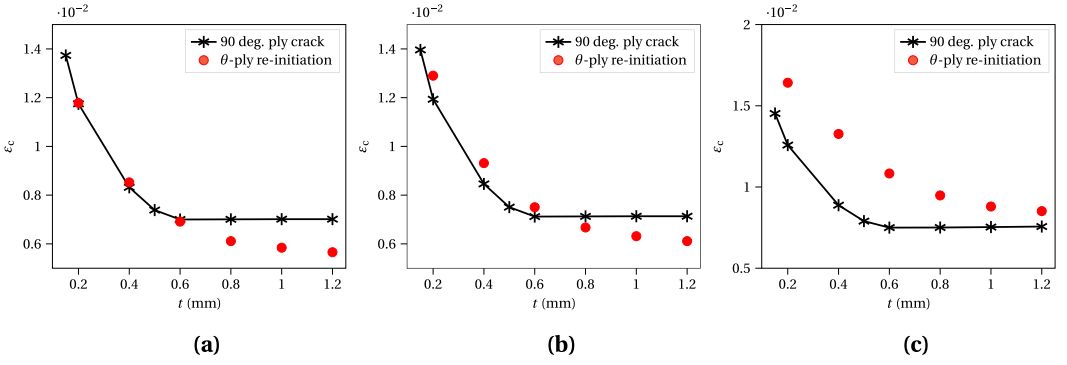

Figure 12. Imposed strain at θ-ply crack re-initiation as a function of the ply thickness compared to the imposed strain at 90° crack initiation for (a) $\theta = 80°$, (b) $\theta = 70°$, (c) $\theta = 50°$.

Figure 12 shows θ-ply crack re-initiation imposed strain as a function of the ply thickness compared to the imposed strain at 90° ply crack initiation for several ply orientations, resulting in different possible scenarii. If the ply orientation is close to 90° (Figure 12a), crack re-initiation is likely to occur whatever the ply thickness. We thus expect to observe experimentally cracks in both plies just after initiation. On the contrary, if the ply disorientation with respect to 90° is too large (Figure 12c), no crack re-initiation is expected to occur just after transverse crack initiation, it would require a larger imposed loading. For intermediate orientations (Figure 12b), crack re-initiation is expected to occur just after transverse crack initiation only for thick enough plies ($t > 0.6$ mm).

We finally compare the three damage mechanisms, namely transverse crack initiation, debonding and θ-ply crack re-initiation (Figure 13) for several ply orientation. For ply orientation close to 90° (Figure 13a) and thick enough plies ($t > 1$ mm), both debonding or crack re-initiation are likely to occur just after transverse crack initiation. For thin plies ($t < 6$ mm), the damage sequence that is likely to occur is the following order:

(i) transverse crack initiation
(ii) θ-ply crack re-initiation at a slightly larger imposed strain
(iii) possible inter-ply debonding.

For intermediate ply thicknesses, crack re-initiation is likely to occur just after transverse crack initiation without any imposed strain increase, and debonding may occur for a larger imposed

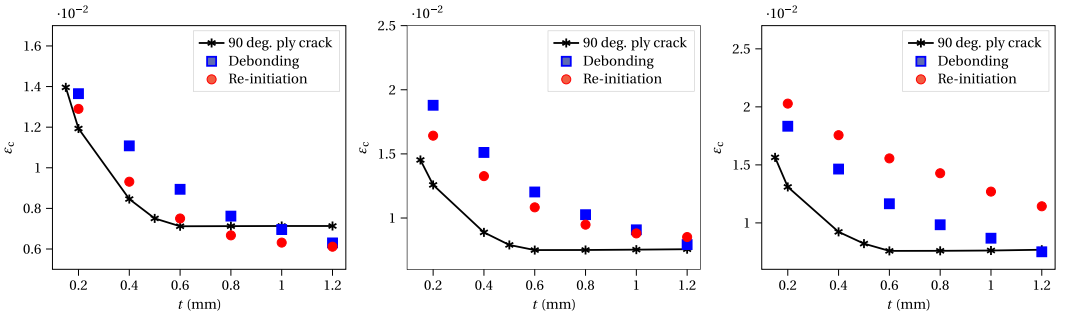

Figure 13. Imposed strain at (i) 90° ply transverse cracking (solid line), (ii) inter-ply debonding (square symbols) or (iii) θ-ply crack re-initiation (disk symbols) as a function of the ply thickness t obtained for (a) $\theta = 70°$, (b) $\theta = 50°$, (c) $\theta = 30°$.

strain. For ply orientation different enough from 90° (Figure 13c), whatever the ply thickness, the most likely damage sequence is transverse crack initiation followed by debonding at a larger imposed strain. Crack re-initiation could possibly occur at a larger imposed strain. For intermediate ply orientation (Figure 13b), whatever the ply thickness, the most likely damage sequence is transverse crack initiation followed by crack re-initiation at a larger imposed strain. The observed change in the predicted sequence of damage mechanisms for different theta ply angles can be explained due to the critical strain for re-initiation changes a lot with θ ply misorientation, whereas the critical strain for debonding changes much less.

5. Discussions and conclusion

Composite materials offer significant potential for optimization in terms of the number of plies, ply orientations, and stacking sequences. However, the potential offered by new manufacturing techniques, such as automated fibre placement, is not being fully exploited due to the conservative practices currently in place. These practices are used to address the lack of predictive tools for mechanisms that may lead to domino cracking through the thickness of the laminate. In this article, we propose an approach based on the use of the coupled criterion, implemented using 3D finite element calculations.

To attain this objective, numerical simulations were conducted to investigate the damage mechanisms occurring in laminates with θ-plies adjacent to 90° plies. The results indicate that the damage sequence depends on the orientation mismatch between the 90° ply and the θ-ply. Several mechanisms can be identified. The deformation leading to the initiation of the first crack depends on both the ply thickness and the angle between the fiber orientation in the ply and the applied loading direction. For equivalent ply thicknesses, the greater the misorientation of the ply with respect to the loading axis, the smaller the deformation leading to the initiation of the first crack. However, this conclusion is called into question by the thickness of the plies. For instance, a thin ply oriented at 90° may undergo greater deformation before failure than a thicker, less misoriented ply. This conclusion is supported by experimental results. In the $[70_2/0/90_2/0/-70_2]_s$ laminate, the first cracks are initiated almost simultaneously in the doubled-thickness outer 70° ply and in the quadrupled-thickness inner −70° ply.

This mechanism possibly enables two other mechanisms (that cannot occur without the presence of this first crack), namely either inter-ply debonding or crack re-initiation in adjacent θ-ply. These two mechanisms may possibly occur at the same imposed loading as the one

necessary for transverse crack initiation, if the ply is the θ-ply orientation close enough to 90° This conclusion is supported by experimental results. In the $[70_2/0/90_2/-70_2/0]_s$ laminate, the first cracks are initiated simultaneously in the ±70° and 90° plies. Moreover, all the cracks in the adjacent plies are continuous. Based on the results obtained for the previous laminate, it can be concluded that the crack first initiates in the outer 70° ply, leading to the failure of the adjacent plies.

If the angle offset between two adjacent plies is large, the most likely mechanism is debonding at the interface, initiated at the tip of the transverse crack. As observed experimentally in the $[70_2/0/90_2/0/-70_2]_s$ layup, a highly oriented ply (0° in this case), acts as a barrier, preventing crack re-initiation.

This study thus provides insight towards optimal, less empirical and less restrictive design of laminate stacking sequences. The results presented in this article were obtained using a thermoset matrix composite. Future work will focus on extending this study to thermoplastic matrix composites, which have much higher critical energy release rates. Moreover, for the $[30_2/90_2/-30_2/0]_s$ laminate, the cracks in the 90° ply appear to be slightly inclined, which motivates the investigation of the underlying phenomenon.

Declaration of interests

The authors do not work for, advise, own shares in, or receive funds from any organization that could benefit from this article, and have declared no affiliations other than their research organizations.

Dedication

The manuscript was written through contributions of all authors. All authors have given approval to the final version of the manuscript.

Acknowledgment

This manuscript is dedicated to our friend and colleague Dominique Leguillon, whose remarkable contributions to the field of Fracture Mechanics—both through his groundbreaking research and his profound personal influence—continue to inspire us all.

References

[1] MIL-HDBK-17-3F, *Composite Materials Handbook Volume 3. Polymer Matrix Composites Materials Usage, Design, and Analysis*, SAE International: USA, 2012.

[2] A. Parvizi, K. W. Garrett and J. E. Bailey, "Constrained cracking in glass fibre-reinforced epoxy cross-ply laminates", *J. Mater. Sci.* **13** (1978), pp. 195–201.

[3] M. R. Wisnom, B. Khan and S. R. Hallett, "Size effects in unnotched tensile strength of unidirectional and quasi-isotropic carbon/epoxy composites", *Compos. Struct.* **84** (2008), no. 1, pp. 21–28.

[4] M. R. Wisnom and S. R. Hallett, "The role of delamination in strength, failure mechanism and hole size effect in open hole tensile tests on quasi-isotropic laminates", *Compos. A: Appl. Sci. Manuf.* **40** (2009), no. 4, pp. 335–342.

[5] L. Lagunegrand, T. Lorriot, R. Harry, H. Wargnier and J. M. Quenisset, "Initiation of free-edge delamination in composite laminates", *Compos. Sci. Technol.* **66** (2006), no. 10, pp. 1315–1327.

[6] F. X. Irisarri, D. H. Bassir, N. Carrère and J. F. Maire, "Multiobjective stacking sequence optimization for laminated composite structures", *Compos. Sci. Technol.* **69** (2009), no. 7, pp. 983–990.

[7] K. S. Pister and S. B. Dong, "Elastic bending of layered plates", *J. Eng. Mech. Div., Proc. Am. Soc. Civil Eng.* **85** (1959), no. EM4, pp. 1–12.

[8] S. W. Tsai and H. T. Hahn, *Introduction to Composite Materials*, CRC Press: USA, 1980.
[9] F. Laurin, N. Carrere and J. F. Maire, "A multiscale progressive failure approach for composite laminates based on thermodynamical viscoelastic and damage models", *Compos. A: Appl. Sci. Manuf.* **38** (2007), no. 1, pp. 198–209.
[10] E. Iarve, M. Gurvich, D. Mollenhauer, C. Rose and C. Dávila, "Mesh-independent matrix cracking and delamination modeling in laminated composites", *Int. J. Numer. Meth. Eng.* **88** (2011), no. 8, pp. 749–773.
[11] S. R. Hallett, B. G. Green, W. G. Jiang and M. R. Wisnom, "An experimental and numerical investigation into the damage mechanisms in notched composites", *Compos. A: Appl. Sci. Manuf.* **40** (2009), no. 5, pp. 613–624.
[12] P. Journoud, C. Bouvet, B. Castanié, F. Laurin and L. Ratsifandrihana, "Experimental and numerical analysis of unfolding failure of L-shaped CFRP specimens", *Compos. Struct.* **232** (2020), article no. 111563.
[13] D. Leguillon, "A criterion for crack nucleation at a notch in homogeneous materials", *C. R. Acad. Sci. - Ser. IIB - Mech.* **329** (2001), no. 2, pp. 97–102.
[14] D. Leguillon, "Strength or toughness? A criterion for crack onset at a notch", *Eur. J. Mech. - A/Solids* **21** (2002), no. 1, pp. 61–72.
[15] E. Martin, D. Leguillon and N. Carrère, "Finite fracture mechanics: a useful tool to analyze cracking mechanisms in composite materials", in *Multi-scale Modelling of the Structural Integrity: 50 Years of Carbon Fiber Composite Materials* (P. W. R. Beaumont and C. Soutis, eds.), Springer: USA, 2016, pp. 529–548.
[16] P. P. Camanho, G. H. Ercin, G. Catalanotti, S. Mahdi and P. Linde, "A finite fracture mechanics model for the prediction of the open-hole strength of composite laminates", *Compos. A: Appl. Sci. Manuf.* **43** (2012), pp. 1219–1225.
[17] E. Martin, D. Leguillon and N. Carrère, "A coupled strength and toughness criterion for the prediction of the open hole tensile strength of a composite plate", *Int. J. Sol. Struct.* **49** (2012), no. 26, pp. 3915–3922.
[18] E. Martin, D. Leguillon and N. Carrère, "An extension of the point-stress criterion based on a coupled stress and energy fulfilment: application to the prediction of the open-hole tensile strength of a composite plate", in *Woodhead Publishing Series in Composites Science and Engineering, Structural Integrity and Durability of Advanced Composites*, Woodhead Publishing: UK, 2015, pp. 425–444.
[19] J. Felger, N. Stein and W. Becker, "Mixed-mode fracture in open-hole composite plates of finite-width: An asymptotic coupled stress and energy approach", *Int. J. Solids Struct.* **122–123** (2017), pp. 14–24.
[20] G. Catalanotti and P. P. Camanho, "A semi-analytical method to predict net-tension failure of mechanically fastened joints in composite laminates", *Compos. Sci. Technol.* **76** (2013), pp. 69–76.
[21] N. Carrere, N. Tual, T. Bonnemains, E. Lolive and P. Davies, "Modelling of the damage development in carbon/epoxy laminates subjected to combined seawater ageing and mechanical loading", *Proc. Inst. Mech. Eng. L: J. Mater.: Des. Appl.* **232** (2016), no. 9, pp. 761–768.
[22] M. Kashtalyan, I. G. García and V. Mantič, "Coupled stress and energy criterion for multiple matrix cracking in cross-ply composite laminates", *Int. J. Sol. Struct.* **139–140** (2018), pp. 189–199.
[23] A. Doitrand, G. Molnár, D. Leguillon, E. Martin and N. Carrère, "Dynamic crack initiation assessment with the coupled criterion", *Eur. J. Mech. - A/Solids* **93** (2022), article no. 104483.
[24] I. G. García, B. J. Carter, A. R. Ingraffea and V. Mantič, "A numerical study of transverse cracking in cross-ply laminates by 3D finite fracture mechanics", *Compos. B Eng.* **95** (2016), pp. 475–487.
[25] J. Vereecke, C. Bois, J. C. Wahl, T. Briand, L. Ballère and F. Lavelle, "Explicit modelling of meso-scale damage in laminated composites – Comparison between finite fracture mechanics and cohesive zone model", *Compos. Sci. Technol.* **253** (2024), article no. 110640.
[26] I. G. García, V. Mantič and A. Blázquez, "The effect of residual thermal stresses on transverse cracking in cross-ply laminates: an application of the coupled criterion of the finite fracture mechanics", *Int. J. Fract.* **211** (2018), pp. 61–74.
[27] I. G. García, J. Justo, A. Simon and V. Mantič, "Experimental study of the size effect on transverse cracking in cross-ply laminates and comparison with the main theoretical models", *Mech. Mater.* **128** (2019), pp. 24–37.
[28] E. Martin, D. Leguillon and N. Carrere, "A twofold strength and toughness criterion for the onset of free-edge shear delamination in angle-ply laminates", *Int. J. Solids Struct.* **47** (2010), no. 9, pp. 1297–1305.
[29] A. Doitrand, C. Fagiano, N. Carrère, V. Chiaruttini and M. Hirsekorn, "Damage onset modeling in woven composites based on a coupled stress and energy criterion", *Eng. Fract. Mech.* **169** (2017), pp. 189–200.
[30] A. Doitrand, C. Fagiano, F. Hild, V. Chiaruttini, A. Mavel and M. Hirsekorn, "Mesoscale analysis of damage growth in woven composites", *Compos. A: Appl. Sci. Manuf.* **96** (2017), pp. 77–88.
[31] J. Li, E. Martin, D. Leguillon and C. Dupin, "A finite fracture model for the analysis of multi-cracking in woven ceramic matrix composites", *Compos. B Eng.* **139** (2018), pp. 75–83.
[32] T. Gentieu, J. Jumel, A. Catapano and J. Broughton, "Size effect in particle debonding: comparisons between finite fracture mechanics and cohesive zone model", *J. Compos. Mater.* **53** (2018), no. 14, pp. 1941–1954.
[33] E. Martin, D. Leguillon, A. Catapano and N. Carrère, "Prediction of interfacial debonding between stiff spherical particles and a soft matrix with the coupled criterion", *Theor. Appl. Fract. Mech.* **109** (2020), article no. 102749.

[34] V. Mantič, "Interface crack onset at a circular cylindrical inclusion under a remote transverse tension. Application of a coupled stress and energy criterion", *Int. J. Sol. Struct.* **46** (2009), pp. 1287–1304.

[35] V. Mantič and I. G. García, "Crack onset and growth at the fibre-matrix interface under a remote biaxial transverse load. application of a coupled stress and energy criterion", *Int. J. Sol. Struct.* **49** (2012), pp. 2273–2290.

[36] I. G. García, M. Paggi and V. Mantič, "Fiber-size effects on the onset of fiber–matrix debonding under transverse tension: A comparison between cohesive zone and finite fracture mechanics models", *Eng. Fract. Mech.* **115** (2014), pp. 96–110.

[37] M. Muñoz-Reja, L. Távara, V. Mantič and P. Cornetti, "Crack onset and propagation at fibre–matrix elastic interfaces under biaxial loading using finite fracture mechanics", *Compos. A: Appl. Sci. Manuf.* **82** (2016), no. x, pp. 267–278.

[38] H. Girard, A. Doitrand, B. Koohbor, R. G. Rinaldi, N. Godin and J. Bikard, *Comparison between 2D and 3D fiber-matrix debonding simulation for inverse identification of interface fracture properties*, preprint, 2024. Online at https://hal.science/hal-04431332.

[39] H. Girard, A. Doitrand, B. Koohbor, R. G. Rinaldi, N. Godin, D. Long and J. Bikard, "Influence of nearby fiber on fiber–matrix debonding: Coupled Criterion prediction and debonding shape determination", *J. Mech. Phys. Solids* **183** (2024), article no. 105498.

[40] Z. Hamam, N. Godin, P. Reynaud, C. Fusco, N. Carrére and A. Doitrand, "Transverse cracking induced acoustic emission in carbon fiber-epoxy matrix composite laminates", *Materials* **15** (2022), article no. 394.

[41] B. Mittelman and Z. Yosibash, "Asymptotic analysis of the potential energy difference because of a crack at a V-notch edge in a 3D domain", *Eng. Fract. Mech.* **131** (2014), pp. 232–256.

[42] B. Mittelman and Z. Yosibash, "Energy release rate cannot predict crack initiation orientation in domains with a sharp V-notch under mode III loading", *Eng. Fract. Mech.* **141** (2015), pp. 230–241.

[43] Z. Yosibash and B. Mittelman, "A 3-D failure initiation criterion from a sharp V-notch edge in elastic brittle structures", *Eur. J. Mech. A/Sol.* **60** (2016), pp. 70–94.

[44] R. Papšík, O. Ševeček, A. K. Hofer, I. Kraleva, J. Kreith and R. Bermejo, "Prediction of edge and tunnelling crack formation in layered ceramics using a stress-energy fracture criterion", *J. Eur. Ceram. Soc.* **43** (2023), no. 7, pp. 2928–2934.

[45] M. Burhan, T. Scalici, Z. Ullah, Z. Kazanci and G. Catalanotti, "A three-dimensional Finite Fracture Mechanics model to predict free edge delamination in angle-ply laminates", *Eng. Fract. Mech.* **306** (2024), article no. 110156.

[46] D. Leguillon, "An attempt to extend the 2D coupled criterion for crack nucleation in brittle materials to the 3D case", *Theor. Appl. Fract. Mech.* **74** (2014), pp. 7–17.

[47] A. Doitrand and D. Leguillon, "3D application of the coupled criterion to crack initiation prediction in epoxy/aluminum specimens under four point bending", *Int. J. Sol. Struct.* **143** (2018), pp. 175–182.

[48] A. Doitrand and D. Leguillon, "Comparison between 2D and 3D applications of the coupled criterion to crack initiation prediction in scarf adhesive joints", *Int. J. Adhes. Adhes.* **85** (2018), pp. 69–76.

[49] A. Doitrand and D. Leguillon, "Numerical modeling of the nucleation of facets ahead of a primary crack under modeI+III", *Int. J. Fract.* **123** (2018), no. 1, pp. 37–50.

[50] A. Doitrand, R. Estevez and D. Leguillon, "Experimental characterization and numerical modeling of crack initiation in rhombus hole PMMA specimens under compression", *Eur. J. Mech. Sol.* **76** (2019), pp. 290–299.

[51] O. Sevecek, J. Hanak, Z. Majer, D. Drdlik, Z. Chlup and M. Kotoul, "Prediction of the ceramic foam structure failure using a detailed finite element model", *Key Eng. Mater.* **827** (2019), pp. 222–227.

[52] A. Doitrand, R. Henry, H. Saad, S. Deville and S. Meille, "Determination of interface fracture properties by micro- and macro-scale experiments in nacre-like alumina", *J. Mech. Phy. Sol.* **145** (2020), article no. 104143.

[53] A. Doitrand, R. Henry, I. Zacharie-Aubrun, J.-M. Gatt and S. Meille, "UO_2 micron scale specimen fracture: parameter identification and influence of porosities", *Theor. Appl. Fract. Mech.* **108** (2020), article no. 102665.

[54] N. Carrère, A. Doitrand, E. Martin and D. Leguillon, "Theoretical study based on 2D assumptions of the influence of small pores on crack initiation in adhesively bonded joints", *Int. J. Adhes. Adhes.* **111** (2021), article no. 102979.

[55] J. Körbelin, P. Goralski, B. Kötter, F. Bittner, H. F. Endres and B. Fiedler, "Damage tolerance and notch sensitivity of bio-inspired thin-ply Bouligand structures", *Compos. C: Open Access* **5** (2021), article no. 100146.

[56] T. Yokozeki, T. Aoki and T. Ishikawa, "Consecutive matrix cracking in contiguous plies of composite laminates", *Int. J. Solids Struct.* **42** (2005), pp. 2785–2802.

[57] S. Kobayashi, N. Takeda, S. Ogihara and A. Kobayashi, "Effects of stacking sequence on the transverse cracking in quasi-isotropic interleaved CFRP laminates", in *Proceedings of the 1999 International Conference on Composite Materials, Paris, France*.

[58] P. P. Camanho, C. G. Dávila, S. T. Pinho, L. Iannucci and P. Robinson, "Prediction of in situ strengths and matrix cracking in composites under transverse tension and in-plane shear", *Compos. A: Appl. Sci. Manuf.* **37** (2006), pp. 165–176.

[59] K. Marlett, *Hexcel 8852 AS4 unidirectional prepreg at 190 gsm and 35% RC qualification material property data report*, tech. rep., National Institute for Aviation Research. Wichita State University: Wichita, Kansas, 2010.

ACADÉMIE DES SCIENCES
INSTITUT DE FRANCE

Comptes Rendus. Mécanique
2025, Vol. 353, p. 725-745
https://doi.org/10.5802/crmeca.302

Research article / *Article de recherche*

3D finite fracture mechanics under mode I loading: the flat elliptical crack

Mécanique de la rupture finie en 3D sous chargement en mode I : la fissure elliptique plane

Pietro Cornetti[*,a], **Vladislav Mantič**[b] **and Zohar Yosibash**[c]

[a] Department of Structural, Geotechnical and Building Engineering, Politecnico di Torino, Corso Duca degli Abruzzi 24, 10129 Torino, Italy

[b] Grupo de Elasticidad y Resistencia de Materiales, Escuela Técnica Superior de Ingeniería, Universidad de Sevilla, Camino de los Descubrimientos s/n, Sevilla, 41092, Spain

[c] Computational Mechanics and Experimental Biomechanics Lab, School of Mechanical Engineering, Iby and Aladar Fleischman Faculty of Engineering, Tel Aviv University, Ramat Aviv 69978, Israel

E-mail: pietro.cornetti@polito.it (P. Cornetti)

Abstract. The determination of the remote stress causing crack propagation in an infinite 3D domain with an embedded flat elliptical crack is here revisited in the framework of the Coupled Criterion of Finite Fracture Mechanics. We started reviewing Linear Elastic Fracture Mechanics approaches, which differ by accounting for different infinitesimal crack growths. Then, we provide the solution based on Finite Fracture Mechanics: if the elliptical flaw is sufficiently small, the crack grows along iso-stress lines. For larger sizes, other crack growths may take place. Thus, the present investigation shows that assuming an iso-stress crack front may effectively provide the exact Finite Fracture Mechanics solution, particularly for small defects; on the other hand, it can be wrong for larger size, providing moreover un-conservative predictions. However, for the geometry at hand, it yields failure stress estimates differing from the actual one by a few percents. Thus, the iso-stress assumption, conjectured by Leguillon [D. Leguillon, "An attempt to extend the 2D coupled criterion for crack nucleation in brittle materials to the 3D case", *Theor. Appl. Fract. Mech.* **74** (2014), pp. 7–17]—implying strong simplifications in the numerical implementation of the coupled criterion in 3D problems—seems to be largely justified by the present results. Moreover, regardless of the initial crack size, the finite growth predicted by the model results in a new elliptical crack shape closer to the circular one, meaning the eccentricity consistently decreases as the crack propagates.

Résumé. La détermination de la contrainte à distance provoquant la propagation d'une fissure dans un domaine 3D infini contenant une fissure elliptique plane est ici revisitée dans le cadre du Critère Couplé de la Mécanique de la Rupture Finie. Nous commençons par passer en revue les approches de la Mécanique Linéaire de la Rupture, qui diffèrent selon la prise en compte de différentes croissances infinitésimales de la fissure. Ensuite, nous présentons la solution basée sur la Mécanique de la Rupture Finie : si le défaut elliptique est suffisamment petit, la fissure croît le long de lignes iso-contraintes. Pour des tailles plus grandes, d'autres modes de croissance de fissure peuvent se produire. Ainsi, cette étude montre que supposer un front de fissure iso-contraintes peut effectivement fournir la solution exacte en Mécanique de la Rupture Finie, en particulier pour les petits défauts ; en revanche, cela peut être erroné pour des défauts de plus grande taille, entraînant de surcroît des prédictions non conservatrices. Toutefois, pour la géométrie considérée,

* Corresponding author

cela donne des estimations de contrainte de rupture ne différant que de quelques pourcents de la valeur réelle. Ainsi, l'hypothèse d'iso-contraintes, avancée par Leguillon [D. Leguillon, "An attempt to extend the 2D coupled criterion for crack nucleation in brittle materials to the 3D case", *Theor. Appl. Fract. Mech.* **74** (2014), pp. 7-17], impliquant des simplifications importantes dans l'implémentation numérique du critère couplé dans des problèmes 3D, semble largement justifiée par les résultats présents. En outre, quelle que soit la taille initiale de la fissure, la croissance finie prédite par le modèle aboutit à une nouvelle forme elliptique de la fissure, plus proche d'un cercle, ce qui signifie que l'excentricité diminue systématiquement au fur et à mesure de la propagation de la fissure.

Keywords. Coupled criterion, Finite fracture mechanics, 3D linear elastic fracture mechanics, Elliptical cracks, Quasi-brittle materials.

Mots-clés. Critère couplé, Mécanique de la rupture finie, Mécanique de la fracture élastique linéaire en 3D, Fissures elliptiques, Matériaux quasi-fragile.

Funding. NEWFRAC Project (Marie Sklodowska-Curie grant agreement No. 861061), Pazy Research Foundation, Spanish Ministry of Science and Innovation, European Regional Development Fund (PID2021-123325OB-I00).

Manuscript received 6 February 2025, revised 17 May 2025, accepted 19 May 2025.

1. Introduction

The Coupled Criterion of Finite Fracture Mechanics (CCFFM), introduced for the first time by Leguillon [1] in 2002, has proven to be an effective, yet simple, fracture criterion for obtaining the failure load in a variety of structural problems, spanning from size effect (e.g. [2]) to stress concentration/intensification (e.g. [3–5]) in homogeneous materials, from composite materials (e.g. [6–8]) to bonded joints (e.g. [9]), from static loadings to dynamic (e.g. [10,11]) and fatigue (e.g. [12,13]) loadings. With respect to Linear Elastic Fracture Mechanics (LEFM), a major advantage is its applicability to any geometry, cracked or plain (i.e. not only cracked). With respect to more sophisticated models like the Cohesive Crack Model (CCM) or the Phase Field (PF) model for fracture, the numerical implementation of the CCFFM is usually much easier, often allowing for an analytical or semi-analytical solution for the problem at hand. Moreover, the CCFFM has proven to be often in agreement with CCM and PF models: for a comparison between CCFFM and CCM the reader is referred to [14–19]; and for a comparison between CCFFM and PF to [20–24].

Most of the CCFFM applications address two-dimensional problems, where cracks/V-notch tips are straight lines through-the-thickness. However, recently, attention has also been focussed to 3D problems, starting from Leguillon's pioneering work [25]. The application of the CCFFM to 3D problems is challenging because the finite crack advance, differently from the 2D case, can be of any shape [26]. To overcome this difficulty, researchers often assumed a finite crack growth occurring along an iso-stress line, see e.g. [27–29]. One of our main purposes is investigating this assumption for a model problem allowing an analytical derivation in the framework of the CCFFM: a flat elliptical flaw in an infinite linear elastic medium subjected to a remote tensile stress orthogonal to the crack plane.

The linear elastic stress-strain solution for an elliptical flaw under remote tensile stress dates back to Green and Sneddon [30], following (and including) the one for a penny-shaped crack provided by Sneddon [31]. Later, Irwin [32] provided the Stress Intensity Factor (SIF) values along the elliptical crack front. More recent contributions related to the stress field in the vicinity of the crack front can be found in [33,34]. For what concerns crack propagation, Lazarus [35], among different flaw shapes, considered the elliptical one and analysed the crack growth for a brittle fracture (assuming propagation where the SIF reaches the fracture toughness and regularising the crack front) and fatigue (using Paris' equation). More numerical/practical contributions along with experimental data validation (under cycling loading) about crack propagation from

flat elliptical cracks can be found, e.g., in [36–38]. Finally, we refer to a recent numerical investigation where the CCFFM criterion has been exploited to deal with free edge delamination in angle-ply laminates, assuming a semi-elliptical crack shape, under static [39], fatigue [40] and thermal [41] loadings. These papers provide details on the numerical implementation of the Coupled Criterion for geometries similar to the one addressed herein.

The paper is organised as follows. In Section 2 we focus on LEFM, deriving the general expression of the mode I failure stress in the presence of a flaw of any shape under the assumption of an infinitesimal iso-stress crack growth. Then, we specify the failure stress for the flat elliptical crack, providing its closed form estimate by means of SIFs. Thereafter, we show the same result can be achieved by evaluating the Strain Energy Release Rate (SERR). Following this latter procedure, we also consider the infinitesimal elliptical crack growth along the minor axis alone, showing it provides failure stress estimates lower than the iso-stress one.

In Section 3 we derive the failure stress provided by the CCFFM for the flat elliptical crack. We assume the finite crack propagation to be characterised by an elliptical crack front of any shape/size. Thus, the new crack front is characterised by two parameters (the increments of the semi-axes); CCFFM implies solving a minimisation problem upon the variation of these two parameters. It will be shown that, based on the crack shape and size, two different scenarios (i.e. iso-stress and minor-axis crack propagations) can occur and the corresponding fracture stress is finally provided. The results are commented and in Section 4 some conclusions are drawn.

2. LEFM approach

We first provide the failure stress according to LEFM for a flat crack with an arbitrary shape subject to a mode I loading, then specify it for the elliptical crack. Two procedures, based on SIF or SERR, are outlined and exploited.

2.1. *Planar crack of arbitrary shape: iso-stress crack growth*

Let us consider a planar crack of arbitrary shape in an infinite body, made by a homogeneous isotropic linear elastic brittle material. Let the plane of the crack be (x, y). The remote loading is a uniform tensile stress σ in the z direction as in Figure 1. Under this assumption the crack is in pure mode I condition (or—the same—in opening mode, since, because of isotropy, the displacement field is symmetrical to the crack plane).

Except for the penny-shaped crack, the SIF varies along the contour C of the crack, i.e. $K_I = K_I(s)$, s being the curvilinear abscissa along the contour C (Figure 1b). Denoting by $K_{I,\min}$ and the by $K_{I,\max}$ the minimum and maximum value of the SIF respectively, we can write:

$$K_{I,\min} \le K_I(s) \le K_{I,\max}. \tag{1}$$

Assume $K_I = K_I(s)$ is available in an analytic or numerical form, and the fracture toughness K_{Ic} of the material is known. One is interested in σ_{f}, the remote stress causing crack growth, i.e. failure, according to LEFM. Because of mode I, the crack expands in its plane (x, y). However, if one wishes to consider the Griffith's SERR, there are an infinite possible shapes of infinitesimal crack growth, unlike in 2D domains where only a collinear crack growth is possible along an infinitesimal length da (a being the crack length).

A reasonable starting point is assuming (yet, an assumption) an infinitesimal crack growth defined by an iso-stress line. Since the asymptotic stress field in the direction normal to the crack contour (r is the coordinate along the normal $\hat{n}$ starting from the crack contour C, see Figure 1b) is:

$$\sigma_z \cong \frac{K_I}{\sqrt{2\pi r}} \tag{2}$$

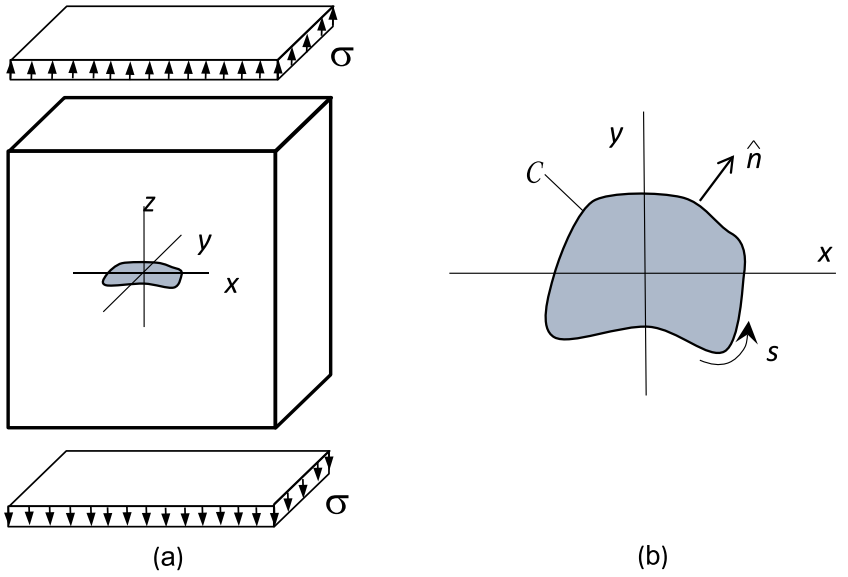

Figure 1. A planar crack of arbitrary shape in an infinite 3D domain under uniform tensile stress normal to the crack plane (a). Crack geometry (b).

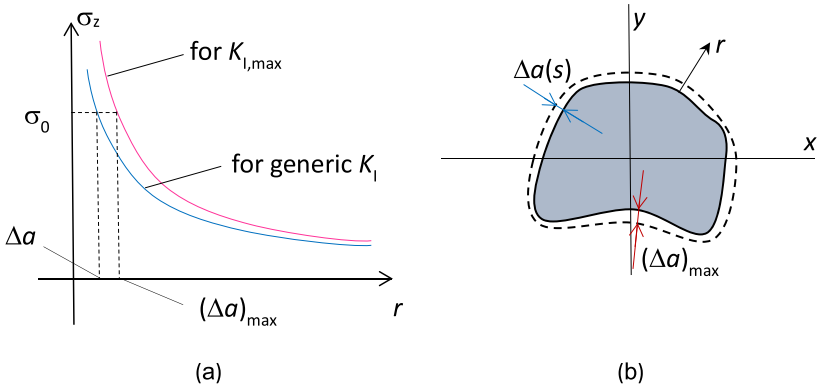

Figure 2. Asymptotic stress field ahead the crack front (a) and iso-stress crack growth (b).

The same stress level (e.g. σ_0) is achieved at different distances from the contour C, larger where K_I is larger, smaller where K_I is smaller (see Figure 2a). Where K_I is maximum, the stress σ_0 is achieved at a distance $(\Delta a)_{\max}$:

$$(\Delta a)_{\max} \cong \frac{K_{I,\max}^2}{2\pi\sigma_0^2} \tag{3}$$

while in a generic point we have:

$$(\Delta a) \cong \frac{K_I^2}{2\pi\sigma_0^2} \tag{4}$$

Dividing Equation (3) by (4), one obtains:

$$\frac{\Delta a}{(\Delta a)_{\max}} \cong \left(\frac{K_I}{K_{I,\max}}\right)^2 = \frac{G}{G_{\max}} \tag{5}$$

where the last expression is a consequence of Irwin's relationship $G = K_I^2/E'$, G being the SERR and E' the Young modulus of the material under plane strain conditions. As Δa tends to zero, Equation (5) defines the shape of the infinitesimal iso-stress crack growth (see Figure 2b).

Expressing the Griffith infinitesimal energy balance according to LEFM (G_c being the material fracture energy) by an integral along the curve C, one obtains:

$$\oint_C G(s)\Delta a\,\mathrm{d}s = \oint_C G_c \Delta a\,\mathrm{d}s \tag{6}$$

Dividing both sides of Equation (6) by $(\Delta a)_{\max}$ and substituting Equation (5) into Equation (6), one obtains the condition for crack growth:

$$G_{\mathrm{iso}} = \frac{\oint_C G^2(s)\,\mathrm{d}s}{\oint_C G(s)\,\mathrm{d}s} = G_c \tag{7}$$

The ratio between the integrals is somehow an equivalent-2D SERR, since crack growth occurs whenever this value reaches the material fracture energy G_c, like in 2D problems. We named it G_{iso} since it is the equivalent-2D SERR under the assumption of iso-stress crack growth. Note that, from a mathematical point of view, G_{iso} is the contra-harmonic mean (sum of the squared values divided by sum of values, see Appendix A) of the SERR values evaluated along the crack contour. Among different averages (i.e. harmonic, geometric, arithmetic, quadratic, etc.) the contra-harmonic mean is the highest one, thus affected by large values and close to the maximum value of the variable. By Irwin's relationship we can get also the equivalent-2D SIF $K_{I,\mathrm{iso}}$, which provides the failure stress when it equals the material fracture toughness K_{Ic}:

$$K_{I,\mathrm{iso}} = \sqrt{\frac{\oint_C K_I^4(s)\,\mathrm{d}s}{\oint_C K_I^2(s)\,\mathrm{d}s}} = K_{\mathrm{Ic}} \tag{8}$$

2.2. *Elliptical crack: iso-stress crack growth by SIF values*

As a particular case, we consider the elliptical flat crack shown in Figure 3a. The failure stress according to LEFM assuming an iso-stress crack growth is here obtained by the results in Section 2.1 (Equation (8)). The ellipse in Figure 3b is defined by semi-axes a and b ($a \geq b$) defined as:

$$\frac{x^2}{a^2} + \frac{y^2}{b^2} = 1 \tag{9}$$

or in parametric form ($0 \leq \varphi < 2\pi$):

$$\mathbf{P}(\varphi) = \begin{cases} x = a\cos\varphi \\ y = b\sin\varphi \end{cases} \tag{10}$$

The aspect of the ellipse is univocally defined either by the aspect ratio $\gamma = b/a$ ($0 < \gamma < 1$) or by the eccentricity $k = \sqrt{1-(b/a)^2}$ ($0 < k < 1$).

The SIF along the crack front is [32]:

$$K_I = \frac{\sigma\sqrt{\pi b}}{E(k^2)}\sqrt[4]{1-k^2\cos^2\varphi} \tag{11}$$

where $E(k_2)$ is the complete elliptic integral of the second kind (see Appendix B). From Equation (11) the maximum value of the SIF $K_{I,\max}$ is at point B (i.e. on the minor axis, $\varphi = \pi/2$) while the minimum value of the SIF $K_{I,\min}$ is at point A (i.e. on the major axis, $\varphi = 0$):

$$K_{I,\max} = (K_I)_B = \frac{\sigma\sqrt{\pi b}}{E(k^2)} \tag{12}$$

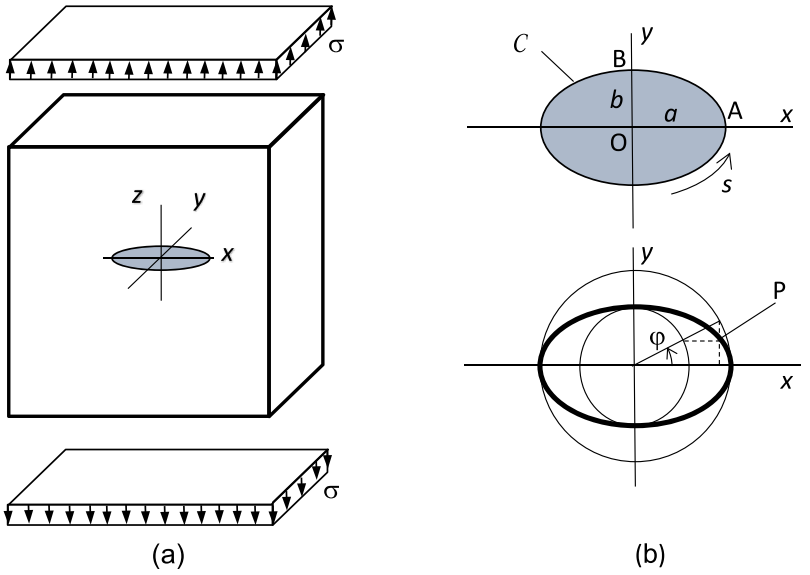

Figure 3. An elliptical (planar) crack in an infinite medium under uniform tensile stress normal to the crack plane (a). Crack geometry (b).

$$K_{I,\min} = (K_I)_{\mathrm{A}} = \frac{\sigma b}{E(k^2)}\sqrt{\frac{\pi}{a}} = K_{I,\max}\sqrt{\frac{b}{a}} \tag{13}$$

For what concerns $K_{I,\max}$, Equation (12) encompasses the limit cases of a penny-shaped crack ($k = 0$ or $\gamma = 1$):

$$K_I = \frac{2}{\pi}\sigma\sqrt{\pi b} \tag{14}$$

constant all around the crack front, and of a through-the-thickness crack of length $2b$ (corresponding to $k = 1$ or $\gamma = 0$):

$$K_I = \sigma\sqrt{\pi b} \tag{15}$$

To obtain the failure stress, we have to compute the 2D-equivalent SIF by means of Equation (8). Using the parametric expression of the ellipse (Equation (10)), the equivalent SIF (Equation (8)) reads:

$$K_{I,\mathrm{iso}} = \sqrt{\frac{\int_0^{\pi/2} K_I^4(\varphi)\left\|\frac{\mathrm{d}\mathbf{P}}{\mathrm{d}\varphi}\right\|\mathrm{d}\varphi}{\int_0^{\pi/2} K_I^2(\varphi)\left\|\frac{\mathrm{d}\mathbf{P}}{\mathrm{d}\varphi}\right\|\mathrm{d}\varphi}} = \frac{\sigma\sqrt{\pi b}}{E(k^2)}\sqrt{\frac{\int_0^{\pi/2}\left(1-k^2\cos^2\varphi\right)^{3/2}\mathrm{d}\varphi}{\int_0^{\pi/2}\left(1-k^2\cos^2\varphi\right)\mathrm{d}\varphi}} \tag{16}$$

where the double symmetry of the ellipse has been exploited to limit the integration interval to $[0,\pi/2]$. By analytical manipulations, the integrals in Equation (16) can be cast in terms of complete elliptic integrals of first ($K(k^2)$) and second ($E(k^2)$) kind (see Appendix B) as:

$$K_{I,\mathrm{iso}} = \frac{2\sigma\sqrt{b}}{E(k^2)}\sqrt{\frac{2(2-k^2)E(k^2)-(1-k^2)K(k^2)}{3(2-k^2)}} \tag{17}$$

Thus, according to LEFM and iso-stress crack growth, failure is achieved whenever the above quantity reaches the material fracture toughness. Hence, the corresponding failure stress $(\sigma_{\mathrm{f}})_{\text{LEFM-iso}}$ is:

$$(\sigma_{\mathrm{f}})_{\text{LEFM-iso}} = \frac{\sqrt{3}}{2}\frac{K_{\mathrm{Ic}}}{\sqrt{b}}E(k^2)\sqrt{\frac{2-k^2}{2(2-k^2)E(k^2)-(1-k^2)K(k^2)}} \tag{18}$$

Note that, as expected for any LEFM approach, the failure stress tends to infinity as the crack vanishes (i.e. $\sigma_f \to \infty$ as $b \to 0$).

2.3. *Elliptical crack: iso-stress crack growth by SERR evaluation*

We show in this sub-section that same results in Section 2.2 are obtained also by proper evaluation of the SERR. This procedure will be exploited in the following to remove the assumption of iso-stress crack growth.

Computation of the SERR G can be performed without the need of SIF (i.e. without exploiting Irwin's relationship). It is the way followed originally by Griffith in his 1921 seminal work. Accordingly, under load control, one has:

$$G = \lim_{\Delta A \to 0} \frac{\Delta \Phi}{\Delta A} \tag{19}$$

To compute G_{iso} (i.e. the SERR assuming an iso-stress crack growth) by Equation (19) one need to know (i) the iso-stress contour lines and (ii) the change in strain energy $\Delta\Phi$ due to the (finite) variation ΔA of the crack surface. These ingredients can be derived by Green and Sneddon [30] solution. Accordingly, because of the remote stress the planar elliptical crack takes the shape of an ellipsoid whose semi-axes are a, b and $w_{\max}$ (the maximum crack opening displacement), the last one given by:

$$w_{\max} = \frac{2\sigma b}{E(k^2)E'} \tag{20}$$

By looking at the load as a uniform remote tensile stress field plus a uniform compressive stress applied on the crack faces, and by means of Clapeyron's theorem, the strain energy Φ increment due to the presence of the crack can be computed as:

$$\Phi = \frac{\sigma V}{2} \tag{21}$$

where V is the volume of the (deformed) crack (i.e. the ellipsoid), whose value is:

$$V = \tfrac{4}{3}\pi a b w_{\max} \tag{22}$$

Hence, by combining Equations (20) to (22):

$$\Phi = \frac{4\pi}{3E(k^2)} \frac{\sigma^2 a b^2}{E'} \tag{23}$$

The iso-stress lines can also be derived from Green and Sneddon [30]. From their solution, the σ_z stress field on the crack plane (outside the crack faces) is amenable of the following analytical expression:

$$\frac{\sigma_z}{\sigma} = 1 + \frac{1}{E(k^2)} \left[\frac{a}{\sqrt{\xi}} \sqrt{\frac{b^2+\xi}{a^2+\xi}} - E\left(\arcsin \frac{a}{\sqrt{a^2+\xi}} | \, k^2 \right) \right] \tag{24}$$

where $E(\varphi|k^2)$ is the incomplete elliptic integral of the second kind (see Appendix B) and ξ is an ellipsoidal coordinate. On the crack plane ($z = 0$), ξ = constant ($\xi \geq 0$) corresponds to a family of ellipses with equation:

$$\frac{x^2}{a^2+\xi} + \frac{y^2}{b^2+\xi} = 1 \tag{25}$$

Hence, we get a relevant information: *the iso-stress curves are a particular family of ellipses*. More precisely, Equations (24) and (25) show that, as ξ increases from 0 to ∞, the stress value decreases from ∞ to σ and the corresponding isostress lines are ellipses of increasing size and decreasing eccentricity. As an example, some of them are plotted in Figure 4a for an elliptical crack with aspect ratio $\gamma = 0.5$. Naming by Δa and Δb the increment of the semi-axes of the generic iso-stress

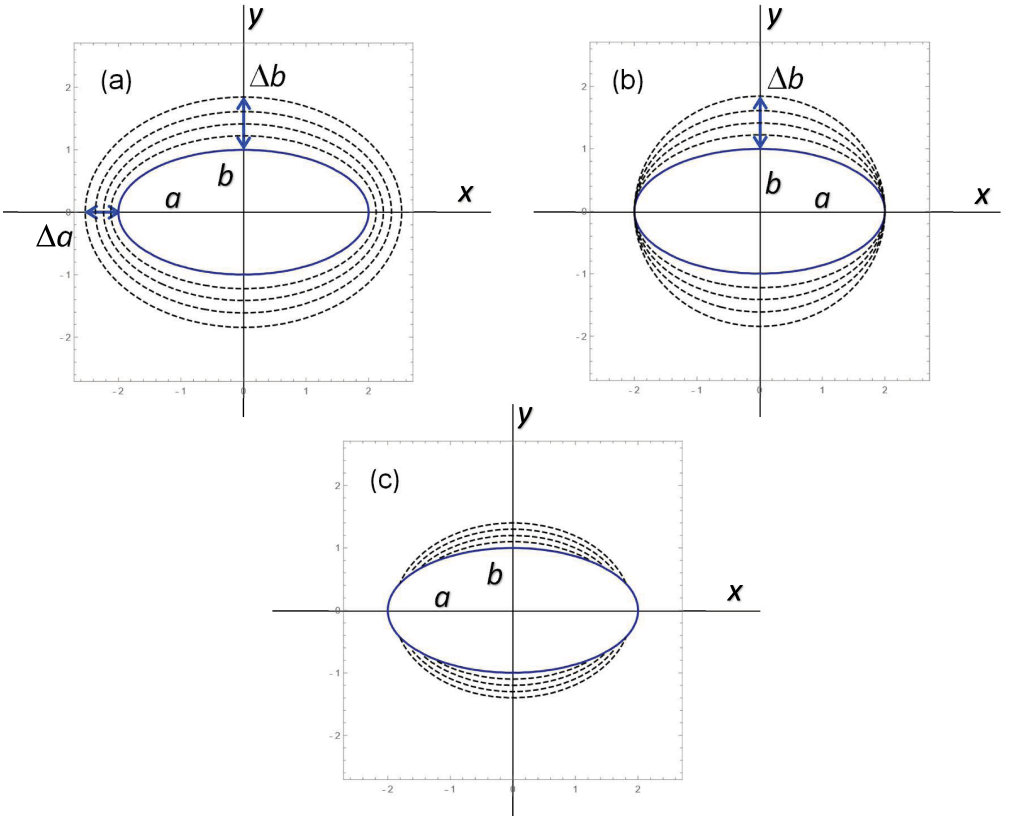

Figure 4. Possible crack growths: (elliptical) *iso-stress crack growth* (a); elliptical, with increment along minor axis alone (b), named *minor-axis crack growth*; non-elliptical crack growth, not considered in the current investigation (c).

line with respect to the ones of the original elliptical flaw, from Equation (25) the relationship between them may be obtained (see details in Appendix C):

$$\Delta a = \sqrt{a^2 + 2b\Delta b + (\Delta b)^2} - a \tag{26}$$

Let us assume the crack grows by a finite amount up to a given iso-stress line, which in turns is defined by a given ξ, value. From Equation (23), the energy variation $\Delta\Phi$ is:

$$\Delta\Phi = \frac{4\pi\sigma^2}{3E'}\left\{\frac{\left(b^2+\xi\right)\sqrt{a^2+\xi}}{E\left[(a^2-b^2)/(a^2+\xi)\right]} - \frac{ab^2}{E(1-b^2/a^2)}\right\} \tag{27}$$

while the newly created crack surface is (difference between elliptical areas):

$$\Delta A = \pi\left[\sqrt{a^2+\xi}\sqrt{b^2+\xi} - ab\right] \tag{28}$$

The following step is inserting Equations (27) and (28) into Equation (19). Then, the limit for $\Delta A \to 0$ (i.e. $\xi \to 0$) has to be evaluated. The limit takes the undetermined form 0/0, but the application of De l'Hôpital rule along with property (B4) allows the computation of the limit. Finally equating the SERR G_{iso} to the fracture energy G_{c} along with Irwin relationship yields failure stress $(\sigma_{\text{f}})_{\text{LEFM-iso}}$, which coincides with Equation (18). Thus, despite the different lines of thought (local vs. global), we checked that the SIF- and SERR-based procedures yield the same outcome, Equation (18).

2.4. *Elliptical crack: minor axis crack growth*

On the basis of the analysis in the previous section, we are able to evaluate the failure stress for any elliptical crack growth (i.e. not only the iso-stress crack growth). The criterion that mostly agrees with LEFM is the G-max, i.e. the crack growth actually occurring is the one providing the maximum SERR and consequently the minimum failure stress. Since the SIF is higher at the edge of the minor axis, among all elliptical crack extensions, the one resulting in the largest SERR is the one at which only the minor axis is increasing.

Let us denote by Δb the increment of the minor axis (see Figure 4b). The energy available for a finite elliptical crack growth along the minor axis by Δb is:

$$\Delta\Phi = \frac{4\pi\sigma^2}{3E'}\left\{\frac{a\,(b+\Delta b)^2}{E\left[1-(b+\Delta b)^2/a^2\right]} - \frac{ab^2}{E\left(1-b^2/a^2\right)}\right\} \tag{29}$$

The energy needed to create the new surface is:

$$\Delta\Phi = G_c\pi\left[a\,(b+\Delta b) - ab\right] \tag{30}$$

The corresponding failure stress $(\sigma_f)_{\text{LEFM-minor}}$ is obtained by equating Equations (29)–(30) and taking the limit for $\Delta b \to 0$, or, by introducing the ratio ε_b between the final value of the minor axis and its initial value, letting $\varepsilon_b \to 1$:

$$\varepsilon_b = \frac{b+\Delta b}{b} \tag{31}$$

$$\begin{aligned}(\sigma_f)_{\text{LEFM-minor}} &= \lim_{\varepsilon_b\to 1}\sqrt{\frac{3}{4}\frac{K_{Ic}^2}{b}\frac{\varepsilon_b-1}{\frac{\varepsilon_b^2}{E\left[1-\varepsilon_b^2(1-k^2)\right]}-\frac{1}{E(k^2)}}} \\ &= \frac{\sqrt{3}}{2}\frac{K_{Ic}}{\sqrt{b}}E(k^2)\frac{k}{\sqrt{(1+k^2)E(k^2)-(1-k^2)K(k^2)}}\end{aligned} \tag{32}$$

where again De l'Hôpital rule along with property (B4) has been used.

A further, third, estimate of the failure stress is obtained by setting $K_{I,\max} = K_{Ic}$. This condition is sometime referred to as Irwin criterion (as opposed to the previous ones, based on Equation (19), referred to as Griffith criterion, see e.g. [42]). Note that, differently from 2D problems where the two criteria coincide, the equality $K_{I,\max} = K_{Ic}$ does not rely on any energy balance; however, it is interesting because it provides conservative predictions with respect to the previous estimates Equations (18) and (32). Let us denote $(\sigma_f)_{\text{Irwin}}$ the new failure stress estimate. By Equation (12) one easily obtains:

$$(\sigma_f)_{\text{Irwin}} = K_{Ic}\frac{E(k^2)}{\sqrt{\pi b}} \tag{33}$$

In Figure 5 the dimensionless failure stress estimates Equations (18), (32), (33) are plotted vs. the ellipse eccentricity. Note that all predictions are close, since the contra-harmonic mean (of $G \sim K_I^2$), as already observed, is close to its maximum value. In Figure 5a the estimates are compared at constant minor axis length. As k increases, so does the major axis and, obviously, the failure stress decreases. LEFM based on minor-axis crack growth provides predictions closer (or equal) to G-max criterion: however, we cannot state Equation (32) coincides with G-max criterion since infinitesimal crack extensions other than the elliptical ones could take place (see e.g. Figure 4c). It is apparent that, according to G-max criterion the effective failure stress lies in between Equations (32) (upper bound) and (33) (lower bound). Reasonably, it will be closer to minor-axis crack growth for small eccentricity and closer to Irwin estimate for large eccentricity, where an elliptical crack growth is unlikely: e.g., for $k = 1$, we know the failure stress

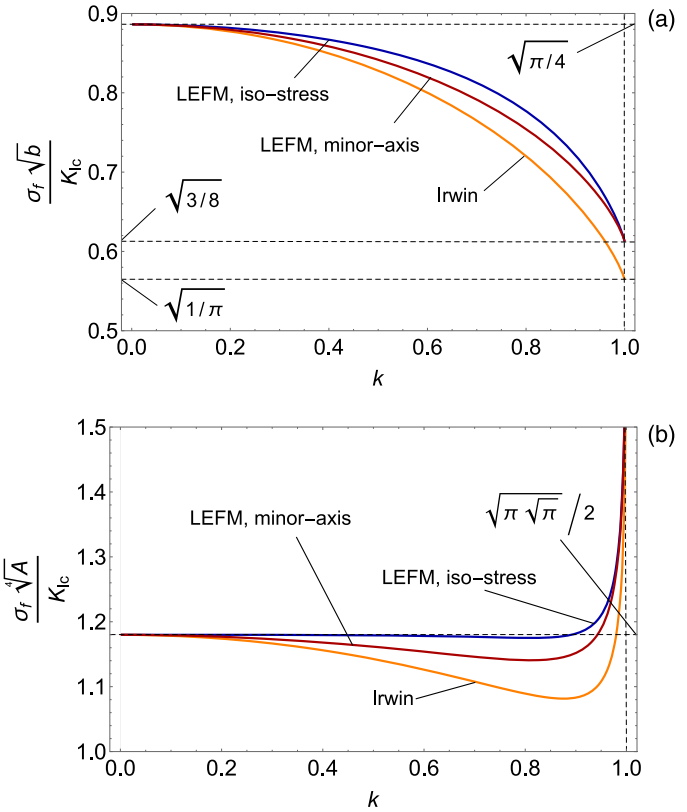

Figure 5. LEFM failure stress estimates vs. ellipse eccentricity k for an infinitesimal iso-stress crack growth (LEFM, iso-stress), an infinitesimal minor axis crack growth (LEFM, minor-axis), $K_{I,\max} = K_{Ic}$ (Irwin): at constant defect minor axis b (a) and at constant defect area A (b); $k = 0$ refers to a penny-shaped crack while $k = 1$ refers to a through-the-thickness crack.

is $\sigma_f = K_{Ic}/\sqrt{(\pi b)}$, since the geometry becomes the 2b-long through-the-thickness crack, while LEFM-minor (and LEFM-iso) provides $\sigma_f = K_{Ic}\sqrt{3}/\sqrt{(8b)}$, see Figure 5a.

In Figure 5b the same estimates are plotted at constant defect area $A = \pi ab$. It is evident that the effect of eccentricity is very low up to eccentricity values close to unity, i.e. what really affect failure stress is the defect area and not its shape. This result agrees with the ones provided by David and Lazarus [43], related to (flat) defects of almost any shape.

3. FFM approach

The estimates provided in the previous section are based on a LEFM approach. As such, they share the well-known drawback that can be applied only to cracked bodies, or, the same, they provide infinite failure stress as the defect size vanishes. On the other hand, for quasi-brittle materials, we expect the failure stress to approach the material tensile strength σ_c as the defect size vanishes. Thus, more refined models able to take into account the material tensile strength beyond the fracture toughness (or fracture energy) have to be used to deal with defects of any size. Herein, we resort to the CCFFM, whose predictions will match LEFM just for relatively large defect size, where energy alone rules crack growth and propagation.

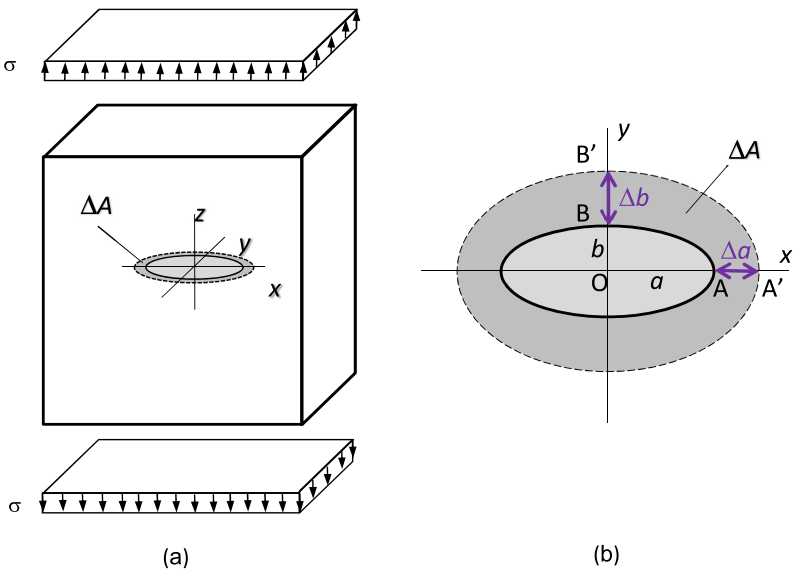

Figure 6. An elliptical (planar) crack in an infinite medium under uniform tensile stress normal to the crack plane: solution by FFM (a); crack geometry and elliptical finite crack growth of any shape (b).

The CCFFM assumes crack growth by a finite increment ΔA (whence the name FFM), see Figure 6a. This increment as well as the failure load are determined based on the finite energy balance and a stress condition (whence the name CC)—the stress must exceed the material tensile strength over the newly created crack surface ΔA. While in 2D the finite crack extension is simply determined by its length and, possibly, by its direction, in 3D problems the crack extension can have any shape (the actual one will be the one minimising the failure load), even in cases where the crack plane is already known, as in the present case. The application of FFM to 3D problems is thus a challenging task. Up to now, a common approach in the literature has been to consider finite crack growth following the iso-stress lines [25,27–29]. This assumption greatly simplifies the problem, allowing the crack growth to be described by just one parameter; moreover, it makes the fulfilment of the stress requirement trivially checked. However, a check of the approximation introduced by considering just (finite) iso-stress crack growths is not available; our goal is to provide it for the model problem at hand (the flat elliptical crack).

Thus, let us derive the CCFFM failure stress for the planar elliptical crack (Figure 2). Here we don't restrict the analysis to finite iso-stress crack growth, since the results in the previous section allow us to consider the crack growth of any (yet elliptical) shape.

Hence, let us assume a finite crack growth where the new crack front has the shape of an ellipse (see Figure 6b) (whose symmetry axes coincide with the ones of the original flaw elliptical geometry). Its shape is univocally determined by two parameters, namely the increment of the minor axis Δb and the increment of the major axis Δa. As such, this approach includes as particular cases the iso-stress crack growth (Figure 4a) and the minor-axis crack growth (Figure 4b). Since the iso-stress lines are also elliptical, the lowest stress level within the crack extension (darker area in Figure 6) is reached either at A' or B' (Figure 6b). Thus, in order the stress condition to be fulfilled, it is enough to check that $\sigma_z(A') \geq \sigma_c$ and $\sigma_z(B') \geq \sigma_c$; meanwhile FFM also requires that the energy available for crack growth $\Delta\Phi$ is larger than the

energy dissipated to create the new fracture surface ΔA. That is:

$$\begin{cases} \sigma_z(A') \geq \sigma_c \\ \sigma_z(B') \geq \sigma_c \\ \Delta\Phi \geq G_c \Delta A \end{cases} \tag{34}$$

It is worth noting the analogy with the approach presented in [44], where the growth of an embedded elliptical crack under fatigue loading was analysed by analytically coupling and solving the Paris laws at points A and B, while assuming that the crack front maintains an elliptical shape throughout its propagation.

Beyond the ratio ε_b between the final value of the minor axis and its initial value—Equation (31)—we now also introduce the ratio ε_a between the final value of the major axis and its initial value:

$$\varepsilon_a = \frac{a + \Delta a}{a} \tag{35}$$

The first inequality in Equation (34) is achieved by means of Equation (24) along with the following ξ value (coming from Equation (25)):

$$\sqrt{a^2 + \xi} = a + \Delta a \Rightarrow \xi = (\varepsilon_a^2 - 1) a^2 \tag{36}$$

yielding (by Equation (35) as well):

$$\frac{\sigma}{\sigma_c} \geq E(k^2) \left[\frac{1}{\varepsilon_a} \sqrt{\frac{\varepsilon_a^2 - k^2}{\varepsilon_a^2 - 1}} + E(k^2) - E\left(\arcsin \frac{1}{\varepsilon_a} \,|\, k^2 \right) \right]^{-1} = f_{Sa}(\varepsilon_a, k^2) \tag{37}$$

The second inequality in Equation (34) is achieved by means of Equation (24) along with the following ξ value (coming again from Equation (25)):

$$\sqrt{b^2 + \xi} = b + \Delta b \Rightarrow \xi = \left(\varepsilon_b^2 - 1\right) b^2 \tag{38}$$

yielding (by Equation (31) as well):

$$\frac{\sigma}{\sigma_c} \geq E(k^2) \left[\frac{\varepsilon_b^2}{\sqrt{\varepsilon_b^2 - 1} \sqrt{\left(1 - k^2\right) \varepsilon_b^2 + k^2}} + E(k^2) - E\left(\arcsin \frac{1}{\sqrt{\left(1 - k^2\right) \varepsilon_b^2 + k^2}} \,|\, k^2 \right) \right]^{-1} = f_{Sb}\left(\varepsilon_b, k^2\right) \tag{39}$$

The third inequality in Equation (34) follows from Equation (23) and the area of the crack increment ΔA:

$$\Delta\Phi = \frac{4\pi}{3} \frac{\sigma^2}{E'} \left\{ \frac{(a + \Delta a)(b + \Delta b)^2}{E\left[1 - \left(\frac{b + \Delta b}{a + \Delta a}\right)^2\right]} - \frac{a b^2}{E\left[1 - \left(\frac{b}{a}\right)^2\right]} \right\} \tag{40}$$

$$\Delta A = \pi \left[(a + \Delta a)(b + \Delta b) - a b \right] \tag{41}$$

Let us introduce the dimensionless flaw size β as:

$$\beta = \frac{b}{(K_{Ic}/\sigma_c)^2} = \frac{b}{l_{ch}} \tag{42}$$

where l_{ch} is (Irwin's) material characteristic length. Equation (42) highlights that the crack size is a relative concept: what really matters is the ratio of the size to the characteristic length. Note also that β is the square of the inverse of the so-called brittleness number introduced by

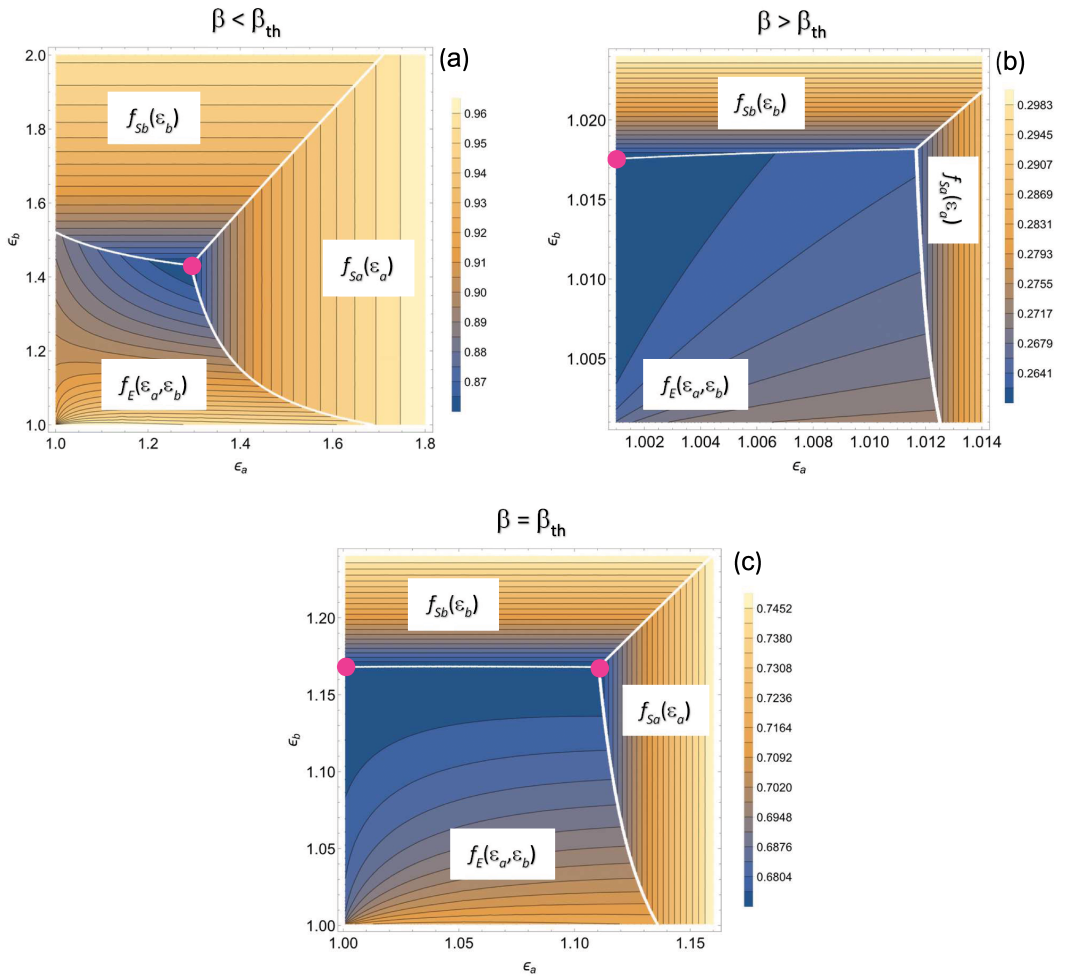

Figure 7. Graphical representation of the minimum search—Equation (44)—for ellipse eccentricity k (flaw shape) equal to 0.8. The dots correspond to the position of the minimum. Small flaw size ($\beta = 0.8$), corresponding to iso-stress crack growth scenario (a); large flaw size ($\beta = 10$), corresponding to minor-axis crack growth scenario (b); limit ($\beta \cong 1.45$) case (c).

Carpinteri [45], $s = K_{\mathrm{Ic}}/(\sigma_{\mathrm{c}}\sqrt{b})$. By Equations (40) and (41), the third inequality in Equation (34) in dimensionless form finally reads:

$$\frac{\sigma}{\sigma_{\mathrm{c}}} \geq \frac{\sqrt{3}}{2\sqrt{\beta}} \sqrt{\frac{\varepsilon_a \varepsilon_b - 1}{\frac{\varepsilon_a \varepsilon_b^2}{E\left[1-\frac{(1-k^2)\varepsilon_b^2}{\varepsilon_a^2}\right]} - \frac{1}{E(k^2)}}} = \frac{1}{\sqrt{\beta}} f_E(\varepsilon_a, \varepsilon_b, k^2) \tag{43}$$

Hence, according to FFM, for a given defect shape (k) and size (β), the relative failure stress $\sigma_{\mathrm{f}}/\sigma_{\mathrm{c}}$ is univocally determined. More precisely, σ_{f} is the minimum value, for any crack increment $\varepsilon_a > 1$ and $\varepsilon_b > 1$, satisfying the three inequalities in Equation (34). That is:

$$\sigma_{\mathrm{f}} = \sigma_{\mathrm{c}} \times \min_{\substack{\varepsilon_a > 1 \\ \varepsilon_b > 1}} \max \left\{ f_{Sa}\left(\varepsilon_a, k^2\right), f_{Sb}\left(\varepsilon_b, k^2\right), \frac{1}{\sqrt{\beta}} f_E\left(\varepsilon_a, \varepsilon_b, k^2\right) \right\} \tag{44}$$

Let us fix k, e.g. $k = 0.8$. Depending on β, we may have just two scenarios, as evident in Figure 7. For small β (Figure 7a), i.e. for relatively small flaw size, the minimum load is achieved for iso-stress crack growth (Figure 4a). The finite crack growth is significant (i.e. ε_a and ε_b significantly larger than unity) and the relationship between the increment of the two semi-axes is given by Equation (26) that, in terms of ε_a and ε_b, can be more conveniently expressed as (see Appendix C for details):

$$\varepsilon_a = \sqrt{k^2 + \left(1 - k^2\right)\varepsilon_b^2} \tag{45}$$

Note that in this case the three inequalities in Equation (34) are strictly fulfilled. This former scenario is the iso-stress one.

The second scenario (Figure 7b) is linked to large β, i.e. for relatively large flaw size: the minimum load is achieved for minor-axis crack growth (Figure 4b). The finite crack growth is relatively small (i.e. ε_b slightly higher than unity) and, of course, $\varepsilon_a = 1$ since there is no increment in the major axis of the flaw. Note that in this latter case the second and third inequalities in Equation (34) are strictly fulfilled while the first one is over fulfilled. This latter scenario is the minor-axis one. The discriminant between the two scenarios is when the failure stress is the same (see Figure 7c), i.e.:

$$f_E\left(\varepsilon_a = 1, \varepsilon_b\right) = f_E\left(\varepsilon_a = \sqrt{k^2 + (1 - k^2)\varepsilon_b^2}, \varepsilon_b\right) \tag{46}$$

This is an equation in the unknown ε_b. Let us name $\overline{\varepsilon}_b$ its solution. The corresponding dimensionless threshold size β_{th} is obtained by equating the stress condition (either the first or the second one in Equation (34)) with the energy one (third condition in Equation (34)). That is:

$$\beta_{\text{th}} = \left[\frac{f_E\left(\varepsilon_a = 1, \overline{\varepsilon}_b\right)}{f_{Sb}\left(\overline{\varepsilon}_b\right)}\right]^2 \tag{47}$$

For $k = 0.8$, we found $\beta_{\text{th}} \cong 1.45$. Then, if $\beta < \beta_{\text{th}}$, iso-stress scenario takes place. Accordingly, the finite crack growth (through ε_b) is given by the solution of the following equation:

$$\sqrt{\beta}\, f_{Sb}\left(\varepsilon_b\right) = f_E\left(\varepsilon_a = \sqrt{k^2 + (1 - k^2)\varepsilon_b^2}, \varepsilon_b\right) \tag{48}$$

On the other hand, if $\beta > \beta_{\text{th}}$, minor-axis scenario takes place. Accordingly, the finite crack growth (through ε_b) is provided by solving:

$$\sqrt{\beta}\, f_{Sb}\left(\varepsilon_b\right) = f_E\left(\varepsilon_a = 1, \varepsilon_b\right) \tag{49}$$

Let us denote by $\varepsilon_{b\text{c}}$ the solution of either Equation (48) or (49). In both cases the failure stress is given by either the stress or energy condition. Taking the first we have:

$$\sigma_{\text{f}} = \sigma_{\text{c}}\, f_{Sb}\left(\varepsilon_{b\text{c}}\right) \tag{50}$$

For clarity, the flow chart providing the finite crack growth and the failure stress is given in Figure 8.

In Figure 9 the failure stress vs. flaw size plots for different ellipse eccentricity values are drawn. The threshold size according to which there is the switch between scenarios is also highlighted. While the iso-stress scenario prevails for small eccentricity (being the only one for a penny-shaped crack), the minor-axis scenario becomes predominant for large eccentricity. Note also that FFM reverts to LEFM (in its minor-axis crack growth version) as the flaw size increases; on the other hand, for small flaw size, LEFM provides unrealistically high failure stresses, while FFM predictions remain always lower than the material tensile strength.

In Figure 10a the different curves in Figure 9 are compared altogether, including the ones referring to a through-the-thickness crack of semi-length b ($k = 1$) and to a penny-shaped crack of radius b ($k = 0$). Note that these two latter cases are 2D geometries (the first one is actually a 2D problem; the second one is a pseudo 3D problem, due to the radial symmetry); as such,

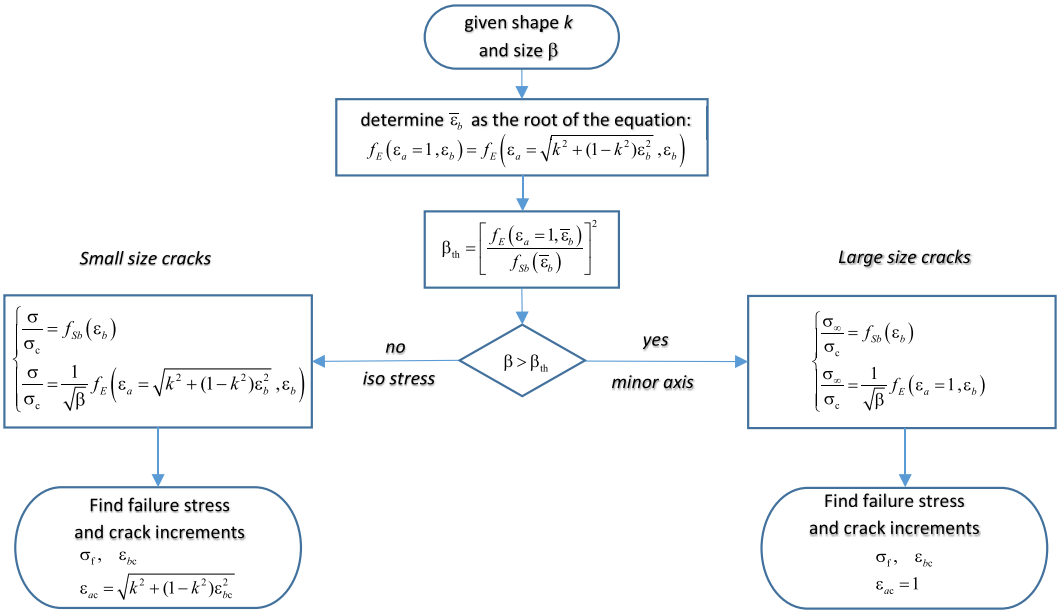

Figure 8. Flowchart to determine the failure stress σ_f for a given flaw shape (k) and size (β).

their solution is simpler and already available in the literature [16,17]. Of course, the comparison being made at constant b, the failure stress decreases as the eccentricity increases. In Figure 10b the same comparison is provided at a constant flaw area (the through-the-thickness crack case is somewhat meaningless, since A constant and a infinite yield b null). Again, as in the LEFM analysis, it is apparent that, for relatively small eccentricity, the parameter governing failure stress is the flaw area. In other words, for flaw aspect ratio b/a between 0.5 and 1, the failure stress due to the presence of an elliptical crack is (almost) equal to the one due to a penny-shaped crack of the same area.

Note that, whatever is the scenario, the elliptical crack always grows toward an elliptical shape closer to that of a circle (with respect to the original elliptical shape), i.e. the eccentricity diminishes. This is a common finding in the literature, even for original flaws of shape other than the elliptical one [35,38,43,44].

Regarding the difference between iso-stress and non-iso-stress finite crack growth, for small sizes fracture propagates actually by iso-stress lines. For larger size (i.e. $\beta > \beta_{th}$) the iso-stress failure stress prediction becomes larger than the minor axis one. Let us consider for instance the case considered in Figure 7b, where $k = 0.8$ and $\beta = 10$: although it is clear that the minimum load is achieved for minor-axis growth ($\varepsilon_a = 1$), it is also apparent that the failure stress corresponding to iso-stress crack growth is just slightly larger. Actually the difference between the two predictions increases with size, i.e. β. For $\beta \to \infty$, FFM reverts to LEFM and the difference between minor-axis and iso-stress predictions can be directly determined from Figure 5a. For instance, for $k = 0.8$, the relative difference (i.e. the error made using the iso-stress assumption) is about 3%, which is almost negligible from an engineering point of view. Figure 5a also shows that the largest error takes place when $\beta \to \infty$ and $k = 1$, i.e. a large through-the-thickness crack: in this extreme case the difference is $[\sqrt{(3/8)} - \sqrt{(1/\pi)}/\sqrt{(1/\pi)}] \cong 8.5\%$. Thus, we can conclude that, for the geometry at hand and for ellipse aspect ratios not really close to zero (i.e. except for case $b \ll a$), the error made by using the iso-stress crack growth assumption is reasonably small. Of course, this does not mean that this is always the case, but the present case corroborates the

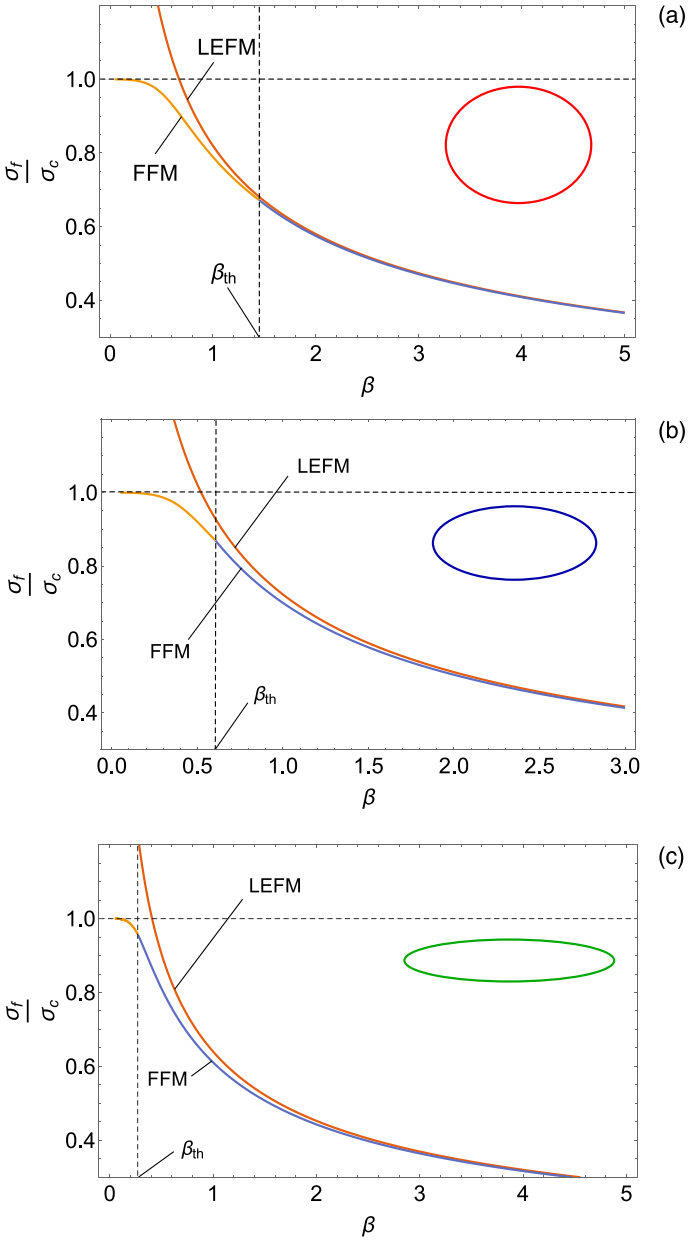

Figure 9. Failure stress vs. dimensionless flaw size $\beta = b/l_{ch}$ for different flaw shape (i.e. ellipse eccentricity k or aspect ratio $\gamma = b/a$) according to LEFM (minor axis crack growth) and to FFM: $\gamma = 0.8$, $k = 0.6$ (a); $\gamma = 0.5$, $k \cong 0.85$ (b); $\gamma = 0.2$, $k \cong 0.98$ (c). Threshold value of β dividing iso-stress (left) and minor axis (right) finite crack growth are also highlighted.

conjecture made by Leguillon [25], i.e. iso-stress crack growth can be a reasonable and effective simplifying assumption.

Finally, note that extending our analysis to a more complex stress state, such as the one occurring to the present geometry when the remote tensile stress is not normal to the crack plane, would broaden the applicability of the paper. However, given the mode mixity (I, II, III)

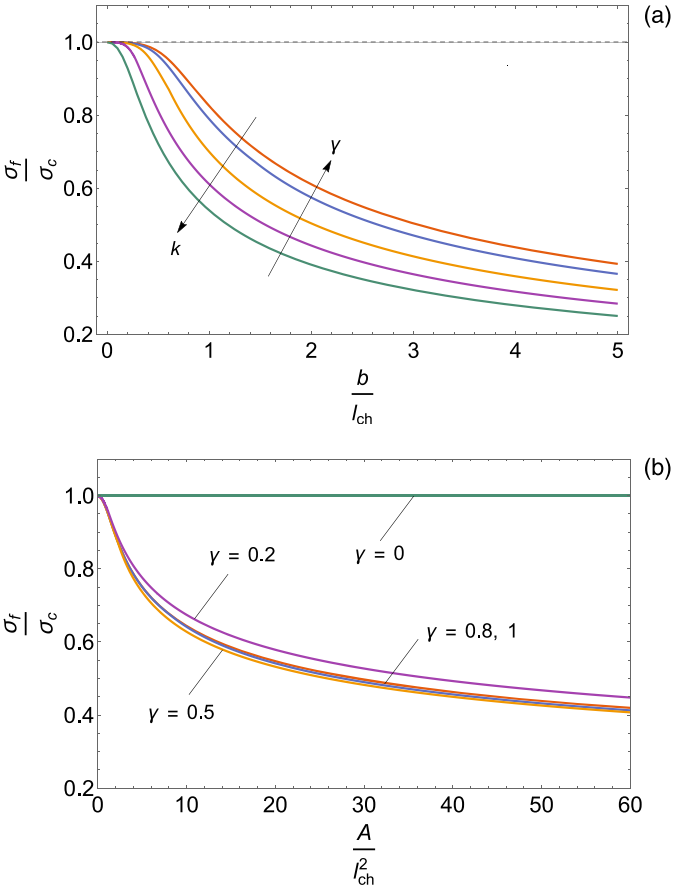

Figure 10. FFM estimates of the failure stress for different flaw shape ($k \cong 0$, 0.6, 0.85, 0.98, 1; i.e. $\gamma = 1$, 0.8, 0.5, 0.2, 0) vs. dimensionless flaw size $\beta = b/l_{ch}$ (a) and vs. dimensionless flaw area (A/l_{ch}^2) (b).

and the expected non-planar (unknown) crack growth, this is a major, challenging task going beyond the scope of the current manuscript. In this sense, it would be reasonable to start with an inclined penny shaped crack, which is a configuration investigated in the past with simpler fracture criteria, see e.g. [46]; see also [47] for recent interesting experimental data.

4. Conclusions

The failure remote stress causing (unstable) crack propagation in an infinite linear elastic 3D domain containing a flat elliptical crack has been obtained in an analytical form by means of the CCFFM, under the assumption that the finite crack growth can be of any elliptical shape. It is found that finite crack growth always leads to elliptical crack geometries with lower eccentricity, i.e. the crack shape tends to that of a penny-shaped crack. Differently from other investigations available in the literature, in this 3D application of FFM we removed the assumption of iso-stress crack growth. Particularly for large flaws we found failure stress values lower than the ones obtained by the iso-stress assumption, which, thus, must be seen as potentially dangerous since providing non-conservative predictions. Nevertheless, the difference appears to be of a few percents and, thus, the iso-stress assumption when applying CCFFM is regarded as more

than reasonable in engineering practice. It is noteworthy that for small elliptical defects, the failure remote stress predicted by the present FFM procedure can be significantly smaller than that obtained by LEFM assuming infinitesimal crack growth. Notably, the failure remote stress predicted by LEFM depends on the assumed shape of the infinitesimal crack increment.

Declaration of interests

The authors do not work for, advise, own shares in, or receive funds from any organization that could benefit from this article, and have declared no affiliations other than their research organizations.

Acknowledgements

The present manuscript is the final version of what presented in the Sevilla workshop within NEWFRAC Project (Marie Sklodowska-Curie grant agreement No. 861061), which is gratefully acknowledged by all the Authors, and later, at the International Conference of Fracture held in Atlanta, June 2023 (ICF15). In Atlanta the Authors had—as usual—fruitful and stimulating discussions about the topic investigated in the present manuscript with Prof. Dominique Leguillon: although he passed away, we wish to thank him and dedicate the present work to his memory. ZY is grateful for the partial support of this research by the Pazy Research Foundation. The research of VM was partially supported by the Spanish Ministry of Science and Innovation and the European Regional Development Fund (PID2021-123325OB-I00). Finally, PC wishes to thank also Prof. Veronique Lazarus for pleasant and useful discussions had at Sorbonne Université, where he was upon Prof. Leguillon's invitation.

Appendix A.

The Contra-harmonic mean (C) was introduced by Eudoxus from Cnidus (408–355 B.C.) as the ratio between the sum of the squares of the values and the sum of the values themselves. The name is due to the fact that, if we consider two values a and b, the distance between the Arithmetic mean (A) and the Harmonic mean (H) is equal to the one between the Contra-harmonic mean (C) and the Arithmetic mean (A):

$$A(a,b) = \frac{a+b}{2} \tag{A1}$$

$$H(a,b) = \frac{2}{1/a+1/b} \tag{A2}$$

$$C(a,b) = \frac{a^2+b^2}{a+b} \tag{A3}$$

$$C(a,b) - A(a,b) = A(a,b) - H(a,b) \tag{A4}$$

For instance, if $a = 9$ and $b = 1$, $A = 5$, $H = 1.8$, $C = 8.2$ ($C-A = 3.2 = A-H$).

Appendix B.

The complete elliptic integral of the first kind reads:

$$K(m) = \int_0^{\pi/2} \frac{1}{\sqrt{1-m\sin^2\varphi}}\,\mathrm{d}\varphi \tag{B1}$$

The complete elliptic integral of the second kind reads:

$$E(m) = \int_0^{\pi/2} \sqrt{1 - m\sin^2\varphi}\,\mathrm{d}\varphi \tag{B2}$$

The derivative of the elliptic integral of the second kind with respect to m is:

$$\frac{\mathrm{d}E(m)}{\mathrm{d}m} = \frac{E(m) - K(m)}{2m} \tag{B3}$$

The incomplete elliptic integral of the second kind is:

$$E\left(\varphi \mid m\right) = \int_0^{\varphi} \sqrt{1 - m\sin^2\vartheta}\,\mathrm{d}\vartheta \tag{B4}$$

The relationship between the incomplete elliptic integral and its complete counterpart is:

$$E\left(\frac{\pi}{2} \mid m\right) = E(m) \tag{B5}$$

Appendix C.

Here we derive the relationship between the semi-axes increments in case of iso-stress crack growth, in dimensional—Equation (26)—and dimensionless—Equation (45)—form.

From Equation (36) we have:

$$\Delta a = \sqrt{a^2 + \xi} - a \tag{C1}$$

while, from Equation (38):

$$\xi = (\Delta b + b)^2 - b^2 \tag{C2}$$

Replacing (C2) into (C1), we get Equation (26).

From Equation (36) we have also:

$$\varepsilon_a^2 = \frac{\xi}{a^2} + 1 \tag{C3}$$

while, from Equation (38):

$$\xi = b^2\left(\varepsilon_b^2 - 1\right) \tag{C4}$$

Replacing (C4) into (C3) and recalling that, by eccentricity definition, $(b/a)^2 = 1 - k^2$, we get Equation (45).

References

[1] D. Leguillon, "Strength or toughness? A criterion for crack onset at a notch", *Eur. J. Mech. A/Solids* **21** (2002), pp. 61–72.

[2] P. Cornetti, N. Pugno, A. Carpinteri and D. Taylor, "Finite fracture mechanics: a coupled stress and e nergy failure criterion", *Eng. Fract. Mech.* **73** (2006), pp. 2021–2033.

[3] Z. Yosibash, E. Priel and D. Leguillon, "A failure criterion for brittle elastic materials under mixed-mode loading", *Int. J. Fract.* **141** (2006), pp. 291–312.

[4] P. Cornetti, A. Sapora and A. Carpinteri, "Mode mixity and size effect in V-notched structures", *Int. J. Solids Struct.* **50** (2013), pp. 1562–1582.

[5] P. Lazzarin, A. Campagnolo and F. Berto, "A comparison among some recent energy- and stress-based criteria for the fracture assessment of sharp V-notched components under mode I loading", *Theor. Appl. Fract. Mech.* **71** (2014), pp. 21–30.

[6] V. Mantič, "Interface crack onset at a circular cylindrical inclusion under a remote transverse tension. Application of a coupled stress and energy criterion", *Int. J. Solids Struct.* **46** (2009), pp. 1287–1304.

[7] E. Martin, D. Leguillon and N. Carrère, "A twofold strength and toughness criterion for the onset of free-edge shear delamination in angle-ply laminates", *Int. J. Solids Struct.* **47** (2010), pp. 1297–1305.

[8] P. P. Camanho, G. H. Erçin, G. Catalanotti, S. Mahdi and P. Linde, "A finite fracture mechanics model for the prediction of the open-hole strength of composite laminates", *Compos.-A: Appl. Sci. Manuf.* **43** (2012), pp. 1219–1225.

[9] P. Weissgraeber and W. Becker, "Finite Fracture Mechanics model for mixed mode fracture in adhesive joints", *Int. J. Solids Struct.* **50** (2013), pp. 2383–2394.

[10] A. Doitrand, G. Molnár, D. Leguillon, E. Martin and N. Carrère, "Dynamic crack initiation assessment with the coupled criterion", *Eur. J. Mech. A/Solids* **93** (2022), article no. 104483.
[11] A. Chao Correas, P. Cornetti, M. Corrado and A. Sapora, "Finite fracture mechanics extension to dynamic loading scenarios", *Int. J. Fract.* **239** (2023), pp. 149–165.
[12] A. Sapora, P. Cornetti, A. Campagnolo and G. Meneghetti, "Fatigue limit: crack and notch sensitivity by finite fracture mechanics", *Theor. Appl. Fract. Mech.* **105** (2020), article no. 102407.
[13] A. M. Mirzaei, P. Cornetti and A. Sapora, "A novel finite fracture mechanics approach to assess the lifetime of notched components", *Int. J. Fatigue* **173** (2023), article no. 107659.
[14] C. Henninger, D. Leguillon and E. Martin, "Crack initiation at a V-notch-comparison between a brittle fracture criterion and the Dugdale cohesive model", *C. R. Mèc.* **335** (2007), pp. 388–393.
[15] I. G. García, M. Paggi and V. Mantič, "Fiber-size effects on the onset of fiber-matrix debonding under transverse tension: a comparison between cohesive zone and finite fracture mechanics models", *Eng. Fract. Mech.* **115** (2014), pp. 96–110.
[16] P. Cornetti, A. Sapora and A. Carpinteri, "Short cracks and v-notches: finite fracture mechanics vs cohesive crack model", *Eng. Fract. Mech.* **168** (2016), pp. 2–12.
[17] P. Cornetti and A. Sapora, "Penny-shaped cracks by Finite Fracture Mechanics", *Int. J. Fract.* **219** (2019), pp. 153–159.
[18] F. Ferrian, P. Cornetti, L. Marsavina and A. Sapora, "Finite fracture mechanics and cohesive crack model: size effects through a unified formulation", *Frat. Integrità Strut.* **16** (2022), pp. 496–509.
[19] A. Chao Correas, A. Sapora, J. Reinoso, M. Corrado and P. Cornetti, "Coupled versus energetic nonlocal failure criteria: A case study on the crack onset from circular holes under biaxial loadings", *Eur. J. Mech. A/Solids* **101** (2023), article no. 105037.
[20] J. Reinoso, A. Arteiro, M. Paggi and P. P. Camanho, "Strength prediction of notched thin ply laminates using finite fracture mechanics and the phase field approach", *Compos. Sci. Technol.* **150** (2017), pp. 205–216.
[21] G. Molnár, A. Doitrand, R. Estevez and A. Gravouil, "Toughness or strength? Regularization in phase-field fracture explained by the coupled criterion", *Theor. Appl. Fract. Mech.* **109** (2020), article no. 102736.
[22] A. Doitrand, G. Molnár, R. Estevez and A. Gravouil, "Strength based regularization length in phase field fracture", *Theor. Appl. Fract. Mech.* **124** (2023), article no. 103728.
[23] G. Molnár, A. Doitrand and V. Lazarus, "Phase-field simulation and coupled criterion link echelon cracks to internal length in Antiplane shear", *J. Mech. Phys. Solids* **188** (2024), article no. 105675.
[24] S. Jiménez-Alfaro, D. Leguillon, C. Maurini and J. Reinoso, "A dialogue between finite fracture mechanics and phase field approaches to fracture for predicting crack nucleation at the microscale", *Int. J. Fract.* **249** (2025), article no. 13.
[25] D. Leguillon, "An attempt to extend the 2D coupled criterion for crack nucleation in brittle materials to the 3D case", *Theor. Appl. Fract. Mech.* **74** (2014), pp. 7–17.
[26] Z. Yosibash and B. Mittelman, "A 3-D failure initiation criterion from a sharp V-notch edge in elastic brittle structures", *Eur. J. Mech.-A/Solids* **60** (2016), pp. 70–94.
[27] I. G. García, B. J. Carter, A. R. Ingraffea and V. Mantič, "A numerical study of transverse cracking in cross-ply laminates by 3D finite fracture mechanics", *Compos. B: Eng.* **95** (2016), pp. 475–487.
[28] A. Doitrand and D. Leguillon, "3D application of the coupled criterion to crack initiation prediction in epoxy/aluminum specimens under four point bending", *Int. J. Solids Struct.* **143** (2018), pp. 175–182.
[29] A. Doitrand and D. Leguillon, "Comparison between 2D and 3D applications of the coupled criterion to crack initiation prediction in scarf adhesive joints", *Int. J. Adhes. Adhes.* **85** (2018), pp. 69–76.
[30] A. E. Green and I. N. Sneddon, "The distribution of stress in the neighbourhood of a flat elliptical crack in an elastic solid", *Proc. Camb. Philos. Soc.* **46** (1950), pp. 159–164.
[31] I. N. Sneddon, "The distribution of stress in the neighbourhood of a crack in an elastic solid", *Proc. R. Soc. Lond. A* **187** (1946), pp. 229–260.
[32] G. R. Irwin, "Crack-Extension Force for a Part-Through Crack in a Plate", *ASME J. Appl. Mech.* **29** (1962), pp. 654–661.
[33] X. K. Zhu, G. T. Liu and Y. J. Chao, "Three-dimensional stress and displacement fields near an elliptical crack front", *Int. J. Fract.* **109** (2001), pp. 383–401.
[34] Y. Schapira and Z. Yosibash, "Asymptotic solution of the elasticity equations in the vicinity of an elliptical crack front", *Eng. Fract. Mech.* **223** (2020), article no. 106774.
[35] V. Lazarus, "Brittle fracture and fatigue propagation paths of 3D plane cracks under uniform remote tensile loading", *Int. J. Fract.* **122** (2003), pp. 23–46.
[36] B. K. Hachi, Y. Belkacemi, S. Rechak, M. Haboussi and M. Taghite, "Fatigue growth prediction of elliptical cracks in welded joint structure: Hybrid and energy density approach", *Theor. Appl. Fract. Mech.* **54** (2010), pp. 11–18.

[37] M. Morishita, K. Gotoh, Y. Anai, S. Tsumura and T. Niwa, "Fatigue surface crack growth behavior in flat plate and out-of-plane gusset-welded joints under biaxial cyclic loads with different phases", *J. Mar. Sci. Technol.* **26** (2021), pp. 655–672.

[38] G. Villani, V. G. Belardi, P. Salvini and F. Vivio, "Energetic approach to predict the elliptical crack growth", *Procedia Struct. Integr.* **47** (2023), pp. 873–881.

[39] M. Burhan, T. Scalici, Z. Ullah, Z. Kazancí and G. Catalanotti, "A three-dimensional Finite Fracture Mechanics model to predict free edge delamination in angle-ply laminates", *Eng. Fract. Mech.* **306** (2024), article no. 110156.

[40] M. Burhan, Z. Ullah, Z. Kazancí and G. Catalanotti, "A finite fracture mechanics approach to assess the fatigue life of laminates exhibiting free edge effects", *Compos. Struct.* **354** (2025), article no. 118797.

[41] M. Burhan, Z. Ullah, Z. Kazancí and G. Catalanotti, "Predicting free edge delamination induced by thermal loading using finite fracture mechanics", *Int. J. Fract.* **250** (2025), article no. 110156.

[42] M. Bach, S. Nazarov and W. Wendland, "Stable propagation of a mode-1 planar crack in an isotropic elastic space. Comparison of the Irwin and the Griffith approaches", in *Problemi Attuali Dell'Analisi e Della Fisica Matematica. Atti del 20 Simposio internazionale (Taormina 15–18 Ottobre 1998)* (P. E. Ricci, ed.), Aracne: Rome, 2000, pp. 167–190.

[43] L. David and V. Lazarus, "On the key role of crack surface area on the lifetime of arbitrarily shaped flat cracks", *Int. J. Fatigue* **154** (2022), article no. 106512.

[44] Y. Mikata, "Analytical solution for fatigue crack propagation of an embedded elliptical crack", *Int. J. Fract.* **229** (2021), pp. 245–251.

[45] A. Carpinteri, "Static and energetic fracture parameters for rocks and concrete", *Mater. Struct.* **14** (1981), pp. 151–162.

[46] J. P. Pereira, C. A. Duarte and X. Jiao, "Three-dimensional crack growth with hp-generalized finite element and face offsetting methods", *Comput. Mech.* **46** (2010), pp. 431–453.

[47] J. Xu, H. Li, H. Wang and L. Tang, "Experimental study on 3D internal penny-shaped crack propagation in brittle materials under uniaxial compression", *Deep Undergr. Sci. Eng.* **2** (2023), pp. 37–51.

ACADÉMIE DES SCIENCES
INSTITUT DE FRANCE

Comptes Rendus. Mécanique
2025, Vol. 353, p. 601-614
https://doi.org/10.5802/crmeca.296

Research article / *Article de recherche*

Some remarks concerning the nucleation and initiation lengths of fractures in brittle materials in the light of Dominique Leguillon's energy criterion

Quelques remarques sur la nucléation et les longueurs d'initiation des fissures dans les matériaux fragiles à la lumière du critère énergétique de Dominique Leguillon

Luc Dormieux [a], Eric Lemarchand [*, a], Laurent Jeannin [b] and Djimedo Kondo [c]

[a] Laboratoire Navier (UMR 8205), École nationale des ponts et chaussées - Institut Polytechnique de Paris, CNRS, Université Gustave Eiffel, 6 et 8 avenue Blaise Pascal 77455 cedex-2 Marne-la-Vallée, France

[b] STORENGY, 12 rue Raoul Nordling - Djinn - CS 70001, 92274 Bois Colombes Cedex, France

[c] Sorbonne Universités, Institut Jean Le Rond d'Alembert, UMR 7190 CNRS-SU, F-75005, Paris, France

E-mails: luc.dormieux@enpc.fr (L. Dormieux), eric.lemarchand@enpc.fr (E. Lemarchand), laurent.jeannin@storengy.com (L. Jeannin), djimedo.kondo@sorbonne-universite.fr (D. Kondo)

Abstract. Crack nucleation has been the subject of important contributions in the two last decades. Starting from the energy criterion of Leguillon (*Eur. J. Mech.—A/Solids* **21** (2002)), the present paper examines some consequences that follow directly from the perfectly brittle model. This enables to discuss whether a quasi-static modelling of nucleation is possible. Rigorous bounds for the loading level that triggers nucleation as well as for the set of observable crack lengths under dynamic conditions are established.

Résumé. La nucléation des fissures a fait l'objet de contributions importantes au cours des deux dernières décennies. En partant du critère énergétique proposé par Leguillon (*Eur. J. Mech.—A/Solids* **21** (2002)), le présent article examine certaines conséquences qui découlent directement du modèle parfaitement fragile. Cela permet de discuter de la possibilité d'une modélisation quasi-statique de la nucléation. Des bornes rigoureuses sont établies pour le niveau de chargement déclenchant la nucléation ainsi que pour l'ensemble des longueurs de fissures observables dans des conditions dynamiques.

Keywords. Crack initiation, Crack nucleation, Energy criterion, Dynamic, Bounds.

Mots-clés. Initiation de fissure, Nucléation de fissure, Critère énergétique, Dynamique, Bornes.

Manuscript received 11 February 2025, revised and accepted 10 April 2025.

* Corresponding author

1. Introduction

The pioneering paper [1] of Leguillon was, without a doubt, a major step in the direction of understanding and quantifying the crack nucleation process. Its starting point was a seemingly simple remark concerning the potential energy release occuring during the process:

$$-\delta\mathscr{E}_{\text{pot}} \geq G_c \delta S \tag{1}$$

in which G_c denotes the fracture energy per unit surface. As opposed to the Griffith concept of rate of energy release [2], it is emphasized that the above inequality refers to a finite variation δS of surface. The significance of (1), that is generally referred to as energy criterion, is now widely acknowledged. In [1], it was proposed that (1) should be combined with a stress criterion to be fulfilled in the area where the crack is nucleated. This is intended to determine the critical loading level of nucleation as well as its extent. This approach is therefore often referred to as the double or coupled criterion (CC) method. Ever since, the latter was applied to deal with a number of different situations, first in its initial quasi-static framework and more recently with account for dynamic effects [3].

More recently, in the case of stable nucleation processes, [4] argued that Leguillon's energy criterion was sufficient for characterizing the occurrence and the extent of nucleation. This new methodology was first applied to study fracture nucleation that occurs during tunnelling in the context of nuclear waste storage. It was also illustrated in various problems of rock mechanics (e.g. [5,6]). Finally, an extension to the case of saturated porous materials was proposed [7].

The modelling of crack nucleation must address the determination of the geometry of the crack and its evolution in time. For simplicity, considering the case of a straight line crack, it amounts to determine the interval $\mathscr{I}$ of observable crack lengths ℓ together with the crack velocity $\dot{\ell}$. The next question is how the loading level affects the minimum and maximum (if any) in $\mathscr{I}$ as well as the evolution law.

Among these questions, the determination of the minimum of $\mathscr{I}$, which can be termed the initiation crack length, is of paramount importance. More precisely, the question is whether it has a non-zero value or if the interval $\mathscr{I}$ of observable crack lengths truly starts at 0. It has been argued [3] that a non zero initiation length is an artefact of the quasi-static description of nucleation. It was also suggested in [3] that an appropriate dynamic description of crack initiation could account for a progressive extension of crack length starting from 0. It seems however that the issue is still opened and that some arguments are in favor of a strictly positive initiation length, irrespective of whether the description is dynamic or not. Furthermore, the question that comes next is whether the model of brittle material is able, by itself, to describe the transition from the initial state (no crack) to that of a cracked state. We shall see that the energy criterion in the form (1) is a good starting point to contribute to this discussion.

More generally, the choice between quasi-static and dynamic modelling of nucleation is in itself an important issue that the present paper would like to consider. Indeed, as pointed out in [3], the very nature of nucleation is the creation of a crack in short amount of time. Therefore, a quasi-static modelling of such a process seems a priori questionable, although it is widely used. At least, it deserves a thorough investigation in order to clarify in which case it can be implemented.

The methodology adopted in this paper consists to strictly rely on the model of perfectly brittle material without additionnal assumption. The purpose is to draw the necessary conditions following from this basis. Accordingly, as regards the description of the crack nucleation process, the relevant material constant is the fracture energy G_c with which both the Griffith criterion as well as (1) can be formulated. In short, the main objective is to determine what can be derived from this model as well as what is out of reach and would require a more elaborated framework or further hypotheses.

2. Dynamic energy release rate

Let Ω denote the mechanical system in which possible crack nucleation is considered. The geometry of the crack is described by a formal parameter ℓ. This is for instance the length in 2D or the area in 3D. It controls the energy $G_c\ell$ that is dissipated during nucleation. During the nucleation process, ℓ increases from 0 to a limit value ℓ^* for which stability is recovered under the loading that has triggered the nucleation.

The starting point is the Clausius–Duhem inequality [8,9]: In isothermal conditions, it states that the external power ($\mathscr{P}_e$) provided to the system Ω is transformed into the rate of change of free energy ($\dot{\Psi}$) and the rate of change of the kinetic energy ($\dot{K}$) or dissipated in the crack nucleation process (dissipation rate $\mathscr{D}$):

$$\mathscr{D} = \mathscr{P}_e - \dot{\Psi} - \dot{K} \geq 0. \tag{2}$$

As already stated in the introduction of the present paper, this is also the starting point of the celebrated work of Leguillon [1] in which (2) is considered in an integrated form with respect to time:

$$\Delta\Psi - \mathscr{W}_e + K + \int \mathscr{D}\,\mathrm{d}t = 0. \tag{3}$$

For simplicity, we assume steady state conditions for the mechanical loading $\mathscr{L}$, the latter being defined by body forces $\underline{F}$, prescribed surface forces $\underline{T}^d$ on $\partial\Omega_T$, prescribed displacements $\underline{\xi}^d$ on $\partial\Omega_\xi$, the boundary of the material system being $\partial\Omega = \partial\Omega_\xi \cup \partial\Omega_T$. The external power provided to the system thus reads:

$$\mathscr{P}_e = \int_\Omega \underline{F}\cdot\dot{\underline{\xi}}\,\mathrm{d}V + \int_{\partial\Omega_T} \underline{T}^d\cdot\dot{\underline{\xi}}\,\mathrm{d}S.$$

Since we aim at describing the crack propagation occuring in the framework of crack nucleation, we focus on a time interval of crack length increase ($\dot{\ell} > 0$). This makes the relation between time and crack length a bijective one, so that the velocity $\dot{\underline{\xi}}$ can be put in the form:

$$\dot{\underline{\xi}} = \frac{\partial \underline{\xi}}{\partial \ell}_{|\mathscr{L}}\dot{\ell}.$$

For the same reason, the time derivatives of the free energy and the kinetic energy are replaced by derivatives with respect to the crack length:

$$\dot{\Psi} = \frac{\partial \Psi}{\partial \ell}_{|\mathscr{L}}\dot{\ell}; \quad \dot{K} = \frac{\partial K}{\partial \ell}_{|\mathscr{L}}\dot{\ell}. \tag{4}$$

Under steady loading conditions, the external power is due to crack propagation only:

$$\mathscr{P}_{e|\mathscr{L}} = \frac{\partial \Phi}{\partial \ell}_{|\mathscr{L}}\dot{\ell} \quad \text{with} \quad \Phi = \int_\Omega \underline{F}\cdot\underline{\xi}\,\mathrm{d}V + \lambda_T(t)\int_{\partial\Omega_T}\underline{T}^0\cdot\underline{\xi}\,\mathrm{d}S \tag{5}$$

where Φ is the potential of the given loads. Eventually, the combination of (2), (4) and (5) yields:

$$\mathscr{D} + \frac{\partial K}{\partial \ell}_{|\mathscr{L}}\dot{\ell} = -\frac{\partial \mathscr{E}^{\mathrm{dyn}}_{\mathrm{pot}}}{\partial \ell}_{|\mathscr{L}}\dot{\ell} \tag{6}$$

which introduces the potential energy $\mathscr{E}^{\mathrm{dyn}}_{\mathrm{pot}} = \Psi - \Phi$, where the upperscript dyn recalls that it is evaluated from the dynamic evolution of the displacement. If the dissipation process can be described by the concept of specific fracture energy, (6) takes the form:

$$G_c + \frac{\partial K}{\partial \ell}_{|\mathscr{L}} = -\frac{\partial \mathscr{E}^{\mathrm{dyn}}_{\mathrm{pot}}}{\partial \ell}_{|\mathscr{L}}. \tag{7}$$

The derived expression is formally very similar to the classical rate of energy release (see e.g. [10]), except for the fact that it comprises a term of kinetic energy. Furthermore, unlike the quasistatic case, the rate of potential energy release cannot be evaluated a priori. Indeed, it must be

calculated from the strain and displacement fields which are solution to the dynamic evolution of the system. It is therefore appropriate to refer to a dynamic potential energy release rate. Qualitatively, (7) states that the released energy is not entirely dissipated since a part of it is transformed into kinetic energy.

Note that (7) can be put in the equivalent form:

$$G_c = -\frac{\partial \mathscr{E}_{\text{mec}}^{\text{dyn}}}{\partial \ell}_{|\mathscr{L}} \tag{8}$$

where $\mathscr{E}_{\text{mec}}^{\text{dyn}}$ is the mechanical energy $\mathscr{E}_{\text{pot}} + K$. This suggests an alternative definition to the dynamic energy release rate.

3. The assumption of quasistatic nucleation process

To begin with, let us however leave the dynamic aspect of the process aside which amounts to assuming that the kinetic energy term is negligible. In this section, we shall therefore examine the assumption of a quasistatic nucleation process under a given constant loading level. The quasistatic assumption means that each state in the nucleation process is an equilibrium state. From a practical point of view, the great advantage of this assumption is clearly that, by nature, it avoids the determination of a dynamic problem. The potential energy therefore becomes a function of the crack length.

For instance, let us assume that the loading is defined[1] by a single scalar parameter Q, and that the corresponding work of external forces reads $\Phi = Q\xi$. The free energy takes the form $\Psi = (1/2)C(\ell)\xi^2$ where $C(\ell)$ represents the elastic stiffness of the cracked structure. In view of further use, let us introduce the functions $\mathbb{C}(\ell)$ and $\mathscr{C}(\ell)$:

$$\mathbb{C}(\ell) = \frac{1}{\ell}(C(0) - C(\ell)); \quad \mathscr{C}(\ell) = \frac{1}{\ell}\left(\frac{1}{C(\ell)} - \frac{1}{C(0)}\right). \tag{9}$$

In particular, the function $\mathscr{C}(\ell)$ is going to play a very important role in the following discussion. It involves informations concerning the geometry of the structure and the boundary conditions used for defining the loading. It represents the rate of change of the structural compliance. The static potential energy of the solution reads:

$$\mathscr{E}_{\text{pot}}^{\text{stat}} = \min_{\xi}\left(\frac{1}{2}C(\ell)\xi^2 - Q\xi\right) = -\frac{Q^2}{2C(\ell)}.$$

Considering any stage in the propagation process associated with some crack length ℓ, the energy balance reads:

$$\frac{Q^2}{2}\left(\frac{1}{C(\ell)} - \frac{1}{C(0)}\right) = \int \mathscr{D}\,\mathrm{d}t.$$

We now assume that the dissipation process can be described by the concept of a constant fracture energy G_c per unit surface. Accordingly, the above equation takes the form:

$$\frac{Q^2}{2}\mathscr{C}(\ell) = \frac{\mathscr{E}_{\text{pot}}^{\text{stat}}(0) - \mathscr{E}_{\text{pot}}^{\text{stat}}(\ell)}{\ell} = G_c. \tag{10}$$

Note that the above equation is also obviously retrieved from (3) in which the kinetic energy term is omitted. (10) indeed very much recalls the incremental form of the energy criterion of Leguillon. However, attention is drawn to the fact that we herein consider an equality which is made possible from the fact that we handle with a quasistatic process. Once again, such a framework is necessary for a practical determination of the energy release associated with the crack nucleation. This information is namely provided by the function $\mathscr{C}(\ell)$. The determination

[1] The boundary conditions could also be defined on the displacemnt. This would affect the definition of the potential energy.

of the latter only requires the resolution of standard elastostatic problems. It is worth noticing that the first equality in (10), that is:

$$\frac{Q^2}{2}\mathscr{C}(\ell) = \frac{\mathscr{E}_{\text{pot}}^{\text{stat}}(0) - \mathscr{E}_{\text{pot}}^{\text{stat}}(\ell)}{\ell}$$

can be regarded as a more general definition of function $\mathscr{C}(\ell)$. Its interest is to avoid to rely upon the stiffness function $C(\ell)$ which cannot be defined in the case of an infinite body. In contrast, the incremental energy release rate

$$G_{\text{inc}}(\ell) = \frac{\mathscr{E}_{\text{pot}}^{\text{stat}}(0) - \mathscr{E}_{\text{pot}}^{\text{stat}}(\ell)}{\ell}$$

introduced by Leguillon overcomes this shortcoming. Besides, in many cases, an analytical form of $\mathscr{C}(\ell)$ can be derived from the stress intensity factors (see e.g. [11]) by means of Irwin equation (see for example Section 4.2). Indeed, according to the latter, the incremental energy release rate of Leguillon is immediately derived by integration of the square of the stress intensity factor.

Nevertheless, it may be useful to observe that it is equivalent to give oneself the stiffness function $C(\ell)$ or the function $\mathscr{C}(\ell)$ appearing in the static incremental energy release rate. Indeed, the latter can obviously be derived from the former by (9). And in return, even if the stiffness function does not exist as such (typically the case of an infinite body), it is always possible to introduce $C(\ell) = 1/(a + \ell\mathscr{C}(\ell))$. The choice of the positive constant a is arbitrary provided that $\lim_{\ell\to 0}\ell\mathscr{C}(\ell) = 0$. This constant vanishes in the expressions of energy criteria.

Similarly, it is equivalent to give oneself the compliance function $S(\ell) = 1/C(\ell)$ or the function $\mathscr{C}(\ell)$ appearing in the static incremental energy release rate. Again, the latter can be derived from the former by (9). And in return, even if the compliance function cannot be defined (typically the case of an infinite body where the compliance tends to 0), it is possible to introduce $S(\ell) = a + \ell\mathscr{C}(\ell)$. As before, the choice of the positive constant a is arbitrary.

We shall see now that the quasistatic assumption has drastic consequences.

3.1. *The case of a monotonic $\mathscr{C}(\ell)$ function*

The very concept of energy release suggests that the stiffness function is monotonically decreasing, or that the elastic compliance function is monotonically increasing. This obviously does not imply that $\mathscr{C}(\ell)$ shares this property. We first consider the case where the $\mathscr{C}(\ell)$ function is indeed a strictly increasing function (see Figure 1 case (a)).

From a mathematical point of view, this is in particular the case if the stiffness function is a decreasing strictly concave function:

$$(\forall \ell \geq 0) \quad C'(\ell) \leq 0 \quad \text{and} \quad C''(\ell) < 0.$$

From a second order Taylor–Lagrange expansion:

$$(\exists \theta \in [0,1]) \quad C(0) = C(\ell) - \ell C'(\ell) + \tfrac{1}{2}C''(\theta\ell)\ell^2$$

it is found that $\mathbb{C}(\ell) + C'(\ell) < 0$. Observing that

$$\mathscr{C}'(\ell) = \frac{1}{C(0)C(\ell)\ell}\left(-\frac{C(0)}{C(\ell)}C'(\ell) - \mathbb{C}(\ell)\right)$$

and recalling that $C(0) > C(\ell)$, we conclude that $\mathscr{C}'(\ell) > 0$. It can be also readily shown that $\mathscr{C}(\ell)$ is monotonically increasing if the compliance function $S(\ell)$ is convex.

More concretely speaking, let us consider the example of a semi-infinite body subjected to a remote traction stress σ_∞ with an edge-crack normal to the boundary. The (mode I) stress

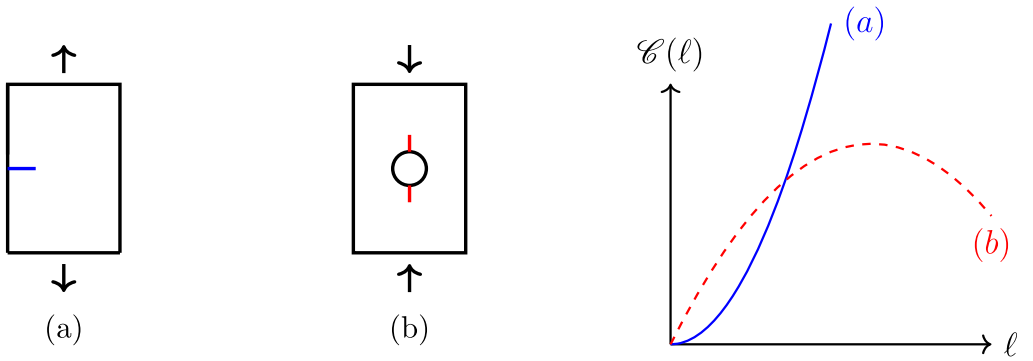

Figure 1. Various patterns of the rate of change of structural compliance $\mathscr{C}(\ell)$: (a) example of the monotonic increasing case; (b) example of the existence of a maximum.

intensity factor is of the form $\sigma_\infty\sqrt{\pi\ell}F$ where F is a scalar coefficient ($F \approx 1.12$, [11]). By integration of Irwin equation, this implies, in the present example, that the $\mathscr{C}(\ell)$ function is proportional to the crack length:

$$\mathscr{C}(\ell) = F^2\pi\frac{1-\nu^2}{E}\ell. \tag{11}$$

Let us go back to the general case of a strictly increasing function $\mathscr{C}(\ell)$. It follows that (10) with unknown ℓ has a unique solution ℓ^* (provided that $Q^2 < 2G_c/\mathscr{C}(0)$, if $\mathscr{C}(0) > 0$). This obviously implies that the nucleation process **is not** the propagation of a crack from 0 to the final length ℓ^*. In other words, within the quasistatic framework, it is impossible to observe any crack having a length $\ell < \ell^*$.

Let us assume that the crack with length ℓ^* has been indeed created. Following the quasistatic assumption, the current state is a (possibly not stable) equilibrium state. In any case, the rate of energy release in its differential form must comply with the standard Griffith criterion:

$$G_{\text{diff}}(\ell^*) = -\frac{\partial\mathscr{E}_{\text{pot}}^{\text{stat}}}{\partial\ell}(\ell^*) = \frac{Q^2}{2}\frac{d}{d\ell}(\ell\mathscr{C}(\ell))(\ell^*) \le G_c. \tag{12}$$

Since $\mathscr{C}'(\ell^*) > 0$, we have:

$$\frac{\mathrm{d}}{\mathrm{d}\ell}(\ell\mathscr{C}(\ell))(\ell^*) = \mathscr{C}(\ell^*) + \ell^*\mathscr{C}'(\ell^*) > \mathscr{C}(\ell^*)$$

from which it follows that (10) and (12) **are not** compatible. In other words, in the case of a strictly concav stiffness function, or more generally when $\mathscr{C}(\ell)$ is a monotonic increasing function, the quasistatic assumption fails to describe the nucleation process. As stated above (see (11)), this approach is therefore disqualified for a wide class of structures. This suggests that any method that aims at predicting the crack formation should take into account inertia effects, that is, should be developed in a dynamic framework.

3.2. *The case of a non monotonic $\mathscr{C}(\ell)$ function*

We now assume that $\mathscr{C}(\ell)$ is increasing on some interval $[0, \ell_{\text{cr}}]$ and decreases for $\ell > \ell_{\text{cr}}$ (see Figure 1 case (b)). This implies that $\mathscr{C}'(\ell_{\text{cr}}) = 0$. For given elastic properties, it is important to note that this property and in particular the critical length ℓ_{cr} are, by nature, independent of the loading level. Indeed, the practical determination of $\mathscr{C}(\ell)$ incorporates informations concerning the type of boundary conditions and the geometry of the body and of the crack. This is all the

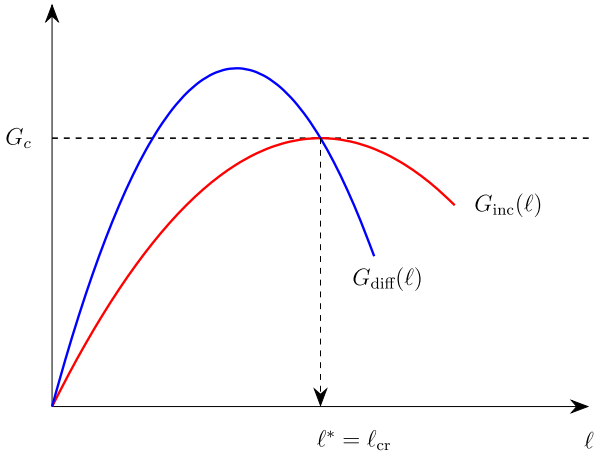

Figure 2. Characterization of the nucleated crack length ℓ^*: differential $G_{\text{diff}}(\ell)$ and incremental $G_{\text{inc}}(\ell)$ energy release rates for the critical loading level Q^* of (14).

more clear when $\mathscr{C}(\ell)$ is determined by integration of the (square of the) stress intensity factor in Irwin equation.

An example of this situation is the (mode I) crack that appears in a plate with circular hole under compression (see Section 4.2). The crack is expected to develop from the cavity boundary along the direction of compression. The analysis of the physical dimensions at stake indicates that the critical length ℓ_{cr} is expected to be proportional to the hole diameter R.

Let us examine if a quasistatic nucleation is compatible with this new framework. Clearly enough, this implies (necessary condition) that the sought crack length ℓ^* complies with (10) and (12) which are repeated here for convenience:

$$\frac{\mathscr{E}_{\text{pot}}^{\text{stat}}(0) - \mathscr{E}_{\text{pot}}^{\text{stat}}(\ell^*)}{\ell^*} = \frac{Q^2}{2}\mathscr{C}(\ell^*) = G_c; \quad -\frac{\partial \mathscr{E}_{\text{pot}}^{\text{stat}}}{\partial \ell}(\ell^*) = \frac{Q^2}{2}(\mathscr{C}(\ell^*) + \ell^*\mathscr{C}'(\ell^*)) \leq G_c. \tag{13}$$

The compatibility of these conditions appears to be $\mathscr{C}'(\ell^*) = 0$, which means that the nucleation crack length ℓ^* is none but the critical length ℓ_{cr}. Following the previous remarks concerning the latter, it is emphasized that the nucleation crack length predicted in this framework is determined a priori, without reference to the loading level that is responsible for nucleation.

The next question is to determine this loading level. The answer follows directly from (13):

$$Q^* = \sqrt{\frac{2G_c}{\mathscr{C}(\ell_{\text{cr}})}}. \tag{14}$$

We thus note that both the nucleation crack length and the loading level are determined in a unique way [12]. If $Q < Q^*$, the energy criterion is not fulfilled, in the sense that the energy release is not sufficient for the creation of the crack. If $Q > Q^*$, a dynamic process is intuitively expected, in which inertia effects have to be accounted for. This conclusion will be justified more thoroughly at the next section.

The loading level Q^* is such that the plot of the incremental energy release rate $G_{\text{inc}}(\ell)$ is tangent to the line $G = G_c$ at the point with abscissa ℓ_{cr}. The relative position of the plots of $G_{\text{inc}}(\ell)$ and $G_{\text{diff}}(\ell)$ in Figure 2 is obtained from the expressions of these quantities recalled in (13).

Again, it is noteworthy that no crack with length $\ell < \ell_{\text{cr}}$ can be observed. This suggests that the nucleation process that yields the critical crack length $\ell^* = \ell_{\text{cr}}$ cannot be described with the conventional concept of fracture energy G_c and the corresponding so-called Griffith criterion.

The opinion of the authors is that more elaborated modellings such as the idea of gradient damage [13] can be helpful for describing this maturation phase that precedes nucleation.

Anyway, under the loading Q^*, the structure is left in a state of stable equilibrium with a created crack of length $\ell_{\rm cr}$. Here, the physical interpretation of quasistatic nucleation is that the energy release exactly reaches the amount required for the creation of the crack and, so to speak, nothing is left for kinetic energy.

4. The non quasistatic nucleation process

4.1. *Rigorous bounds for the set of observable crack lengths*

At Section 3.1, we have seen that the quasistatic assumption fails to describe the nucleation process. This means that the latter cannot be viewed as a sequence of equilibrium states. It also fails in the framework of Section 3.2 if the loading level is greater than the threshold given by (14). In both cases, the reason is obviously related to non negligible inertia effects. This is also most consistent with the widespread physical intuition of nucleation as a sudden phenomenon taking place during a short amount of time. From now on, the set of observable crack lengths is denoted by $\mathscr{I}^{\rm dyn}$.

The inequality (1) derived by Leguillon, already stated in the introduction of this paper, appears as an appealing way to approach the modelling of nucleation in a more realistic manner. The latter relies upon the simple but very effective remark that the starting point being an equilibrium state, the variation of kinetic energy is necessarily positive. The profound interest of (1) is clearly that it is most general. Nevertheless, the question that arises is: how can we evaluate the potential energy in the lefthand side, with due account for the fact that the kinetic energy is not negligible? This very fact prohibits an approximation of the *dynamic* potential energy $\mathscr{E}_{\rm pot}^{\rm dyn}$ by its *static* counterpart $\mathscr{E}_{\rm pot}^{\rm stat}$. This can be highlighted in re-stating (1) in the explicit form:

$$-\delta\mathscr{E}_{\rm pot}^{\rm dyn} \geq G_c\delta S. \tag{15}$$

Some insight in this matter can be gained from an elementary argument, namely the so-called principle of minimum potential energy in linear elasticity. More precisely, for a given crack length ℓ and for the associated geometry Ω_ℓ, we are faced with two displacement fields: the solution $\underline{\xi}^{\rm dyn}$ to the "real" dynamic evolution and the solution $\underline{\xi}^{\rm stat}$ to the elastostatic problem. The displacement field $\underline{\xi}^{\rm dyn}$ is, by nature, kinematically admissible, so that the theorem ensures that $\mathscr{E}_{\rm pot}^{\rm dyn} > \mathscr{E}_{\rm pot}^{\rm stat}$. An immediate consequence is that $-\delta\mathscr{E}_{\rm pot}^{\rm dyn} < -\delta\mathscr{E}_{\rm pot}^{\rm stat}$ and further that:

$$-\delta\mathscr{E}_{\rm pot}^{\rm stat} > -\delta\mathscr{E}_{\rm pot}^{\rm dyn} \geq G_c\delta S. \tag{16}$$

This provides a simple justification of Leguillon's seminal intuition to the use of a static estimate of the potential energy in (1). Let us now interpret the consequence of this result as far as the modelling of nucleation is concerned. The obvious but also considerable interest of the static potential energy is that it is a function of the crack length and that it does not require the solution to an evolution problem. Accordingly, any crack length in the *dynamic* nucleation process must comply with (16):

$$(\forall\,\ell \in \mathscr{I}^{\rm dyn}) \quad \frac{Q^2}{2}\mathscr{C}(\ell) > G_c. \tag{17}$$

Let us first consider the case of the monotonic increasing function $\mathscr{C}(\ell)$.

> The equation $Q^2\mathscr{C}(\ell) = 2G_c$ with unknown ℓ has therefore a unique solution which, owing to (17), proves to be a **lower bound** for any observable crack length during the dynamic evolution process, that is, of the interval $\mathscr{I}^{\rm dyn}$. It is therefore denoted by $\ell^{lb}(Q)$ and defined by:
>
> $$\frac{Q^2}{2}\mathscr{C}(\ell^{lb}) = G_c; \quad (\forall\,\ell \in \mathscr{I}^{\rm dyn}) \quad \ell > \ell^{lb}(Q). \tag{18}$$

The very fact that $\mathscr{I}^{\text{dyn}}$ has a non-zero lower bound leads to introduce the concept of initiation length, denoted by $\ell_{\text{init}}^{\text{dyn}}$, and being the smallest crack length that can be observed in the dynamic nucleation process. Clearly enough, $\ell^{lb}(Q)$ is also a rigorous lower bound for ℓ_{init} that can be determined from the associated static problem:

$$\ell_{\text{init}}^{\text{dyn}} > \ell^{lb}(Q).$$

Using again that $\mathscr{C}(\ell)$ is an increasing function, it follows from (18) that $\ell^{lb}(Q)$ is a bijective decreasing function of Q. As stated at the end of Section 3.1, and despite the static nature of $\ell^{lb}(Q)$, it should be remembered that any attempt to determine the exact value of the initiation length should account for dynamic effects.

Let us now consider the case of a non monotonic function $\mathscr{C}(\ell)$.

Again, the starting point is that observable crack lengths must comply with (17). This is a necessary condition for the very existence of a crack of length ℓ in a dynamic process of nucleation. For a given value of Q, this implies that ℓ meets the following requirement:

$$Q > \sqrt{\frac{2Gc}{\mathscr{C}(\ell)}}.$$

A necessary condition for the existence of a solution ℓ in the above inequality is:

$$Q > \sqrt{\frac{2Gc}{\max \mathscr{C}(\ell)}} = \sqrt{\frac{2Gc}{\mathscr{C}(\ell_{\text{cr}})}} = Q^* \tag{19}$$

in which we recognize the threshold Q^* introduced at (14) as the unique loading level being compatible with a quasistatic nucleation process. We now gain a new interpretation of the latter: Q^* is in fact a rigorous lower bound for any loading level able to initiate a crack. In other words, we draw the conservative conclusion that no crack nucleation should be observed, neither quasistatic nor dynamic, is $Q < Q^*$.

We now assume that $Q > Q^*$. Let $\ell^{lb}(Q)$ and $\ell^{ub}(Q)$ be the solutions of the equation $Q^2\mathscr{C}(\ell) = 2G_c$ with unknown ℓ as shown on Figure 3. The condition (17) implies that these lengths indeed provide bounds for $\mathscr{I}^{\text{dyn}}$. The latter is therefore a bounded interval of the form $[\ell_{\text{init}}^{\text{dyn}}, \ell_{\text{nuc}}^{\text{dyn}}]$ and we have:

$$\ell^{lb}(Q) \le \ell_{\text{init}}^{\text{dyn}} \le \ell_{\text{nuc}}^{\text{dyn}} \le \ell^{ub}(Q). \tag{20}$$

In particular, for values of $Q > Q^*$ in the neighborhood of Q^*, it may be concluded that the initiation and nucleation lengths should be very close and that ℓ_{cr} is a good estimate of them (see Figure 3).

It is emphasized that the bounds $\ell^{lb}(Q)$ and $\ell^{ub}(Q)$ are very simply determined within an **elastostatic framework** and are therefore elastostatic by nature. Furthermore, for any loading level $Q > Q^*$, we have seen that the nucleation process is not a quasistatic one. It is all the more remarkable that $\ell^{lb}(Q)$ and $\ell^{ub}(Q)$ nevertheless provide rigorous bounds for the interval $\mathscr{I}^{\text{dyn}}$ of observable crack lengths in a dynamic process.

4.2. *The example of an infinite medium with circular hole*

Let us apply the developments of Section 4.1 to the classical problem of an infinite medium with a circular hole subjected to remote uniaxial compression in plane strains. In this case, it is wellknown that the nucleation of a stable crack is expected (e.g. [6,14]).

Figure 4 presents the quasistatic incremental energy release rate for two different remote stresses. In the present case, an analytical expression can be provided. The starting point is the stress intensity factor for a given remote stress state [14]:

$$K_I(\ell) \approx -\frac{1.1\sqrt{\ell/R}}{(1+\ell/R)^{3.3}}\sigma_\infty\sqrt{\pi R}. \tag{21}$$

Irwin's formula in plane strains relates the stress intensity factor to the rate of energy release $G(\ell)$:

$$G(\ell) = -\frac{\partial \mathscr{E}_{\text{pot}}^{\text{stat}}}{\partial \ell} = \frac{1-\nu^2}{E}K_I^2. \tag{22}$$

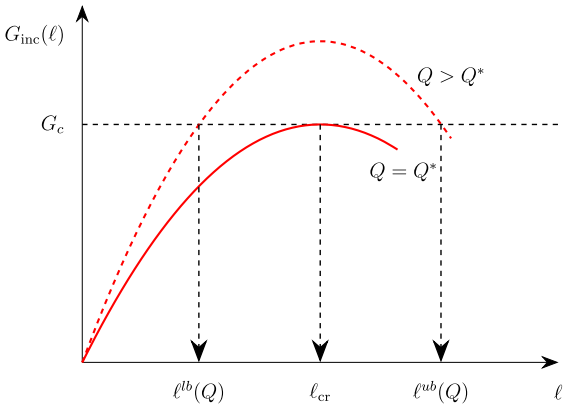

Figure 3. Lower and upper bounds of $\mathscr{J}^{\text{dyn}}$ in the case of non monotonic $\mathscr{C}(\ell)$.

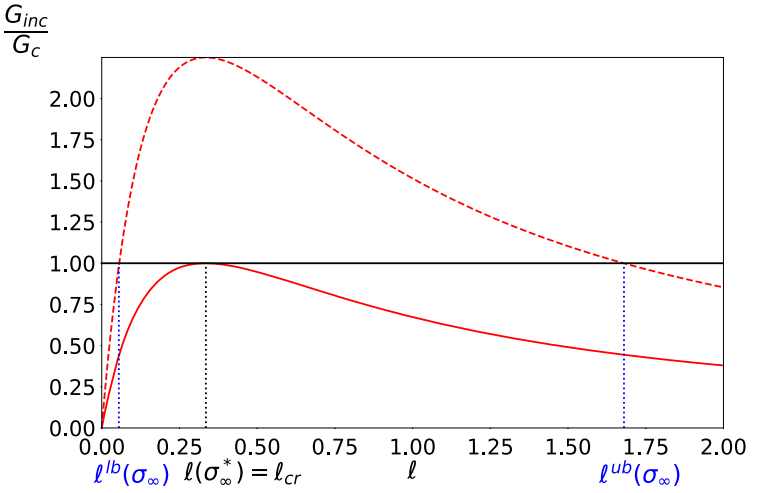

Figure 4. Circular hole in an infinite medium. Incremental energy release rate for two different stress levels: the critical stress level σ_∞^* (solid line); $\sigma_\infty = 1.5\sigma_\infty^*$ (dashed line).

$G_{\text{inc}}(\ell)$ is readily obtained by integration:

$$G_{\text{inc}}(\ell) = \frac{1-\nu^2}{E\ell}\int_0^\ell K_I^2(u)\mathrm{d}u \tag{23}$$

which yields, with $\lambda = \ell/R$:

$$G_{\text{inc}}(\ell) = \Gamma\left(\frac{1}{21.29\lambda}\left(1-\frac{1}{(1+\lambda)^{4.6}}\right)-\frac{1}{4.63(1+\lambda)^{5.6}}\right) \quad \text{with } \Gamma = \frac{\pi R{\sigma_\infty}^2(1-\nu^2)}{E}. \tag{24}$$

Figure 5 presents the variation of the lower and upper bounds of $\mathscr{J}^{\text{dyn}}$ as functions of the remote compression stress. Interestingly, when the remote stress is slightly greater than the critical stress level σ_*^∞, the dynamic lower and upper bounds are very close to the static critical length $\ell^* = \ell_{\text{cr}}$.

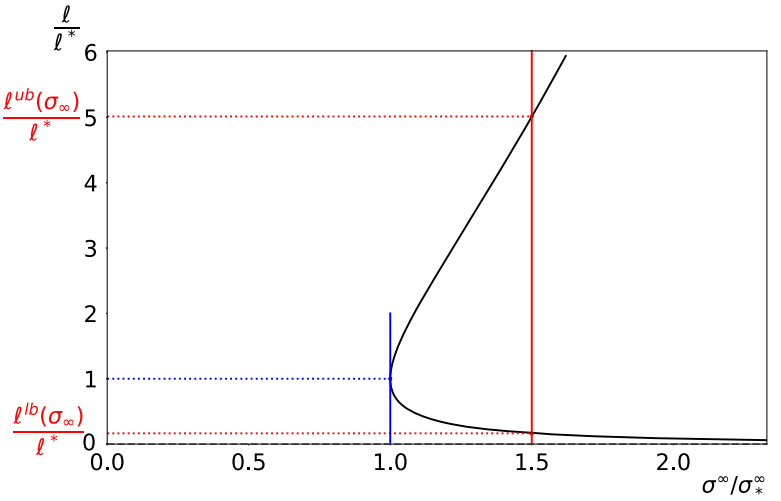

Figure 5. Circular hole in an infinite medium. Normalized lower and upper bounds of $\mathscr{J}^{\text{dyn}}$ as functions of the normalized loading level $\sigma^\infty/\sigma^\infty_*$.

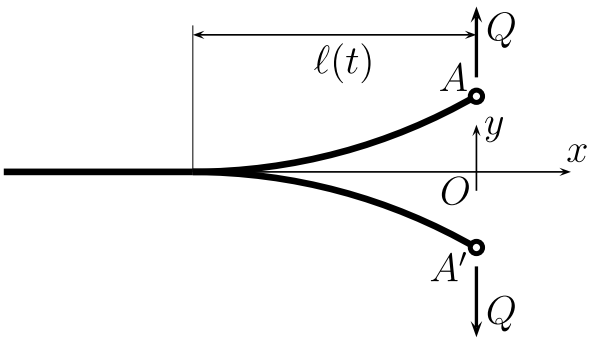

Figure 6. Double cantilever beam. The crack tip is located at $x = -\ell(t)$ (left extremity of the beams).

4.3. *A simplified dynamic example: the double cantilever beam*

Let us investigate the concept of crack initiation length into more details in the framework of a one-dimensional continuous medium. The example is that of a double cantilever elastic beam (flexural rigidity EI, width b). Two opposite forces $\pm Q\underline{e}_y$ act on two identical masses m located at the symmetric right extremities A and A' of the beams (see Figure 6). The vertical displacement of the upper beam is denoted by $\xi_y(x,t)$. Let denote $u(t) = 2\xi_y(0,t) = AA'$ and $v(t) = \xi_y(0,t)$. The inertia effects are accounted for through the kinetic energy of the two point masses while preserving the possibility to derive an analytical solution. At point $(-\ell,0)$, the boundary conditions are $\xi_y(-\ell(t),t) = 0$ and $\partial\xi_y/\partial x(-\ell(t),t) = 0$.

For symmetry reasons, we focus on the upper beam. We shall introduce the three following quantities, which have the dimension of a length, among which the last one κ is time dependent:

$$\lambda = \sqrt{\frac{EI}{G_c b}}; \quad \ell_0 = \frac{\sqrt{EIG_c b}}{Q}; \quad \kappa = \frac{K}{Q}.$$

Let denote $V(x,t)$ and $M(x,t)$ the shear force and the bending moment. Moment balance yields:

$$-V+Q=m\ddot{v} \quad \text{and} \quad \frac{\mathrm{d}M}{\mathrm{d}x}+V=0 \quad \Rightarrow M(x,t)=(m\ddot{v}-Q)x.$$

The displacement $\xi_y(x,t)$ is therefore obtained by two integrations from the curvature $\chi = \partial^2\xi_y/\partial x^2$:

$$EI\frac{\partial^2\xi_y}{\partial x^2}(x,t)=(m\ddot{v}-Q)x.$$

The term $m\ddot{v}$ incorporates the inertia effect and is responsible for the discrepancy between the dynamic solution and the static one. Owing for the boundary conditions at $x=-\ell(t)$, it is found that:

$$EI\xi_y(x,t)=(m\ddot{v}-Q)\left(\frac{x^3}{6}-\frac{\ell(t)^2x}{2}-\frac{\ell^3}{3}\right)$$

and eventually at $x=0$:

$$EIv(t)=(Q-m\ddot{v})\frac{\ell(t)^3}{3}.$$

The dynamic equation of the beam written for $u(t)=2v(t)$ therefore takes a familiar shape:

$$\mu\ddot{u}+C(\ell)u=Q$$

with $\mu=m/2$ and $C(\ell)=(3/2)(EI/\ell^3)$. The total kinetic energy is $K=(1/2)\mu\dot{u}^2$ and, after integration of the elastic energy density $(1/2)EI\chi^2$, the total elastic energy is $(1/2)C(\ell)u^2$. Eventually, the dynamic potential energy reads:

$$\mathscr{E}_{\mathrm{pot}}^{\mathrm{dyn}}=\tfrac{1}{2}C(\ell)u^2-Qu$$

which is formally identical to the expression of the static potential energy, except of course for the fact that $u(t)$ is not equal to the static solution $u^{\mathrm{stat}}=(2Q\ell^3)/(3EI)$ which yields

$$\mathscr{E}_{\mathrm{pot}}^{\mathrm{stat}}=-\frac{Q^2\ell^3}{3EI}. \tag{25}$$

According to definition (9), it is found that

$$\mathscr{C}(\ell)=\frac{2\ell^2}{3EI}$$

which is monotonic increasing. Following the conclusions of Sections 3.1 and 4.1, a lower bound of the initiation crack length can be derived from (18):

$$\ell_{\mathrm{init}}^{\mathrm{dyn}}>\sqrt{3}\ell_0 \tag{26}$$

and we know that the damage process that leads to the crack of length $\ell_{\mathrm{init}}^{\mathrm{dyn}}$ cannot be a quasistatic one.

It is recalled that the previous bound is derived from the inequality $\mathscr{E}_{\mathrm{pot}}^{\mathrm{dyn}}>\mathscr{E}_{\mathrm{pot}}^{\mathrm{stat}}$ which follows from the theorem of minimal potential energy. As previously stated, it holds true for any dynamic evolution. But the very fact that it does not require the determination of the dynamic evolution suggests that it could be improved if the latter were considered. Following this idea, we now aim at improving the lower bound (26). With the expressions of $\mathscr{E}_{\mathrm{pot}}^{\mathrm{dyn}}$ and K, the energy balance (3) reads:

$$\frac{\mathrm{d}}{\mathrm{d}t}\left(\frac{1}{2}C(\ell)u^2-Qu+\frac{1}{2}\mu\dot{u}^2+G_cb\ell\right)=0$$

which can be put in the form:

$$\dot{\ell}(\tfrac{1}{2}C'(\ell)u^2+G_cb)+\dot{u}(\mu\ddot{u}-Q+C(\ell)u)=0.$$

The combination with the momentum balance equation yields $\dot{\ell}((1/2)C'(\ell)u^2+G_cb)=0$. Therefore, once the crack has been created ($\ell\geq\ell_{\mathrm{init}}^{\mathrm{dyn}}$) and propagates ($\dot{\ell}>0$), we have to write together

$$\tfrac{1}{2}C'(\ell)u^2+G_cb=0$$

and the energy balance in the integrated form:

$$\tfrac{1}{2}C(\ell)u^2 - Qu + G_c b\ell + K = 0$$

where K is the current value of the kinetic energy. Note that these equations are the particular form in the present example of (7) and (3) respectively. This yields

$$K + \frac{4}{3}G_c b\ell - \frac{2}{3}\ell^2 Q\sqrt{\frac{G_c b}{EI}} = 0$$

or

$$\ell(t)^2 - 2\ell_0\ell(t) - \frac{3}{2}\kappa(t)\lambda = 0 \quad \Rightarrow \quad \ell(t) = \ell_0\left(1 + \sqrt{1 + \frac{3\lambda\kappa(t)}{2\ell_0^2}}\right).$$

Since $\kappa(t)$ is a positive number, the above expression of $\ell(t)$ provides a new lower bound of the initiation length:

$$\ell_{\text{init}}^{\text{dyn}} = \ell_0\left(1 + \sqrt{1 + \frac{3\lambda\kappa_{\text{init}}}{2\ell_0^2}}\right) \geq 2\ell_0.$$

The improvement of the lower bound as compared to (26) underlines that the initiation state is not an equilibrium state, even when we take the limit $\kappa_{\text{init}} \to 0$. It is noteworthy that the present approach cannot per se determine the value of the constant κ_{init} which is necessary for deriving the exact value of the initiation length.

5. Conclusion

The purpose of this paper was to highlight what can be said about the nucleation process with the standard model of perfectly brittle material as a modelling basis. It is important to underline that the developments presented herein are based on the assumption that the crack is indeed nucleated. For instance, the lower bound of $\mathscr{J}^{\text{dyn}}$ provided in (18) explicitely assumes this prerequisite. Similarly, (19) is a necessary condition for crack nucleation and the model cannot say whether it is sufficient. To do so, further material parameters, such as the tensile strength occurring in the CC (coupled criterion), would be required. With this in mind, let us briefly review the main conclusions drawn in this framework.

A very important characteristic involving the geometry of the structure together with the way the loading is applied is the rate of change of the structural compliance. In the simple case of a straightline crack, it becomes a function $\mathscr{C}(\ell)$ of the crack length. The latter is easily determined analytically from the knowledge of stress intensity factors or numerically from the solution to elastostatic problems. It is appropriate to distinguish two cases whether this function is monotonically increasing or not.

When the function $\mathscr{C}(\ell)$ is a monotonically increasing one, a quasistatic description of nucleation is not possible irrespective of the loading level. In contrast, when the function $\mathscr{C}(\ell)$ reaches a maximum at $\ell = \ell_{\text{cr}}$, there exists a unique loading level Q^* that is compatible with a quasistatic process of nucleation. The critical crack length ℓ_{cr} is only a function of the geometry at stake. Any loading level $Q > Q^*$ will induce dynamic effects.

An appropriate use of the classical theorem of minimum potential energy reveals that the dynamic potential energy release is upper bounded by its static counterpart, that is, for the same crack length change. This enables to use various mathematical descriptors issued from a quasistatic framework fro the design of dynamic bounds. For instance, a rigorous strictly positive lower bound of the (dynamic) initiation length $\ell_{\text{init}}^{\text{dyn}}$ can be determined as a function of the loading level. In other words, the theoretical framework of perfectly brittle material in itself contradicts the existence of a length crack $\ell < \ell_{\text{init}}^{\text{dyn}}$. The description of the damage process yielding the initiation length should resort to more elaborated material modellings (see e.g. [15–17]).

When the function $\mathscr{C}(\ell)$ is non monotonic, the set $\mathscr{I}^{\text{dyn}}$ of observable crack lengths is lower and upper bounded. The closer the loading level to the critical one (14), the narrower the set $\mathscr{I}^{\text{dyn}}$ in the neighborhood of the critical length ℓ_{cr}.

Declaration of interests

The authors do not work for, advise, own shares in, or receive funds from any organization that could benefit from this article, and have declared no affiliations other than their research organizations.

References

[1] D. Leguillon, "Strength or toughness: a criterion for crack onset at a notch", *Eur. J. Mech.—A/Solids* **21** (2002), pp. 61–72.

[2] A. A. Griffith, "The phenomenon of rupture and flow in solids", *Philos. Trans. R. Soc. Lond.* **221** (1921), pp. 163–198.

[3] A. Doitrand, G. Molnar, D. Leguillon, E. Martin and E. Carrère, "Dynamic crack initiation assessment with the coupled crterion", *Eur. J. Mech. A, Solids* **93** (2022), article no. 104483.

[4] T. Carlioz, *Nucléation et propagation de fissures en conditions anisotropes*, Thèse de doctorat, Université Paris-Est, 2017.

[5] L. Jeannin, L. Dormieux and T. Carlioz, "Nucleation of thermal cracks at the wall of a rock mass", *Mech. Res. Commun.* **97** (2019), pp. 57–62.

[6] L. Jeannin, L. Dormieux, E. Lemarchand and T. Carlioz, "Analysis of fracture nucleation around wellbores", *Int. J. Fracture* **230** (2021), pp. 157–178.

[7] L. Dormieux, E. Lemarchand, T. Carlioz and L. Jeannin, "Crack nucleation in saturated porous media", *Int. J. Numer. Anal. Meth. Geomech.* **5** (2020), pp. 553–574.

[8] L. Dormieux and D. Kondo, *Micromechanics of Fracture and Damage*, ISTE-Wiley: London, 2016.

[9] J. R. Rice, "Thermodynamics of the quasi-static growth of Griffith cracks", *J. Mech. Phys. Solids* **26** (1978), pp. 61–78.

[10] J. B. Leblond, *Mécanique de la rupture fragile et ductile*, Hermes Science Publications: Lavoisier, Paris, 2003.

[11] G. C. Sih, *Handbook of Stress Intensity Factors for Researchers and Engineers*, Lehigh University: Bethlehem, 1973.

[12] T. Carlioz, L. Dormieux and E. Lemarchand, "Thermodynamics of crack nucleation", *Contin. Mech. Thermodyn.* **32** (2020), pp. 1515–1531.

[13] K. Pham and J.-J. Marigo, "Gradient damage models and their use to approximate brittle fracture", *Int. J. Damage Mech.* **4** (2011), pp. 618–652.

[14] C. G. Sammis and M. F. Ashby, "The failure of brittle porous solids under compressive stress states", *Acta Metall.* **34** (1986), no. 3, pp. 511–526.

[15] B. Bourdin, G. A. Francfort and J.-J. Marigo, "The variational approach to fracture", *J. Elast.* **91** (2008), pp. 5–148.

[16] R. De Borst and C. V. Verhoosel, "Gradient damage vs phase-field approaches for fracture: similarities and differences", *Comput. Meth. Appl. Mech. Engrg.* **312** (2016), pp. 78–94.

[17] K. Pham and J.-J. Marigo, "From the onset of damage to rupture: construction of responses with damage localization for a general class of gradient damage models", *Contin. Mech. Thermodyn.* **25** (2013), no. 2, pp. 147–171.

ACADÉMIE DES SCIENCES
INSTITUT DE FRANCE

Comptes Rendus. Mécanique
2025, Vol. 353, p. 627-646
https://doi.org/10.5802/crmeca.293

Research article / *Article de recherche*

Particle size effect on the strength of particle-reinforced composites. Experimental analysis and comparison with the coupled criterion

Effet de la taille des particules sur la résistance des composites renforcés par particules : analyse expérimentale et comparaison avec le critère couplé

Israel García García [*, a], Jesús Justo [a], Alejandro Zurita Van-Dinter [a] and Vladislav Mantič [a]

[a] Departamento de Mecánica de Medios Continuos y Teoría de Estructuras, Escuela Técnica Superior de Ingeniería, Escuela Politécnica Superior. Universidad de Sevilla. Camino de los Descubrimientos s/n, 41092 Sevilla, Spain

E-mails: israelgarcia@us.es (I. G. García), jjusto@us.es (J. Justo), azurita.etsi@gmail.com (A. Zurita Van-Dinter), mantic@us.es (V. Mantič)

This article is dedicated to the memory of Professor Dominique Leguillon

Abstract. Particle-reinforced composites are widely used in industry, primarily due to their versatile fabrication methods and the ability to tailor their properties. In many cases, extensive experimental campaigns are required to determine the optimal characteristics of the system to enhance specific properties. Micromechanical models can serve as a useful alternative or initial approach during the material design process. One of the easiest characteristics that can be modified is the size of the reinforcement, which, according to some models and preliminary evidence, can significantly affect the mechanical properties of the material.

The objective of this work is to experimentally evaluate the size effect of reinforcement on the composite strength and to compare it with the predictions by the coupled criterion of finite fracture mechanics (CC-FFM). A secondary objective is to visualize the initiation of the failure mechanism, which starts at the particle-matrix interface and progresses toward a crack that splits the specimen. To achieve this, a new specimen design is proposed along with an optimized fabrication procedure. The tests were recorded using a high-speed camera, which allowed for the visualization of crack initiation at the particle-matrix interface.

The experimental results show a strong size effect, where smaller particles correspond to higher apparent strength. The results are in relatively good agreement with the predictions of the CC-FFM.

Résumé. Les composites renforcés par particules sont largement utilisés dans l'industrie, principalement en raison de la diversité de leurs méthodes de fabrication et de la possibilité d'adapter leurs propriétés. Dans de nombreux cas, des campagnes expérimentales approfondies sont nécessaires pour optimiser les caractéristiques du système et améliorer certaines propriétés spécifiques. Les modèles micromécaniques constituent une alternative utile ou une première approche lors du processus de conception des matériaux. L'une des caractéristiques les plus faciles à modifier est la taille du renfort, qui, selon certains modèles et preuves préliminaires, peut influencer significativement les propriétés mécaniques du matériau.

* Corresponding author

L'objectif de cette étude est d'évaluer expérimentalement l'effet de la taille du renfort sur la résistance du composite et de le comparer aux prédictions du critère couplé de la mécanique de la rupture finie (CC-MRF). Un objectif secondaire est d'observer le mécanisme d'amorçage de la rupture, qui débute à l'interface particule-matrice et évolue vers une fissure scindant l'éprouvette. Pour cela, un nouveau design d'éprouvette est proposé, ainsi qu'un procédé de fabrication optimisé. Les essais ont été enregistrés à l'aide d'une caméra à haute vitesse, permettant de visualiser l'initiation de la fissure à l'interface particule-matrice.

Les résultats expérimentaux mettent en évidence un fort effet de taille, où des inclusions plus petites entraînent une résistance apparente plus élevée. Ces résultats sont en accord relativement bon avec les prédictions du CC-MRF.

Keywords. Size effect, Particle-reinforced composites, Spherical inhomogeneity, Coupled criterion, Finite fracture mechanics, Experimental fracture mechanics.

Mots-clés. Effet de taille, Composites renforcés par particules, Inhomogénéité sphérique, Critère couplé, Mécanique de la rupture finie, Mécanique expérimentale de la rupture.

Funding. Ministerio de Ciencia e Innovación de España (Projects PID2020-117001GB-I00/AEI/10.13039/501100011033, PID2021-123325OB-I00), European Regional Development Fund (Project UNSE15-CE-3581).

Manuscript received 31 October 2024, revised 9 March 2025, accepted 10 March 2025.

1. Introduction

Particle-reinforced composites are becoming more and more prevalent in industrial applications [1]. This type of composite materials is particularly adequate for tailoring certain properties of the unreinforced matrix without increasing significantly the complexity of the fabrication process. The addition of particles to certain materials is able to enhance some properties, such as electrical or thermal conductivity [2], stiffness [3], tensile strength [4], or fracture toughness [5,6].

The mechanical properties of this type of material can be effectively enhanced by carefully selecting the particles to be added. The modification of these properties depends not only on the type and volumetric fraction of the added materials but also on the particle shape and size. This relationship has been shown in various experiments, see [7] for a review. Given the influence of micromechanics on macroscopic behavior, it is essential to fully understand the failure mechanisms at the microscale, as highlighted in [8] in a similar material system. This understanding is crucial for predicting and tailoring mechanical performance, ultimately ensuring reliability in both macroscopic and mesoscopic models, which are based primarily on phenomenological observations [9,10].

The first stage of the failure mechanism in particle-reinforced composites is typically associated with the particle-matrix interface. There are two main reasons for this: (a) the stress concentration generated by the presence of a particle, either at the poles for particles stiffer than the matrix, see e.g. [11], or at the equator for softer particles, and (b) the usually lower strength and fracture toughness properties of the interface. For stiffer particles, which is the typical case when enhancing mechanical properties is the main objective of the added particles, the failure initiates as small debonds at the particle-matrix interface [11]. Typically, in the most simple case of uniaxial tension, the debond appears initially at the interface poles, progressing along the interface and finally kinking towards the matrix [12]. The first stage of the failure mechanism is similar to the related problem of debonding at the fiber-matrix interface, see, e.g., [13,14].

In this initiation stage, two micromechanical characteristics strongly influence the initiation and progression of failure mechanisms: (i) the strength and fracture toughness of the interface and (ii) the size and shape of the particle, see a review in [15].

The influence of the interface properties has been reported both theoretically [16] and experimentally [12]. Similar results have been reported in [13] for a similar system with fibrous reinforcement. The authors carried out experiments on dog-bone specimens with a single fiber

embedded. The 3D digital image correlation technique allowed them to characterize the whole sequence of the failure mechanism in this very related problem.

The influence of the shape and size of the particles has been reported by some limited experiments [11]. The size effect has been explained by using diverse models: In [17], the authors compared different models predicting the size effect and found an accurate correlation with experiments with a stress model combined with the effect of nanoscale damage at the interface. In [16], a model was presented based on prescribing a cohesive law at the interface and a coupled plasticity-damage model for the matrix in a Representative Volume Element (RVE). The prediction of this model match the experimental results in terms of the stress–strain curve. However, the size effect was not studied, but was expected to be inherent in the approaches used. In the same line, in [18] a computational approach was presented based on micromechanical simulations prescribing a non-local plasticity model in the matrix and a non-local ductile damage model based on the well-known Gurson-Tvergaard-Needleman model, within a Fast-Fourier-Transform approach. The results show a strong size effect, even for systems with relatively high volumetric fractions.

Among the diverse approaches used to predict this size effect, it is worth highlighting the coupled criterion of finite fracture mechanics (CC-FFM). This is an interesting approach not only to predict, but also to provide a physical explanation for the size effect. This criterion, proposed in [19,20], postulates that debonding will initiate with a finite extension when both stress and energy conditions are met simultaneously, see [21] for a recent review on this criterion. Size effect has been predicted by this approach for very diverse problems, see e.g. [22–28], and even used to explain the size effect found by other approaches [29,30]. In this sense, the present authors [31] proposed a model based on the CC-FFM to predict the crack initiation at the particle-matrix interface. The model presents, among other results, a strong size effect, predicting a delay in crack initiation for smaller particles under monotonous loading. A more general model was presented in [32], including residual thermal stresses and different volumetric fractions with multi-particle models. In [33], a comparison of the predictions of the CC-FFM with a computational model using a cohesive zone model at the particle-matrix interface was presented. The results show a good agreement between the two on a qualitative level, but a quantitative divergence in the asymptotic tendency for small particles, in line with the results in [29] for the problem of fiber-matrix debonding.

Despite the fact that different models predict the size effect on this type of material, the experimental results validating this size effect are limited. It is worth highlighting the experiments in [11], which demonstrate a strong size effect that aligns, at least qualitatively, with the predictions of most previous models, particularly those based on the CC-FFM. However, these experimental results are limited because of the use of multi-particle specimens with no control over the inter-particle distance, and thus the influence of nearby particles. Lauke [34] presented a specimen specifically designed to study the effect of multiaxial loading in the failure mechanisms around the spherical particle. However, to the best of our knowledge, there are no experimental results in the literature using this proposal yet. In view of these facts, it is necessary to obtain new experimental evidence to validate the main results predicted by these models.

The objective of the present work is to design a single-particle specimen to be tested under tension. The key idea is to validate the predictions on the size effect, keeping the specimen as simple as possible to avoid any influence of other parameters, such as volume fraction, interface finish, or multiaxial loading. These effects could be the objective of further work once the model is validated for the simplest case. The secondary objective is to observe the sequence of the failure mechanism, the symmetry of debonding, and the manner in which the crack migrates towards the matrix. This observation will contribute to validating the failure sequence assumed by the theoretical models.

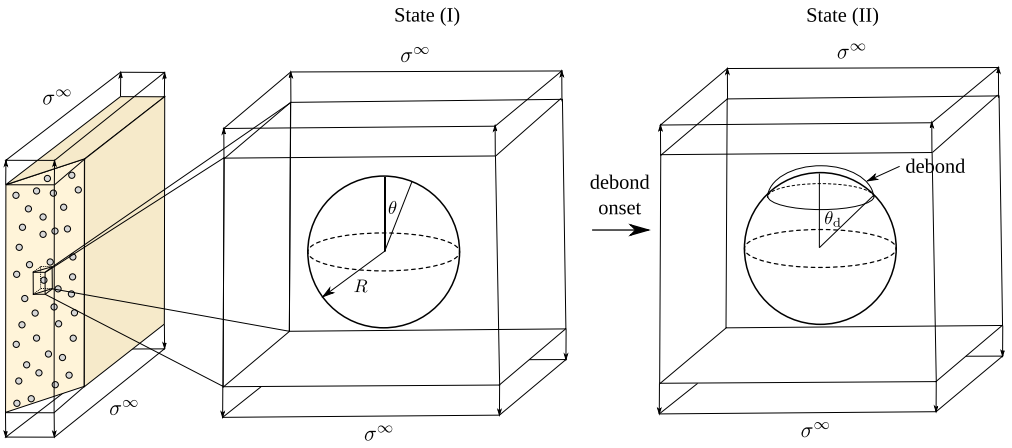

Figure 1. Schematic of the problem under study.

The document is organized as follows: First, the CC-FFM model for this problem will be briefly introduced in Section 2. The experimental setup will be described in terms of specimen design and fabrication in Section 3. Finally, the experimental results are presented and discussed in Section 4, where they are compared with the predictions given by the CC-FFM model.

2. Coupled criterion analysis

The problem under study is schematized in Figure 1, where a particle-reinforced material is subjected to uniaxial tension. Assuming a low volumetric fraction, a spherical particle of radius R surrounded by an infinite matrix can be studied as a representative volume element, neglecting the effect of nearby particles. The particle material is considered to be stiffer than the matrix. This simplified axisymmetric model allows focusing the analysis on the sequence of events of the failure mechanism and the size effect. In addition, this simplicity and the CC-FFM allow us to obtain quasi-analytical expressions for the stresses leading to the formation of the first debond. Note that the schematic assumes that the debond will appear in only one of the poles, in a non-symmetric manner. This result is predicted by the CC-FFM, as proved in [31] and discussed in detail for a related problem in [35]. Thus, this result is also to be validated by the experiments presented here.

The CC-FFM is based on assuming that a finite-length crack onset takes place when two conditions are met simultaneously: a stress condition defined on the stresses before the crack onset and an energy condition based on an energetic balance between the states before and after the crack onset. In this case, the states before and after the debond are represented in Figure 1. In what follows, the two criteria will be briefly studied in Sections 2.1 and 2.2 to be subsequently combined in Section 2.3, where the expression that will be compared with the experiments is fully developed.

2.1. *Stress criterion*

The stress criterion is based on the evaluation of the stresses before the debond onset, i.e. the state (I) in Figure 1. According to the CC-FFM, a debond onset is possible only at those points with angle $\theta \in [0°, 180°]$ of the interface where a certain combination of the interface normal and shear tractions, $\sigma(\theta)$ and $\tau(\theta)$, respectively, is greater or equal to a critical value. Since the poles are the

most stressed points at the interface, it is assumed that the debond onset will always occupy the pole ($\theta = 0°$) and surrounding points up to a certain angle $\Delta\theta$. In this case, the condition given by the stress criterion for a debond onset will be:

$$\sigma_{\text{eq}}(\sigma,\tau) = \sqrt[p]{\left\langle \operatorname{sgn}(\sigma)\,|\sigma|^p + \left(\frac{|\tau|}{\mu}\right)^p \right\rangle_+} \geq \sigma_{\text{c}} \quad \forall\theta \in [0,\Delta\theta], \tag{1}$$

where σ_{c} is the interface tensile strength, and $\mu = \tau_{\text{c}}/\sigma_{\text{c}}$ is the ratio of interface shear to interface tensile strength. The exponent $p \geq 1$ controls the coupling between normal and shear tractions, see [36] for more details about this expression for the stress criterion.

Assuming linear elastic behavior for the spherical particle and matrix material and assuming a perfect interface before the debond onset, the normal σ and shear τ tractions can be obtained exactly using the expressions by [37] as,

$$\sigma(\theta) = \sigma^{\infty}\hat{\sigma}(\theta) = \sigma^{\infty}(k + m\cos 2\theta), \quad \tau(\theta) = \sigma^{\infty}\hat{\tau}(\theta) = \sigma^{\infty} m \sin 2\theta \tag{2}$$

where σ^{∞} is the remote tension and k and m depend on the elastic properties of particle and matrix in the following form:

$$k = \frac{1}{2}\frac{1+\alpha}{1+\beta}\frac{2+\alpha-\beta}{1+\alpha-2\beta}, \tag{3a}$$

$$m = \frac{1+\alpha}{1+\beta}, \tag{3b}$$

$$\alpha = \frac{\mu_1(\kappa_2+1) - \mu_2(\kappa_1+1)}{\mu_1(\kappa_2+1) + \mu_2(\kappa_1+1)}, \tag{4a}$$

$$\beta = \frac{\mu_1(\kappa_2-1) - \mu_2(\kappa_1-1)}{\mu_1(\kappa_2+1) + \mu_2(\kappa_1+1)}, \tag{4b}$$

where $\mu_i = E_i/(2(1+\nu_i))$ and $\kappa_i = 3-4\nu_i$, E_i and ν_i denoting Young's modulus and Poisson's ratio, respectively, of particle ($i=1$) and matrix ($i=2$), and α and β are Dundurs parameters of the bimaterial.

Introducing (2) in (1) and after some rearrangements, the expression obtained for the stress criterion is:

$$\frac{\sigma^{\infty}}{\sigma_{\text{c}}} \geq s(\Delta\theta) = \max_{\theta\in[0,\Delta\theta]} \frac{1}{\sqrt[p]{\left\langle \operatorname{sgn}(k+m\cos 2\theta)\,|k+m\cos 2\theta|^p + \left(\frac{|m\sin 2\theta|}{\mu}\right)^p \right\rangle_+}}. \tag{5}$$

The dimensionless function $s(\Delta\theta)$ gives the minimum value required for the remote tension as a function of the size of the debond at its onset.

The expression presented here is the most simple, assuming linearity in the material behavior and conditions, in order to keep the comparison as simple as possible to be able to understand the basic behavior. The extension of the stress criterion to take into account viscous, nonlinear material effects and even higher volumetric fractions could be obtained by using the expressions in [38].

2.2. *Energy criterion*

The energy criterion, within the context of the finite fracture mechanics, postulates that the debond onset is possible if the energetic balance between the states before (I) and after the debond onset (II) is thermodynamically admissible. This is an extension of the classical Griffth criterion [39] to an incremental balance between two states, rather than a differential approach. In this sense, the incremental balance can be written as:

$$\Delta\Pi + \Delta E_{\text{k}} + E_{\text{d}} = 0, \tag{6}$$

where $\Delta\Pi$ and ΔE_{k} are the increments of potential elastic and kinetic energy, respectively. The term E_{d} refers to the energy dissipated during the crack initiation process. If the initial state is assumed to be static, $\Delta E_{\mathrm{k}} \geq 0$, the expression in (6) can be rewritten as:

$$-\Delta\Pi \geq E_{\mathrm{d}}, \tag{7}$$

so the application of the energy criterion reduces to evaluate the change in potential elastic energy and the dissipated energy.

The change in potential elastic energy $\Delta\Pi$ can be obtained in different manners, see Section 3.4.1 in [40] for a review. In this case, in line with [31], this term will be obtained by integrating the energy release rate (ERR) G for a crack slowly growing from a debond angle $\theta_{\mathrm{d}} = 0$ to an angle $\theta_{\mathrm{d}} = \Delta\theta$ from the pole

$$-\Delta\Pi = \int_{\theta_{\mathrm{d}}=0}^{\theta_{\mathrm{d}}=\Delta\theta} G(\theta_{\mathrm{d}}) 2\pi R^2 \sin(\theta_{\mathrm{d}}) \mathrm{d}\theta_{\mathrm{d}}, \tag{8}$$

where $G(\theta_{\mathrm{d}})$ can be extracted from simple and linear elastic computational analyses, with a set of models with debonds with angle θ_{d}, see [31] for details and computation.

Assuming linearity of the models with the remote tension σ^{∞}, and after a dimensional analysis of the problem, the dependence of the ERR $G(\theta_{\mathrm{d}})$ can be expressed as follows defining a dimensionless ERR $\hat{G}$,

$$\hat{G}\left(\theta_{\mathrm{d}}; k, m, \frac{\mu_1}{\mu_2}\right) = \frac{E^*}{(\sigma^{\infty})^2 R} G\left(\theta_{\mathrm{d}}; E_1, E_2, \nu_1, \nu_2, \sigma^{\infty}, R\right), \tag{9}$$

where R is the particle radius and,

$$E^* = \frac{2}{\frac{1-\nu_1^2}{E_1} + \frac{1-\nu_2^2}{E_2}} \tag{10}$$

is the harmonic mean of the plane-strain elastic moduli. The terms k and m in (9) refer to the two independent bimaterial elastic properties defined in (3) and μ_1/μ_2 is the ratio of particle to matrix shear moduli.

The dimensionless expression of $G(\theta_{\mathrm{d}})$ in (9) allows to reduce the number of computational analyses and show explicitly the dependence on the particle radius R, making the resulting size effect explicit. Thus, introducing (9) in (8), $\Delta\Pi$ can be obtained for any radius R and remote tension σ^{∞} directly from a set of computations for different values of the debond angle θ_{d},

$$-\Delta\Pi = \frac{(\sigma^{\infty})^2 R^3}{E^*} \int_{\theta_{\mathrm{d}}=0}^{\theta_{\mathrm{d}}=\Delta\theta} \hat{G}(\theta_{\mathrm{d}}; k, m) \mathrm{d}\theta_{\mathrm{d}}. \tag{11}$$

Concerning the dissipated energy, it can be calculated following the same strategy: integrating the fracture energy along all the path of the new crack,

$$E_{\mathrm{d}} = \int_{\theta=0}^{\theta=\Delta\theta} G_{\mathrm{c}}(\theta) 2\pi R^2 \sin(\theta) \mathrm{d}\theta, \tag{12}$$

where $G_{\mathrm{c}}(\theta)$ is the interface fracture energy, that could depend on the point of the interface θ. Assuming a uniform interface, the main variation in $G_{\mathrm{c}}(\theta)$ could come from the variation of the fracture mode-mixity along the interface and the effect of this variation on $G_{\mathrm{c}}(\theta)$. In the context of the finite fracture mechanics, this effect has been taken into account in various ways, see [36,41] for a discussion. The expression can be normalized with the value of the interface fracture energy in pure mode 1, $G_{1\mathrm{c}}$, and the particle radius R,

$$E_{\mathrm{d}} = G_{1\mathrm{c}} 2\pi R^2 \int_{\theta=0}^{\theta=\Delta\theta} \hat{G}_{\mathrm{c}}(\theta) \sin\theta \mathrm{d}\theta. \tag{13}$$

In the present case, the dimensionless value of $\hat{G}_c(\theta)$ is calculated using the Hutchinson and Suo phenomenological law [42], which has been shown in [31] to capture very accurately the fracture energy in a similar system,

$$\hat{G}_c(\phi) = 1 + \tan^2[(1-\lambda)\phi], \tag{14}$$

where λ is a dimensionless parameter modulating the influence of the fracture mode-mixity on the fracture toughness. The term ϕ is a measure of this mixity, which has been evaluated following different alternatives in the literature, see [36], Section 4.2, for a discussion. In the present case, for the reasons given in [36], the value of ϕ is based on the stress state before the crack onset as follows:

$$\phi(\theta) = \tan^{-1}\left(\frac{\tau(\theta)}{\sigma(\theta)}\right), \tag{15}$$

where $\sigma(\theta)$ and $\tau(\theta)$ are calculated using (2).

Introducing the expressions for the change in potential elastic energy (11) and dissipated energy (13) in the energy balance in (7), the following expression can be obtained:

$$\frac{(\sigma^\infty)^2 R}{E^*}\int_{\theta_d=0}^{\theta_d=\Delta\theta} \hat{G}(\theta_d;k,m)\sin(\theta_d)\mathrm{d}\theta_d \geq G_{1c}\int_{\theta=0}^{\theta=\Delta\theta}\hat{G}_c(\theta)\sin(\theta)\mathrm{d}\theta. \tag{16}$$

To express this condition in a form similar to the stress criterion in (5), it is rearranged so that it is explicitly expressed in terms of the remote tension σ^∞ divided by the interface tensile strength σ_c,

$$\frac{\sigma^\infty}{\sigma_c} \geq \gamma\sqrt{g(\Delta\theta)} = \underbrace{\frac{1}{\sigma_c}\sqrt{\frac{G_c E^*}{R}}}_{\gamma}\underbrace{\sqrt{\frac{\int_{\theta=0}^{\theta=\Delta\theta}\hat{G}_c(\theta)\sin(\theta)\mathrm{d}\theta}{\int_{\theta_d=0}^{\theta_d=\Delta\theta}\hat{G}(\theta_d;k,m)\sin(\theta_d)\mathrm{d}\theta_d}}}_{\sqrt{g(\Delta\theta)}}, \tag{17}$$

where γ is a brittleness number proposed in [22] and $g(\Delta\theta)$ is a dimensionless function, analogous to $s(\Delta\theta)$ defined for the stress criterion. Similarly, but modulated with γ, this function represents the value of the remote tension σ^∞ required for a certain debond onset with angle $\Delta\theta$ to be admissible from the energetic point of view.

2.3. *Combining the stress and energy criteria*

Once the stress and energy criteria have been developed separately, Leguillon's postulate [19] establishes that the debond onset will occur when the conditions for the two criteria are met simultaneously. Assuming that the remote tension is increased quasistatically from zero to the value leading to the debond onset, the value of the remote tension $\sigma^\infty_{\text{onset}}$ for which it occurs is the minimum value meeting both criteria, thus given by the next optimization problem

$$\frac{\sigma^\infty_{\text{onset}}}{\sigma_c} = \min_{\Delta\theta}\left(\max\left\{s(\Delta\theta), \gamma\sqrt{g(\Delta\theta)}\right\}\right), \tag{18}$$

where it can be observed that the debond angle at onset $\Delta\theta$ is the optimization variable and is obtained as a result of the optimization process. The manner in which this problem is solved is widely discussed in [31].

Note that γ depends explicitly on the particle radius with $\gamma \propto 1/\sqrt{R}$, so it is expected that, if the energy criterion plays a role in the optimization problem in (18), a size effect will be predicted.

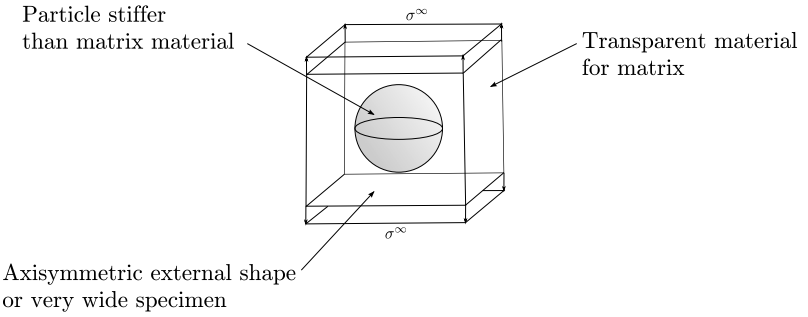

Figure 2. Requirements for the design of the specimen used to evaluate the size effect of the particle on the initiation of the failure mechanism and the observation of this initiation.

3. Specimen design and fabrication

This section is devoted to describe and justify the design and fabrication of the non-standard specimens proposed and used in the experiments. The design is based on two objectives, as enumerated in the introductory section: (i) to evaluate the effect of the size of the particle on the first stages of the failure mechanism and (ii) to directly observe and characterize the failure sequence in the first stage of the failure mechanism. These two objectives will constrain the design.

In view of the objectives, some requirements are prescribed for the design of the specimen, see Figure 2,

- The material of the matrix is required to be transparent, to allow optical observation of the first stages of the failure mechanism, that are expected to occur at the particle-matrix interface.
- The specimen should contain only a single particle due to several reasons: first, the presence of several particles does not allow to fix the observation in detail in the failure, because it would be difficult to know, a priori, which is the particle around which the failure will start. The second reason is that in typical particle-reinforced composites, nearby particle can affect strongly the initiation of the failure mechanism, see e.g. [18,43]. This fact would generate scatter in the experimental results, because it would add the non-controlled influence of the nearby particles. Thus, the strategy is to approach the real problem for nearby particles as a perturbation of the failure mechanism for an isolated particle.
- The particles should be spherical and with a very high quality in terms of dimensional and geometrical tolerances. Variations from the perfect sphere would generate scatter in the result, given the strong influence of the shape on the failure initiation [44]. The particles should be available in different sizes with a high quality in their calibration.
- All the specimen dimensions should keep fixed ratios between them to reduce the influence of geometrical parameters to one: the particle size.

Based on the above requirements, the following decisions were made in the selection of materials and elements and in the design:

The spherical particles used for the fabrication of the specimens were stainless steel bearing balls. They have the advantage of having a very high quality in terms of geometrical and dimensional tolerances. In addition, the surface finishing is very accurate, presenting an extremely low roughness, necessary for the regular purpose of these elements. Finally, they are available in a wide range of well-calibrated sizes.

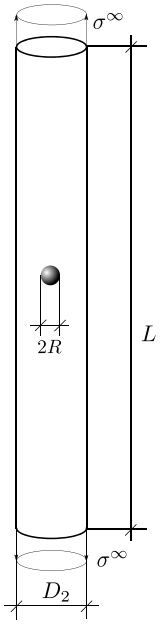

Figure 3. Schematic of the specimen design.

The matrix should be significantly softer than the particle material. A low-viscosity room-temperature curing epoxy resin is selected: Resoltech WWA/WWB4. The low-viscosity property is key in ensuring that the space around the sphere is perfectly filled, avoiding trapped air and bubbles. The room-temperature curing will allow to control carefully the location of the spherical particle, which will require, as shown below, a set of auxiliary elements.

The specimen will be subjected to uniaxial tension, thus, the typical bar-type specimen is selected. In particular, a cylindrical shape is chosen here to keep the axisymmetry inherent to the spherical particle. Dog-bone or other kind of geometries to increase the extreme sections are typically included in this type of specimens to promote failure in the central section of the specimen, where the stresses are better known. However, in this case, the presence of a stiff particle in the central part of the specimen already introduces a stress concentration. Thus, the specimen will be totally cylindrical, as can be seen in Figure 3.

In what follows, the optimized fabrication procedure for the specimen is outlined, remarking the decisions taken to guarantee that the failure behavior of the specimens would be representative of what was wanted to be observed:

(1) External molds were prepared with different internal diameters, corresponding to the external diameters required for the specimens. The molds were fabricated from tubes of Polyvinyl chloride (PVC), typically used in plumbing. After being cut and machined at the required length, the extremes were closed with PVC pipe plugs and some adhesive, see Figure 5a. Finally, three holes per specimen were machined, one in the center to introduce the spherical particle, as will explained later, and two near the extremes to allow the air to escape during the resin filling, see Figure 5b. After trying several strategies, this approach proved to be the optimal one. The finished mold can be observed in Figure 5c.

(2) The steel spheres were washed with alcohol before being placed for the fabrication. The objective was to achieve a complete and homogeneous adhesion along the interface but

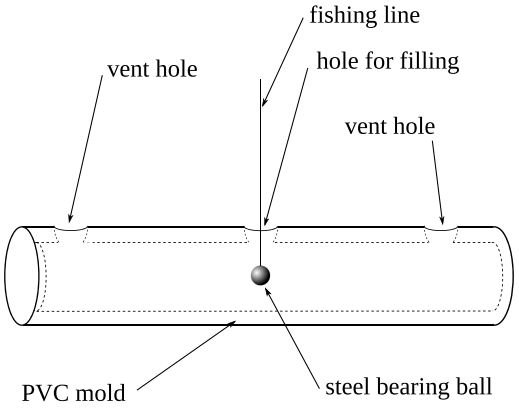

Figure 4. Details of the mould proposed for the fabrication.

limiting the adhesion strength, since a high strength could avoid failure initiation at the interface. Tabiai et al. [13] showed the strong influence of the interfacial bonding on the qualitative and quantitative progress of the failure mechanism in the problem of fiber-matrix, which presents many similarities with the present problem. Similar results were found in [12], where the effect of different surface treatments on this problem was studied. They found that, in the absence of adhesion, the failure mechanism is an equatorial crack, so this is an aspect that will be checked in the post-mortem analysis.

(3) Several strategies were tested to place the spherical particle in the middle of the specimen during the curing of the epoxy. The optimum solution was to adhere a thin fishing line to the ball in one extreme and to a small bar in the other extreme, that helped to situate the spherical particle in the required position during the curing, see Figure 5d. The fishing line could be considered an imperfection, but it is situated in the equator of the sphere, far from the pole where it is expected the debond to appear. Since the failure mechanism will be recorded, it will be possible to evaluate if debond starts at the pole without any influence of the fishing line.

(4) The bi-component epoxy, Resoltech WWA, is mixed with Resoltech WWB4 in a weight ratio of 100:40. After mixing for 10 min with a slow stir to avoid bubbles, the epoxy resin is ready for filling and can begin the curing process. The spherical particle should be positioned inside the mold using its central hole prior to this, see Figure 4.

(5) All the molds filled with the epoxy resin and the spherical particle adequately placed were introduced in a climate chamber with the temperature controlled at 35 °C during 20 h, see Figure 5e. Subsequently, a post-cured stage was carried out at 60° for 4 h. Once both stages were completed, the temperature was slowly decreased to room temperature and the molds were extracted from the climate chamber and left to consolidate during 1 week.

(6) The mold was removed by machining the specimen with a lathe and removing the pipe plugs by cutting the specimen, see Figure 5f. The specimens were machined up to arrive to the calibrated external diameter planned. Finally, the region near the spherical particle was finely polished to enhance the transparency, in order to observe the failure mechanism during the test.

(7) All the specimens were carefully inspected. A total of 4 types of specimens were fabricated with spherical particles of radius 1.5, 2.0, 3.0 and 4.0 mm. Absence of air bubbles, correct positioning of the spherical particle, correct filling and dimensional toler-

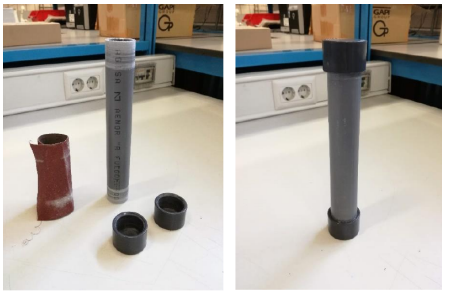

(a) Base elements for moulds fabrication.

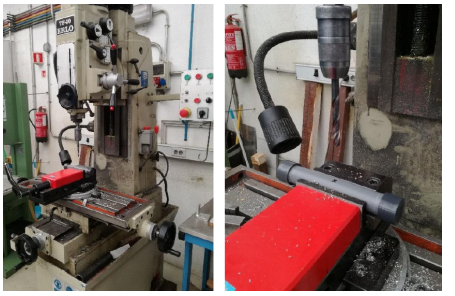

(b) Moulds machining.

(c) Finished moulds.

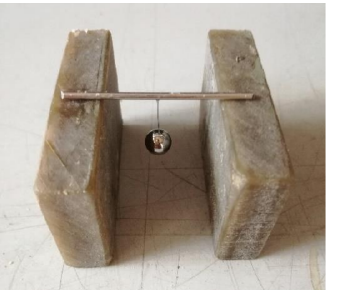

(d) System for the correct positioning of the spherical particle.

(e) Curing of the specimens.

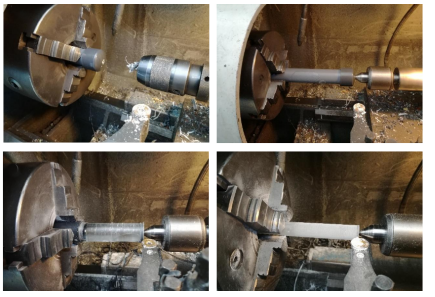

(f) Machining for moulds removal.

Figure 5. Details of the fabrication procedure.

ance were evaluated. The details of the measures are shown in Table 2 along with the test results. In parallel, a set of cylindrical specimens without particle were fabricated using exactly the same procedure with external radius of 8.25 mm, in order to evaluate the mechanical properties of the epoxy resin employed. One specimen for each set is shown in Figure 6.

4. Experimental results

The specimens were tested on tensile testing machines INSTRON 8802 (for particle radii 2, 3 and 4 mm) and INSTRON 4482 (for particle radii 1.5 mm and specimens without particle). The length between the grips was controlled and set to follow the same length-to-particle-radius ratio for all the specimens. The specimens were subjected to monotonic tensile testing at a low strain rate, which can be considered quasistatic loading. The strain rate is the same for all the sets of

Figure 6. Examples of fabricated specimens.

Table 1. Details of the experimental set-up

Particle radius (mm)	Free length (mm)	Deformation rate (mm/min)
4.0	80.0	1.000
3.0	60.0	0.750
2.0	40.0	0.500
1.5	30.0	0.375

Table 2. Details of the dimensions and results for all the specimens

Specimen	Part. radius (mm)	Sp. diameter (mm)	Stress at failure (MPa)	Deb. poles
P8-1	4.0	24.23	10.78	1
P8-2	4.0	24.26	13.95	1
P8-3	4.0	24.05	13.70	1
P8-5	4.0	24.29	14.64	1
P6-1	3.0	17.90	14.08	1
P6-3	3.0	18.02	16.02	1
P6-4	3.0	18.02	22.66	2
P4-1	2.0	11.89	17.71	1
P4-2	2.0	12.07	21.70	1
P4-3	2.0	11.89	21.36	1
P4-5	2.0	11.92	18.38	1
P3-2	1.5	9.32	22.20	1
P3-3	1.5	9.23	23.81	1

specimens, thanks to fixing the deformation rate-to-free-length ratio for all the sets, see Table 1 for details. In this manner, viscous effects, if any, are expected to affect similarly to all sets.

A high-speed visualization system was set and used to observe the first stages of the failure mechanism. The system is composed by a Photron camera able to record at 0.9 Mfps and a set of powerful light system. For this test, the camera was set to 216 kfps with a resolution of

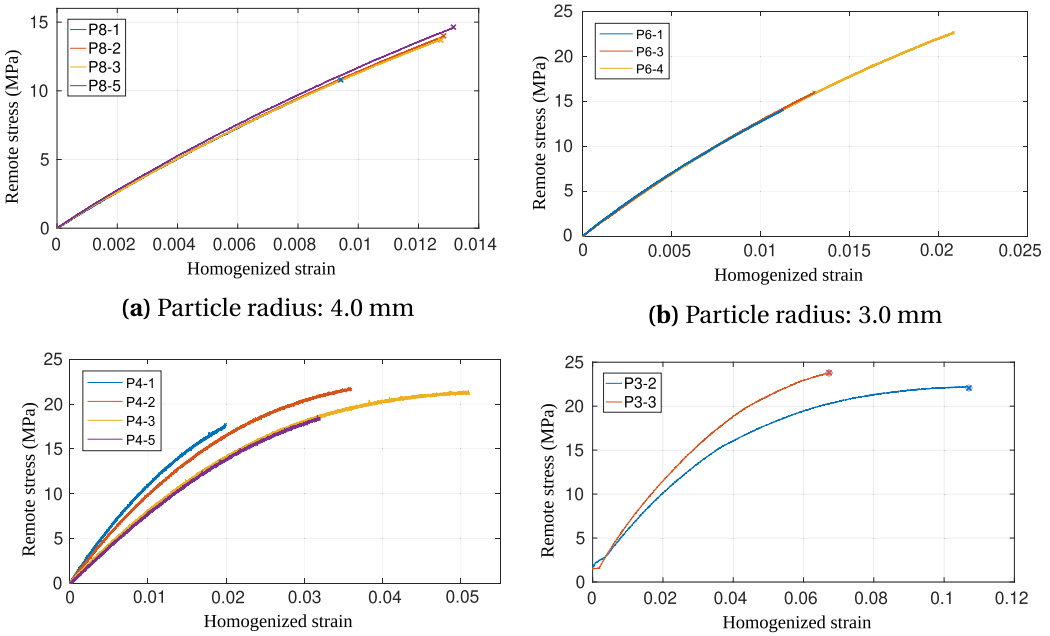

(a) Particle radius: 4.0 mm

(b) Particle radius: 3.0 mm

(c) Particle radius: 2.0 mm

(d) Particle radius: 1.5 mm

Figure 7. Stress–strain curves for all the specimens.

128 × 80 pixels. The failure in all the specimens was recorded in order to evaluate the hypothesis on the failure mechanism, but also to check if the fabrication procedure was correct and was not affecting the failure in the first stages.

Figure 7 shows the stress–strain curves for all the specimens with particles. The stress represented corresponds to the engineering stress, i.e. the force measured by the load cell divided over the initial cross section. The represented homogenized strain corresponds to the displacement of the moving clamp divided by the initial free length. The curves are grouped for sets. As it can be observed, the stiffness is more regular for sets with larger particles, which could be due to two reasons: (i) for larger specimens it is easier to reach accurate levels of fabrication standards and (ii) stress at failure is lower for larger particles, avoiding the activation of nonlinear phenomena at higher stress levels. This is in accordance with the observation of a more nonlinear behavior for the specimens with smaller particles. A possible reason of the behavior observed for the smallest diameters is the ductility observed by [45] when the triaxiality is decreased. The spherical particle could have this effect on the stress state for high level of strain. The effect of the triaxiality could be tested using the proposal by [46].

According to the stress–strain curves, for all the sets and specimens, the results show a total failure of the specimens after the first failure event. The stress level at this failure event, along with the real dimensions of the specimens and the post-mortem observation of the symmetry of the failure, are presented in Table 2. It is interesting to remark that the observed failure was non-symmetric in all the cases except for specimen P6-4.

Given that all the stages of the failure mechanism occur dynamically, it is necessary to observe the high-speed recording to visualize the different stages. Figure 8 shows the key frames to visualize the failure mechanism for the specimen P6-3. In the first frame (a) the interface is intact. A small debond is observed in the second frame, which progresses along the interface and migrates towards the matrix in frame (c). This already existing matrix crack progresses quickly

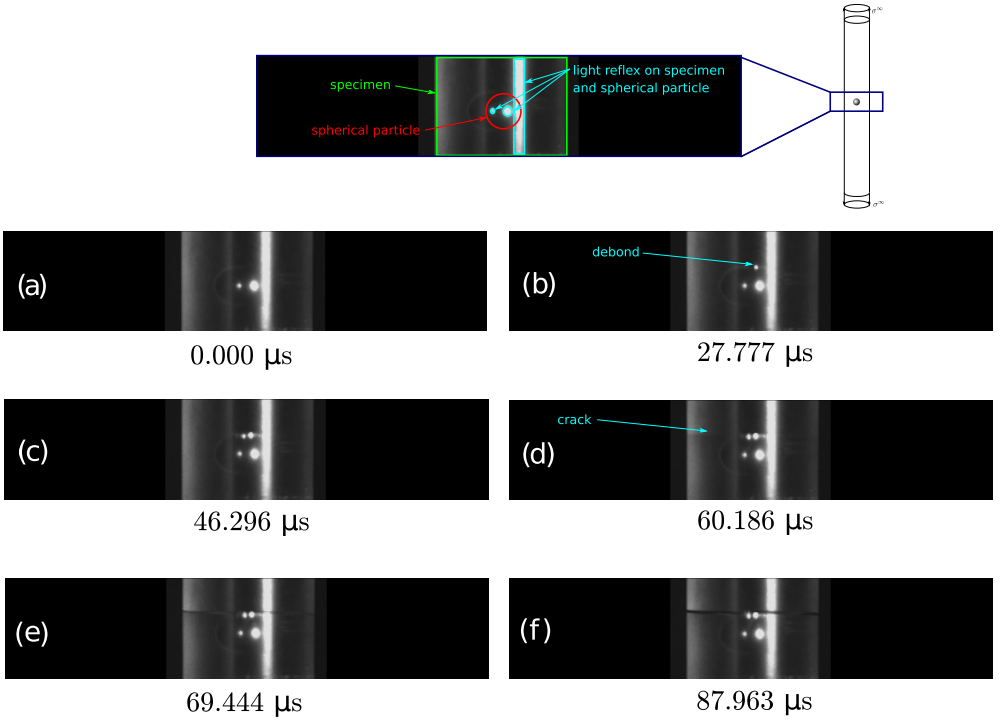

Figure 8. Failure sequence observed with the high-speed visualization system for specimen P6-3.

along the matrix to reach the free edge in frames (d), (e) and (f). The whole failure sequence occurs in 88 µs, which shows the highly dynamic character of this failure.

The sequence presented before is representative of all the specimens except for the specimen P6-4, which is the only one where a symmetric failure in the two poles was found in the post-mortem observation. To clarify what happened in this case, Figure 9 shows its failure sequence. As it can be observed, the first stages of the failure mechanisms are the same that for the other specimens, leading to a non-symmetric total failure of the specimen. However, the subsequent vibration of the two parts of the specimen generated a debond onset at the other pole, that slowly progressed along the interface to finally end in the total failure of the matrix dynamically again. This result confirms the theoretical prediction by the CC-FFM, according to which the non-symmetric debond in only one of the poles is the preferred solution. This was predicted in [31] for this problem and physically explained in detail in [35] for a related system.

Figure 10 shows the fracture surface for the specimen P6-3. First, it is interesting to observe the debond at the spherical particle, perfectly located around the pole. The migration toward the matrix is also visible and occurs at a distance from the pole that is very uniform. In addition, the migration seems to have taken place at different points of the interface simultaneously, as evidenced by the fact that the fracture surface at the matrix presents some steps. This is a consequence of crack migration towards the matrix at different points of the interface at the same time. These steps are a consequence of the slight difference in the debond angle at which the crack migrated. This shows an almost perfect axisymmetry in the problem, allowing to neglect any effect of the fishing line on the failure mechanism. Finally, the reduction of the step when the fracture surface approaches the external edge is an evidence of the direction of crack growth, from the spherical particle to the external boundary.

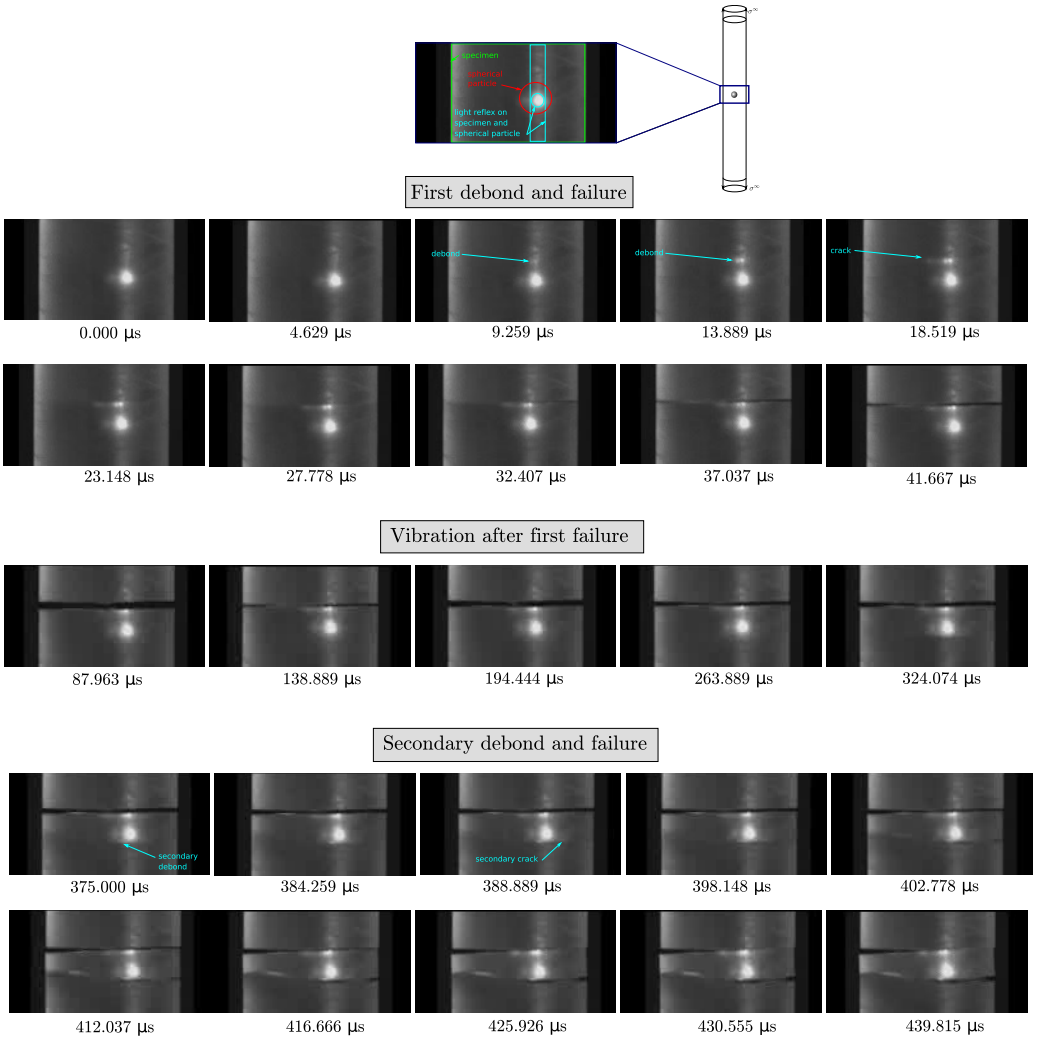

Figure 9. Failure sequence observed for the only specimen (P6-4) presenting a 2-debond fracture surface in the post-mortem analysis.

Figure 11 shows the results of the stress at failure for all the specimens as a function of the particle radius. As already predicted [44] and observed in some previous works in the literature [11], the apparent strength increases for smaller particle radii. This is qualitatively in agreement with the predictions given by the model presented in Section 2. The quantitative comparison requires the value of certain properties, some of which are represented in Table 3. The properties of AISI 52100 steel used for bearing balls are nominal values. For epoxy resin, elastic modulus and tensile strength are extracted from the experimental tests carried out on specimens without particles. Poisson's ratio is taken as value of reference and the fracture toughness is taken from experiments carried out in similar resins in the laboratory.

The values of the fracture toughness and strength of the interface are very difficult to obtain directly. This fact has motivated the proposal of indirect methods, see e.g. [12,47]. To ensure the representativeness of the results provided by these methods, it is key to mimic all the conditions involved in the interface behavior. These conditions, such as surface finish, surface treatment,

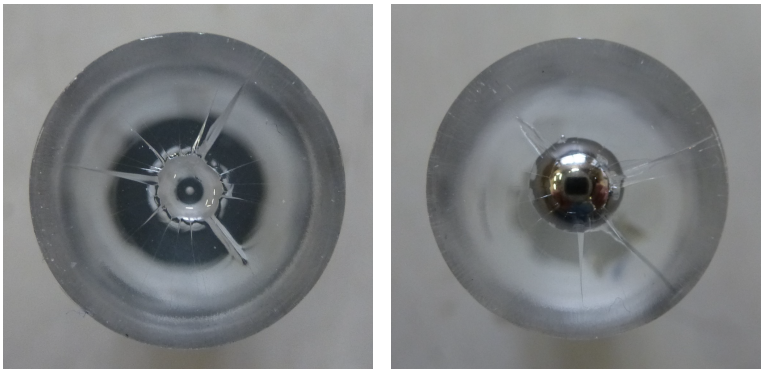

Figure 10. Post-mortem observation of the specimen P6-3, where the spherical particle can be observed on the right.

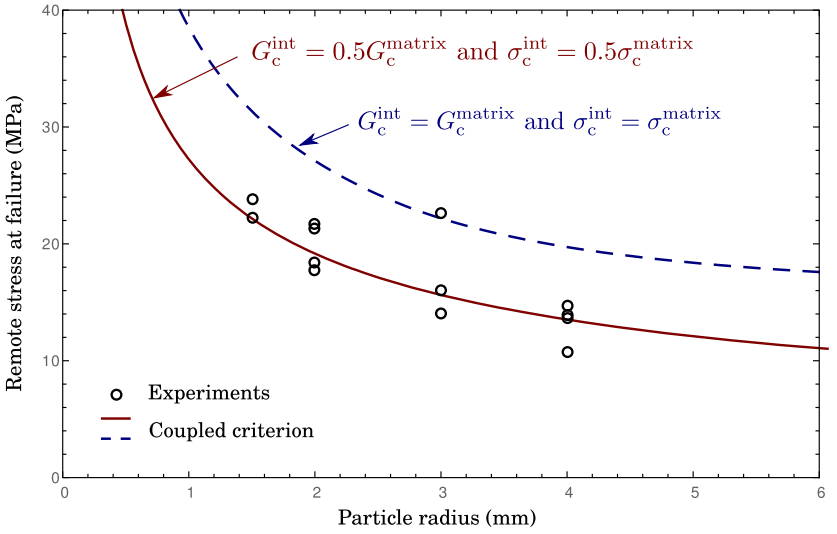

Figure 11. Stress at failure as a function of the particle radius. Comparison with the predictions of the CC-FFM.

Table 3. Material properties for particle and matrix

Material	AISI 52100 Steel	Resoltech WWA/WWB4 epoxy
Elastic modulus (GPa)	200	2.10
Poisson's ratio	0.3	0.3
Tensile strength (MPa)	-	27.7
Fracture toughness (N/mm)	-	0.478

temperature and pressure at curing in the local region of the interface, are difficult to mimic. That is the reason why, in many cases, it is preferential to employ indirect methods. In this case, the fact that failure starts at the interface is evidence that fracture toughness and strength are lower at the interface than in the bulk, as the most stressed point is not located at the interface, as was discussed by [48], among others. For comparison and following [31], the exponent of the stress criterion is set to $p = 2$, the shear-to-tensile interface strength $\tau_c/\sigma_c = 2$, and the sensitivity parameter to the fracture mode mixity $\lambda = 0.11$.

In view of this, the comparison presented here is made for an extreme case where the tensile strength and fracture toughness of the interface are the same as those of the epoxy resin, and for another case where the two properties are half of the corresponding values at the interface. As can be observed, the results of this second hypothesis agree well with the experiments, whereas the prediction when the epoxy and the interface are similar in terms of strength and fracture toughness overestimates the stress at failure, as expected.

The size effect found here has a physical interpretation from the point of view of the CC-FFM, in particular the energy criterion: When all dimensions are scaled for a given load level, the energy available to be released increases with the cube of the scale factor (because it is stored in a volume), whereas the dissipated energy scales quadratically with the scale factor (because it is associated with a surface). As a result, a large size requires a lower load level to meet the energy balance of the energy criterion.

The results found here for the size effect are in agreement with the results presented in the review in [15]. A qualitatively similar size effect was found in [33] when the interface failure is modeled using cohesive zone model for this region. However, they found that the asymptotic tendency for the smaller particles is different for CZM and CC-FFM predictions. Whereas CC-FFM predicts a critical stress proportional to $1/\sqrt{R}$, the CZM approach gives an asymptotic tendency proportional to $1/R$. These results were found also by other authors, such as [29,49]. In fact, a physical interpretation for this mismatch was proposed in [29]. Even for more complex models, such as the one proposed in [18], based on predicting ductile damage at the bulk, the asymptotic tendency for the size effect matches the results for CZM.

5. Concluding remarks

A new type of specimen has been proposed to evaluate the first stages of the failure mechanism in particle-reinforced composites. This specimen is relatively easy to fabricate and allows visualization of the failure mechanism and verification of the size effect predicted by diverse models in the literature. The experiments performed on these specimens confirmed a strong size effect on the failure mechanism.

The experimental results were compared with the predictions of the CC-FFM. The prediction of a non-symmetric initiation of the failure as a debond in only one of the poles was confirmed in all the specimens. The tendency of the size effect was correctly captured qualitatively with increasing apparent strength for smaller particle. However, the quantitative comparison requires a set of interface properties which are not available. They could be obtained in further experimental campaigns adapting the procedure proposed in [47]. The comparison with some estimated properties showed a good agreement. In addition, as highlighted in [50], the origins of the size effect are multiple. The CC-FFM is able to account for the size effect with an energetic origin, but not for those with a statistical origin. Further developments should include them.

Some authors [51] have highlighted the effect of the viscous phenomena in the mechanical behavior of the particle reinforced composites. In the experiments presented here, an attempt has been made to keep this effect from affecting the size-effect results, by setting the deformation rate directly proportional to the free length of the specimen in order to keep the strain rate as similar as possible for all the specimens. This allows comparison with the CC-FFM model, which does not include viscous effects at this time. However, viscous effects could be introduced in the context of the CC-FFM.

Polymeric matrices can also present a nonlinear mechanical behavior. That could be at the origin of the nonlinear results observed in Figure 7. The CC-FFM model could be extended also to take into account this nonlinear effect, in line with the developments in [52,53]. The inclusion of plasticity could also improve the predictions, see e.g. [18].

The model described here is based on the assumption of zero-thickness for the interface. However, the model could be extended to take into account a finite-thickness interface, even including anisotropy with the expressions from [54]. In this case, the zero-thickness assumption is very representative of the situation because no surface treatment was implemented during the fabrication.

Multiaxial effects can play an important role in the initiation of this failure mechanism in particle-reinforced composites. In this sense, the experiments presented here could be extended to include multiaxial loading. With this objective, a specimen shape has been proposed by [34,46] along a detailed stress-field calculation which could be used for an analysis based on the CC-FFM.

Declaration of interests

The authors do not work for, advise, own shares in, or receive funds from any organization that could benefit from this article, and have declared no affiliations other than their research organizations.

Dedication

The manuscript was written through contributions of all authors. All authors have given approval to the final version of the manuscript.

Acknowledgments

The advice of Antonio Cañas about the specimen fabrication is greatly appreciated. IGG and VM acknowledge the support of Ministerio de Ciencia e Innovación de España (Projects PID2020-117001GB-I00/AEI/10.13039/501100011033 and PID2021-123325OB-I00, respectively). IGG, JJ and VM acknowledge the support of the European Regional Development Fund (Project UNSE15-CE-3581).

References

[1] D. K. Rajak, D. D. Pagar, R. Kumar and C. I. Pruncu, "Recent progress of reinforcement materials: a comprehensive overview of composite materials", *J. Mater. Res. Technol.* **8** (2019), no. 6, pp. 6354–6374.

[2] Y. Murakami, Y. Ichiba, T. Kawashima and N. Hozumi, "Filler particle size effect on electrically and thermally properties of thermal conductive thermoplastic polyimide/hexagonal boron nitride composite materials fabricated by the electrostatic adsorption method", *IEEJ Trans. Electr. Electron. Eng.* **19** (2024), no. 10, pp. 1590–1595.

[3] X. Zhang, X. Li, F. Chi, et al., "Synergistic enhancement of modulus and ductility in Mg matrix composites: A new strategy for GNPsMgOnp and SiCp hybrid reinforcement", *Compos. Part A: Appl. Sci. Manuf.* **187** (2024), article no. 110110.

[4] S. Sathees Kumar, S. Seenivasan, I. Isaac Premkumar, S. Vijayakumar, P. Anusha and A. Pradeep, "Analysis of wear mechanisms in AA2024/TiB2 composites under different loads", *Interactions* **245** (2024), no. 1, pp. 245–257.

[5] A. C. Garg and Y.-W. Mai, "Failure mechanisms in toughened epoxy resins-A review", *Compos. Sci. Technol.* **31** (1988), no. 3, pp. 179–223.

[6] N. Yoshinobu, M. Yamaguchi, M. Okubo and T. Matsumoto, "Effects of particle size on mechanical and impact properties of epoxy resin filled with spherical silica", *J. Appl. Polym. Sci.* **45** (1992), no. 7, pp. 1281–1289.

[7] H. M. Enginsoy, F. Gatamorta, E. Bayraktar, M. H. Robert and I. Miskioglu, "Experimental and numerical study of Al-Nb 2 Al composites via associated procedure of powder metallurgy and thixoforming", *Compos. Part B: Eng.* **162** (2019), pp. 397–410.

[8] F. París, *A Study of Failure Criteria of Fibrous Composite Materials*, Technical Report, National Aeronautics and Space Administration (NASA), 2001.

[9] A. Z. Khurshudyan, "Derivation of a mesoscopic model for nonlinear particle-reinforced composites from a fully microscopic model", *Acta Mech.* **230** (2019), no. 10, pp. 3543–3554.

[10] M. Majewski, P. Holobut, M. Kursa and K. Kowalczyk-Gajewska, "Packing and size effects in elastic-plastic particulate composites: Micromechanical modelling and numerical verification", *Int. J. Eng. Sci.* **151** (2020), article no. 103271.

[11] J. Cho, M. S. Joshi and C. T. Sun, "Effect of inclusion size on mechanical properties of polymeric composites with micro and nano particles", *Compos. Sci. Technol.* **66** (2006), no. 13, pp. 1941–1952.

[12] P. H. Harding and J. C. Berg, "The characterization of interfacial strength using single-particle composites", *J. Adhes. Sci. Technol.* **11** (1997), no. 8, pp. 1063–1076.

[13] I. Tabiai, R. Delorme, D. Therriault and M. Levesque, "In-situ full field measurements during inter-facial debonding in single fiber composite under transverse load", *Exp. Mech.* **58** (2018), no. 9, pp. 1451–1467.

[14] K. Uddin, H. Girard, N. Mennie, A. Doitrand and B. Koohbor, "Simultaneous measurement of fiber-matrix interface debonding and tunneling using a dual-vision experimental setup", *Exp. Mech.* **64** (2024), no. 9, pp. 1497–1511.

[15] S.-F. Fu, X.-Q. Feng, B. Lauke and Y.-W. Mai, "Effects of particle size, particle/matrix interface adhesion and particle loading on mechanical properties of particulate–polymer composites", *Compos. Part B: Eng.* **39** (2008), no. 6, pp. 933–961.

[16] J. Ye, C. Chu, Z. Zhai, Y. Wang, B. Shi and Y. Qiu, "The interphase influences on the particle-reinforced composites with periodic particle configuration", *Appl. Sci.* **7** (2017), no. 1, pp. 1–13.

[17] Y. Liu, J. Chen and X. Dong, "A particle debonding model considering interface nanoscale damage effect", *Model. Simul. Mat. Sci. Eng.* **29** (2021), no. 1, article no. 015007.

[18] M. Magri, L. Adam and J. Segurado, "Particle size effects in ductile composites: An FFT homogenization study", *J. Mech. Phys. Solids* **160** (2021), article no. 104759.

[19] D. Leguillon, "Strength or toughness? A criterion for crack onset at a notch", *Eur. J. Mech. Solids* **21** (2002), no. 1, pp. 61–72.

[20] P. Cornetti, N. Pugno, A. Carpinteri and D. Taylor, "Finite fracture mechanics: A coupled stress and energy failure criterion", *Eng. Fract. Mech.* **73** (2006), no. 14, pp. 2021–2033.

[21] A. Doitrand, T. Duminy, H. Girard and X. Chen, "A review of the coupled criterion", *J. Theor. Comput. Appl. Mech.* (2024), pp. 1–37.

[22] V. Mantič, "Interface crack onset at a circular cylindrical inclusion under a remote transverse tension. Application of a coupled stress and energy criterion", *Int. J. Solids Struct.* **46** (2009), no. 6, pp. 1287–1304.

[23] A. Sapora and P. Cornetti, "Crack onset and propagation stability from a circular hole under biaxial loading", *Int. J. Fract.* **214** (2018), no. 1, pp. 97–104.

[24] A. Doitrand, R. Henry, T. Lube and S. Meille, "Size effect assessment by Weibull's approach and the coupled criterion", *Eng. Fract. Mech.* **256** (2021), article no. 107979.

[25] A. Chao Correas, M. Corrado, A. Sapora and P. Cornetti, "Size-effect on the apparent tensile strength of brittle materials with spherical cavities", *Theor. Appl. Fract. Mech.* **116** (2021), article no. 103120.

[26] F. Ferrian, A. Chao Correas, P. Cornetti and A. Sapora, "Size effects on spheroidal voids by Finite Fracture Mechanics and application to corrosion pits", *Fatigue Fract. Eng. Mater. Struct.* **46** (2023), no. 3, pp. 875–885.

[27] M. Baldassari, A. Monaco, A. Sapora and P. Cornetti, "Size effect on flexural strength of notched and unnotched concrete and rock specimens by Finite Fracture Mechanics", *Theor. Appl. Fract. Mech.* **125** (2023), article no. 103787.

[28] M. T. Aranda, I. G. García, A. Quintanas-Corominas and J. Reinoso, "Crack impinging on a curved weak interface: Penetration or deflection?", *J. Mech. Phys. Solids* **178** (2023), article no. 105326.

[29] I. G. García, M. Paggi and V. Mantič, "Fiber-size effects on the onset of fiber-matrix debonding under transverse tension: A comparison between cohesive zone and finite fracture mechanics models", *Eng. Fract. Mech.* **115** (2014), pp. 96–110.

[30] G. Molnár, A. Doitrand, R. Estevez and A. Gravouil, "Toughness or strength? Regularization in phase-field fracture explained by the coupled criterion", *Theor. Appl. Fract. Mech.* **109** (2020), article no. 102736.

[31] I. G. García, V. Mantič and E. Graciani, "A model for the prediction of debond onset in spherical-particle-reinforced composites under tension: Application of a coupled stress and energy criterion", *Compos. Sci. Technol.* **106** (2015), pp. 60–67.

[32] E. Martin, D. Leguillon, A. Catapano and N. Carrère, "Prediction of interfacial debonding between stiff spherical particles and a soft matrix with the coupled criterion", *Theor. Appl. Fract. Mech.* **109** (2020), article no. 102749.

[33] T. Gentieu, J. Jumel, A. Catapano and J. Broughton, "Size effect in particle debonding: Comparisons between finite fracture mechanics and cohesive zone model", *J. Compos. Mater.* **53** (2019), no. 14, pp. 1941–1954.

[34] B. Lauke, "Stress field calculation around a particle in elastic-plastic polymer matrix under multiaxial loading as basis for the determination of adhesion strength", *Compos. Interfaces* **23** (2016), no. 1, pp. 1–14.

[35] I. G. García, V. Mantič and E. Graciani, "Debonding at the fibre-matrix interface under remote transverse tension. One debond or two symmetric debonds?", *Eur. J. Mech. A/Solids* **53** (2015), pp. 75–88.

[36] I. G. García and D. Leguillon, "Mixed-mode crack initiation at a V-notch in presence of an adhesive joint", *Int. J. Solids Struct.* **49** (2012), no. 15–16, pp. 2138–2149.

[37] J. N. Goodier, "Concentration of stress around spherical and cylindrical inclusions and flaws", *J. Appl. Mech.* **55** (1933), pp. 39–44.

[38] C. Kammer and P. P. Castañeda, "Variational estimates for the effective properties and field statistics of composites with variable particle interaction strengths", *J. Mech. Phys. Solids* **167** (2022), article no. 104996.

[39] A. A. Griffith, "The phenomena of rupture and flow in solids", *Phil. Trans. R. Soc. Lond. A.* **221** (1921), pp. 163–198.

[40] I. G. García, *Crack initiation in composites at micro and meso scales, Development and applications of finite fracture mechanics*, PhD thesis, School of Engineering, University of Seville, 2014.

[41] A. Talmon l'Armée, S. Hell, P. L. Rosendahl, J. Felger and W. Becker, "Nonlinear crack opening integral: Mode mixity for finite cracks", *Eng. Fract. Mech.* **186** (2017), pp. 283–299.

[42] J. W. Hutchinson and Z. Suo, "Mixed mode cracking in layered materials", *Adv. Appl. Mech.* **29** (1992), pp. 63–191.

[43] Q. Liu, F. gong Qi, H. min Ding, X. liang Fan and Y. Tue, "Distribution of stress and strain between adjacent particles in particulate reinforced metal matrix composites", *Trans. Nonferrous Met. Soc. China* **28** (2018), no. 11, pp. 2314–2323.

[44] T. Gentieu, J. Jumel, A. Catapano and J. Broughton, "Size effect in particle debonding: Comparisons between finite fracture mechanics and cohesive zone model", *J. Compos. Mater.* **53** (2018), no. 14, pp. 1941–1954.

[45] B. Fiedler, M. Hojo, S. Ochiai, K. Schulte and M. Ochi, "Finite-element modeling of initial matrix failure in CFRP under static transverse tensile load", *Compos. Sci. Technol.* **61** (2001), no. 14, pp. 95–105.

[46] B. Lauke, "Determination of adhesion strength between a coated particle and polymer matrix", *Compos. Sci. Technol.* **66** (2006), no. 16, pp. 3153–3160.

[47] H. Girard, A. Doitrand, B. Koohbor, R. Rinaldi, N. Godin, D. Long, J. Bikard and L. Trouillet-Fonti, "Numerical simulation of fiber–matrix debonding: Inverse identification of interface properties", *Eng. Fract. Mech.* **286** (2023), article no. 109254.

[48] F. Qi, H. Ding, X. Wang, Q. Liu, B. Du and X. Zhang, "The stress and strain field distribution around the reinforced particles in Al/TiC composites: A finite element modeling study", *Comput. Mater. Sci.* **137** (2017), pp. 297–305.

[49] A. Doitrand, R. Estevez and D. Leguillon, "Comparison between cohesive zone and coupled criterion modeling of crack initiation in rhombus hole specimens under quasi-static compression", *Theor. Appl. Fract. Mech.* **99** (2019), pp. 51–59.

[50] D. Leguillon, E. Martin and M.-C. Lafarie-Frenot, "Flexural vs. tensile strength in brittle materials", *C. R. Méc.* **343** (2015), no. 4, pp. 275–281.

[51] J.-K. Chen and M. Yuan, "Decoupling of viscous dissipation and damage dissipation in particulate-reinforced polymeric materials", *Comput. Mater. Sci.* **40** (2007), no. 2, pp. 267–274.

[52] P. L. Rosendahl, Y. Staudt, A. P. Schneider, J. Schneider and W. Becker, "Nonlinear elastic finite fracture mechanics: Modeling mixed-mode crack nucleation in structural glazing silicone sealants", *Mater. Des.* **182** (2019), article no. 108057.

[53] A. Leite, V. Mantič and F. París, "Crack onset in stretched open hole PMMA plates considering linear and non-linear elastic behaviours", *Theor. Appl. Fract. Mech.* **114** (2021), article no. 102931.

[54] D. C. Pham, T. K. Nguyen and B. V. Tran, "Macroscopic elastic moduli of spherically-symmetric-inclusion composites and the microscopic stress-strain fields", *Int. J. Solids Struct.* **169** (2019), pp. 141–165.

ACADÉMIE DES SCIENCES
INSTITUT DE FRANCE

Comptes Rendus. Mécanique
2025, Vol. 353, p. 901-922
https://doi.org/10.5802/crmeca.309

Research article / *Article de recherche*

Towards the determination of optimal 3D initiation crack shapes

Vers la détermination des formes optimales de fissures à l'amorçage en 3D

Hugo Girard [a,*], Aurélien Doitrand [a], Milena Tosti Umemura [a], Behrad Koohbor [b], Renaud G. Rinaldi [a], Nathalie Godin [a] and Jérôme Bikard [c]

[a] Univ. Lyon, INSA Lyon, Université Claude Bernard Lyon 1, CNRS, MATEIS, UMR5510, 69621 Villeurbanne, France

[b] Department of Mechanical Engineering, Rowan University, 201 Mullica Hill Rd., Glassboro, NJ 08028, United States of America

[c] Axel'One (Syensqo), 87 Avenue des Frères Perret, CS 70061, 69192 Saint Fons, France

E-mails: hugo.girard@insa-lyon.fr, aurelien.doitrand@insa-lyon.fr, milena.umemura@insa-lyon.fr, koohbor@rowan.edu, renaud.rinaldi@insa-lyon.fr, nathalie.godin@insa-lyon.fr, jerome.bikard@syensqo.com

Abstract. An approach is proposed to determine the optimal initiation crack shapes when using the Coupled Criterion (CC) to assess 3D debonding initiation at a fiber-matrix interface. The optimal crack shapes are determined among potential crack shapes described by their length along the fiber-matrix interface, their angle at the free surface and the shape of the debonding front. The optimal crack shapes actually correspond to the crack shapes maximizing the energy criterion, regardless of the interface fracture properties. Stress-isocontours fail to replicate the debonding shapes that were experimentally observed on the side of a single glass fiber-transparent epoxy sample, unlike the energy-based crack shapes. Both methods yield similar interface strength identification, however, the energy-based shapes result in larger identified critical energy release rates.

Résumé. Une méthode est proposée pour déterminer les formes optimales de fissures à l'amorçage, en utilisant le Critère Couplé (CC) pour prédire l'amorçage d'une décohésion à l'interface fibre-matrice en 3D. Les formes optimales de fissures sont déterminées parmi un ensemble de formes potentielles, décrites par leur longueur le long de l'interface fibre-matrice, leur angle à la surface libre et la forme du front de décohésion. Les formes de fissures optimales correspondent en réalité à celles qui maximisent le critère en énergie, indépendamment des propriétés à rupture de l'interface. Les iso-contours de contrainte ne parviennent pas à reproduire les formes de décohésion observées expérimentalement sur le flanc d'un échantillon composé d'une seule fibre de verre dans une matrice d'époxy transparente, contrairement aux formes de fissures basées sur l'énergie. Les deux méthodes permettent une identification similaire de la résistance de l'interface ; cependant, les formes basées sur l'énergie conduisent à des taux de restitution d'énergie critiques plus élevés.

Keywords. Coupled criterion, crack, shape, 3D, fiber-matrix, debonding.

Mots-clés. Critère couplé, fissure, forme, 3D, interface fibre-matrice, décohésion.

Manuscript received 17 March 2025, revised and accepted 12 June 2025.

* Corresponding author

1. Introduction

The Coupled Criterion (CC), introduced by Leguillon [1], is an approach for predicting crack initiation and associated crack size across various configurations [2]. It is particularly efficient under linear elastic assumption, as its solution can be obtained from a single calculation, independent of the material fracture properties. This approach allows for the inverse identification of fracture properties to be performed as a post-processing step [3], unlike computationally expensive approaches such as the Cohesive Zone Model (CZM) [4,5] or the Phase-Field (PF) method for fracture [6]. Moreover, the CC provides a deeper understanding of the fracture phenomenon since it involves studying configurations that are not favorable in order to explain the transition to initiation configurations, based on the combined analysis of the energy and stress criteria. Indeed, further analysis is needed to clarify the role of each criterion in the initiation process, whether it is predominantly triggered by energy, stress, or both [7].

Yet, implementing the CC requires the crack path to be pre-determined, which is not necessary with PF, for example. Several possibilities exist for describing the potential initiation crack shapes. For instance, following the stress isocontours which is computationally efficient as it only requires an elastic calculation without cracks [8,9]. Mittelman and Yosibash [10] studied mode III crack initiation and found that the crack path maximizing the energy release rate, along the V-notch bisector, did not correspond to the experimental one, whether the crack shape is circular or elliptical. Instead, they noted that the crack path observed experimentally matched the maximum normal stress location [11]. Duminy et al. [12] used stress isocontours to describe interface crack path in nacre-like alumina. In different configurations, stress-isocontours based crack shapes may not be optimal for the energy criterion, which can drive the initiation of the crack, see [13–16]. Another solution is to assume the shape of the crack, choosing for instance a geometric shape, such as in [14,17], to obtain a configurable description of the cracks. Papšík et al. [18] compared CC solutions of indentation induced-cracking obtained using different crack paths, starting from the contact surface between the indenter and the sample, thus identifying the optimal one. Elliptical cracks were assumed in [19] to study crack initiation in layered ceramics. Nevertheless, the above-mentioned approach does not consider all possible crack geometries. As a consequence, it is yet not established which initiation crack shape among all possible crack shapes is the most favorable, i.e., results in the minimum imposed loading at initiation. In our previous work [20], all possible geometrical debonding shapes were compared using a 2D model consisting of two neighboring fibers in model macro fiber composites. Stress-based and energy-based shape solutions, corresponding respectively to the shapes maximizing either stress or energy conditions, were compared to the optimal CC solution. Stress-based shapes provided the optimal CC solutions for relatively small interface brittleness numbers. For larger brittleness numbers, energy-based shapes yielded the optimal CC solution. There exists a transition zone though, for intermediate brittleness numbers, where neither the stress nor the energy-based shapes were able to provide the optimal CC solution. A similar methodology for determining the optimum initiation crack shape in 3D has yet to be developed.

Determining the crack path in 3D is challenging because the third dimension increases drastically the number of possible crack shapes. To overcome this drawback, García et al. [17] used configurable rectangles whose dimensions can be varied using two variables. Burhan et al. [21] investigated configurable semi-elliptical shapes to study interlaminar crack initiation in composite materials, optimal crack shapes were selected as those minimizing the CC solution. Interlaminar strength and critical energy release rate were then identified by minimizing the difference between the CC and experimental test results for both failure stresses and crack initiation length. Leguillon [8] attempted to determine the crack shapes at an interface corner based on stress isocontours. Fracture properties identified in 3D were similar to those obtained

with 2D simulations. However, Doitrand et al. [14] found that stress isocontours-based shapes did not fulfill the energy criterion in woven composites when the CC solution was found to be driven solely by the energy condition. In such a configuration, idealized crack surfaces spanning the whole ply thickness and having straight crack fronts were assumed. These surfaces may not be the optimal ones compared to energy-based shapes to describe the 3D potential crack shapes when dealing with energy-driven configurations. With regard to the fiber-matrix debonding configuration studied previously, stress isocontours-based shapes did not allow the identification of shear fracture properties because they are mainly subjected to mode I loading, see Girard et al. [22]. In addition, they provided concave debonding shapes and large debonding angles that were not observed experimentally. In this sense, energy-based shapes or intermediate shapes lying in between stress isocontours-based or energy-based ones could better describe the experimentally observed debonding shapes and allow for the shear fracture properties to be determined. However, their determination is computationally expensive, as an infinite number of possible debonding shapes need to be investigated.

A methodology is therefore presented in this article to efficiently determine the optimal 3D debonding initiation shapes provided that debonding initiates from the fiber pole located at the free surface as observed experimentally. The experimental configuration consisting of a single glass fiber embedded in a transparent epoxy matrix is presented in Section 2, together with the obtained experimental results. Then the CC predictions obtained with the stress-based and energy-based shapes are compared for a wide range of interface fracture properties in Section 3 to assess the relevance of the stress-based or energy-based shapes in adequately describing the optimal CC solution. Optimal debonding shapes are then compared to the experimental observation. Finally, inverse identification of the fracture properties of the fiber-matrix interface is performed in Section 4 using both approaches to quantify the differences they yield.

2. Experimental characterization of the fiber-matrix debonding

2.1. *Sample preparation and testing*

The configuration consists in a single glass fiber embedded into an epoxy matrix tensile specimen. The geometry and dimensions of the samples are given in Figure 1a.

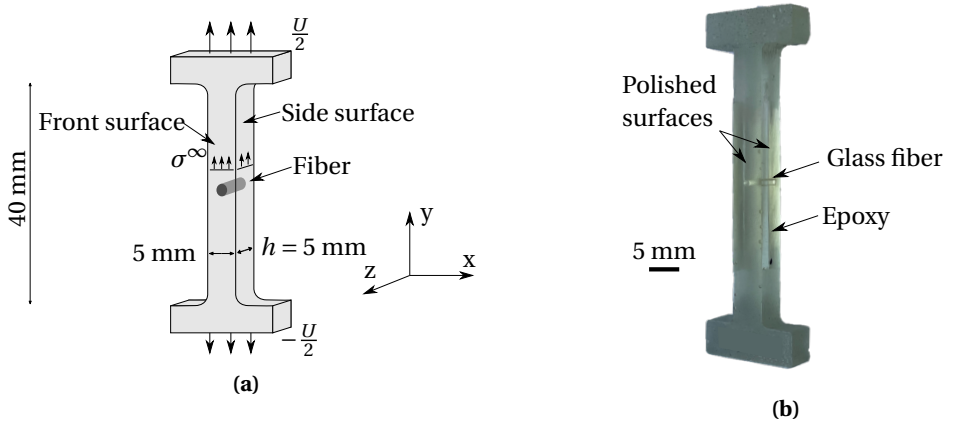

Figure 1. (a) Single fiber specimen geometry, dimensions and testing. (b) As prepared sample with the glass fiber embedded into an epoxy matrix.

The isotropic elastic properties of the epoxy matrix (SD2505/SR1500, Sicomin, France) are determined in-house, using 5 cured samples with the same epoxy mixture as the single-fiber samples. Tensile tests are carried out on the samples at room temperature under quasi-static loading with a cross-head speed of 0.18 mm/min. The average elastic properties obtained from the 5 samples are given in Table 1, together with those of the 1 mm glass fiber supplied by the manufacturer (quartz glass fiber, McMaster-Carr, USA).

Table 1. Linear elastic properties of the epoxy matrix and glass fiber.

Properties	**Epoxy**	**Glass fiber**
E [GPa]	2.7 ± 0.2	72
ν	0.41 ± 0.04	0.17

Three single fiber samples are fabricated by embedding a 1 mm diameter glass fiber in an epoxy matrix, denoted sample 1, 2 and 3. The dimensions of the samples are defined for use in a micro tensile testing machine (see Figure 1a). The fiber is held in place at the intersection of the 2 symmetry axes using a 3D printed support. The surface of the fiber is cleaned with isopropanol. The matrix is then poured into a silicone mold, where the mold is drilled at the location of the fiber to allow it to slightly protrude from the final sample. This eliminates the need to polish the end of the fiber beforehand. Curing time is one month at room temperature. After curing, the front surface of the sample is lightly polished with fine sandpaper (10 µm grit). The side surfaces are also polished, first with fine sandpaper (8 µm grit), then using a rotating cotton disc coupled with a polishing solution to obtain a translucent and smooth side surface. A speckle pattern is then applied to the front surface to enable 2D Digital Image Correlation (DIC). A dual-vision system consisting of two perpendicularly positioned cameras (FLIR Grasshopper GS3-U3-41C6M-C) is installed [23]. The front camera allows DIC close to the fiber-matrix interface, while the second side camera is used to observe the fiber side.

2.2. *Experimental characterization of the debonding initiation and propagation*

The geometric characteristics that can be extracted from the two cameras after debonding initiation are depicted in Figure 2.

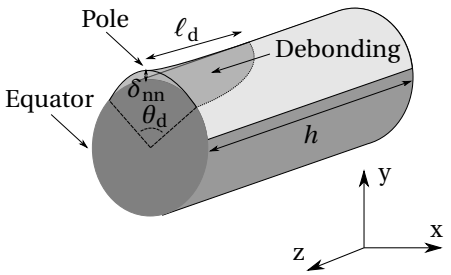

Figure 2. Set of geometrical parameters used to describe the debonding geometry.

The debonding can be described by its angle θ_d at the front surface, corresponding to the angle between the two tips of the debonding, see [24] for more information about its experimental determination using the side camera. The quantity δ_{nn} corresponds to the maximum normal opening of the debonding located at the pole of the fiber with respect to the loading direction [22]. The interface opening reflects the distance between the two lips of the debonding and it can be

determined by performing DIC at the front surface. The debonding length through the thickness is described by ℓ_d, which corresponds to the maximum length in the z direction at the pole of the fiber [23]. Figure 3 illustrates the variation of the different geometric characteristics as a function of the remote loading applied (σ^∞) to the sample 3. The results obtained for sample 3 are representative of all three samples tested, using the same approaches as described above.

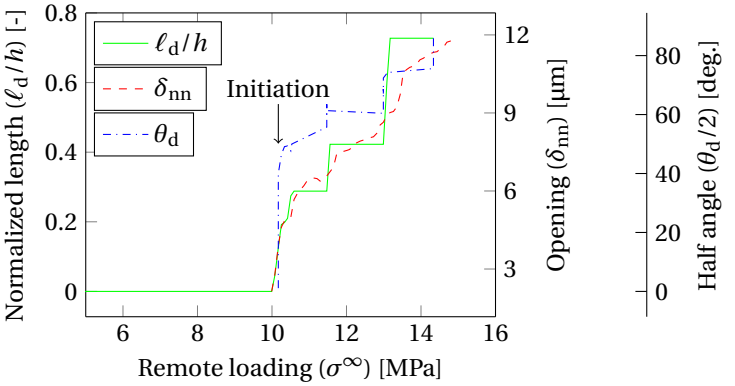

Figure 3. Variation of the geometrical characteristics of the debonding as a function of the remote loading for the sample 3.

All the debonding characteristics enable the determination of a similar initiation remote stress around 10 MPa. They evidence a step-wise debonding process. Unstable debonding propagation phases are followed by either stable propagation phase or debonding arrest. During the unstable propagation phases, both the debonding length and angle increase, as well as the opening. During the debonding arrest phase, both the length and angle remain constant contrary to the opening which increases with an increase in the tensile loading. During the stable propagation phase, the debonding angle increases while its length remains constant. Table 2 summarizes the different characteristics magnitude after debonding initiation with the associated remote loading for the 3 samples.

Table 2. Fiber-matrix debonding geometric parameters obtained experimentally from the three samples after initiation.

	Sample 1	**Sample 2**	**Sample 3**
σ^∞ [MPa]	7.25 ± 0.04	8.03 ± 0.04	10.04 ± 0.04
$\theta_d/2$ [deg.]	29	37	40
ℓ_d/h [-]	0.03	0.02	0.05
δ_{nn} [µm]	1.5 ± 1.0	2.1 ± 0.8	2.1 ± 1.0

Accurate debonding topology is also assessed after initiation for one specimen using Computed Tomography (CT), the equipment is manufactured by the Phoenix X-ray company. A voxel size of 5 µm is achieved. The approach is more challenging than using the dual-vision system since it requires adding contrast penetrant to highlight the debonding location. Contrast penetrant similar to that in [25] is employed. As a consequence, only one scan is performed, just after debonding initiation observed using the side camera. The loading is maintained constant while the penetrant is added. The debonding observed probably has a larger surface area than that at initiation, having potentially propagated when the penetrant is added. Nevertheless, the

shape observed is close to that of the initiation and can therefore still be used as a target for the experimental-numerical dialogue. Figure 4 presents the experimental debonding topology after initiation. The debonding front, indicated by the white line, exhibits a convex shape.

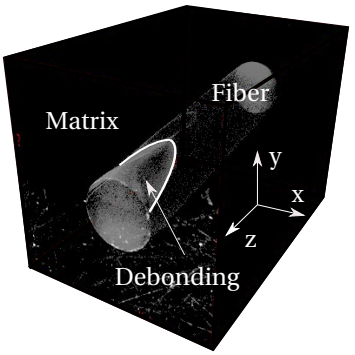

Figure 4. Debonding topology observed after initiation using X-ray tomography. The debonding zone is highlighted using a contrast penetrant while the debonding front is depicted by a white thick line. The volume of the scan is 3 mm in the x-direction and y-direction, 5 mm in the z-direction.

3. Determination of the optimal initiation crack shape

This section provides a methodology to determine the optimal initiation debonding shape to be used when implementing the CC.

3.1. *The fiber-matrix interface model*

A 3D model is employed to account for the singularity at the free surface of the sample, caused by the fiber-matrix elastic mismatch. The model is established to compare stress-based and energy-based crack shapes to describe the potential debonding path. The model consists of either 1/4 or 1/8 simplification of the real geometry, using ten-node quadratic elements under the assumption of small strain and linear elasticity. A 1/4 simplification is used for the calculation of energy-based shapes, as it allows a single initiation site to be studied. A second 1/8 simplified model is used with stress-based shapes as they provide a two-site initiation, i.e., at both free surfaces, so that additional symmetry can be added to the model [22]. Two mesh convergence studies are performed since the CC involves both stress and energy conditions. Overall, a difference of less than 2% is achieved, compared to a converged solution, on the stress fields at the fiber-matrix interface and the elastic strain energy released for a fixed debonding surface. A mesh size of 20 μm is thus adopted at the fiber-matrix interface.

3.2. *Implementation of the CC*

The debonding initiation is predicted by means of the CC similar to Mantič [13] and Girard et al. [16]. The CC combines two conditions to provide the initiation loading, the debonding surface and shape. The energy condition is based on an energy conservation principle before and after crack initiation. It is a necessary condition but it is not sufficient. It is similar to the Griffith criterion but considers an incremental balance instead of a differential one. As a result, the

variation in the external work forces has to be equal to the variation of other sources of energy such as:

$$\Delta W_{\mathrm{k}} + \Delta W_{\mathrm{el}} + \Delta W_{\mathrm{d}} + \overline{G_{\mathrm{c}}} S = \Delta W_{\mathrm{ext}},$$

where ΔW_{ext} denotes the external work forces, ΔW_{k} the kinetic energy, ΔW_{el} the elastic strain energy, ΔW_{d} the energy dissipated into other mechanisms such as plasticity, diffused damage or friction for instance and $\overline{G_{\mathrm{c}}} S$ the crack surface creation energy, where S is the crack surface and $\overline{G_{\mathrm{c}}}$ is the average critical ERR whose calculation is detailed in Section 3.4. A rigorous description of the energy balance in the thermodynamic context in presented in Dormieux et al. [26]. Different thermal effect occurring at crack initiation could also be accounted in the energy balance, for instance local heating zone resulting from the cracking process, sliding, viscous effects. These effects could be accounted through ΔW_{d}. However, they are difficult to estimate and would require the use of a dedicated numerical model or a thermal camera during the experiments. As a result, crack initiation will be assumed to be isothermal and all dissipated energy will not be taken into account. Furthermore, although the dissipated energies are not taken into account in the energy balance, they are in fact accounted for phenomenologically through the critical ERR during its determination, under the assumption that these effects do not vary with the crack surface. Dormieux et al. [26] also proposed rigorous bounds for the loading level at crack initiation and associated observable crack length. They discussed conditions under which quasi-static crack initiation can be considered. The validity of the quasi-static crack initiation assumption depends on the variation of the Incremental Energy Release Rate (IERR) G_{inc}:

$$G_{\mathrm{inc}}(\Gamma, \sigma^{\infty}) = \frac{\Delta W_{\mathrm{ext}} - \Delta W_{\mathrm{el}} - \Delta W_{\mathrm{k}}}{S} = \overline{G_{\mathrm{c}}},$$

where Γ denotes the debonding path and σ^{∞} the remote tensile stress. Noting that the ERR can be obtained from the IERR using:

$$G = \underbrace{G_{\mathrm{inc}}}_{=\overline{G_{\mathrm{c}}}} + S \frac{\mathrm{d}G_{\mathrm{inc}}}{\mathrm{d}S},$$

and that $G_{\mathrm{inc}} = \overline{G_{\mathrm{c}}}$ at initiation. So to ensure a stable crack initiation with $G \leq \overline{G_{\mathrm{c}}}$ at initiation, $\frac{\mathrm{d}G_{\mathrm{inc}}}{\mathrm{d}S}$ has to be lower or equal to 0. This case is detailed in Dormieux et al. [26]. It can be obtained when $G_{\mathrm{inc}}/\overline{G_{\mathrm{c}}}$ exhibits a maximum [16] or in the presence of strong singularities [27] for which deceasing variations of G_{inc} and G as a function of the crack surface are obtained. In this case, crack initiation can be studied within the framework of a quasi-static hypothesis with neglected kinetic energy. On the contrary, if $\frac{\mathrm{d}G_{\mathrm{inc}}}{\mathrm{d}S} > 0$, $G > G_{\mathrm{c}}$, unstable crack initiation takes place and the quasi-static assumption is no longer valid. It would be necessary to take kinetic energy into account in the energy balance, see [28,29]. Quasi-static crack initiation is assumed in this work since it can not be quantified experimentally, so the IERR reverts to:

$$G_{\mathrm{inc}}(\Gamma, \sigma^{\infty}) = \frac{W(0, \sigma^{\infty}) - W(\Gamma, \sigma^{\infty})}{S}$$

with W denotes the elastic strain energy of the model. As a consequence, only stable crack initiation can be considered.

The energy condition solely is generally adopted to study the propagation of an already existing semi-infinite crack in an infinite medium. The latter needs to be complemented by a stress condition to predict crack initiation. The stress condition must be satisfied at any location over the entire debonding path Γ before initiation, according to the condition proposed in [1]. This non-local stress condition thus enables its application even if the stress fields are non-monotonic. A quadratic stress criterion σ_{eq} is employed to account for the mode mixity, i.e., the normal stress σ_{nn}, the in-plane and out-of-plane shear stresses, respectively, σ_{nt} and σ_{nz}:

$$\sigma_{\mathrm{eq}}(\vec{x}, \sigma^{\infty}) = \sqrt{\sigma_{\mathrm{nn}}^2(\vec{x}, \sigma^{\infty}) + \frac{1}{\mu^2}\left(\sigma_{\mathrm{nt}}^2(\vec{x}, \sigma^{\infty}) + \sigma_{\mathrm{nz}}^2(\vec{x}, \sigma^{\infty})\right)},$$

where $\vec{x}$ is the location vector and μ the shear to tensile strength ratio. As for the energy condition, this criterion is necessary but not sufficient. These two conditions are combined as follow:

$$\begin{cases} \sigma_{\text{eq}} \geq \sigma_{\text{c}} & \forall\, \vec{x} \in \Gamma, \\ G_{\text{inc}}(\Gamma, \sigma^{\infty}) \geq \overline{G_{\text{c}}}(\Gamma), \end{cases}$$

where σ_{c} is the interface tensile strength.

One of the unknown to be determined in the CC is the initiation crack path. The potential crack path can be chosen in order to minimize the imposed loading that fulfills (i) the stress condition, (ii) the energy condition or (iii) both stress and energy conditions.

3.3. *Stress-based debonding shapes*

Figure 5 illustrates the debonding stress-based shapes whose fronts are defined based on the normal stress isocontours, superimposed on one-quarter of the fiber-matrix interface. Further details about the determination and implementation of the stress-isocontours based debonding shapes can be found in Girard et al. [22].

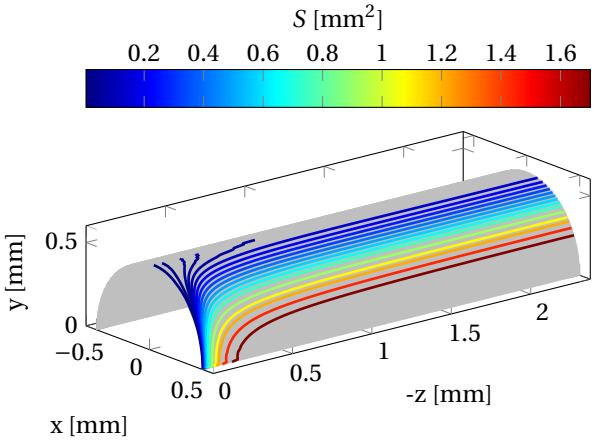

Figure 5. Potential debonding shape fronts obtained using normal stress isocontours superimposed on one-quarter of the fiber-matrix interface for varying S.

Following the stress isocontours before initiation, debonding initiates at the fiber pole with respect to the loading direction and propagates in a concave shape, forming a tunnel for sufficiently large cracks ($S > 0.2$ mm^2). Although only one ratio between fiber diameter and sample thickness is investigated in this work, the debonding shapes derived from the stress isocontours will remain similar for fibers that are sufficiently long with respect to their diameter. In the case of a very thin sample with respect to the fiber diameter, the singularities of the two free surfaces will influence the isocontours. Irrespective of the crack surface, the potential debonding shapes given by the stress criterion significantly differ from the one observed using CT (Figure 4). For small crack surface, the debonding angle given by the stress isocontours is larger than the one observed experimentally, and for larger crack surfaces the debonding shape is concave, contrary to the convex shapes observed experimentally. It can thus be concluded that for the studied configuration, the stress-based crack shapes significantly differ from the crack shapes observed experimentally. This discrepancy suggests the possibility of alternative optimal initiation debonding shapes, which are studied in next sections.

3.4. *Energy-based debonding shapes*

Determining energy-based debonding shapes is challenging because it requires computing the elastic strain energy difference between the states with and without crack. It thus requires one Finite Element (FE) calculation for a given crack shape and there is theoretically an infinite number of 3D crack shapes to be evaluated. The determination of energy-based crack shapes consists in defining the debonding shape that maximizes the IERR to critical ERR ratio for a given crack surface increment. However, it is not possible to test an infinite number of debonding shape configurations. Therefore, assumptions about the potential debonding shapes are made in the following. On the one hand, since the stress criterion reaches a peak at the pole of the fiber at the free surface, it is likely that the debonding emanates from this location, as presented in Figure 4. On the other hand, although experimental observations show convex shapes, both concave and convex shapes are investigated for comparison purposes.

The potential debonding shapes are therefore approximated using a power-law relationship, involving geometric parameters depicted in Figure 2. The location of the debonding front at the free surface is determined by the debonding angle (θ_d), while the debonding length (ℓ_d) determines the location at the pole of the fiber through the thickness. The topology of the debonding front, connecting these two points, can therefore be approximated using a power-law whose exponent n can vary from 0.6 to 4, see (1), where r is the fiber radius.

$$z(x) = -\left(\ell_\mathrm{d}^n\left(1-\left(\frac{x}{\sin\left(\frac{\theta_\mathrm{d}}{2}\right)r}\right)^n\right)\right)^{\frac{1}{n}} \tag{1}$$

Figure 6 shows the influence of the three parameters on the topology of the debonding front.

The influence of the debonding angle on the debonding front shape is shown in Figure 6a, while the exponent and length are arbitrarily fixed. The debonding half-angle $\theta_\mathrm{d}/2$ can be varied between 10 and 80 degrees to assess a wide range of debonding shapes. The influence of debonding length is shown in Figure 6b and the power-law exponent in Figure 6c, the other parameters being fixed. The debonding length varies between 0.05 and 1 mm in Figure 6b. The variation in exponent (Figure 6c) induces a transition from a concave shape, e.g., for an exponent smaller than 1, similar to that provided by stress-based shapes, to a convex shape, e.g., for an exponent larger than 1, tending towards a squared debonding shape for a large exponent. Using the above geometrical parameters, a wide range of debonding shapes can be evaluated to determine the optimal energy-based debonding shapes.

A procedure is established to determine the energy-based debonding shapes by exploring all possible configurations for each exponent n of the power-law description. The first step consists in identifying the couples of debonding angle and length leading to the same debonding surface for a fixed exponent. Figure 7a shows the variation in debonding surface as a function of both debonding angle and length for another fixed $n = 1.5$ exponent.

Increasing both the debonding angle and the length leads to increasing debonding surfaces. Consequently, several couples of angle and length, leading to the same debonding surface, can be determined using the debonding surface isocontours as shown in Figure 7b. The minimum debonding surface considered is 0.001 mm^2, with surfaces smaller than 0.01 mm^2 are not presented in the sequel for the sake of clarity. Ten (ℓ_d, θ_d) couples are selected for each debonding surface isocontour. The different debonding shapes obtained for two selected surfaces of 0.18 mm^2 and 0.3 mm^2 are shown in Figure 8, noting that only five couples of angles and lengths are displayed for the sake of clarity.

This illustrates the variation in debonding angle and length for a similar debonding surface. Noticeably, the debonding shapes corresponding to a surface of 0.18 mm^2 show large variations in length and angle (see Figure 8a). Since a maximum value is set on the length range to conform

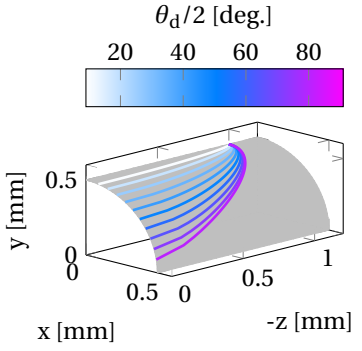

(a) $\ell_d = 1$ mm, $n = 2$

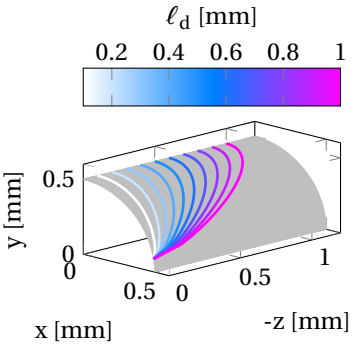

(b) $\theta_d = 80$ deg., $n = 2$

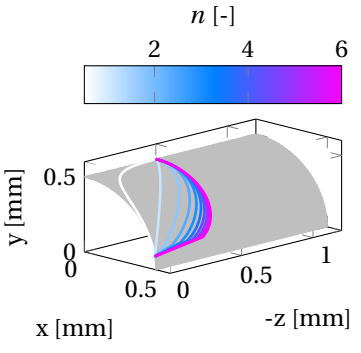

(c) $\ell_d = 1$ mm, $\theta_d = 80$ deg.

Figure 6. Possible debonding shapes superimposed on the fiber-matrix interface obtained by varying (a) the debonding angle, (b) the debonding length and (c) the exponent of the power-law description.

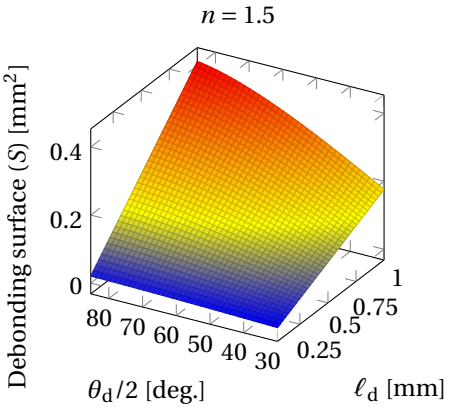

(a)

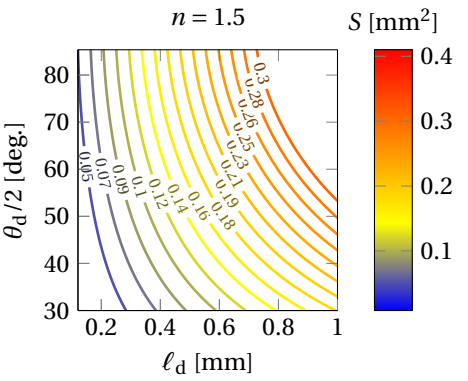

(b)

Figure 7. (a) Variation of the debonding surface as a function of the debonding angle and length. (b) Debonding surfaces isocontours highlighting the ranges of debonding angle and length couples leading to a similar debonding surface.

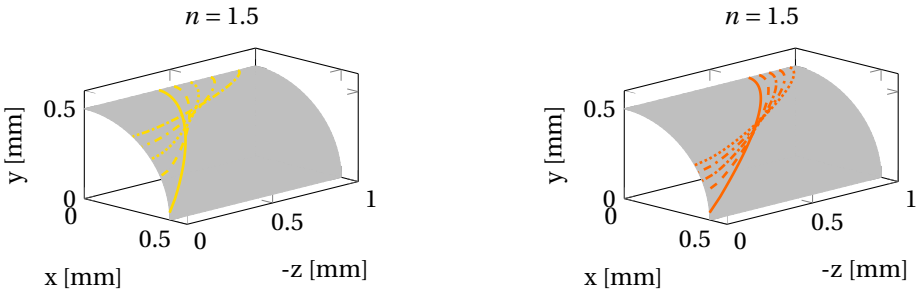

(a) $S = 0.18$ mm^2 **(b)** $S = 0.3$ mm^2

Figure 8. Debonding shape with varying couples of debonding angle and length obtained for a similar debonding surface of (a) 0.18 mm^2 and (b) 0.3 mm^2.

to experimental observations, smaller variations are encountered for a surface of 0.3 mm^2 (see Figure 8b).

The IERR corresponding to each couple can be evaluated by FE using a mesh that includes a debonding profile corresponding to the area delimited by a given debonding front. The debonding shape is projected onto the fiber-matrix interface so that the mesh topology matches the geometrical configuration. As a consequence, one FE mesh is created for each debonding front configuration.

The average critical ERR is calculated using the Hutchinson and Suo [30] relationship, which depends on the mode mixity ψ. A condition is applied to the mode mixity to consider only shear when the interface undergoes compression, see Girard et al. [16] for more details. Mode mixity is evaluated locally which gives a local value of G_c that is averaged on the anticipated crack path, see (2):

$$\overline{G_c}(\Gamma) = \frac{1}{S}\int^{\Gamma} G_{IC}\left[1+\tan^2\left[(1-\lambda)\psi(\vec{x})\right]\right] \mathrm{d}x\,\mathrm{d}y\,\mathrm{d}z. \tag{2}$$

The parameter λ is related to a mode II to mode I critical ERR ratio, see [2].

The IERR to critical ERR ratio variation is shown in Figure 9a as a function of θ_d for each selected (ℓ_d, θ_d) couples and varying debonding surfaces, which values are differentiated using the same color code as Figures 7 and 8.

Overall, for a given debonding surface, there exists a (ℓ_d, θ_d) couple that maximizes the energy criterion, i.e., the IERR to critical ERR ratio, indicated by a round marker. Consequently, these couples lead to the geometrical configuration that is the most favorable from an energy point of view. The maximum of IERR to critical ERR ratio obtained from each surface is shown in Figure 9b, with a similar marker color, as a function of the corresponding debonding surface. It yields the maximum value of IERR that can be attained as a function of the crack surface for given exponent $n = 1.5$ and $\lambda = 0.2$ parameter.

The debonding angle and length couples that maximize the IERR to critical ERR ratio are shown in Figure 10a. These couples therefore correspond to the most energetically favorable geometrical configuration. Since only the debonding initiation is studied here, the angle and length of debonding do not necessarily have to increase monotonically. For instance, a decrease in the debonding angle is observed as the debonding surface increases, see Figure 10a for surfaces close to 0.4 mm^2 (ℓ_d close to 0.8 mm).

The configuration corresponding to the favorable debonding shape is superimposed onto the fiber-matrix interface in Figure 10b. The debonding remains localized near the free surface fiber

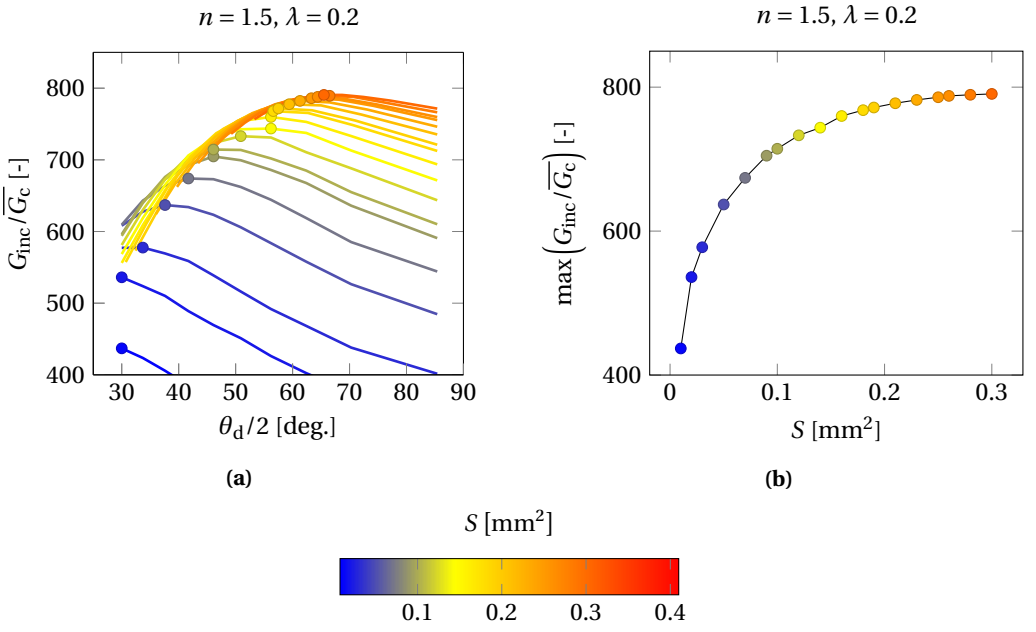

Figure 9. (a) IERR to critical ERR variation obtained for different debonding surfaces as a function of the debonding angle. The maximum is indicated by a marker for each surface. (b) Maximum IERR to critical ERR obtained for each debonding surface.

pole for small surface areas. For a larger debonding area, there is a more pronounced increase in debonding length with respect to the angle.

The debonding shapes shown in Figure 10b are those that maximize the energy condition. However, they are obtained for a fixed power-law exponent n. Thus, the optimum energy conditions obtained for different power-law exponents can be compared to determine the configurations which maximize the energy conditions. Figure 11 shows the variation in the IERR to critical ERR ratio obtained for different exponents. It is found that a $n = 1.5$ exponent yields the most favorable debonding shapes from an energy point of view whatever the debonding surface and λ values explored.

The fiber-matrix interface undergoes both opening and shear modes simultaneously. Consequently, λ can influence the loading required to fulfill the energy condition. Figure 12a shows the influence of λ on the magnitude of the IERR to critical ERR ratio.

The opening critical ERR G_{IC} is fixed while the shear critical ERR G_{IIC} increases, leading to a decrease in λ. The critical ERR in mode II appears to influence the profile of the energy criterion over the full range of the debonding surface, suggesting that small variations in mode mixity are encountered on the different debonding shapes. Overall, increasing G_{IIC} leads to a decrease in the level of the energy criterion. Consequently, a larger loading is required to fulfill the energy criterion as G_{IIC} increases, see Figure 12b. However, the difference in required loading induced by a variation in λ is small, less than 0.5 MPa for a fixed debonding surface. Consequently, the shear component appears to be negligible on the energy-based shapes determined.

Although shear has little influence on the loading required to fulfill the energy condition, it can influence the (ℓ_d, θ_d) couples that describe the energy-based shapes. Figure 13a shows the (ℓ_d, θ_d) couples corresponding to energy-based shapes for two extreme λ of 0.01 and 0.8.

For a relatively small debonding area ($\ell_d < 0.3$ mm and $\theta_d/2 < 45$ deg.), λ has no influence

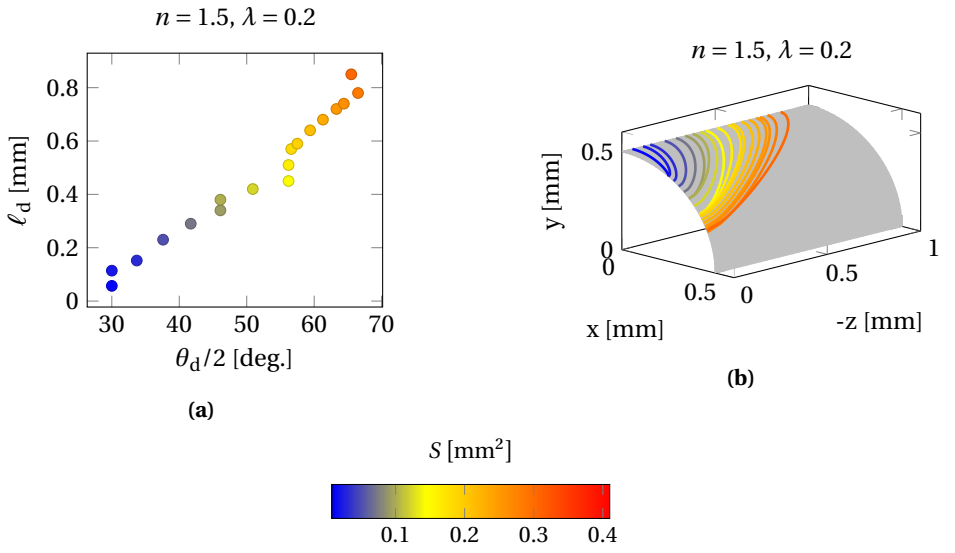

Figure 10. (a) Debonding angle and length couples corresponding to the maximum in IERR to critical ERR ratio in Figure 9a, with the colors corresponding to the debonding surfaces. (b) Optimal potential debonding shapes determined from an energy point of view with an exponent of 1.5, superimposed onto the fiber-matrix interface (gray surface).

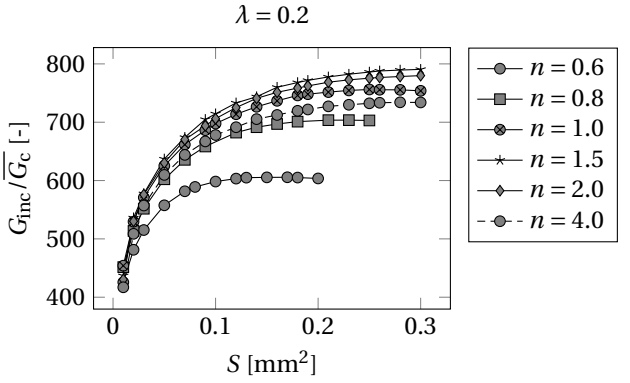

Figure 11. Variation of the optimal IERR to critical ERR ratio as a function of the debonding surface for different power-law exponents, emphasizing the optimal exponent of 1.5 for the defined $\lambda = 0.2$.

on the energy-based debonding shape, which mainly undergoes opening mode. However, for a larger debonding surface, smaller λ results in both decreasing θ_d and increasing ℓ_d. This difference can be explained by the stress shear component that is higher close to the fiber equator, i.e., at large debonding angles. Consequently, the increase in the critical ERR in mode II makes debonding initiation for a large angle less favorable than for a small G_{IIC}. This is illustrated in Figure 13b, where the optimum debonding shapes obtained for three different debonding surfaces and the two extreme values of λ are superimposed with the field of variation in mode mixity at the fiber-matrix interface. Overall, mode mixity is similar to that observed with a front 2D modeling (see Girard et al. [16]) for a sufficiently large distance from the free surface and

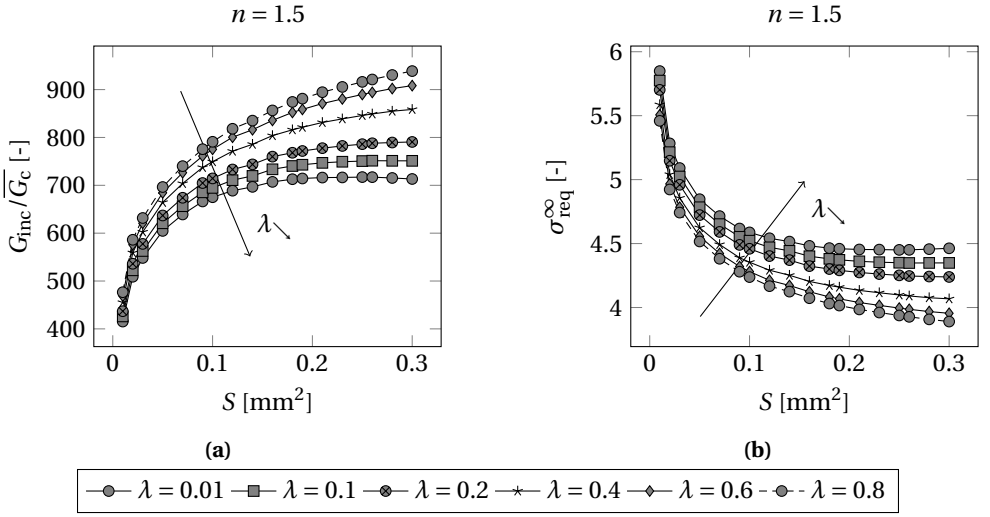

Figure 12. Influence of λ on (a) the IERR to critical ERR ratio and (b) the loading required to fulfill the energy criterion ($\sigma^{\infty}_{\text{req}}$) for a fixed exponent of $n = 1.5$.

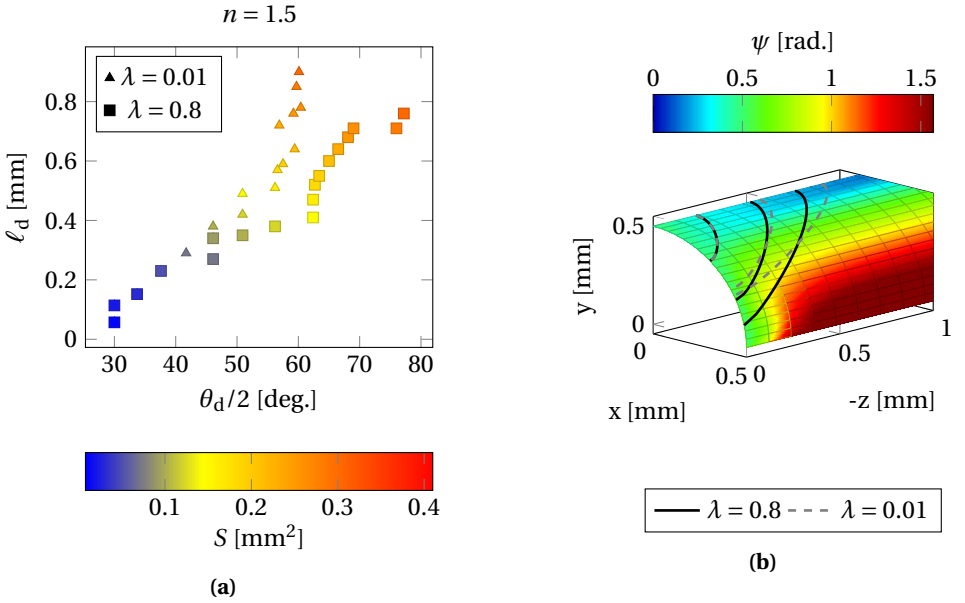

Figure 13. (a) Debonding geometrical parameters (ℓ_{d}, θ_{d}) corresponding to the energy-based debonding shapes for two extremes values of λ. (b) Energy-based shapes obtained for three surfaces and two λ values highlighting the influence of the mode mixity (whose variation is superimposed on the fiber-matrix interface) on the debonding shapes.

it is affected by the singularity at the free surface. As with debonding shapes based on stress isocontours, the fiber diameter to sample thickness ratio should not affect energy-based shapes for a fiber that is sufficiently long in relation to its diameter.

3.5. *Energy-based vs stress-based: CC solution*

Once the potential initiation debonding shapes based on stress isocontours or energy are determined, the CC can be implemented. The loading required to fulfill one or other of the criteria (σ_σ^∞, σ_G^∞) is compared in Figure 14 on the basis of the stress isocontours-based and energy-based debonding shapes for two brittleness numbers:

$$\gamma = \frac{1}{\sigma_\mathrm{c}}\sqrt{\frac{G_\mathrm{IC}E^*}{r}}, \tag{3}$$

where E^* denotes the harmonic mean of the effective elastic moduli of the two constituents. The λ and μ parameters are selected on the basis of those identified in [16]. The minimum loading for which both criteria are fulfilled is the initiation loading and the corresponding debonding surface is the initiation crack surface, which are indicated by the round marker in Figure 14.

For both stress-based and energy-based debonding shapes, the stress condition increases monotonically since the equivalent stress decreases with the debonding surfaces. The energy condition obtained with the energy-based debonding shapes monotonically decreases, unlike the one obtained using the stress-based shapes which provides local minima. Overall, the stress-based shapes result in the most favorable solution in terms of stress conditions, whatever the debonding surface considered, consistently with their definition. On the contrary, the energy condition provided by energy-based shapes is smaller than that of stress-based shapes, whatever the debonding surface. For a relatively small brittleness number (Figure 14a), the energy-based shapes provide the most favorable configuration compared to that provided by the stress-based shapes. This differs from the results obtained in 2D [20], where the stress-based shapes are the optimal debonding shapes for a small brittleness numbers, i.e., smaller than 1. In 3D, the energy condition, which is significantly larger for the stress-based shapes, appears to control debonding initiation even for a small brittleness number. The stress-based and energy-based shapes provide debonding initiation surfaces with relative difference of 140%. For a relatively large brittleness number (Figure 14b), the energy-based debonding shapes also lead to the most favorable configuration for predicting debonding initiation. The stress-based shapes require a larger loading to fulfill the energy condition. A similar result was obtained in 2D for large brittleness numbers [20]. The debonding initiation configuration (surface S_c) obtained for the stress-based and energy-based debonding shapes and the two brittleness numbers are compared in Figure 14. For a small brittleness number, the stress-based surface remains close to the free surface with a debonding angle spanning over the whole fiber circumference. The energy-based surface has a smaller angle and length, thus a smaller surface than stress-based surface. The difference between the two debonding initiation surfaces becomes more pronounced as the brittleness number increases, as shown in Figure 14d. The stress-based surface provides a tunnel between the two free surface debondings. In contrast, the energy-based surface shape is similar to that obtained with a small brittleness number, with increased surface area.

Similarly, the debonding initiation surfaces obtained using stress-based and energy-based shapes are compared for a range of interface brittleness numbers, see Figure 15a. The brittleness number range is selected to ensure that the CC solution is provided by the intersection of both stress and energy conditions.

For interface brittleness numbers smaller than 2, the initiation surfaces predicted by the two approaches are in the same order of magnitude. However, for large brittleness number, the initiation surfaces predicted by the stress isocontours approach is larger than those provided by the energy-based debonding shapes. This phenomenon is caused by the tunneling effect of the stress-based shapes, which induces a sharp increase in the debonding surface for solutions triggered by the energy condition. The remote stress required to fulfill the CC is assessed in

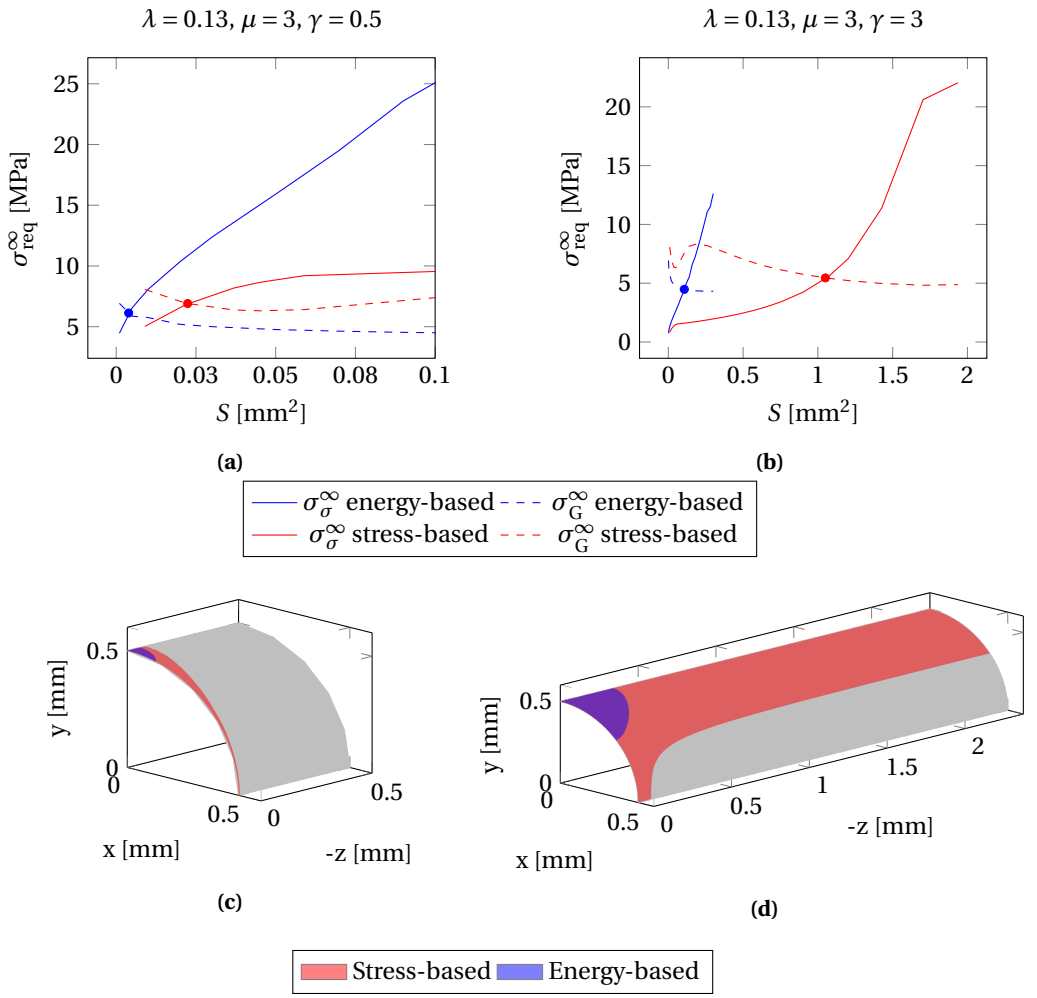

Figure 14. Required loading to fulfill both the stress (solid lines) and energy (dashed lines) criteria obtained using the stress-based and energy-based shapes. Two interface brittleness numbers are investigated, (a) a relatively small one $\gamma = 0.5$ and (b) a relatively large one $\gamma = 3$. Comparison of the debonding initiation surfaces (S_c) obtained in (a) and (b), respectively (c) and (d).

Figure 15b, for the same range of brittleness number as Figure 15a, so that the relevancy of the stress isocontours approach in predicting the optimal CC solution can be evaluated. The stress-based shapes yield larger initiation remote stress than the energy-based ones whatever the brittleness number over the range 0.3–8. In fact, it is observed that the energy-based debonding shapes are close to the ones that allow fulfilling the CC for a minimum imposed loading, as they yield differences smaller than 0.1% in the initiation remote loading compared to these optimum solutions.

For relatively small interface brittleness numbers ($\gamma < 1$), limited difference of less than 15% is made by the stress-based shapes. For intermediate brittleness numbers ($1 < \gamma < 6$), the difference reaches a peak to 30% caused by energy driven solutions. The difference decreases to 15% for larger brittleness numbers ($\gamma > 6$). The differences in initiation loading are larger than in

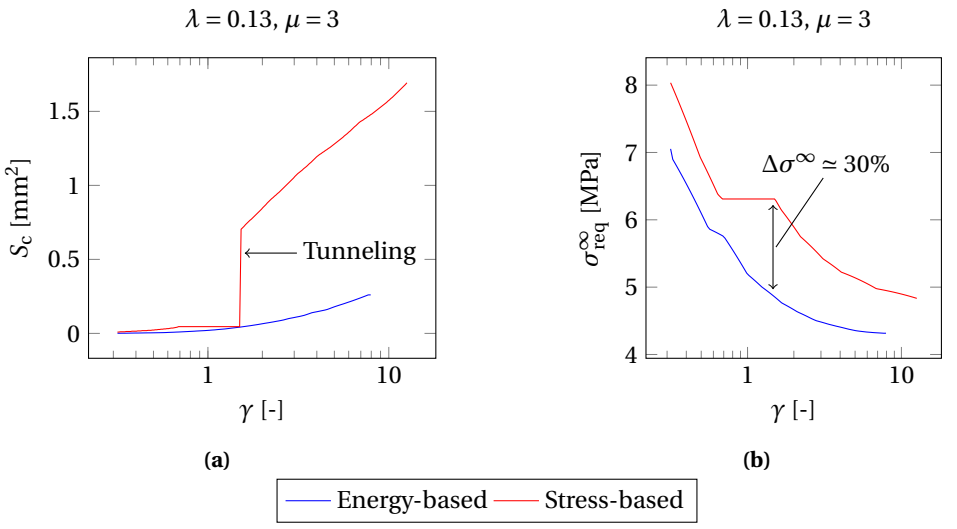

Figure 15. (a) Debonding initiation surfaces and (b) corresponding loading predicted by the stress-based and energy-based shapes.

2D, where it remains smaller than 5% whether stress-based or energy-based crack shapes are used [20].

3.6. *Comparison with experimental observations*

Initiation debonding shapes are now compared to the ones observed experimentally just after initiation. The debonding side views are shown in Figure 16a and Figure 16c just after initiation for sample 1 and 3, respectively. Note that these two samples represent two independent cases subjected to the same experimental conditions. The debonding zone in each case is highlighted with white pixels, similar to Uddin et al. [23].

Three brittleness numbers are selected and their corresponding debonding shapes are superimposed on the zoomed experimental side view, see Figure 16b and Figure 16d. On the one hand, there are energy-based shapes that correspond to the experimental debonding angle and length after initiation for a given range of brittleness numbers. For sample 1, experimental observations yield an upper limit of 0.6 as an acceptable γ, and 1.2 for sample 3, otherwise excessive debonding angles are encountered. These restrictions are applied to the inverse identification in the following. Energy-based shapes are able to reproduce the experimental debonding configuration, in terms of angle, length and shape. On the other hand, as pointed out previously, stress-based shapes significantly overestimate the debonding angle, regardless of γ, while accurately predicting the debonding length, for a range of γ. The upper limit of the acceptable γ range based on the experimental debonding length can be determined as 0.56 for sample 1 and 0.65 for sample 3. Nevertheless, the shape provided by the stress isocontours does not capture the experimentally observed debonding zone, overestimating the debonding area whatever the brittleness number. This corroborates the fact that shapes based on stress isocontours are not optimal for the configuration studied, while not providing the optimum CC solution in terms of debonding shape. Similar observations are obtained for sample 2.

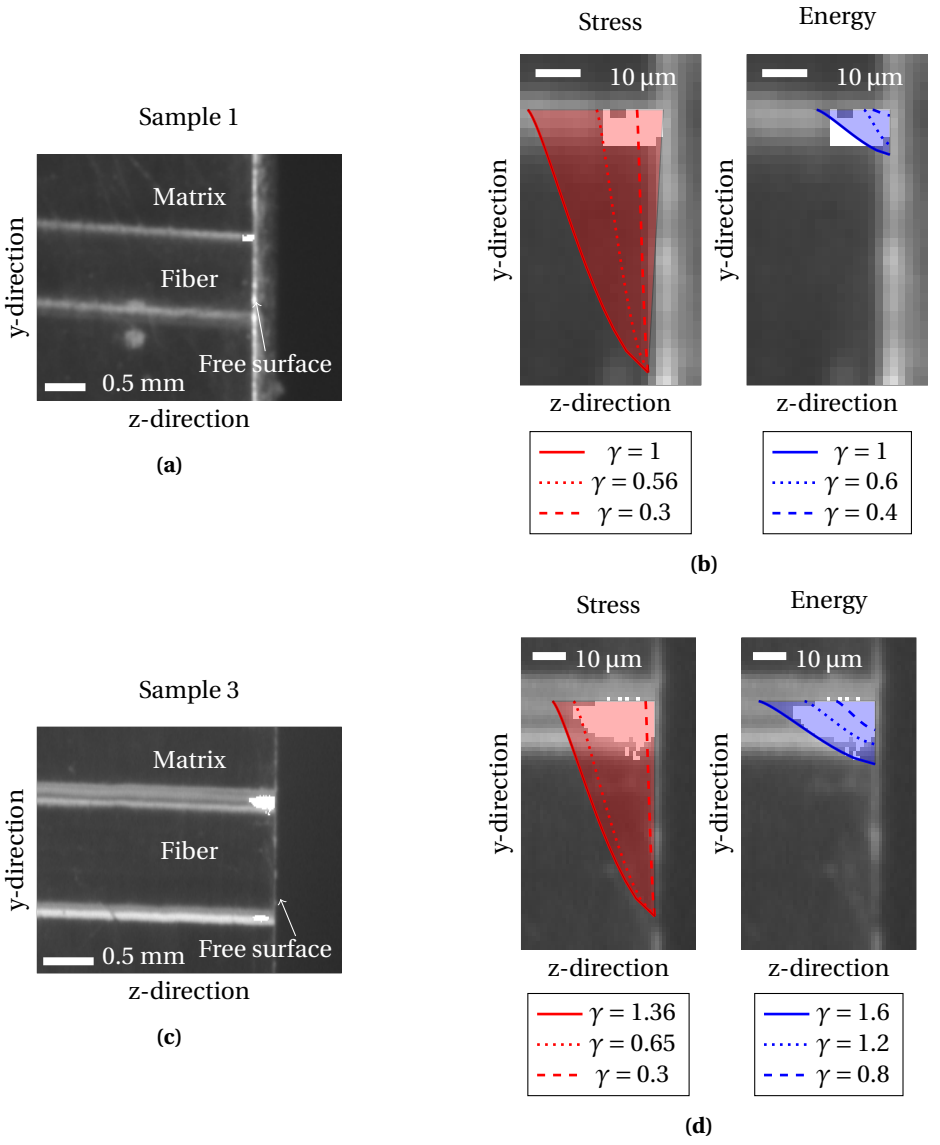

Figure 16. (a) Side view of the debonding just after debonding initiation. The debonded area is highlighted using a threshold and the white pixels. (b) Debonding shapes obtained with the CC and several brittleness numbers for both stress-based and energy-based shapes, corresponding to the red and blue shaded areas, superimposed on the side view.

4. Inverse identification of the interface fracture properties

The couples of tensile strength and critical ERR in mode I identified leading to equivalent remote stress (σ^{∞}) to the experimental one can be identified. The identification is made on the basis of the energy-based debonding shapes with $\lambda = 0.13$ and $\mu = 1$. Since the mode II has no influence at initiation, the λ and μ values are kept constants for the inverse identification as their influence is negligible. As a results, no shear fracture properties are identified. In addition, stress-based debonding shapes are also used for the inverse identification. Similarly, no shear

fracture properties can be identified, see [22]. Once the range of fracture properties are identified, additional restrictions can be applied to the range of properties identified on the basis of the geometrical parameters obtained experimentally, whose values are given in Table 2, and shown in Figure 16. The initiation surface provided by the CC can be either smaller than or equal to the arrest surface observed experimentally, as unstable debonding propagation can occur, see Section 3.2. The initiation surface reverts to the arrest surface when initiation is driven by the maximum of $G_{\text{inc}}/\overline{G_{\text{c}}}$. However, the energy-based debonding shapes yield $G_{\text{inc}}/\overline{G_{\text{c}}}$ that increases monotonically for the brittleness numbers identified so that no stable debonding can occur after initiation, see Dormieux et al. [26] or Girard et al. [16] for the determination of the crack initiation surfaces bounds. Similarly, when the CC solution is given by the intersection of both stress and energy conditions, further debonding propagation takes place after initiation. Therefore, without the use of a high-speed camera, the experimentally observed debonding surface after initiation actually corresponds to the arrest surface that has potentially already propagated. The geometrical parameters shown in Table 2 therefore serve as an upper limit to those obtained using the CC and therefore allow the identified couples of fracture properties to be restricted, as explained in Section 3.6. It is worth recalling that, except for the debonding opening, the determination of the debonding angle and length is limited by the pixel size (see [23]). The results derived from these two quantities may therefore be underestimated as sub-pixel phenomena may have occurred. Consequently, the maximum uncertainties in the calculation of the debonding opening is considered for the restriction of the identified fracture properties. The restricted identified properties are summarized in Table 3.

Table 3. Interface fracture properties identified for sample 1, 2 and 3 and a μ ratio of 1 and $\lambda = 0.13$.

	Sample 1	
σ^{∞} [MPa]	7.25 ± 0.04	
	Stress-based	Energy-based
γ	0.3 - 0.56	0.3 - 0.60
σ_{c} [MPa]	11.9 - 16.8	13.0 - 20.7
G_{IC} [J/m^2]	2.7 - 4.2	3.9 - 5.8
	Sample 2	
σ^{∞} [MPa]	8.03 ± 0.04	
	Stress-based	Energy-based
γ	0.3 - 0.5	0.3 - 0.74
σ_{c} [MPa]	13.9 - 18.6	12.4 - 22.9
G_{IC} [J/m^2]	3.3 - 4.9	4.8 - 8.2
	Sample 3	
σ^{∞} [MPa]	10.04 ± 0.04	
	Stress-based	Energy-based
γ	0.3 - 0.65	0.3 - 1.16
σ_{c} [MPa]	14.8 - 23.3	11.1 - 29.8
G_{IC} [J/m^2]	5.2 - 8.9	7.6 - 15.8

The debonding angle is not taken into account for restrictions applied to properties identified with the stress-based shapes. Overall, similar strength ranges are identified between the stress-based and energy-based shapes, regardless of the sample, in contrast to the critical ERR in mode I. Smaller critical ERR are identified using stress-based shapes due to less favorable energy

conditions. The fracture properties identified are in line with those identified in [16], although the epoxy system and glass fiber used are different.

5. Conclusion

The stress-based or energy-based debonding shapes are used to assess the fiber-matrix debonding initiation shape using the CC on an epoxy single glass fiber specimen under transverse tension. Energy-based shapes require additional effort to be determined because they require all possible shape configurations to be compared. On the basis of experimental observation, restrictions are made about the initiation location and the shape description. A power-law with an exponent of 1.5 is found to be optimal regardless of the critical ERR in mode II. Overall, the critical ERR in mode II has a negligible influence on the magnitude of the IERR to critical ERR ratio. The predicted debonding shape results in a smaller angle with larger length with increasing critical ERR in mode II, due to increased mode mixity in the vicinity of the fiber equator.

Energy-based shapes provide the optimal solution regardless of the brittleness number. The stress-based shapes overestimate the optimal CC solution by up to 15% for either small ($\gamma < 1$) or large ($\gamma > 6$) brittleness numbers. Larger differences, up to 30%, are encountered for intermediate brittleness numbers ($1 < \gamma < 6$). The energy condition causes this difference, the latter being less favorable using stress-based shapes, especially for intermediate brittleness numbers, where the energy condition triggers the CC solution. Energy-based debonding shapes provide a debonding topology consistent with the experimental observations, predicting the length, angle and the opening of the debonding compatible with those measured experimentally. Stress-based shapes are unable to provide an accurate shape with respect to experimental observation. It should be noted that the results obtained depend on the configuration studied (e.g., geometry, materials, boundary conditions). Therefore, the approach presented must be reproduced in each configuration in order to determine whether stress-based or energy-based shapes are optimal. In addition, the determination of energy-based shapes must be simplified using mathematical expressions, as their calculation is computationally expensive. Additionally, the debonding surface predicted by the CC corresponds to the initiation surface that is likely to propagate after initiation to the arrest surface. Further study of debonding propagation would be required, which could be approximated using an algorithm that iteratively varies the debonding front to obtain a constant stress intensify factor at the front for different increasing debonding surfaces.

Inverse identification is carried out on the basis of the stress-based and energy-based debonding shapes. Only the opening fracture properties are identified, since shear fracture properties slightly influence the CC solution for small surface such as the ones observed experimentally. The two approaches give similar fracture properties in terms of tensile strength, while the difference becomes more pronounced in terms of critical ERR. Admissible tensile strengths ranging from 11 to 30 MPa and a mode I critical ERR of 4 to 16 J/m^2 are identified with the energy-based debonding shapes for the three samples. Further refinement of the interface fracture properties range could be obtained by determining the critical ERR based on the debonding propagation stage.

Dedication

The manuscript was written through contributions of all authors. All authors have given approval to the final version of the manuscript.

Declaration of interests

The authors do not work for, advise, own shares in, or receive funds from any organization that could benefit from this article, and have declared no affiliations other than their research organizations.

References

[1] D. Leguillon, "Strength or toughness? A criterion for crack onset at a notch", *Eur. J. Mech. A Solids* **21** (2002), pp. 61–72.

[2] A. Doitrand, T. Duminy, H. Girard and X. Chen, "A review of the coupled criterion", *J. Theor. Comput. Appl. Mech.* (2024), article no. 11072.

[3] A. Doitrand, R. Henry, H. Saad, S. Deville and S. Meille, "Determination of interface fracture properties by micro- and macro-scale experiments in nacre-like alumina", *J. Mech. Phys. Solids* **145** (2020), article no. 104143.

[4] G. I. Barenblatt, "The formation of equilibrium cracks during brittle fracture. General ideas and hypotheses. Axially-symmetric cracks", *J. Appl. Math. Mech.* **23** (1959), no. 3, pp. 622–636.

[5] D. S. Dugdale, "Yielding of steel sheets containing slits", *J. Mech. Phys. Solids* **8** (1960), no. 2, pp. 100–104.

[6] B. Bourdin, G. A. Francfort and J.-J. Marigo, "Numerical experiments in revisited brittle fracture", *J. Mech. Phys. Solids* **48** (2000), no. 4, pp. 797–826.

[7] D. Leguillon, M. C. Lafarie-Frenot, Y. Pannier and E. Martin, "Prediction of the surface cracking pattern of an oxidized polymer induced by residual and bending stresses", *Int. J. Solids Struct.* **91** (2016), pp. 89–101.

[8] D. Leguillon, "An attempt to extend the 2D coupled criterion for crack nucleation in brittle materials to the 3D case", *Theor. Appl. Fract. Mech.* **74** (2014), pp. 7–17.

[9] A. Doitrand and D. Leguillon, "3D application of the coupled criterion to crack initiation prediction in epoxy/aluminum specimens under four point bending", *Int. J. Solids Struct.* **143** (2018), pp. 175–182.

[10] B. Mittelman and Z. Yosibash, "Energy release rate cannot predict crack initiation orientation in domains with a sharp V-notch under mode III loading", *Eng. Fract. Mech.* **141** (2015), pp. 230–241.

[11] Z. Yosibash and B. Mittelman, "A 3-D failure initiation criterion from a sharp V-notch edge in elastic brittle structures", *Eur. J. Mech. A Solids* **60** (2016), pp. 70–94.

[12] T. Duminy, R. Henry, J. Adrien, A. Doitrand and S. Meille, "Anisotropic fracture in nacre-like alumina", *Theor. Appl. Fract. Mech.* **123** (2023), article no. 103710.

[13] V. Mantič, "Interface crack onset at a circular cylindrical inclusion under a remote transverse tension. Application of a coupled stress and energy criterion", *Int. J. Solids Struct.* **46** (2009), no. 6, pp. 1287–1304.

[14] A. Doitrand, C. Fagiano, N. Carrère, V. Chiaruttini and M. Hirsekorn, "Damage onset modeling in woven composites based on a coupled stress and energy criterion", *Eng. Fract. Mech.* **169** (2017), pp. 189–200.

[15] E. Martin, B. Poitou, D. Leguillon and J. M. Gatt, "Competition between deflection and penetration at an interface in the vicinity of a main crack", *Int. J. Fract.* **151** (2008), no. 2, pp. 247–268.

[16] H. Girard, A. Doitrand, B. Koohbor, R. G. Rinaldi, N. Godin, D. Long, J. Bikard and L. Trouillet-Fonti, "Numerical simulation of fiber-matrix debonding: inverse identification of interface properties", *Eng. Fract. Mech.* **286** (2023), article no. 109254.

[17] I. G. García, B. J. Carter, A. R. Ingraffea and V. Mantič, "A numerical study of transverse cracking in cross-ply laminates by 3D finite fracture mechanics", *Compos. B. Eng.* **95** (2016), pp. 475–487.

[18] R. Papšík, O. Ševeček, E. Martin and R. Bermejo, "Prediction of ring crack initiation in ceramics and glasses using a stress-energy fracture criterion", *J. Am. Ceram. Soc.* **106** (2023), no. 7, pp. 4329–4342.

[19] R. Papšík, O. Ševeček, A.-K. Hofer, I. Kraleva, J. Kreith and R. Bermejo, "Prediction of edge and tunnelling crack formation in layered ceramics using a stress-energy fracture criterion", *J. Eur. Ceram. Soc.* **43** (2023), no. 7, pp. 2928–2934.

[20] H. Girard, A. Doitrand, B. Koohbor, R. G. Rinaldi, N. Godin, D. Long and J. Bikard, "Influence of nearby fiber on fiber-matrix debonding: Coupled Criterion prediction and debonding shape determination", *J. Mech. Phys. Solids* **183** (2024), article no. 105498.

[21] M. Burhan, T. Scalici, Z. Ullah, Z. Kazancı and G. Catalanotti, "A three-dimensional Finite Fracture Mechanics model to predict free edge delamination in angle-ply laminates", *Eng. Fract. Mech.* **306** (2024), article no. 110156.

[22] H. Girard, A. Doitrand, B. Koohbor, R. G. Rinaldi, N. Godin and J. Bikard, "Comparison between 2D and 3D fiber-matrix debonding simulation for inverse identification of interface fracture properties", *J. Theor. Comput. Appl. Mech.* (2025), article no. 12997 (21 pages).

[23] K. Z. Uddin, H. Girard, N. B. Mennie, A. Doitrand and B. Koohbor, "Simultaneous measurement of fiber-matrix interface debonding and tunneling using a dual-vision experimental setup", *Exp. Mech.* **64** (2024), no. 9, pp. 1497–1511.

[24] H. Girard, B. Koohbor, A. Doitrand and R. Livingston, "Experimental characterization of in-plane debonding at fiber-matrix interface using single glass macro fiber samples", *Compos. A. Appl. Sci. Manuf.* **171** (2023), article no. 107573.

[25] B. Yu, R. S. Bradley, C. Soutis, P. J. Hogg and P. J. Withers, "2D and 3D imaging of fatigue failure mechanisms of 3D woven composites", *Compos. A. Appl. Sci. Manuf.* **77** (2015), pp. 37–49.

[26] L. Dormieux, E. Lemarchand, L. Jeannin and D. Kondo, "Some remarks concerning the nucleation and initiation lengths of fractures in brittle materials in the light of Dominique Leguillon's energy criterion", *C. R. Méc.* **353** (2025), no. G1, pp. 601–614.

[27] M. T. Aranda and D. Leguillon, "Prediction of failure of hybrid composites with ultra-thin carbon/epoxy layers using the Coupled Criterion", *Eng. Fract. Mech.* **281** (2023), article no. 109053.

[28] A. Doitrand, G. Molnár, D. Leguillon, E. Martin and N. Carrère, "Dynamic crack initiation assessment with the coupled criterion", *Eur. J. Mech. A Solids* **93** (2022), article no. 104483.

[29] X. Chen, A. Doitrand, N. Godin and C. Fusco, "Crack initiation in PMMA plates with circular holes considering kinetic energy and nonlinear elastic material behavior", *Theor. Appl. Fract. Mech.* **124** (2023), article no. 103783.

[30] J. W. Hutchinson and Z. Suo, "Mixed mode cracking in layered materials", in *Advances in Applied Mechanics, vol. 29* (J. W. Hutchinson and T. Y. Wu, eds.), Advances in Applied Mechanics, vol. 29, Elsevier, 1991, pp. 63–191.

ACADÉMIE DES SCIENCES
INSTITUT DE FRANCE

Comptes Rendus. Mécanique
2025, Vol. 353, p. 1365-1383
https://doi.org/10.5802/crmeca.319

Research article

Evaluation of the incremental ERR in interface cracks with frictional contact and its application in the coupled criterion of finite fracture mechanics

Enrique Graciani [a] **and Vladislav Mantič** [*, a]

[a] Grupo de Elasticidad y Resistencia de Materiales, Escuela Técnica Superior de Ingeniería, Universidad de Sevilla, Camino de los Descubrimientos s/n, 41092 Sevilla, Spain

E-mails: egraciani@us.es, mantic@us.es

This article is dedicated to the memory of Dr. Dominique Leguillon

Abstract. A crack located in a straight and perfectly bonded interface between dissimilar isotropic linear elastic materials with a frictional contact zone adjacent to the crack tip is considered under plane strain conditions. Assuming the Coulomb friction law, the crack-tip stress singularity in such a crack is weaker than the classical square-root singularity. The main difficulty in predicting propagation of such an interface crack is that the Energy Release Rate (ERR) is zero, which is a direct consequence of this weak stress singularity at the crack tip. Therefore, the Griffith fracture criterion, which assumes infinitesimal crack advances, cannot be applied in this case. To overcome this problem a new approach to predict the propagation of an interface crack with a frictional contact zone at the crack tip, based on the Coupled stress and energy Criterion (CC) of Finite Fracture Mechanics (FFM), is proposed and analyzed. In contrast to previous approaches, the critical finite crack advance Δa_c is determined by the CC as a structural parameter given by the overall problem configuration. Two methods for calculating the incremental ERR $G_{II}(\Delta a)$ are considered which differ in the treatment of the frictional energy dissipated along the crack advance Δa. Closed-form expressions for $G_{II}(\Delta a)$ are derived for sufficiently large interface cracks when the most singular term of the asymptotic expansion of the elastic solution at the crack tip is dominant along the path of crack advance Δa before the crack propagation occurs. In this case, closed-form expressions for the critical crack advance Δa_c and the critical stress intensity factor K_{IIc} are derived.

Keywords. Interface crack, Comninou contact model, Coulomb friction law, weak singularity, energy release rate, Irwin integral, VCCT.

Funding. The research was conducted with the support of the Spanish Ministry of Science, Innovation and Universities, Agencia Estatal de Investigación, and European Regional Development Fund: PID2021-123325OB-I00 and PID2021-126279OB-I00.

Manuscript received 18 December 2024, revised 29 July 2025, accepted 3 August 2025.

* Corresponding author

1. Introduction

Interface cracks are present in many types of heterogeneous materials and structural elements, such as composites, multilayers, and polycrystals (e.g., metals, ceramics, rocks, ice, and solar cells), at different scales, from nanoscale to macroscale. Interface cracks in laminates and multilayers are commonly referred to as delaminations, and in polycrystals as intergranular fractures. As follows from the seminal contributions to the theory of interface cracks by Comninou and co-workers [1–4], there is often a relevant contact zone adjacent to an interface crack tip. Such configurations are usually analyzed by means of the so-called contact model of interface cracks, contrary to the widely used open model of interface cracks introduced by Williams [5], and further developed in [6–11] among others. It should be noted that the crack tip solution of the open model has a very peculiar oscillatory character associated with the complex singularity exponent λ for non-zero values of the Dundurs bimaterial parameter $\beta \neq 0$, i.e. for dissimilar materials, with an infinite number of traction oscillations and an infinite number of overlapping zones very near the crack tip. For a comprehensive review of both the contact and open models of interface cracks, see [12–16]. Recall that in all these works a perfectly bonded interface is considered, i.e., the traction equilibrium and displacement compatibility are fulfilled along the undamaged interface part. The same hypothesis is considered in the present work.

In many engineering problems the contact zone adjacent to the interface crack tip is negligibly small, so the Small-Scale Contact (SSC) assumption proposed by Rice [9] is adequate, allowing to apply the open model of interface cracks, as comprehensively studied by Hutchinson and Suo [10] for isotropic bimaterials and Banks-Sills [17] for anisotropic bimaterials. However, there are also many practical applications where the size of the near-tip contact zone is relevant in comparison with some characteristic length of the problem, e.g., the interface crack size or the adjacent lamina thickness, and the SSC hypothesis is not valid, so the Comninou contact model of interface cracks must be applied.

In the frictionless case, see Leblond [18] for a review of this problem, the size of the contact zone adjacent to the crack tip can be estimated quite accurately as shown in [12,19,20].

In the friction case, frictional sliding takes place in the near-tip contact zone, which leads to a specific crack tip solution studied for the first time by Comninou [2] for isotropic bimaterials, considering the Coulomb law of friction. See [4,16,21–36], for subsequent studies on various aspects of this problem. A remarkable feature of this interface crack tip solution with frictional sliding at the crack tip is that, for dissimilar materials with a nonzero value of the Dundurs parameter $\beta \neq 0$, the stress singularity is weaker than that appearing in a classical crack in a homogeneous material, as shown by Comninou [2] for a stationary crack under monotonic loading, and in the general case of an interface crack propagating quasi-statically by Audoly [27]. See also [26,35,36], for an analysis of interface cracks in anisotropic bimaterials. This is consistent with the physical intuition that friction can only make the stress state at the crack tip less severe, i.e. less singular. Thus, the singularity exponent λ for an interface crack between dissimilar materials with a sliding frictional contact zone at the crack tip is greater than 0.5, $0.5 < \lambda < 1$, whereas $\lambda = 0.5$ for a crack in a homogeneous material or an interface crack between similar materials with $\beta = 0$. Following [37] we will refer to this kind of stress singularity as weak singularity.

A fundamental consequence of this weak stress singularity in frictional interface cracks is that the Energy Release Rate (ERR) vanishes for such cracks. Considering the two basic options for computing ERR, either the Irwin [38] crack closure integral to compute the incremental ERR $G(\Delta a)$ due to a small crack advance $\Delta a > 0$, or the Rice[39] J-Integral along a small circular path of radius $\delta > 0$ enclosing the crack tip, both lead to essentially the same conclusion, namely, the

vanishing incremental ERR [24,25]

$$\lim_{\Delta a \to 0} G(\Delta a) = 0, \tag{1}$$

and the vanishing J-integral, which is path-dependent due to the frictional dissipation in the contact zone [21,22,27–29],

$$\lim_{\delta \to 0} J(\delta) = 0. \tag{2}$$

In addition, Leblond and Frelat [30] showed that the Stress Intensity Factors (SIFs) tend to zero for vanishing extension of a kink crack from such a frictional interface crack.

These observations raise the fundamental question of how to predict the propagation of such cracks and indeed how such interface cracks can propagate, see [21,22,24,25,28,30]. In the past, several proposals have been introduced to address this issue by establishing a suitable fracture criterion. Deng [22], in view of the vanishing J-integral with decreasing radius of the integration path $\delta \to 0$, suggested that the SIF K_{II} should be used instead as a better measure of the fracture driving force.

Sun and Qian [24] and Qian and Sun [25] considered the released energy due to a fixed finite crack extension Δa in their crack closure integral. A similar assumption of a fixed crack extension was made by Graciani et al. [33], although a different approach was used for the crack closure integral computation. In fact, these works [24,25,33] are related to the so-called Theory of Critical Distances (TCD) [40], which could also be applied to assess the initiation of propagation of such a frictional interface crack, although to the best of the authors' knowledge, no work has been reported in the literature attempting this. Audoly [28] proposed to use the $J(\delta)$-integral for a usually very small Barenblatt's [41] length δ_{c}. However, the meaning of using $J(\delta_{\mathrm{c}})$ is not clear as it represents the dissipation due to the frictional sliding behind the crack tip along the a priori existing crack faces (extrinsic toughness) and does not include the energy available for breaking interface bonds in front of the crack tip (intrinsic toughness).

Another widely developed and thoroughly studied way to overcome this difficulty is to consider an imperfect interface with a cohesive constitutive law [42–49], assuming a gradual increase of the friction effect with the gradual increase of the interface damage. See [50], for a review of coupling Cohesive Zone Models (CZM) and frictional contact.

Focusing hereinafter on perfectly bonded interfaces, the key observation regarding the J-integral is that, considering an infinitesimal growth of a frictional interface crack between dissimilar materials ($\beta \neq 0$), the energy flowing into the crack tip region circumvented by the integration path is completely consumed by the frictional dissipation along the parts of crack faces inside this crack tip region. Thus, such J-integral is path independent assuming fixed endpoints of the integration path, cf. [31,51]. In view of the above, we can conclude that an infinitesimal growth of such interface crack with frictional sliding contact zone adjacent to the crack tip, and thus with the vanishing ERR, $G = 0$, is not possible.

As mentioned above, by relaxing the hypothesis of classical fracture mechanics of an infinitesimal crack growth by allowing finite crack advances Δa, and calculating the so-called incremental ERR $G(\Delta a)$, makes it possible to avoid the above difficulty associated with the null ERR resulting from an infinitesimal advance of such frictional interface crack in (1). Therefore, the aim of the present article is to introduce some new ideas by further developing the original proposal of a finite crack extension Δa by Sun and Qian [24], see also Graciani et al. [33]. The main concept is based on:

(1) Considering a finite crack advance, instead of the infinitesimal crack advance assumed in the classical Linear Elastic Fracture Mechanics (LEFM), as Hashin [52] proposed in the framework of Finite Fracture Mechanics (FFM), see also [24,33].

(2) The Coupled Criterion (CC), coupling the classical stress criterion (in terms of the interface shear strength τ_c) and the incremental energy criteria (in terms of the fracture energy in Mode II G_{IIc}) in the framework of FFM, proposed by Leguillon [53] and later by Cornetti et al. [54], see Weissgraeber et al. [55] and Doitrand et al. [56], for a review of CC-FFM. Thus, only finite crack extensions with sufficiently high stresses acting along the path of this extension are considered when looking for the minimum load fulfilling both stress and incremental energy criteria. Thus, the length of such crack extension becomes a structural parameter, a function of the whole problem configuration, instead of being fixed as considered in previous works [24,33].

Noteworthy, the present work differs from the first application of CC-FFM to the propagation of interface cracks, in mixed mode and with a non-zero Dundurs parameter $\beta \neq 0$, developed by Mantič [57], because in that work the open model of interface cracks was considered, with an oscillating singularity associated with a complex singularity exponent λ.

In Section 2, the most singular term in the asymptotic expansion of the crack tip solution is analyzed. Several approaches to compute the incremental ERR are presented and compared in Section 3. Section 4 discusses the application of the fracture criterion considering a finite crack extension and different methods for the incremental ERR calculation. The Coupled Criterion (CC) is used in Section 5 to predict the propagation of a frictional interface crack. Finally, some concluding remarks are made in Section 6.

2. Asymptotic solution in the vicinity of an interfacial crack tip with friction

Consider two isotropic and linearly elastic adherents perfectly bonded along a straight interface, except for a debonded region where an interface crack of length a is located. Assuming the plane-strain hypotheses, a 2D model can be used to study such configuration. For simplicity, unit thickness is assumed. Focusing on the right crack tip with a frictional sliding contact zone on the left and a perfectly bonded interface on the right, the Cartesian and polar coordinates systems, (x, y) and (r, θ), centered at this crack tip denoted as O, will be used as shown in Figure 1.

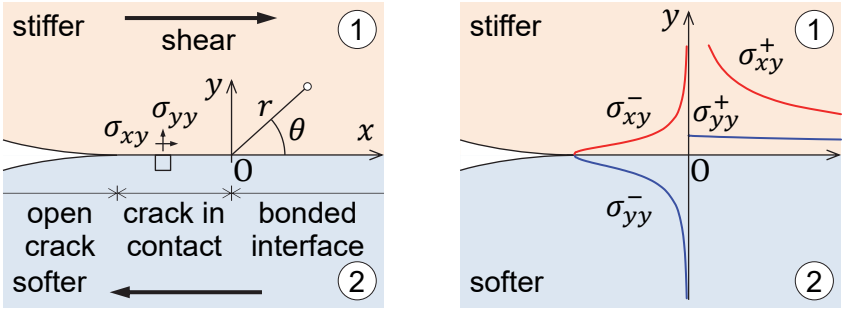

Figure 1. Near-tip elastic solution in the vicinity of a frictional interfacial crack tip.

Considering the polar coordinate system, Comninou [2] obtained the following asymptotic elastic solution in plane strain, for the interface tractions and the relative tangential displacement, in the vicinity of the frictional interfacial crack tip, for $r \to 0$,

$$\sigma_{xy}(r,0) = K_{\mathrm{II}}(2\pi r)^{(\lambda-1)}, \tag{3}$$

$$\sigma_{xy}(r,\pm\pi) = K_{\mathrm{II}}\cos[(1-\lambda)\pi](2\pi r)^{(\lambda-1)}, \tag{4}$$

$$\sigma_{yy}(r,\pm\pi) = -K_{\mathrm{II}}\beta\sin[(1-\lambda)\pi](2\pi r)^{(\lambda-1)}, \tag{5}$$

$$\Delta u_x(r) = K_{\mathrm{II}}\frac{\sin[(1-\lambda)\pi]}{\widehat{E}\lambda(2\pi)^{1-\lambda}}r^{\lambda} = u_x(r,\pi) - u_x(r,-\pi), \tag{6}$$

where K_{II} is the SIF. The real singularity exponent λ can be obtained from the interfacial friction coefficient f and the Dundurs bimaterial parameter β by

$$\lambda = 1 - \frac{1}{\pi}\operatorname{arccot}(f\beta). \tag{7}$$

The Dundurs bimaterial parameter β is defined as

$$\beta = \frac{\mu_1(\kappa_2-1) - \mu_2(\kappa_1-1)}{\mu_1(\kappa_2+1) + \mu_2(\kappa_1+1)}, \tag{8}$$

where μ_1 and μ_2 are the shear moduli of the materials, and the Kolosov constants κ_1 and κ_2 are defined by the Poisson ratios ν_1 and ν_2 as $\kappa_m = 3-4\nu_m$, with $m = 1,2$. Recall that $\beta = 0$ for identical or similar materials, and $\beta \neq 0$ for dissimilar materials.

The bimaterial stiffness parameter $\widehat{E}$ in (6) is defined as

$$\frac{1}{\widehat{E}} = \frac{1-\beta^2}{2}\left[\frac{1-\nu_1^2}{E_1} + \frac{1-\nu_2^2}{E_2}\right], \tag{9}$$

where E_1 and E_2 are the Young moduli of the materials.

As shown in [2,26,27,30] there is only one allowable direction of sliding near the crack tip given by the condition $f\beta > 0$. Then, the expression (7) leads to $0.5 < \lambda < 1$, which means that stress singularity at the crack tip is weak, i.e. weaker than in a classical crack in a homogeneous material, cf. [2,37]. Some of the consequences of this weak stress singularity were discussed in the introduction.

For the sake of simplicity and without loss of generality, it will be assumed that $\beta > 0$, which can be interpreted as the subscript 1 denoting the stiffer material and the subscript 2 denoting the softer material. Then, assuming this material definition, the friction coefficient should be positive $f > 0$. Notice that in this case $K_{\mathrm{II}} > 0$.

3. Incremental ERR in an interfacial crack with friction

In this section, the so-called incremental ERR associated to a finite crack extension Δa along the interface of two materials will be derived. The aim is to apply it in the prediction of such crack propagation by the CC-FFM. Let us consider Problems A and B, depicted in Figure 2, respectively, corresponding to an interface crack of length a, Problem A, and the same interface crack after a relatively small crack extension of length Δa has taken place, Problem B. For simplicity, a straight crack under plane strain conditions is considered as in the previous section.

As shown in Figure 2, a local Cartesian reference system located at the crack tip is employed in each problem, with the x coordinate oriented in the direction of crack propagation, to define the components of the stress tensor and the relative displacement, while a polar reference system, also located at the crack tip, will be employed to define the point locations. For the

sake of simplicity, the following notation will be used to denote the near-tip stresses and relative displacements, with $i, j = x, y$ and $0 < \rho < \Delta a$,

$$\sigma_{ij}^{\mathrm{A}+} = \sigma_{ij}^{\mathrm{A}}(\rho, 0), \quad \sigma_{ij}^{\mathrm{A}-} = \sigma_{ij}^{\mathrm{A}}(\Delta a - \rho, \pi), \tag{10}$$

$$\sigma_{ij}^{\mathrm{B}+} = \sigma_{ij}^{\mathrm{B}}(\rho, 0), \quad \sigma_{ij}^{\mathrm{B}-} = \sigma_{ij}^{\mathrm{B}}(\Delta a - \rho, \pi), \tag{11}$$

$$\Delta u_i^{\mathrm{B}} = u_i^{\mathrm{B}}(\Delta a - \rho, \pi) - u_i^{\mathrm{B}}(\Delta a - \rho, -\pi). \tag{12}$$

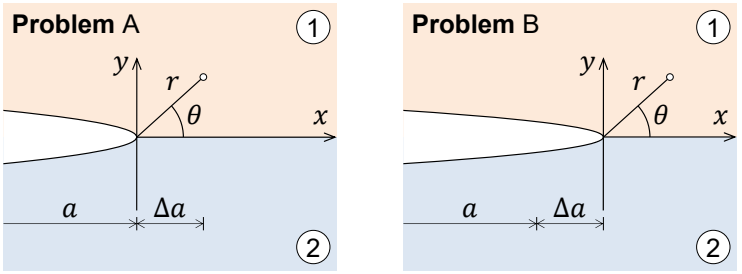

Figure 2. Interfacial crack and reference systems. Problem A before crack extension. Problem B after crack extension.

3.1. *Incremental ERR by Graciani et al. [33]*

By generalizing the Irwin crack closure integral procedure [38] to interface cracks with friction, cf. [51], the balance of mechanical energy leads to the following expression giving the energy available for crack propagation can be evaluated as

$$\widetilde{G}_{\mathrm{II}}(\Delta a)\Delta a = U^{\mathrm{A}} - U^{\mathrm{B}} + \Delta W_{\mathrm{e+f}}^{\mathrm{A}\to\mathrm{B}}, \tag{13}$$

where $\widetilde{G}_{\mathrm{II}}(\Delta a)$ is the incremental ERR in Mode II and U^{A} and U^{B} are the elastic strain energies per unit thickness, respectively, stored in the system in Problems A and B, and $\Delta W_{\mathrm{e+f}}^{\mathrm{A}\to\mathrm{B}}$ is the work per unit thickness carried out by the external forces, including the frictional forces along the (existing) crack faces, during crack propagation.

In this section $\widetilde{G}_{\mathrm{II}}(\Delta a)$ will be evaluated from the near-tip elastic solution, for an interface crack with frictional sliding contact zone, depicted in Figure 3, using a virtual crack propagation technique in presence of frictional sliding contact and a generalization of the Irwin crack closure integral [38], cf. [33]. Notice that the crack faces are in frictional contact during the virtual extension of the crack, thus only the tangential components of the virtual stresses contribute to the variation of the strain energy in the process. Therefore, only the shear component of the stresses and the relative sliding between crack faces are depicted in Figure 3. However, for the sake of clarity, the Mode II propagation has been represented in Mode I fashion.

Starting from the situation described in Problem A depicted in Figure 3, in a first stage, the interface ahead of the crack tip is virtually clamped along a certain length Δa.

Subsequently, in the second stage, the interface is externally cut, thus the interfacial stresses along the virtually clamped length denoted as $\sigma_{ij}^{\mathrm{A}+}$ are transformed into external stresses applied by the virtual grips. No energy variation is observed at these two stages since no change in the displacements takes place.

Finally, in the third stage, the virtual grips are released in a way that the applied stresses $\sigma_{ij}^{\mathrm{A}+}$ are linearly transformed into $\sigma_{ij}^{\mathrm{B}-}$, i.e., into the near-tip contact stresses corresponding to Problem B. Given that the final situation is identical to Problem B, the relative displacements at the virtual

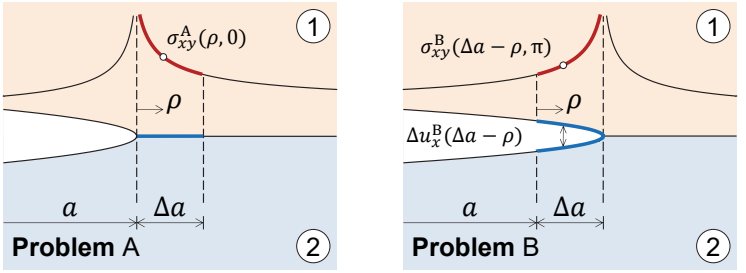

Figure 3. Local elastic solution along the near-tip interface region. Problem A before crack extension. Problem B after crack extension.

grips are given by Δu_i^{B}. Note that the receding nature of this frictional contact problem has been tacitly considered in the previous analysis. It is well known that in general in a receding contact problem its solution is a homogeneous function of degree 1 of a positive scalar factor governing some proportional boundary conditions, i.e., the problem solution behaves linearly with respect to such scalar factor.

The procedure described above permits evaluating the elastic strain energy stored in Problem B as:

$$U^{\mathrm{B}} = U^{\mathrm{A}} + \Delta W_{\mathrm{e+f}}^{\mathrm{A}\to\mathrm{B}} + \Delta W_{\mathrm{v}}^{\mathrm{A}\to\mathrm{B}}, \tag{14}$$

where $\Delta W_{\mathrm{v}}^{\mathrm{A}\to\mathrm{B}}$ is the (negative) work carried out by the virtual stresses during the virtual crack extension.

Introducing (14) into (13) gives the following expression for $\widetilde{G}_{\mathrm{II}}(\Delta a)$

$$\widetilde{G}_{\mathrm{II}}(\Delta a) = -\frac{1}{\Delta a}\Delta W_{\mathrm{v}}^{\mathrm{A}\to\mathrm{B}}. \tag{15}$$

The work per unit area $\mathscr{W}_{\mathrm{v}}^{\mathrm{A}\to\mathrm{B}}$ and the released energy per unit area $\widetilde{\mathscr{G}}_{\mathrm{II}}(\Delta a)$ at each interface point within the crack extension Δa are defined as

$$\Delta W_{\mathrm{v}}^{\mathrm{A}\to\mathrm{B}} = \int_0^{\Delta a} \mathscr{W}_{\mathrm{v}}^{\mathrm{A}\to\mathrm{B}}\,\mathrm{d}\rho, \tag{16}$$

$$\widetilde{G}_{\mathrm{II}}(\Delta a) = \frac{1}{\Delta a}\int_0^{\Delta a} \widetilde{\mathscr{G}}_{\mathrm{II}}(\Delta a)\,\mathrm{d}\rho. \tag{17}$$

In view of Figure 4, $\widetilde{\mathscr{G}}_{\mathrm{II}}(\Delta a)$ and $\mathscr{W}_{\mathrm{v}}^{\mathrm{A}\to\mathrm{B}}$ can be written as

$$\widetilde{\mathscr{G}}_{\mathrm{II}}(\Delta a) = -\mathscr{W}_{\mathrm{v}}^{\mathrm{A}\to\mathrm{B}} = \frac{1}{2}\left[\sigma_{xy}^{\mathrm{A}+} + \sigma_{xy}^{\mathrm{B}-}\right]\Delta u_x^{\mathrm{B}}, \tag{18}$$

and, therefore, the incremental ERR is given by

$$\widetilde{G}_{\mathrm{II}}(\Delta a) = -\frac{1}{\Delta a}\Delta W_{\mathrm{v}}^{\mathrm{A}\to\mathrm{B}} = \frac{1}{2\Delta a}\int_0^{\Delta a}\left[\sigma_{xy}^{\mathrm{A}+} + \sigma_{xy}^{\mathrm{B}-}\right]\Delta u_x^{\mathrm{B}}\,\mathrm{d}\rho. \tag{19}$$

If the crack extension Δa_0 is sufficiently small in comparison with the crack length, $\Delta a_0 \ll a$, the near tip solutions of Problem A and Problem B can be identified as

$$\sigma_{xy}^{+} \equiv \sigma_{xy}^{\mathrm{A}+}, \tag{20}$$

$$\sigma_{xy}^{-} \equiv \sigma_{xy}^{\mathrm{A}-} \cong \sigma_{xy}^{\mathrm{B}-}, \tag{21}$$

$$\Delta u_x \equiv u_x^{\mathrm{A}}\left(\Delta a_0 - \rho, \pi\right) - u_x^{\mathrm{A}}\left(\Delta a_0 - \rho, -\pi\right) \cong \Delta u_x^{\mathrm{B}}. \tag{22}$$

Consequently, $\widetilde{G}_{\mathrm{II}}(\Delta a_0)$ can be obtained from the solution of a single problem as

$$\widetilde{G}_{\mathrm{II}}(\Delta a_0) = \frac{1}{\Delta a_0}\int_0^{\Delta a_0} \widetilde{\mathscr{G}}_{\mathrm{II}}(\Delta a_0)\,\mathrm{d}\rho = \frac{1}{2\Delta a_0}\int_0^{\Delta a_0}\left[\sigma_{xy}^{+} + \sigma_{xy}^{-}\right]\Delta u_x\,\mathrm{d}\rho. \tag{23}$$

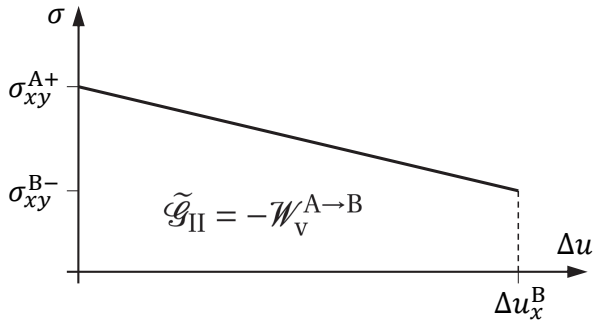

Figure 4. Work per unit area done by the virtual stresses at each interfacial point within the crack extension Δa.

Remark. In this section, a linear transition between the states A and B is considered, despite the generally non-linear character of a frictional contact problem. However, as will be demonstrated below, this linear transition can be considered as a valid approximation of the actual fracture process under the assumption that the interface crack is frictionally sliding in the same direction, as given by the Comninou contact model in the states A and B, in a neighbourhood of the interface crack tip, denoted as V, which is sufficiently large compared to the new crack segment Δa. In this situation, the frictional contact conditions along the interface contact zone in V become linear conditions. Consider a scalar parameter α changing from 0 to 1, $\alpha \in \langle 0,1 \rangle$, which can be used to define a convex combination of the displacement and stress solutions in these states as

$$u_i^\alpha = (1-\alpha)\, u_i^{\mathrm{A}} + \alpha\, u_i^{\mathrm{B}}, \tag{24}$$

$$\sigma_{ij}^\alpha = (1-\alpha)\sigma_{ij}^{\mathrm{A}} + \alpha\sigma_{ij}^{\mathrm{B}}. \tag{25}$$

A similar convex combination of the relative displacement along the new crack segment Δa can be defined as

$$\Delta u_i^\alpha = (1-\alpha)\Delta u_i^{\mathrm{A}} + \alpha\Delta u_i^{\mathrm{B}} = \alpha\Delta u_i^{\mathrm{B}}, \tag{26}$$

where in the last equation it has been considered that $\Delta u_i^{\mathrm{A}} = 0$ because of the perfect interface bonding along Δa in the state A.

Consider Δu_i^α as the imposed relative displacements along the new crack segment Δa, see Section 3.1 for details. Since the frictional sliding contact conditions are satisfied in V by both elastic solutions in the states A and B, these conditions are also satisfied by their convex combinations u_i^α and σ_{ij}^α due to the linear nature of these contact conditions in V. Applying the Saint-Venant principle to the self-balanced load changing with α along the relatively small segment Δa, we can assume that the stress solutions in the states A and B, as well as their convex combinations (σ_{ij}^{A}, σ_{ij}^{B} and σ_{ij}^α), are approximately the same along the outer boundary of V, which is sufficiently far from Δa. Therefore, these convex combinations are sufficiently accurate approximations of the exact solution of the full problem, for a given Δu_i^α, within V, especially near the crack tip. This seems to justify the linear transition assumed in this section. □

3.2. *Incremental ERR by Sun and Qian [24]*

Following the Irwin crack closure integral approach [38], Sun and Qian [24] proposed a slightly different approach to evaluate the incremental ERR associated to a small but finite characteristic interface crack extension with friction, denoted in the following as $\widehat{G}_{\rm II}(\Delta a)$, respecting the notation in [24]. The approach proposed in [24] is somewhat related to the analysis in [51] for frictional cracks in a homogeneous material. According to [24], see also [16], $\widehat{G}_{\rm II}(\Delta a_0)$ can be obtained as

$$\widehat{G}_{\rm II}(\Delta a) = \frac{1}{\Delta a}\int_0^{\Delta a} \widehat{\mathscr{G}}_{\rm II}(\Delta a)\,{\rm d}\rho = \frac{1}{2\Delta a}\int_0^{\Delta a} \left[\sigma_{xy}^{\rm A+} - \sigma_{xy}^{\rm B-}\right]\Delta u_x^{\rm B}\,{\rm d}\rho. \tag{27}$$

Sun and Qian [24] use an energy balance in which external forces and the frictional forces are considered separately

$$\widehat{G}_{\rm II}(\Delta a) = \frac{U^{\rm A} - U^{\rm B}}{\Delta a} + \frac{\Delta W_{\rm e}^{\rm A\to B}}{\Delta a} - G_{\rm d}(\Delta a), \tag{28}$$

where $U^{\rm A}$ and $U^{\rm B}$ are the elastic strain energies, respectively, stored in the system in Problems A and B, $\Delta W_{\rm e}^{\rm A\to B}$ is the work carried out by the external forces and $G_{\rm d}(\Delta a)$ is the dissipation energy rate, associated with the frictional sliding of the existing and newly created crack faces in contact, during crack propagation. The dissipation energy rate due to frictional sliding is given by

$$G_{\rm d}(\Delta a) = G_{\rm d}^{\rm N}(\Delta a) + G_{\rm d}^{\rm e}(\Delta a), \tag{29}$$

where

$$G_{\rm d}^{\rm N}(\Delta a) = \frac{1}{\Delta a}\int_0^{\Delta a} \mathscr{G}_{\rm d}^{\rm N}(\Delta a)\,{\rm d}\rho \tag{30}$$

is associated with the newly formed crack surface, and $G_{\rm d}^{\rm e}(\Delta a)$ is associated with the existing crack surfaces that are in contact. Therefore,

$$\Delta W_{\rm e+f}^{\rm A\to B} = \Delta W_{\rm e}^{\rm A\to B} - G_{\rm d}^{\rm e}(\Delta a)\,\Delta a. \tag{31}$$

and

$$\widetilde{G}_{\rm II}(\Delta a) = \widehat{G}_{\rm II}(\Delta a) + G_{\rm d}^{\rm N}(\Delta a). \tag{32}$$

Then, in each point of the newly formed crack surface it holds that

$$\mathscr{G}_{\rm d}^{\rm N}(\Delta a) = \sigma_{xy}^{\rm B-}\Delta u_x^{\rm B}, \tag{33}$$

as it is depicted in Figure 5, and

$$G_{\rm d}^{\rm N}(\Delta a) = \frac{1}{\Delta a}\int_0^{\Delta a} \sigma_{xy}^{\rm B-}\Delta u_x^{\rm B}\,{\rm d}\rho. \tag{34}$$

If the crack extension is sufficiently small in comparison with the crack length, $\Delta a_0 \ll a$, then in view of (20) and (21)

$$\widehat{G}_{\rm II}(\Delta a_0) = \frac{1}{\Delta a_0}\int_0^{\Delta a_0} \widehat{\mathscr{G}}_{\rm II}(\Delta a_0)\,{\rm d}\rho = \frac{1}{2\Delta a_0}\int_0^{\Delta a_0} \left[\sigma_{xy}^{+} - \sigma_{xy}^{-}\right]\Delta u_x\,{\rm d}\rho, \tag{35}$$

where σ_{xy}^{+}, σ_{xy}^{-} and Δu_x are defined in (20)–(22).

Remark. When analyzing the Finite Element (FE) procedure proposed in [16,24] for energy calculation, the following expressions can be inferred for the incremental ERR, and the dissipated energy rate due to friction along the newly formed crack advance,

$$\widehat{G}_{\rm II}^{\rm FE}(\Delta a) = \frac{1}{2\Delta a}\int_0^{\Delta a} \left[\sigma_{xy}^{\rm A+} + f\sigma_{yy}^{\rm A+}\right]\Delta u_x^{\rm B}\,{\rm d}\rho, \tag{36}$$

and

$$G_{\rm d}^{\rm N,FE}(\Delta a) = \frac{1}{2\Delta a}\int_0^{\Delta a} \left[-f\sigma_{yy}^{\rm A+} - f\sigma_{yy}^{\rm B-}\right]\Delta u_x^{\rm B}\,{\rm d}\rho = \frac{1}{2\Delta a}\int_0^{\Delta a} \left[-f\sigma_{yy}^{\rm A+} + \sigma_{xy}^{\rm B-}\right]\Delta u_x^{\rm B}\,{\rm d}\rho, \tag{37}$$

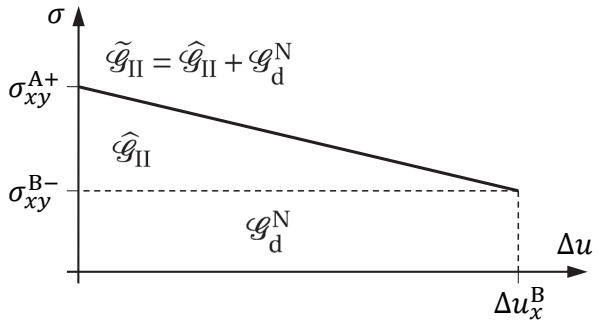

Figure 5. Energies released and dissipated at each interfacial point within the crack extension Δa.

where $f > 0$ is the friction coefficient, and compressive stresses $\sigma_{yy}^{\mathrm{A+}} < 0$ and $\sigma_{yy}^{\mathrm{B-}} < 0$ are assumed. Somewhat surprisingly, these expressions differ from those in (27) and (34), respectively. Nevertheless, it is easy to check that the relationship (32) remains valid, i.e., $\widetilde{G}_{\mathrm{II}}(\Delta a) = \widehat{G}_{\mathrm{II}}^{\mathrm{FE}}(\Delta a) + G_{\mathrm{d}}^{\mathrm{N,FE}}(\Delta a)$. Thus, the expressions (34) and (37) represent different estimations of the dissipation energy rate due to frictional sliding along the newly forming crack extension and, consequently, $\widehat{G}_{\mathrm{II}}(\Delta a)$ and $\widehat{G}_{\mathrm{II}}^{\mathrm{FE}}(\Delta a)$ represent different estimations of the incremental ERR.

The following interpretation to the expression of the incremental ERR in (36) can be given: $\sigma_{xy}^{\mathrm{A+}} + f\sigma_{yy}^{\mathrm{A+}}$ represents the elastic restoring shear traction before crack extension Δa, which decreases to zero during this crack extension. □

3.3. *Comparison of different approaches for large interface cracks and small crack advances*

For a sufficiently large crack in absence of friction, that is, when $f \to 0$ and $\Delta a_0 \ll a$, both $\widetilde{G}_{\mathrm{II}}(\Delta a_0)$ and $\widehat{G}_{\mathrm{II}}(\Delta a_0)$ tend to the Irwin classical expression of the incremental ERR [38]

$$G_{\mathrm{II}}(\Delta a_0) = \frac{1}{2\Delta a_0}\int_0^{\Delta a_0} \sigma_{xy}^{+}\Delta u_x \,\mathrm{d}\rho. \tag{38}$$

Notwithstanding, it must be noticed that the most significant effect of friction is not associated to the appearance of the frictional stresses σ_{xy}^{-} in (23) or (35), but to the fact that the asymptotic behavior of the crack tip solution changes, according to the expressions given in Section 2.

In the frictionless case the square root stress singularity with $\lambda = 0.5$ appears at the crack tip, and consequently $G_{\mathrm{II}}(\Delta a_0)$ tends to a constant positive value when crack extension vanishes (i.e., when $\Delta a_0 \to 0$). In the presence of friction, it holds that $0.5 < \lambda < 1$ and, consequently, both $\widetilde{G}_{\mathrm{II}}(\Delta a_0)$ and $\widehat{G}_{\mathrm{II}}(\Delta a_0)$ vanish when the crack extension vanishes.

Introducing the first term of Comninou's asymptotic solution (3)–(6) into the definitions of $\widetilde{G}_{\mathrm{II}}(\Delta a_0)$, $\widehat{G}_{\mathrm{II}}(\Delta a_0)$ and $G_{\mathrm{II}}(\Delta a_0)$ leads to the following asymptotic power-law expressions

$$\widetilde{G}_{\mathrm{II}}(\Delta a_0) = \widetilde{c}(\lambda)\frac{K_{\mathrm{II}}^2}{\widehat{E}}(\Delta a_0)^{(2\lambda-1)}. \tag{39}$$

$$\widehat{G}_{\mathrm{II}}(\Delta a_0) = \widehat{c}(\lambda)\frac{K_{\mathrm{II}}^2}{\widehat{E}}(\Delta a_0)^{(2\lambda-1)}, \tag{40}$$

$$G_{\mathrm{II}}(\Delta a_0) = \bar{c}(\lambda)\frac{K_{\mathrm{II}}^2}{\widehat{E}}(\Delta a_0)^{(2\lambda-1)}, \tag{41}$$

where

$$\widetilde{c}(\lambda) = \bar{c}(\lambda) + c_{\mathrm{B}}(\lambda), \tag{42}$$

$$\widehat{c}(\lambda) = \bar{c}(\lambda) - c_{\mathrm{B}}(\lambda), \tag{43}$$

and

$$\bar{c}(\lambda) = \frac{\sin[(1-\lambda)\pi]}{2\lambda(2\pi)^{2(1-\lambda)}}\left[\frac{\Gamma(\lambda)\Gamma(1+\lambda)}{\Gamma(1+2\lambda)}\right], \tag{44}$$

$$c_{\mathrm{B}}(\lambda) = \frac{\sin[(1-\lambda)\pi]}{2\lambda(2\pi)^{2(1-\lambda)}}\left[\frac{\cos[(1-\lambda)\pi]}{2\lambda}\right], \tag{45}$$

where $\Gamma(\cdot)$ is the gamma function. Notice that $(\Delta a_0)^{(2\lambda-1)} \to 0$ when $\Delta a_0 \to 0$ and $0.5 < \lambda$. The dimensionless auxiliary functions $\bar{c}(\lambda)$, $\widetilde{c}(\lambda)$, $\widehat{c}(\lambda)$, and $c_{\mathrm{B}}(\lambda)$ are represented in Figure 6.

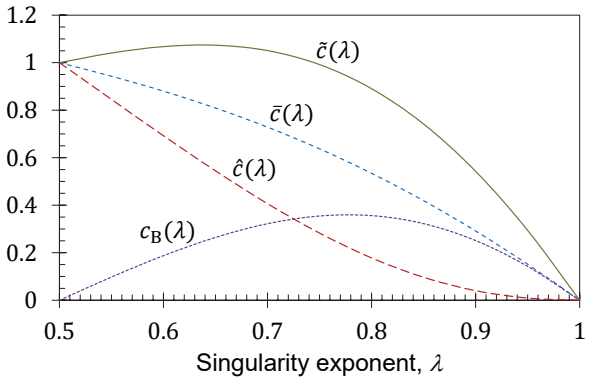

Figure 6. Coefficients $\bar{c}(\lambda)$, $\widehat{c}(\lambda)$, $\widetilde{c}(\lambda)$, and $c_{\mathrm{B}}(\lambda)$ used in the asymptotic expressions of $G_{\mathrm{II}}(\Delta a_0)$, $\widehat{G}_{\mathrm{II}}(\Delta a_0)$ and $\widetilde{G}_{\mathrm{II}}(\Delta a_0)$.

4. Evaluation of the incremental ERR for a finite crack extension

Due to the weak stress singularity at the frictional interface crack tip, when the crack extension vanishes, $\Delta a_0 \to 0$, the three estimations of the incremental ERR, $\widetilde{G}_{\mathrm{II}}(\Delta a_0)$, $\widehat{G}_{\mathrm{II}}(\Delta a_0)$ and $G_{\mathrm{II}}(\Delta a_0)$, presented in the previous sections vanish as well.

Since the incremental ERR is dependent on the crack extension, a characteristic finite crack extension Δa_{c} must be employed as discussed in Section 1. Depending on the approach employed for estimation of the incremental ERR, the following criteria may be used for assessing crack propagation

$$\widetilde{G}_{\mathrm{II}}(\Delta \widetilde{a}_{\mathrm{c}}) = \widetilde{G}_{\mathrm{c}}, \tag{46}$$

$$\widehat{G}_{\mathrm{II}}(\Delta \widehat{a}_{\mathrm{c}}) = \widehat{G}_{\mathrm{c}}, \tag{47}$$

$$G_{\mathrm{II}}\left(\Delta \bar{a}_{\mathrm{c}}\right) = \bar{G}_{\mathrm{c}}. \tag{48}$$

If Δa_{c} is sufficiently small in comparison with the crack length a, in view of the relations shown in (41)–(45), certain relations may be established between the different characteristic finite crack extensions $\Delta \widetilde{a}_{\mathrm{c}}$, $\Delta \widehat{a}_{\mathrm{c}}$ and $\Delta \bar{a}_{\mathrm{c}}$, if the critical ERRs (fracture energies) $\widetilde{G}_{\mathrm{c}}$, $\widehat{G}_{\mathrm{c}}$ and $\bar{G}_{\mathrm{c}}$, are considered equal to the critical ERR of the material G_{IIc}.

Conversely, if a characteristic finite crack extension is considered in the material and $\Delta\widetilde{a}_{\mathrm{c}}$, $\Delta\widehat{a}_{\mathrm{c}}$ and $\Delta\overline{a}_{\mathrm{c}}$ are defined equal to this characteristic finite crack extension, the expressions in (39)–(45) allow relationships to be established between $\widetilde{G}_{\mathrm{c}}$, $\widehat{G}_{\mathrm{c}}$ and $\overline{G}_{\mathrm{c}}$ which allow criteria defined in (46)–(48) to provide identical predictions for crack propagation.

5. Determination of the critical finite crack extension and the critical SIF using CC for large cracks

Although the use of a characteristic finite crack extension as a material parameter controlling crack propagation may have physical sense in some materials, cf. [40], the use of a critical interface strength τ_{c} and a critical Mode II strain energy release rate G_{IIc} are commonly employed in crack propagation criteria of closed cracks. This is the case, e.g., of CZMs [42–50].

The use of the Coupled stress and energy Criterion (CC) of the Finite Fracture Mechanics (FFM) proposed by Leguillon [53] and later by Cornetti et al. [54], allows establishing an unambiguous definition of the critical finite crack extension Δa_{c} as a structural parameter for a frictional interface crack.

If a pointwise stress criterion is used in the considered finite crack extension Δa_0, cf. [53], and the incremental ERR proposed in this paper, $\widetilde{G}_{\mathrm{II}}(\Delta a_0)$, defined in (23), is used for the energy criterion, the CC establishes that crack propagation will take place if the following inequalities are simultaneously fulfilled

$$\sigma^{\mathrm{A}}_{xy}(\rho,0) \geq \tau_{\mathrm{c}} \quad \text{for} \quad 0<\rho<\Delta a_0 \tag{49}$$

and

$$\widetilde{G}_{\mathrm{II}}(\Delta a_0) \geq G_{\mathrm{IIc}}. \tag{50}$$

If the first singular term of the near-tip asymptotic solution is dominant along the crack extension, both criteria can be written in terms of K_{II}, yielding

$$\sigma^{\mathrm{A}}_{xy}(\Delta a_0,0) = K_{\mathrm{II}}(2\pi\Delta a_0)^{(\lambda-1)} \geq \tau_{\mathrm{c}} \tag{51}$$

and

$$\widetilde{G}_{\mathrm{II}}(\Delta a_0) = \widetilde{c}(\lambda)\frac{K_{\mathrm{II}}^2}{\widehat{E}}(\Delta a_0)^{(2\lambda-1)} \geq G_{\mathrm{IIc}}, \tag{52}$$

where it has been considered that $\sigma^{\mathrm{A}}_{xy}(\rho,0)$ decreases when ρ increases.

The critical values of K_{II} and Δa_0, denoted as K_{IIc} and Δa_{c}, can be obtained from the solution of the system of equations

$$\sigma^{\mathrm{A}}_{xy}(\Delta\widetilde{a}_{\mathrm{c}},0) = \tau_{\mathrm{c}} \quad \text{and} \quad \widetilde{G}_{\mathrm{II}}(\Delta\widetilde{a}_{\mathrm{c}}) = G_{\mathrm{IIc}}, \tag{53}$$

which yields

$$\Delta\widetilde{a}_{\mathrm{c}} = \frac{(2\pi)^{2(\lambda-1)}}{\widetilde{c}(\lambda)}\frac{G_{\mathrm{IIc}}\widehat{E}}{\tau_{\mathrm{c}}^2} \tag{54}$$

and

$$\widetilde{K}_{\mathrm{IIc}} = (2\pi\Delta\widetilde{a}_{\mathrm{c}})^{(1-\lambda)}\tau_{\mathrm{c}}. \tag{55}$$

Thus, $\Delta\widetilde{a}_{\mathrm{c}}$ is a multiple of the Irwin length for interface cracks in shear $G_{\mathrm{IIc}}\widehat{E}/\tau_{\mathrm{c}}^2$.

The following non-dimensional variables can be defined using these critical values $\widetilde{K}_{\mathrm{IIc}}$ and $\Delta\widetilde{a}_{\mathrm{c}}$

$$\widetilde{K}^{\mathrm{n}}_{\mathrm{II}} = \frac{K_{\mathrm{II}}}{\widetilde{K}_{\mathrm{IIc}}} \quad \text{and} \quad \Delta\widetilde{a}^{\mathrm{n}}_0 = \frac{\Delta a_0}{\Delta\widetilde{a}_{\mathrm{c}}}, \tag{56}$$

which allows rewriting the CC in the following non-dimensional form, cf. [57]:

$$\widetilde{K}^{\mathrm{n}}_{\mathrm{II}} \geq \left(\Delta\widetilde{a}^{\mathrm{n}}_0\right)^{(1-\lambda)} \tag{57}$$

and

$$\widetilde{K}^{\mathrm{n}}_{\mathrm{II}} \geq \left(\Delta\widetilde{a}^{\mathrm{n}}_0\right)^{\left(\frac{1}{2}-\lambda\right)}. \tag{58}$$

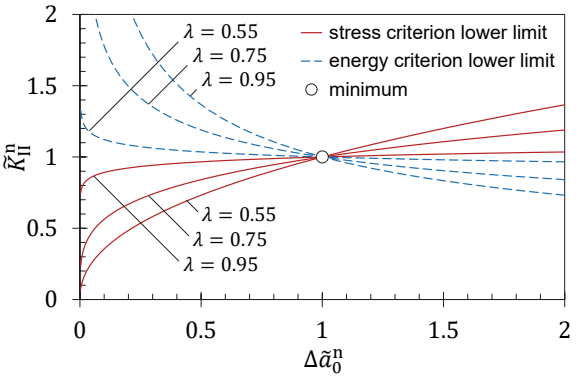

Figure 7. Representation of the non-dimensional form of the coupled stress and energy criterion (CC) for $0.5 < \lambda < 1$.

The non-dimensional form of the CC is depicted in Figure 7 for three different values of λ in the range $0.5 < \lambda < 1$. The lower limit curves of the stress criterion and the energy criterion represent the values of $\widetilde{K}_{\mathrm{II}}^{\mathrm{n}}$ and $\Delta\widetilde{a}_0^{\mathrm{n}}$ that respectively fulfil the equalities in (57) and (58). Consequently, for each value of λ, crack propagation would take place for $\widetilde{K}_{\mathrm{II}}^{\mathrm{n}}$ and $\Delta\widetilde{a}_0^{\mathrm{n}}$ pairs located above the corresponding curves of the stress and energy criteria.

Since, for all λ in the range $0.5 < \lambda < 1$, the stress criterion lower limit increases with $\Delta\widetilde{a}_0^{\mathrm{n}}$ and the energy criterion lower limit decreases with $\Delta\widetilde{a}_0^{\mathrm{n}}$, the minimum value of $\widetilde{K}_{\mathrm{II}}^{\mathrm{n}}$ for which crack propagation can take place is $\widetilde{K}_{\mathrm{II}}^{\mathrm{n}} = 1$ and the corresponding crack extension would be $\Delta\widetilde{a}_0^{\mathrm{n}} = 1$.

In other words, the minimum value of $\widetilde{K}_{\mathrm{II}}$ for which crack propagation can take place is $\widetilde{K}_{\mathrm{IIc}}$ and the corresponding crack extension would be $\Delta\widetilde{a}_{\mathrm{c}}$.

Notice that, in view of the evolution of the lower limit curves of the stress criterion and the energy criterion shown in Figure 7, for all λ in the range $0.5 < \lambda < 1$ the CC for a frictional crack can be written in the following pointwise stress criterion form

$$\sigma_{xy}^{\mathrm{A}}(\Delta\widetilde{a}_{\mathrm{c}}, 0) \geq \tau_{\mathrm{c}} \quad \text{with} \quad \Delta\widetilde{a}_{\mathrm{c}} = \frac{(2\pi)^{2(\lambda-1)}}{\widetilde{c}(\lambda)} \frac{G_{\mathrm{IIc}}\widehat{E}}{\tau_{\mathrm{c}}^2}. \tag{59}$$

Notice that, when $\lambda \to 1$, corresponding to $f \to +\infty$, it holds that $\widetilde{G}_{\mathrm{II}}(\Delta a_0) \to 0$, for a fixed Δa_0, and $\Delta\widetilde{a}_{\mathrm{c}} \to \infty$, and, consequently, crack propagation is not possible in that case.

For the opposite limit case, that is, for $\lambda = 0.5$, which corresponds either to a frictionless crack or to the case of similar materials with the Dundurs parameter $\beta = 0$, the lower limit curve of the energy criterion becomes a horizontal line, $\widetilde{K}_{\mathrm{II}}^{\mathrm{n}} = 1$, see Figure 8. Consequently, the minimum value of $\widetilde{K}_{\mathrm{II}}^{\mathrm{n}}$ for which crack propagation can take place is $\widetilde{K}_{\mathrm{II}}^{\mathrm{n}} = 1$ and the corresponding crack extension would be any $\Delta\widetilde{a}_0^{\mathrm{n}}$ value in the range $0 \leq \Delta\widetilde{a}_0^{\mathrm{n}} \leq 1$. In other words, if the energy criterion is fulfilled, infinitesimal or finite crack extensions can take place. The maximum extent of the crack extension is given by

$$\lambda = 0.5 \quad \Longrightarrow \quad \Delta\widetilde{a}_{\mathrm{c}} = \Delta a_{\mathrm{ch}} = \frac{1}{2\pi} \frac{G_{\mathrm{IIc}}\widehat{E}}{\tau_{\mathrm{c}}^2}. \tag{60}$$

Although the incremental ERR proposed in this paper, $\widetilde{G}_{\mathrm{II}}(\Delta a_0)$, has been used for the derivation of the CC for a frictional interface crack, analogous formulations can be obtained evaluating the incremental ERR using either $G_{\mathrm{II}}(\Delta a_0)$ or $\widehat{G}_{\mathrm{II}}(\Delta a_0)$, just by replacing coefficient $\widehat{c}(\lambda)$ by either $\overline{c}(\lambda)$ or $\widetilde{c}(\lambda)$, respectively. Conclusions obtained using $\widetilde{G}_{\mathrm{II}}(\Delta a_0)$ hold for the other approaches but yielding different critical values of K_{II} and Δa_0, namely $\overline{K}_{\mathrm{IIc}}$ and $\Delta\overline{a}_{\mathrm{c}}$, or $\widehat{K}_{\mathrm{IIc}}$ and $\Delta\widehat{a}_{\mathrm{c}}$, respectively.

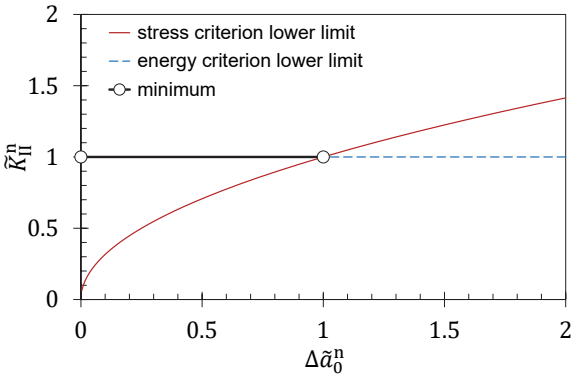

Figure 8. Representation of the non-dimensional form of the coupled stress and energy criterion (CC) for $\lambda = 0.5$.

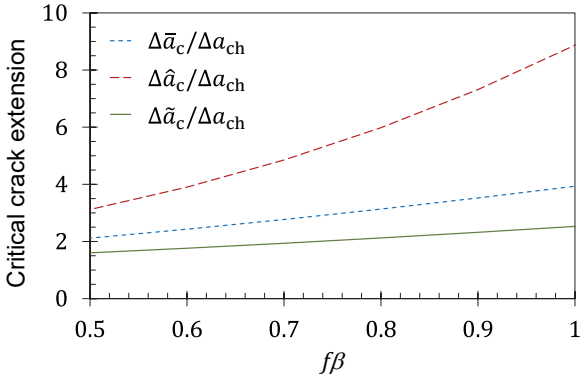

Figure 9. Critical crack extensions given by the different approaches for evaluating incremental ERR in the coupled stress and energy criterion (CC).

Critical crack extensions $\Delta\bar{a}_c$, $\Delta\hat{a}_c$ and $\Delta\tilde{a}_c$ are compared in Figure 9 assuming the same value of G_{IIc}, $\widehat{E}$ and τ_c for all three approaches. When $\lambda = 0.5$ ($f\beta = 0$) the three different critical crack extensions yield the same characteristic length Δa_{ch}.

Considering that the critical interface strength τ_c and the critical Mode II energy release rate G_{IIc} are material parameters, for sufficiently large cracks, criterion in (59) allows predicting crack growth, considering that $\widetilde{G}_{II}(\Delta\tilde{a}_c)$ is the incremental ERR associated with crack propagation. Analogous expressions can be easily obtained for predicting crack growth considering that either $G_{II}(\Delta\bar{a}_0)$ or $\widehat{G}_{II}(\Delta\hat{a}_c)$ are the incremental ERRs associated with crack propagation. A detailed comparison of the aforementioned approaches for determining the incremental ERR associated with a frictional interfacial crack propagation with experimental results or with numerical predictions obtained with different approaches lies beyond the scope of this work.

Nevertheless, Graciani et al. [33] used $\widetilde{G}_{II}(\Delta a_0)$, with a prescribed critical extension $\Delta a_0 = 1\mu m$, to obtain the friction coefficient and the critical Mode II ERR of glass fibre/matrix interface by the best fit between numerical predictions with boundary elements and experimental results of the single fibre fragmentation test, yielding $G_{IIc} = 12.12 J/m^2$ and $f = 1$. Using these values, crack propagation was simulated using a FE model with bilinear cohesive elements (with

$\tau_c = 110\,\text{MPa}$) and frictional contact along the fibre/matrix interface, yielding a remarkably good agreement. Introducing these fibre/matrix interfacial properties (along with the elastic properties of the materials given in [33]) into (54) gives a value of $\Delta\widetilde{a}_c = 1.16\mu\text{m}$. The good agreement between $\Delta\widetilde{a}_c$ and the prescribed critical extension Δa_0 used in [33] supports the use of FFM with the CC to assess frictional interfacial crack growth, using $\widetilde{G}_{II}(\Delta\widetilde{a}_c)$ to determine incremental ERR associated to crack propagation.

6. Concluding remarks

A few concluding remarks are given below to summarise and clarify the results presented and to offer new perspectives on the modelling of frictional interface crack propagation.

(1) A challenging problem of cracks with a relevant frictional contact zone near the crack tip propagating along a perfectly bonded interface between dissimilar linear elastic materials is addressed. The Coulomb friction law is considered in the contact zone between the cracks faces. Since the classical Griffith criterion, which assumes infinitesimal crack growth, cannot be applied to determine the load for which such crack will grow because a null ERR is always obtained, a novel approach using the Coupled Criterion (CC) of Finite Fracture Mechanics (FFM) [53–57] is developed to solve the problem and to determine the critical load associated with crack propagation. To this end, the incremental ERR $G_{II}(\Delta a)$ and the critical crack extension Δa_c associated with crack propagation are used.

Finite crack advances Δa are considered, resulting in nonzero incremental ERR values. To compute the incremental ERR, the main issue is to properly account for the energy dissipated by friction along the contact zone between the crack faces due to a finite crack advance Δa. Two approaches for computing the incremental ERR from the near-tip solution are considered. In the first one, proposed in [33], all the energy released along the segment Δa is taken into account in the evaluation of the incremental ERR denoted as $\widetilde{G}_{II}(\Delta a)$, while in the second one, previously proposed in [24], an estimate of the energy dissipated due to friction along Δa is excluded from the incremental ERR, thus resulting in a different estimation of the incremental ERR denoted as $\widehat{G}_{II}(\Delta a)$. A third option is also studied in which the incremental ERR $G_{II}(\Delta a)$ is calculated ignoring friction effects. The critical values of the incremental ERR and the associated critical crack extension are determined using the CC of FFM.

Special attention is paid to the case where the most singular term in the asymptotic series of the solution at the crack tip governs the elastic solution along the segment Δa before the crack advance. In this case, closed-form expressions for the incremental ERR, the critical crack advance Δa_c and the critical Stress Intensity Factor (SIF) K_{IIc} have been derived for the three aforementioned approaches, showing that the three approaches can be formulated in a unified form. A straightforward comparison of these three approaches is then given, leading to three different definitions of the apparent critical fracture energies $\widetilde{G}_c$, $\widehat{G}_c$ and $\overline{G}_c$, corresponding to the same critical fracture energy of the material G_{IIc}, which result in the same critical load associated with crack propagation obtained from the three approaches.

The limit cases of zero and infinite friction coefficient are briefly analyzed showing that, in the former case, the critical crack advance Δa_c is an upper limit for all possible crack advances, while, in the latter case, no crack advance is possible due to infinite frictional energy dissipation.

(2) Note that the three approaches introduced for calculating the incremental ERR in Mode II provide three different ways of defining the fracture toughness for frictional interface cracks G_{IIc}, each leading to a different value of G_{IIc}. Of the two possible basic dissipation mechanisms ahead of the crack tip — the energy spent in forming a new crack segment Δa and the energy spent in frictional sliding along this new crack segment — these approaches

consider the latter differently. In the first approach, no energy is spent in frictional sliding along Δa_c resulting in $\widetilde{G}_{IIc}$. In the second approach, the energy spent in frictional sliding remains constant as the relative tangential displacement increases, giving $\widehat{G}_{IIc}$. In the third approach, the energy spent in frictional sliding increases linearly with the relative tangential displacement, resulting in $\overline{G}_{IIc}$.

However, it has been shown that, under the assumption that the critical finite crack advance Δa_c is sufficiently small compared to other characteristic lengths in the problem, e.g., the crack length, so that the most singular term in the asymptotic expansion of the crack tip solution governs the solution in the neighbourhood of the crack tip of radius Δa_c, these three approaches are equivalent in the sense that, using the coherent values of G_{IIc} and incremental ERR, essentially the same predictions can be expected for the propagation of frictional interface crack.

Nevertheless, it would be worthwhile trying to discriminate between these approaches by comparing their predictions in situations where Δa_c is not small compared to other characteristic lengths of the problem and the friction coefficient can differ.

(3) The presented procedure is also well suited for computational modeling of stepwise propagation of frictional interface cracks as in each step of the computational process the present approach based on CC predicts a finite crack advance as a function of the overall problem configuration.

(4) The present approach could be applied to several experimental tests on both the macro and micro scales. Typical tests developed for the measurement of Mode II fracture toughness G_{IIc} of an interface in macroscopic specimens include Three-Point and Four-Point End-Notched-Flexure (3P- and 4P-ENF) [58,59]. For an analysis of the influence of friction on delamination propagation, see [60]. Single fibre tests developed to measure G_{IIc} of the fibre-matrix interface in microscopic specimens involving just one fibre. In the Single Fibre Fragmentation Test (SFFT), accounting for the effect of friction is crucial for an accurate measurement of G_{IIc}, as demonstrated in [33,61,62]. In the future, it would be interesting to monitor delamination propagation in 3P- or 4P-ENF tests using digital image correlation (DIC) to characterize the displacement field near the crack, detect the crack tip, and compute the critical SIF K_{IIc} at crack propagation.

(5) Although the present approach has been developed for isotropic materials, it could in principle also be used for anisotropic materials, by taking into account the results of the recent study of asymptotic solutions at the front of frictional interface cracks in anisotropic bimaterials under generalised plane strain in [35,36]. However, the present approach must be adapted to each specific configuration as described in [35,36]. This involves taking into account whether a plane of elastic symmetry in the bimaterial coincides with the interface plane or is perpendicular to the crack front.

Consider first the case of an orthotropic bimaterial with a plane of elastic symmetry coinciding with the interface plane, and another perpendicular to the crack front. In this case, the present approach can be applied quite straightforwardly by replacing the asymptotic solution in Section 2 by its orthotropic counterpart in [35,36].

However, adapting the present approach to more general configurations would be more involved, as it would need to consider the specific features of the asymptotic solution at the crack front, as described in [35,36]. For instance, in the case of a bimaterial with a single plane of elastic symmetry coinciding with the interface plane, the out-of-plane components of displacements and stresses must be considered as well. Considering the results in [35,36], we can conjecture that there will be a competition between two fracture modes: Mode *ii* the crack propagation by finite advances associated with a sliding direction corresponding to $\lambda > 0.5$, with zero ERR but positive incremental ERR (somewhat similar to Mode II in isotropic

or orthotropic bimaterials, but with different angle of sliding), and Mode *iii* an infinitesimal crack propagation associated with a sliding direction corresponding to $\lambda = 0.5$, with a positive ERR (somewhat similar to Mode III in isotropic or orthotropic bimaterials, but with different angle of sliding). A generalisation of the present approach could be used to compute the incremental ERR in the Mode *ii*. The overall problem configuration, mainly determined by the specimen geometry, the (direction of) applied loads and the material properties, would govern the above described competition.

Acknowledgments

This is an expanded version of the talk entitled "Evaluation of the energy release rate in interface cracks with friction: application to a single fibre test in composites", presented at the IUTAM 2012 Symposium Fracture Phenomena in Nature and Technology in Brescia, July 1–5, 2012. The authors thank Prof. Federico París (Universidad de Sevilla) for his motivation and support of this work. Stimulating discussions with Prof. Janis Varna (Luleå University of Technology) are gratefully acknowledged.

Declaration of interests

The authors do not work for, advise, own shares in, or receive funds from any organization that could benefit from this article, and have declared no affiliations other than their research organizations.

References

[1] M. Comninou, "The interface crack", *J. Appl. Mech.* **44** (1977), pp. 631–636.
[2] M. Comninou, "The interface crack with friction in the contact zone", *J. Appl. Mech.* **44** (1977), pp. 780–781.
[3] J. Dundurs and M. Comninou, "Some consequences of the inequality conditions in contact and crack problems", *J. Elasticity* **9** (1979), pp. 71–82.
[4] M. Comninou and J. Dundurs, "Effect of friction on the interface crack loaded in shear", *J. Elasticity* **10** (1980), pp. 203–212.
[5] M. L. Williams, "The stress around a fault of crack in dissimilar media", *Bull. Seism. Soc. Am.* **49** (1959), pp. 199–204.
[6] A. H. England, "A crack between dissimilar media", *J. Appl. Mech.* **32** (1965), pp. 400–402.
[7] J. R. Rice and G. C. Sih, "Plane problems of cracks in dissimilar media", *J. Appl. Mech.* **32** (1965), pp. 418–423.
[8] B. M. Malyshev and R. L. Salganik, "The strength of adhesive joints using the theory of cracks", *Int. J. Fract.* **1** (1965), pp. 114–128.
[9] J. R. Rice, "Elastic fracture mechanics concepts for interfacial cracks", *J. Appl. Mech.* **55** (1988), pp. 98–103.
[10] J. W. Hutchinson and Z. Suo, "Mixed mode cracking in layered materials", in *Advances in Applied Mechanics* (J. W. Hutchinson and T. Y. Wu, eds.), Advances in Applied Mechanics, vol. 29, Academic Press Inc., 1991, pp. 63–191.
[11] V. Mantič and F. París, "Relation between SIF and ERR based measures of fracture mode mixity in interface cracks", *Int. J. Fract.* **130** (2004), pp. 557–569.
[12] D. A. Hills and J. R. Barber, "Interface cracks", *Int. J. Mech. Sci.* **35** (1993), pp. 27–37.
[13] D. A. Hills, P. A. Kelly, D. N. Dai and A. M. Korsunsky, *Solution of crack problems. The distributed dislocation technique*, Solid Mechanics and Its Applications, vol. 44, Springer, 1996.
[14] W. Gerberich and W. Yang, "Interfacial and nanoscale failure", in *Comprehensive structural integrity. Vol. 8* (I. Milne, R. O. Ritchie and B. Karihaloo, eds.), Elsevier, 2003, pp. 1–40.
[15] V. Mantič, A. Blázquez, E. Correa and F. París, "Analysis of interface cracks with contact in composites by 2D BEM", in *Fracture and damage of composites* (M. Guagliano and M. H. Aliabadi, eds.), WIT Transactions on State-of-the-art in Science and Engineering, vol. 21, WIT Press, 2006, pp. 189–248.
[16] C. T. Sun and Z.-H. Jin, *Fracture mechanics*, Academic Press Inc., 2012.
[17] L. Banks-Sills, *Interface fracture and delaminations in composite materials*, SpringerBriefs in Applied Sciences and Technology, Springer, 2018.

[18] J.-B. Leblond, "Basic results for elastic fracture mechanics with frictionless contact between the crack lips", *Eur. J. Mech. A Solids* **19** (2000), pp. 633–647.

[19] E. Graciani, V. Mantič and F. París, "On the estimation of the first interpenetration point in the open model of interface cracks", *Int. J. Fract.* **143** (2007), pp. 287–290.

[20] E. Graciani, V. Mantič and F. París, "Critical study of existing solutions for a penny-shaped interface crack, comparing with a new boundary element solution allowing for frictionless contact", *Eng. Fract. Mech.* **76** (2009), pp. 533–547.

[21] R. G. Stringfellow and L. B. Freund, "The effect of interfacial friction on the buckle-driven spontaneous delamination of a compressed thin film", *Int. J. Solids Struct.* **30** (1993), pp. 1379–1395.

[22] X. Deng, "An asymptotic analysis of stationary and moving cracks with frictional contact along bimaterial interfaces and in homogeneous solids", *Int. J. Solids Struct.* **31** (1994), pp. 2407–2429.

[23] Y. A. Antipov, "An interface crack between elastic materials when there is dry friction", *J. Appl. Math. Mech.* **59** (1995), pp. 273–287.

[24] C. T. Sun and W. Qian, "A treatment of interfacial cracks in the presence of friction", *Int. J. Fract.* **94** (1998), pp. 371–382.

[25] W. Qian and C. T. Sun, "A frictional interfacial crack under combined shear and compression", *Compos. Sci. Technol.* **58** (1998), pp. 1753–1761.

[26] D. Leguillon, "Interface crack tip singularity with contact and friction", *C. R. Acad. Sci., Sér. IIB Mech. Phys. Astron.* **327** (1999), pp. 437–442.

[27] B. Audoly, "Asymptotic study of the interfacial crack with friction", *J. Mech. Phys. Solids* **48** (2000), pp. 1851–1864.

[28] B. Audoly, "Mode-dependent toughness and the delamination of compressed thin films", *J. Mech. Phys. Solids* **48** (2000), pp. 2315–2332.

[29] A. Dorogoy and L. Banks-Sills, "Shear loaded interface crack under the influence of friction: a finite difference solution", *Int. J. Numer. Methods Eng.* **59** (2004), pp. 1749–1780.

[30] J.-B. Leblond and J. Frelat, "Crack kinking from an initially closed, ordinary or interface crack, in the presence of friction", *Eng. Fract. Mech.* **71** (2004), pp. 289–307.

[31] H. D. Bui and A. Oueslati, "The sliding interface crack with friction between elastic and rigid bodies", *J. Mech. Phys. Solids* **53** (2005), pp. 1397–1421.

[32] H. Itou, V. A. Kovtunenko and A. Tani, "The interface crack with Coulomb friction between two bonded dissimilar elastic media", *Appl. Math.* **56** (2011), pp. 69–97.

[33] E. Graciani, J. Varna, V. Mantič, A. Blázquez and F. París, "Evaluation of interfacial fracture toughness and friction coefficient in the single fiber fragmentation test", *Procedia Eng.* **10** (2011), pp. 2478–2483.

[34] E. Graciani, V. Mantič and F. París, "Effect of friction on the size of the near-tip contact zone in a penny- shaped interface crack", *Key Eng. Mater.* **618** (2014), pp. 179–201.

[35] M. A. Herrera-Garrido, *Asymptotic solutions in anisotropic elastic multi-material corners with frictional contact*, PhD thesis, Universidad de Sevilla (Spain), 2024.

[36] M. A. Herrera-Garrido and V. Mantič, "Stress singularities in the generalised Comninou frictional contact model for interface cracks in anisotropic bimaterials", *J. Mech. Phys. Solids* **203** (2025), article no. 106214 (29 pages).

[37] D. Leguillon and E. Sanchez-Palencia, "Fracture in heterogeneous materials, weak and strong singularities", in *New advances in computational structural mechanics* (P. Ladevèze and O. C. Zienkiewicz, eds.), Studies in Applied Mechanics, vol. 32, Elsevier, 1992, pp. 423–434.

[38] G. R. Irwin, "Analysis of stresses and strains near the end of a crack traversing a plate", *J. Appl. Mech.* **24** (1957), pp. 361–364.

[39] J. R. Rice, "A path independent integral and the approximate analysis of strain concentration by notches and cracks", *J. Appl. Mech.* **35** (1968), pp. 379–386.

[40] D. Taylor, *The theory of critical distances: a new perspective in fracture mechanics*, Elsevier, 2007.

[41] G. I. Barenblatt, "The mathematical theory of equilibrium cracks in brittle fracture", *Adv. Appl. Mech.* **7** (1962), pp. 55–129.

[42] M. Raous, L. Cangémi and M. Cocu, "A consistent model coupling adhesion, friction, and unilateral contact", *Comput. Methods Appl. Mech. Eng.* **177** (1999), pp. 383–399.

[43] G. Lin, P. H. Geubelle and N. R. Sottos, "Simulation of fiber debonding with friction in a model composite pushout test", *Int. J. Solids Struct.* **38** (2001), pp. 8547–8562.

[44] G. Alfano and E. Sacco, "Combining interface damage and friction in a cohesive-zone model", *Int. J. Numer. Methods Eng.* **68** (2006), pp. 542–582.

[45] F. Parrinello, B. Failla and G. Borino, "Cohesive–frictional interface constitutive model", *Int. J. Solids Struct.* **46** (2009), pp. 2680–2692.

[46] G. d. Piero and M. Raous, "A unified model for adhesive interfaces with damage, viscosity, and friction", *Eur. J. Mech. A Solids* **29** (2010), pp. 496–507.

[47] L. Snozzi and J. F. Molinari, "A cohesive element model for mixed mode loading with frictional contact capability", *Int. J. Numer. Methods Eng.* **93** (2013), pp. 510–526.

[48] J. Kšiňan and R. Vodička, "An 2-D SGBEM formulation of contact models coupling the interface damage and Coulomb friction in fibre–matrix composites", *Eng. Fract. Mech.* **168(B)** (2016), pp. 76–92.

[49] V. Venzal, S. Morel, T. Parent and F. Dubois, "Frictional cohesive zone model for quasi-brittle fracture: Mixed-mode and coupling between cohesive and frictional behaviors", *Int. J. Solids Struct.* **198** (2020), pp. 17–30.

[50] M. Raous, "Interface models coupling adhesion and friction", *Comptes Rendus. Mécanique* **339** (2011), pp. 491–501.

[51] A. C. Palmer and J. R. Rice, "The growth of slip surfaces in the progressive failure of over-consolidated clay", *Proc. R. Soc. Lond., Ser. A* **332** (1973), pp. 527–548.

[52] Z. Hashin, "Finite thermoelastic fracture criterion with application to laminate cracking analysis", *J. Mech. Phys. Solids* **44** (1996), pp. 1129–1145.

[53] D. Leguillon, "Strength or toughness? A criterion for crack onset at a notch", *Eur. J. Mech. A Solids* **21** (2002), pp. 61–72.

[54] P. Cornetti, N. Pugno, A. Carpinteri and D. Taylor, "Finite fracture mechanics: a coupled stress and energy failure criterion", *Eng. Fract. Mech.* **73** (2006), pp. 2021–2033.

[55] P. Weissgraeber, D. Leguillon and W. Becker, "A review of Finite Fracture Mechanics: crack initiation at singular and non-singular stress raisers", *Arch. Appl. Mech.* **86** (2016), pp. 375–401.

[56] A. Doitrand, T. Duminy, H. Girard and X. Chen, "A review of the coupled criterion", *J. Theor. Comput. Appl. Mech.* (2024). Online at https://jtcam.episciences.org/11072.

[57] V. Mantič, "Interface crack onset at a circular cylindrical inclusion under a remote transverse tension. Application of a coupled stress and energy criterion", *Int. J. Solids Struct.* **46** (2009), pp. 1287–1304.

[58] ASTM International, *Standard test method for determination of the Mode II interlaminar fracture toughness of unidirectional fiber-reinforced polymer matrix composites*, 2019.

[59] X. Sun and B. D. Davidson, "A direct energy balance approach for determining energy release rates in three and four point bend end notched flexure tests", *Int. J. Fract.* **135** (2005), no. 3, pp. 51–72.

[60] B. D. Davidson, X. Sun and A. J. Vinciquerra, "Influences of friction, geometric nonlinearities, and fixture compliance on experimentally observed toughnesses from three and four-point bend end-notched flexure tests", *J. Compos. Mater.* **41** (2007), no. 10, pp. 1177–1196.

[61] E. Graciani, V. Mantič, F. París and J. Varna, "Numerical analysis of debond propagation in the single fibre fragmentation test", *Compos. Sci. Technol.* **69** (2009), pp. 2514–2520.

[62] E. Graciani, V. Mantič, F. París and J. Varna, "Fiber–matrix debonding in composite materials: axial loading", in *Modeling damage, fatigue and failure of composite materials* (R. Talreja and J. Varna, eds.), Woodhead Publishing, 2016, pp. 117–141.

ACADÉMIE DES SCIENCES
INSTITUT DE FRANCE

Comptes Rendus. Mécanique
2025, Vol. 353, p. 339-357
https://doi.org/10.5802/crmeca.285

Review article / *Article de synthèse*

Review of the matched asymptotic approach of the coupled criterion

Revue de l'approche asymptotique du critère couplé

Sara Jiménez-Alfaro [a,*,a,b], **Israel García García** [c] **and Aurélien Doitrand** [d]

[a] Department of Civil and Environmental Engineering, Imperial College London, Exhibition Road, London, SW7 2AZ, UK

[b] Department of Engineering Science, University of Oxford, Parks Road, Oxford, OX1 3PJ, UK

[c] Departamento de Mecánica de Medios Continuos y Teoría de Estructuras, Escuela Técnica Superior de Ingeniería, Escuela Politécnica Superior, Universidad de Sevilla, Camino de los Descubrimientos s/n, 41092 Sevilla, Spain

[d] Université Lyon, INSA-Lyon, UCBL, CNRS, MATEIS, UMR5510, F-69621 Villeurbanne, France

E-mails: sara.jimenezalfaro@eng.ox.ac.uk, s.jimenez-alfaro@imperial.ac.uk (S. Jiménez-Alfaro), israelgarcia@us.es (I. G. García), aurelien.doitrand@insa-lyon.fr (A. Doitrand)

Abstract. Matched Asymptotics is a powerful mathematical technique with broad applicability in various engineering fields. One of its key uses is in Fracture Mechanics, where it provides accurate approximations in the vicinity of the crack tip with low computational complexity. This method can be seamlessly integrated with the Coupled Criterion (CC), which enables the prediction of crack nucleation and propagation in brittle materials. Hence, this paper deeply explains how the MA technique can be applied together with the CC in the context of Fracture Mechanics, providing a detailed literature review of the advances made in the last decade.

Résumé. Les développements asymptotiques raccordés constituent une technique mathématique puissante, largement applicable dans divers domaines de l'ingénierie. L'une de leurs principales utilisations se situe en mécanique de la rupture, où ils permettent d'obtenir des approximations précises à proximité de la pointe des fissures tout en maintenant une faible complexité de calcul. Cette méthode peut être intégrée de manière fluide au critère couplé (CC), qui permet de prédire l'amorçage et la propagation des fissures dans les matériaux fragiles. Cet article explique comment la technique des développements asymptotiques raccordés peut être utilisée conjointement avec le critère couplé dans le cadre de la mécanique de la rupture, tout en offrant une revue détaillée de la littérature sur les avancées réalisées au cours de la dernière décennie.

Keywords. Matched asymptotic expansion, Coupled criterion, Fracture mechanics.

Mots-clés. Développement asymptotique raccordé, Critère couplé, Mécanique de la rupture.

Funding. European Union's Horizon 2020 research and innovation programme under Marie Sklodowska-Curie grant agreement No. 861061-NEWFRAC, Iberdrola Foundation under the Marie Sklodowska-Curie Grant Agreement No 101034297, Ministerio de Ciencia e Innovación de España (Project PID2020-117001GB-I00/AEI/10.13039/501100011033).

Manuscript received 29 October 2024, revised and accepted 14 January 2025.

* Corresponding author

1. Introduction

The matched asymptotic (MA) expansion method is an approach that enables solving an equation or a system of equations [1–5]. It is well adapted to solve singularly perturbed differential equations, for which different approximate solutions are determined, each of which being accurate for a given part of the domain under investigation. These solutions are then combined to give a single approximate solution that is accurate for the whole domain under investigation. The domain may generally be divided into two subdomains. In the first one, the solution (called the outer solution) is accurately approximated by an asymptotic series representing a regular perturbation (i.e. by setting to zero a small parameter representing, e.g., a singular perturbation). The second one consists of a region in which this first approximation is inaccurate, due to perturbation terms that are not negligible. This constitutes the inner solution. The outer and inner solutions are then combined through a process called "matching" in such a way that an approximate solution for the whole domain is finally obtained.

Asymptotic expansions were used to define the elastic constitutive law of the homogeneous equivalent material of a composite when a tangential slip is allowed on the fiber/matrix interface [6]. It was shown that a limit slip coefficient exists beyond which the stiffness of the material rapidly decreased. They were also used in the framework of homogenization as an alternative to the multiple scalings approach [7, 8]. MA expansions were used in combination to the singularity theory to determine the elastic displacements and stress fields corresponding to a class of junctions between rods and bulk bodies modeled as a flexible clamping in the framework of two-dimensional elasticity [9]. Leguillon analysed the problem of crack branching in a homogeneous elastic but non isotropic material. Based on asymptotic expansions, the energy release rate was computed and a revisited Griffith's criterion including anisotropic fracture properties was suggested [10]. Sicsic and Marigo studied the propagation of a crack band and derived the conditions for which it behaves like a Griffith's crack [11]. MA expansions were also used to study the behavior of interface cracks, for instance to further analyse the "Cook and Gordon" [12] interface debonding effect ahead of a primary crack [13], edge debonding in laminates [14] or to analyze the role of residual thermal stresses on the crack deflection or penetration at a bimaterial interface. The 2D and 3D singularities at a bimaterial interface were derived [15], also considering contact and friction between two anisotropic materials [16]. The mode III asymptotic expansions for a crack in or along a joint enabled defining an apparent toughness of the interface to be used for crack propagation [17]. It was also used to derive the stress intensity factors near an angular point on the front of an interface crack [18].

Moreover, the character of the stress singularity at the tip of a classical crack in a homogeneous material was approximated by an asymptotic series for cracks in Mode I, Mode II and Mode III. The first two modes were studied in the work of Williams [19], which is well known by the scientific community, since asymptotic solutions for free–free, clamped–clamped and free–clamped boundary conditions are given therein.

MA expansions are particularly relevant when studying fracture and especially crack initiation in a structure. Indeed, the latter can be studied in the framework of MA expansions as the unbroken problem corrected by the crack that initiates (provided its smallness with respect to the structure characteristic dimensions). This idea was actually made effective by Leguillon [20, 21] who proposed to study crack initiation by coupling a stress criterion and an energy criterion. This approach has spread and is now a common way to study crack initiation, as evidenced by numerous applications summarized in the two review papers [22, 23]. The CC can be implemented through several ways, for instance by solving an implicit equation if analytical solutions can be provided for the stress fields and the energy release rate variation as a function of the crack surface [22, 24–26]. A second way to implement the CC is through finite element

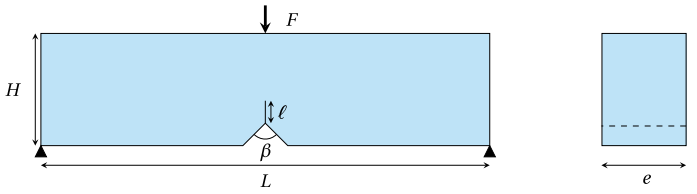

Figure 1. V-notched three-point bending specimen subjected to a force F with a crack (length ℓ) initiating at the V-notch tip. Notice that e represents the notch depth.

(FE) simulations of the full structure under investigation including the crack that initiates [27–30]. In cases where analytical solutions are not available and so as to achieve a numerically more efficient approach than full FE implementation, an effective way to implement the CC is to use MA expansions. The objective of this paper is to give an overview of the matched asymptotic approach of the CC. We first recall the general idea (Section 2) and the formulation (Section 3) of the MA approach. Then, we describe its numerical implementation (Section 4) and provide some application examples (Section 5).

2. The idea behind matched asymptotics

Before presenting the mathematical formalism of the matched asymptotic (MA) approach of the Coupled Criterion (CC), this section is dedicated to provide the philosophy behind it to further understand how it can be set up and define the main required ingredients. In the sequel, the CC is formulated under linear elasticity and small deformation assumptions. Both inertial effects [31, 32] or dissipation mechanisms other than cracking that may occur during initiation, such as, e.g., plasticity [33], diffuse damage [34] or viscous effects, are disregarded. The MA approach of the CC is useful to efficiently study the problem of a small crack initiating in a complex structure subjected to a mechanical or thermal loading. The objective is to determine the loading level at which the crack is likely to initiate as well as the initiation crack length. As a matter of example, we consider the problem of a crack of length ℓ that initiates at the tip of a V-notch (angle β) in a specimen loaded under three-point bending (Figure 1). Notice that this technique is only valid provided ℓ is smaller than a characteristic dimensions of specimen ($\ell \ll e$ in Figure 1), an initial assumption that should be checked after the implementation, once the actual value of ℓ is obtained using the coupled criterion.

2.1. *The coupled criterion*

The main idea behind the CC arises from the following observations:

- Considering an energy criterion only, it enables assessing the propagation of a crack based on the material critical energy release rate $\mathscr{G}_c$ [35–37] but generally fails to study its initiation.
- Considering a stress criterion only, it enables assessing crack initiation based on the material tensile strength σ_c except in the presence of a singular point.

Stress and energy criteria thus appear as complementary and their combination enables assessing crack initiation in many configurations. The stress criterion of the CC is a condition established in the initial domain before crack initiation (thus without crack). It states that the stress normal to the future crack path must be larger than the material strength attained under a similar principal stress state. For instance, it reverts to comparing the opening stress to material tensile strength under uniaxial tensile loading. For the sake of simplicity, we will consider a brittle

material that exhibits a Rankine strength surface in the sequel, which enables defining the material strength surface based on a single parameter, its tensile strength. The stress criterion thus requires the calculation of the stress field before crack initiation. In the vicinity of a V-notch, the stress tensor actually writes as an expansion in powers of r, William's expansion in this case since it is a singularity, Taylor's expansion for a smooth stress field:

$$\underline{\underline{\sigma}} = K r^{\lambda-1} \underline{\underline{s}}(\theta) + o(r^{\lambda-1}), \tag{1}$$

where r and θ are polar coordinates, λ is the characteristic exponent of the singularity and $\underline{\underline{s}}$ is the stress function derived from the characteristic mode of the singularity $\underline{u}$. The characteristic exponent and mode of the singularity are obtained by solving an eigen-value problem [2] . The parameter K is the Generalized Stress Intensity Factor (GSIF) of the singularity, it represents the magnitude of the loading around the V-notch. Notice that in (1) only the dominant term has been represented, assuming that it is real and has multiplicity one, due to the symmetry of the problem represented in Figure 1. However, this is not the case of mixed mode loadings, for example, where two or more singular terms should be considered, with the associated GSIFs.

The energy criterion of the CC is obtained from the energy equilibrium between the states prior to and after crack initiation. The crack surface creation energy $\mathscr{G}_c S$, where S is the crack surface, must be balanced by the variation in external force work (W_{ext}) and in elastic strain energy (W_{el}) so that:

$$\Delta W_{el} + \mathscr{G}_c S = \Delta W_{ext} \tag{2}$$

When solving the CC, the objective is to determine the initiation crack surface S_c and initiation imposed loading (for instance the initiation force F_c based on the example provided in Figure 1) by simultaneously fulfilling both stress and energy criteria. We thus need (i) one calculation on the structure without the crack to compute the stress fields and (ii) several calculations with different crack surfaces to establish the energy equilibrium. If we are considering small cracks in a large structure, this may be computationally costly as fine meshes are required in the area close the crack location. The MA approach provides an alternative and efficient method to apply the CC, which is described in the sequel. Notice that in a bidimensional problem (2) can be expressed as

$$\Delta W_{el} + \mathscr{G}_c \ell = \Delta W_{ext} \tag{3}$$

where ℓ is the newly created crack length (a priori unknown). At the initiation imposed loading $\ell = \ell_c$, the initiation crack length. Moreover, it is important to highlight that in problems where there are notches or pre-existing cracks, the crack nucleation is frequently determined by the initiation GSIFs of the singularity, denoted as K_i. These parameters depend on the initiation imposed loading and the geometry of the problem. In the problem represented in Figure 1, there is only one leading term, see (1), and therefore only one initiation GSIF.

2.2. *The matched asymptotic approach*

The MA approach of the CC is based on the fact that the crack can be considered as a small perturbation to the elasticity problem where the structure is subjected to a given loading. It consists in successively considering two problems to be solved at two scales. The first problem, solved in the so-called outer domain, is obtained by considering the full structure and neglecting the crack that initiates. In complement, the second problem focuses only on the inner domain around the crack initiation point, independently of the whole structure under investigation. The final solution is then obtained by matching both problems to obtain the stress and energy balance required for the CC application.

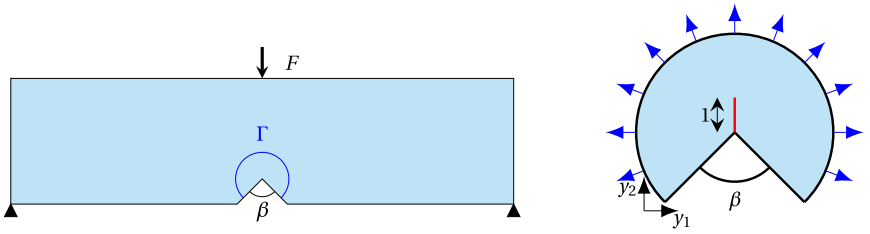

Figure 2. (a) Outer domain where the crack is disregarded, the contour Γ can be used to calculate the Generalized Stress Intensity Factor acting at the V-notch for a given force F. (b) Inner domain where the whole structure is disregarded, the normalized crack length is 1 and the arrows represent the imposed asymptotic displacement fields prescribed at a fictitious boundary sufficiently far from the crack.

Outer domain. In the outer problem, the perturbation (i.e. the crack) is neglected and a solution of the problem without perturbation is provided in the outer domain (i.e. the structure without crack). This solution is valid everywhere except in a zone near the crack initiation location, for which a correction to this solution must be brought. The outer domain corresponding to the example given in Figure 1, is shown in Figure 2a. In the outer domain, the loading is described in terms of prescribed displacement or force. Then, the GSIF of the singular point (here, the V-notch tip) can be calculated for a given applied force or displacement. Under the assumptions of small deformation and linear elasticity, the GSIF is proportional to the imposed force. For a given imposed force, the GSIF can be computed using a contour integral [2] on a closed path surrounding the singular point (e.g., Γ in Figure 2a). The GSIF calculation based on the contour integral can be implemented in 3D [38] or in 2D for isotropic [21, 39] or anisotropic [40, 41] materials, for multi-material configurations [40, 42–44], or even based on displacement fields measured experimentally by digital image correlation [45]. Other approaches also exist to compute the GSIF, such as the quasidual function method [46, 47], least square fitting [48] or an extraction from the strain energy density [49]. The solution obtained in the outer domain is valid except near the crack initiation location, which requires a correction representative of the initial problem (Figure 1).

Inner domain. The correction to the solution obtained in the outer domain without the perturbation is obtained through the second problem which is solved in the inner domain. It consists in focusing only in a zone near the crack initiation location, providing a detailed description of the crack around the singular point, regardless of the entire structure itself. The inner domain thus corresponds to the singular point that would lie in an infinite medium and would be subjected to remote asymptotic displacement or stress fields. The prescribed loading is thus described in terms of GSIF. An example of inner domain corresponding to the problem depicted in Figure 1 is shown in Figure 2b. In the inner domain, the space variables are normalized with respect to the crack length so that the normalized initiation crack length is 1. Since the whole structure geometry and boundary conditions are disregarded in the inner domain, the asymptotic displacement fields are prescribed as boundary conditions in order to obtain the stress and energy balance required to solve the CC. The solution derived in the inner domain is thus accurate in a zone near the crack initiation location.

Matching inner and outer problem solutions. Solving the problems in the outer and inner domains yields two solutions (displacement fields) that accurately represent the initial problem

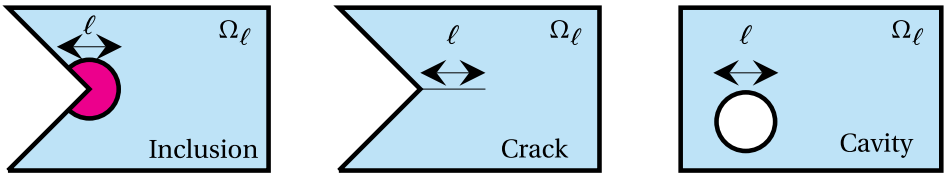

(a) (b) (c)

Figure 3. Examples of configurations: (a) Inclusion, (b) crack ahead of a V-notch or (c) cavity close to a free edge, that can be studied applying the MA approach of the CC. For display purposes in the representation ℓ is purposely not small compared to any dimensions of the structure.

of the structure containing a small crack respectively far from and close to the crack initiation location. Matching both solutions also requires a common description of the applied loading. Since it is only described by the GSIF in the inner domain, it justifies the need of calculating the relation between the GSIF and the applied force or displacement in the outer domain. The next step in the MA approach consists in combining both solutions to finally solve the initial problem. This is done by matching both displacement fields in a zone that is (i) sufficiently far from the singular point in the inner domain and (ii) sufficiently close to it in the outer domain. The matching conditions finally enable obtaining the stress and energy balance corresponding to the initial problem under investigation (Figure 1) and further apply the CC for studying crack initiation.

Solving the CC. The matching of the inner and outer problem solutions provide a general solution that is accurate over the whole domain under investigation. It yields the displacement fields in the whole structure in presence of a crack. It thus enables calculating the stress fields before crack initiation (Equation (1)) as well as the elastic strain energy variation due to crack initiation (Equation (2)) for a given loading. It finally yields all the ingredients required to solve the CC. The remaining step consists in determining the minimum imposed loading and the corresponding crack length for which both stress and energy conditions are fulfilled.

3. Formulation of the approach

The matched asymptotic expansion is used in mechanical engineering to predict the solution, i.e. the displacement field $\underline{U_\ell}(x_1,x_2)$ (where (x_1,x_2) represents the Cartesian coordinates) in the vicinity of an element that can be an inclusion, a crack or a cavity, see Figure 3. This element is frequently called perturbation, since it is assumed that its size ℓ is small compared to any dimensions of the structure.

As an example to illustrate the formulation of the problem, a small cavity located at the tip of a V-notched is considered, see Figure 4, where the notation of the problem that is approximated is represented. The domain Ω_ℓ has an outer contour $\Gamma = \Gamma_V \cup \Gamma_N \cup \Gamma_D \cup \Gamma_\ell$. The contour Γ_D is characterized by an imposed displacement $\bar{U}$, whereas the contours Γ_N, Γ_V and Γ_ℓ have a stress-free boundary conditions. The notation Γ_V is referred to the contour of the V-notch and Γ_ℓ to the one of the small perturbation.

Hence, the set of equations that defines the actual problem is

$$-\nabla_x \cdot \underline{\underline{\sigma_\ell}} = 0 \quad \text{in } \Omega_\ell, \tag{4}$$

$$\underline{\underline{\sigma_\ell}} = \mathbf{C} : \nabla_x \underline{U_\ell}, \tag{5}$$

$$\underline{\underline{\sigma_\ell}} \cdot \underline{n} = \bar{h} \quad \text{on } \Gamma_N, \tag{6}$$

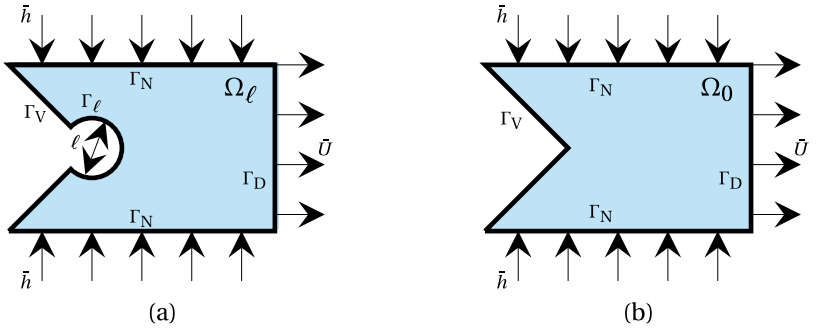

Figure 4. Representation of the notations in (a) the inner domaine and (b) the outer domain for the example of a cavity ahead of a V-notch.

$$\underline{\underline{\sigma_\ell}} \cdot \underline{n} = 0 \quad \text{on } \Gamma_V \cup \Gamma_\ell, \tag{7}$$

$$\underline{U_\ell} = \underline{\bar{U}} \quad \text{on } \Gamma_D, \tag{8}$$

where ∇_x is referred to the coordinates system of the actual domain x_1, x_2. In the MA approach, a twofold representation of $\underline{U_\ell}(x_1, x_2)$ is proposed in the form of an outer and an inner expansion. Notice that it is assumed that the specimen is in the absence of body forces.

Outer expansion. In this approximation, the actual solution is represented as

$$\underline{U_l}(x_1, x_2) = \underline{U_0}(x_1, x_2) + \cdots \tag{9}$$

where $\underline{U_0}(x_1, x_2)$ is the solution of the same elasticity problem considering that the perturbation is not observable in the domain, i.e., solved in an unperturbed domain Ω_0. As an example, Figure 4b represents Ω_0 associated with the actual domain of Figure 4a. The second term in (9) denoted with an ellipsis is a "small correction" that decreases to 0 as $\ell \to 0$. The solution $\underline{U_0}(x_1, x_2)$ is a good approximation of $\underline{U_\ell}(x_1, x_2)$ far away from the perturbation. For this reason, it is called the outer field. The set of equations that defines $\underline{U_0}(x_1, x_2)$ is

$$-\nabla_x \cdot \underline{\underline{\sigma_0}} = 0 \quad \text{in } \Omega_0, \tag{10}$$

$$\underline{\underline{\sigma_0}} = \mathbf{C} : \nabla_x \underline{U_0}, \tag{11}$$

$$\underline{\underline{\sigma_0}} \cdot \underline{n} = \underline{h} \quad \text{on } \Gamma_N, \tag{12}$$

$$\underline{\underline{\sigma_0}} \cdot \underline{n} = 0 \quad \text{on } \Gamma_V, \tag{13}$$

$$\underline{U_0} = \underline{\bar{U}} \quad \text{on } \Gamma_D. \tag{14}$$

Notice that a better approximation of the outer expansion can be achieved by considering higher order terms. Particularly, Leguillon et al. considered the second outer term in [50].

Inner expansion. A second expansion can be used to approximate the actual solution by introducing the change of variables $y_i = x_i/\ell$ and $\rho = r/\ell$. In the limit when $\ell \to 0$ we obtain an unbounded domain Ω_{in} in which the dimensionless characteristic length of the perturbation is now equal to 1, see Figure 5 as an example, where the chosen characteristic length is the diameter of the cavity.

The inner expansion is therefore expressed as

$$\underline{U_\ell}(x_1, x_2) = \underline{U_\ell}(\ell y_1, \ell y_2) = F_0(\ell)\underline{V_0}(y_1, y_2) + F_1(\ell)\underline{V_1}(y_1, y_2) + \cdots \tag{15}$$

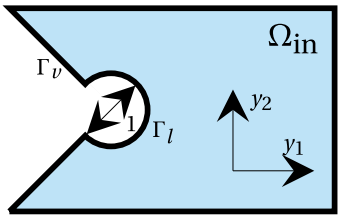

Figure 5. Scheme of the inner problem.

The set of equations related to the two terms $\underline{V_0}(y_1, y_2)$ and $\underline{V_1}(y_1, y_2)$ are

$$\begin{aligned} -\nabla_y \cdot \underline{\underline{\tilde{\sigma}_0}} &= 0 \quad \text{in } \Omega_{\text{in}}, & -\nabla_y \cdot \underline{\underline{\tilde{\sigma}_1}} &= 0 \quad \text{in } \Omega_{\text{in}}, \\ \underline{\underline{\tilde{\sigma}_0}} &= \mathbf{C} : \nabla_y \underline{V_0} & \underline{\underline{\tilde{\sigma}_1}} &= \mathbf{C} : \nabla_y \underline{V_1} \\ \underline{\underline{\tilde{\sigma}_0}} \cdot \underline{n} &= 0 \quad \text{on } \Gamma_{\text{V}} \cup \Gamma_\ell & \underline{\underline{\tilde{\sigma}_1}} \cdot \underline{n} &= 0 \quad \text{on } \Gamma_{\text{V}} \cup \Gamma_\ell \end{aligned}$$

The problems indicated above are well-posed when the so-called matching conditions are added to these sets of equations. As a results, it is obtained an inner expansion that is a good approximation of the actual solution $\underline{U_\ell}(x_1, x_2)$ in the neighbourhood of the perturbation.

Matching conditions. Since the outer expansion is a good approximation of the actual solution far away from the location of the perturbation and the inner expansion is a good approximation in the vicinity of the perturbation, there must exist an intermediate region where both expansions are valid. In that region the matching conditions are defined. The behaviour of the far field near the origin can be described by an expansion in powers of the distance to the singular point r, that can be the Taylor's expansion in the case of a smooth stress field or the Williams' expansion in case of a singularity. Assuming the example of the cavity in a V-notch highlighted in Figure 4, the William's expansion can be applied, normally expressed in polar coordinates as

$$\underline{U}(r, \theta) = \underline{U}(0,0) + K r^\lambda \underline{u}(\theta) + o(r^\lambda), \tag{16}$$

assuming that the dominant term is real and have multiplicity one. The matching conditions can be expressed as

$$F_0(\ell)\underline{V_0}(y_1, y_2) \approx \underline{U}(0,0), \quad \text{when } \rho \to \infty \tag{17}$$

$$F_1(\ell)\underline{V_1}(y_1, y_2) \approx K\ell^\lambda \rho^\lambda \underline{u}(\theta), \quad \text{when } \rho \to \infty \tag{18}$$

where the term $\approx$ means "behaves like" and $\rho = r/\ell = \sqrt{y_1^2 + y_2^2}$. It can thus be set:

$$F_0(\ell) = 1 \quad \text{and} \quad \underline{V_0}(y_1, y_2) \approx \underline{U}(0,0), \quad \text{when } \rho \to \infty \tag{19}$$

$$F_1(\ell) = K\ell^\lambda \quad \text{and} \quad \underline{V_1}(y_1, y_2) \approx \rho^\lambda \underline{u}(\theta). \quad \text{when } \rho \to \infty \tag{20}$$

However, it can be shown that the matching condition over $\underline{V_1}(y_1, y_2)$ does not fulfill the Lax-Milgram theorem, since it has an infinite energy in the unbounded domain Ω_{in}, while it should decrease to 0 at infinity to have a finite energy. For this reason, the superposition principle is applied,

$$\underline{V_1}(y_1, y_2) = \rho^\lambda \underline{u}(\theta) + \underline{\hat{V}_1}(y_1, y_2) \tag{21}$$

where $\underline{\hat{V}_1}(y_1, y_2)$ is the solution to a well-posed problem. The set of equations that defines the new term $\underline{\hat{V}_1}(y_1, y_2)$ is:

$$\begin{aligned} -\nabla_y \cdot \underline{\underline{\hat{\sigma}_1}} &= 0 \quad \text{in } \Omega_{\text{in}}, \\ \underline{\underline{\hat{\sigma}_1}} &= \mathbf{C} : \nabla_y \underline{\hat{V}_1}, \end{aligned}$$

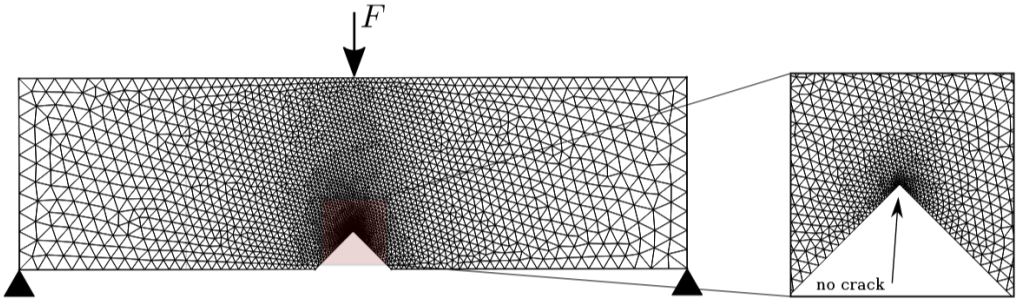

Figure 6. FEM model of the outer domain problem.

$$\begin{aligned}\underline{\underline{\hat{\sigma}_1}}\cdot\underline{n} &= 0 \quad \text{on } \Gamma_\ell,\\ \underline{\hat{V}_1} &\approx 0 \quad \text{as } \rho\to\infty,\\ \underline{\underline{\hat{\sigma}_1}}\cdot\underline{n} &= -\mathbf{C}:\nabla_y\left(\rho\,\underline{u}(\theta)\right)\cdot\underline{n} \quad \text{on } \Gamma_V\end{aligned}$$

Note that the terms $\underline{\hat{V}_1}(y_1,y_2)$ and $\underline{V_1}(y_1,y_2)$ are independent of the global geometry and the applied load, that are included in the GSIF K. Finally, it yields a new expression for the inner expansion, where $\underline{\hat{V}_1}(y_1,y_2)$ has finite energy at infinity,

$$\underline{U_\ell}(x_1,x_2)=\underline{U_\ell}(\ell\,y_1,\ell\,y_2)=F_0(\ell)\underline{U}(0,0)+K\ell^\lambda\left[\rho^\lambda\,\underline{u}(\theta)+\underline{\hat{V}_1}(y_1,y_2)\right]+o(\ell^\lambda). \tag{22}$$

The MA approach thus enables determining the displacement field accounting for the perturbation by the initiation crack length. It yields all the ingredients required to compute the initiation loading and crack length by further implementation of the CC, i.e. the stress field before crack initiation and the elastic strain energy release due to the crack.

4. Numerical implementation of the matched asymptotic approach

The strategy outlined and described in previous sections can be implemented using the typical computational tools employed in solid mechanics, such as the Finite Element Method and the Boundary Element Method. In this work, the applications will focus on the Finite Element Method, but the idea directly applies to other computational methods. The numerical implementation will be applied initially to the problem described in Figure 1 as a simple case and after it will be extended to more complex cases, where some other aspects have to be taken into account.

As described in Section 2.1, the implementation of the coupled criterion requires the evaluation of the stress and energy criteria separately. Thus, the objective of the numerical implementation of the MA will be the evaluation of these two criteria. Following the strategy of the MA approach, two domains, inner and outer, are used for this objective. The numerical implementation will consist on using the Finite Element Methods to compute the necessary elastic solutions in the two domains. Some of them will be used to impose matching between the two domains and others to obtain the stresses or the change in elastic strain energy necessary to evaluate the stress and energy criteria.

In this sense, the steps of a CC analysis assisted by MA and FEM for the problem described in Section 2.1 are the following:

(1) Generation of a FEM model of the outer domain without crack. The mesh should be fine enough around the V-notch in order to approximate accurately the displacement

solution around this point, see Figure 6. The minimum required mesh size can be determined based on a mesh convergence analysis.

(2) Computation of the outer domain model for a certain load. If the problem can be considered linear, i.e. material behavior and boundary conditions are linear and it is possible to assume small deformations, the solution will be linear with the load. In this case, a unit load can be applied and the results obtained can be multiplied by the load to get any result.

(3) The displacements $\underline{u}^{\mathrm{FE}}(\rho,\theta)$ and traction vector $\underline{t}^{\mathrm{FE}}(\rho,\theta)$ in the vicinity of the V-notch are extracted from the outer-domain model in a closed contour around (noted Γ), typically a circle. Since this first problem contains a V-notch, these results can be directly used to compute the value of the GSIF by using the property of orthogonality of modes through the next contour integral:

$$K \approx \frac{\int_\Gamma \underline{t}^{\mathrm{FE}}(\rho,\theta)\cdot\rho^\lambda \underline{u}^-(\theta) - \underline{t}^-(\rho,\theta)\cdot\underline{u}^{\mathrm{FE}}(\rho,\theta)\mathrm{d}\Gamma}{\int_\Gamma \underline{t}(\rho,\theta)\cdot\rho^\lambda \underline{u}^-(\theta) - \underline{t}^-(\rho,\theta)\cdot\rho^\lambda \underline{u}(\theta)\mathrm{d}\Gamma}, \tag{23}$$

where $\underline{u}(\theta)$ is the displacement function of the singular mode corresponding to the exponent λ and the GSIF K and $\underline{u}^-(\theta)$ is the corresponding dual one. The traction vectors $\underline{t}$ and $\underline{t}^-$ respectively correspond to the displacement functions of the singular and dual modes. Once K is known, the stresses before the crack initiation (necessary for the evaluation of the stress criterion) can be extracted directly from the singular expansion, assuming the crack length at initiation is sufficiently small compared with the size of the region governed by the first term of the William's expansion.

(4) Generation of a FE model of the inner domain with crack, see Figure 7. The external radius should be much larger than the crack length. Typically, the dimensionless crack length is set to 1, and the external radius should be at least 200. The displacements given by the singular mode are prescribed at the external boundaries.

(5) Two versions of this model are computed:
   (a) Submodel 0: This submodel corresponds to the state just before the crack initiation. The two crack faces (and then their corresponding nodes) are tied to each other, in order to model the situation without crack.
   (b) Submodel 1: This submodel corresponds to the state just after the crack initiation. Crack faces are stress-free.

   From these two submodels, the change in potential elastic energy ΔW_{el} necessary for the evaluation of the energy criterion (Equation (2)). Several strategies can be used:
   (a) Crack closure technique: The change in potential elastic energy can be obtained by the work of the virtual forces necessary to close the cracks for problems with displacement control loading. Assuming linearity in the process, the change in potential elastic energy can be computed with the following expression:

$$\Delta W_{\mathrm{ext}} - \Delta W_{\mathrm{el}} = \int_{\Gamma_{\mathrm{crack}}} \frac{1}{2}\underline{t}^{0+}\cdot(\underline{u}^{1+} - \underline{u}^{1-})\mathrm{d}\Gamma_{\mathrm{crack}}. \tag{24}$$

   where $\underline{t}^{0+}$ is the traction vector at the submodel 0 at one of the crack faces, named positive. The terms $\underline{t}^{1+}$ and $\underline{t}^{1-}$ refer to the displacements at the positive and the opposite faces respectively in the submodel 1. In case of the existence of force control loads, the below expression should include the work done by the external forces during crack closure. The fact of having to take into account the external forces takes away the advantages of this technique, so the next technique would be recommended in case of force control loading.

(b) Technique based on the change in the work of the external forces applied at the external boundary. The change in potential energy can be computed by:

$$\Delta W_{\text{ext}} - \Delta W_{\text{el}} = \int_{\Gamma_{\text{ext}}} \frac{1}{2} (\underline{t}^0 \underline{u}^1 - \underline{t}^1 \underline{u}^0) \mathrm{d}\Gamma_{\text{ext}}, \tag{25}$$

where $\underline{t}^0$ and $\underline{t}^1$ are the traction vectors at the external boundary in the submodels 0 and 1 respectively. In both strategies, it is more convenient to extract the nodal forces directly from the FEM results and multiply them by the nodal displacement, instead of computing the contour integral.

(c) Technique based on the change in elastic strain energy: This technique is based on computing directly the change in elastic strain energy. This is especially useful when the problem is displacement controlled, otherwise it will be necessary to add the work done by external forces during crack initiation. Thus, the next general expression is:

$$\Delta W_{\text{ext}} - \Delta W_{\text{el}} = \int_{\Gamma_{\text{N}}} \frac{1}{2} \underline{t} \left(\underline{u}^1 - \underline{u}^0 \right) \mathrm{d}\Gamma + \int_{\Omega} \frac{1}{2} \left(\underline{\underline{\sigma}}^0 : \underline{\underline{\varepsilon}}^0 - \underline{\underline{\sigma}}^1 : \underline{\underline{\varepsilon}}^1 \right) \mathrm{d}\Omega \tag{26}$$

where Γ_{N} corresponds to the boundary with Neumann boundary condition. The first term would vanish in case of displacement control.

(6) Since in this problem ℓ is the only characteristic length and the space variables are made dimensionless with respect to ℓ in the inner domain, the dimensionless crack length in the inner domain is 1. Therefore, it is only needed to compute ΔW_{el} for a dimension crack length of 1. In fact, according to the Dimensional Analysis of the inner domain, the change in potential elastic energy in this problem should follow the next expression:

$$\Delta W_{\text{ext}} - \Delta W_{\text{el}} = \frac{K^2}{E} \ell^{2\lambda} A h \tag{27}$$

where h is the thickness, and A is a dimensionless parameter that can be obtained by the steps described before for a unit imposed GSIF K. In case other characteristic lengths are present in the inner domain, such as a blunt notch radius r_{b}, or other unknown about the crack initiation geometry, such as deviation angle α, the term A becomes a dimensionless function that contains this dependence in terms of dimensionless parameters, such as r_{b}/ℓ or α. In next sections more complex problems will be presented in this sense.

(7) Once the value of K is estimated, the coupled criterion of the finite fracture mechanics can be applied in a quite straightforward manner:

- Stress criterion: Combining the first term of the expression in (1) and the condition outlined for the stress criterion, this criterion can be expressed as:

$$K r^{\lambda-1} s(\theta) \geq \sigma_{\text{c}} \, \forall \, r, \quad 0 \leqslant r \leqslant \ell \tag{28}$$

Since for singular cases ($\lambda < 1$) this function is decreasing with r, this condition can also be also written as:

$$K \ell^{\lambda-1} s(\theta) \geq \sigma_{\text{c}}. \tag{29}$$

- Energy criterion: Combining the expression in (27) with the condition in (2), the energy criterion can be expressed as:

$$\frac{K^2}{E} \ell^{2\lambda} A h \geq \mathscr{G}_{\text{c}} \ell h \tag{30}$$

The two criteria have to be fulfilled simultaneously. In this case, since the left term in Equation (29) is a decreasing function of ℓ and the left term in Equation (30) is an increasing function of ℓ, the minimum value of K for which the two conditions are

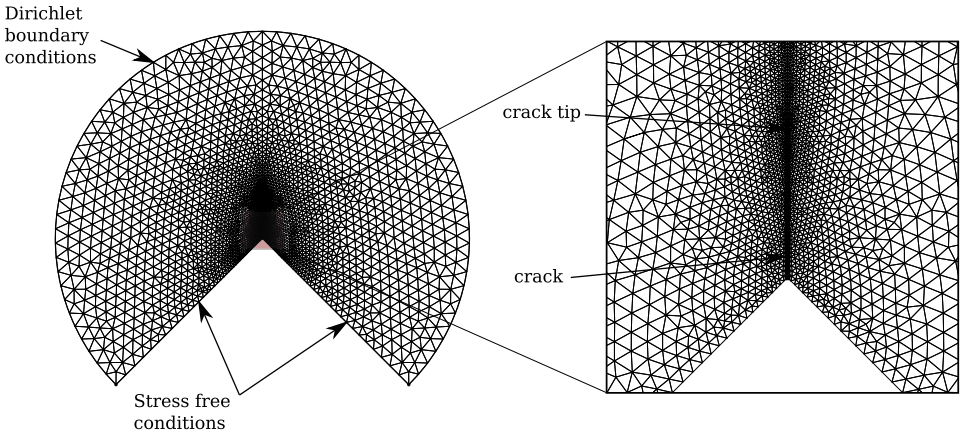

Figure 7. FEM model of the inner domain problem.

fulfilled is given solving the conditions as two equations with two unknowns ℓ and K. The solution, for a critical length ℓ_{i}, is:

$$\ell_{\mathrm{i}} = \frac{\mathscr{G}_{\mathrm{c}} E s(\theta)^2}{A\sigma_{\mathrm{c}}^2} \tag{31}$$

and for the critical GSIF K_{i},

$$K_{\mathrm{i}} = \left(\frac{\mathscr{G}_{\mathrm{c}} E}{A}\right)^{\lambda-1} \left(\frac{\sigma_{\mathrm{c}}}{s(\theta)}\right)^{2\lambda-1} \tag{32}$$

Since K_{i} is directly proportional to the external load, the critical load for crack initiation can be calculated directly from the critical value for K_{i}.

5. Implementation in complex cases and examples

Previous sections were dedicated to present the MA approach of the CC in a relatively simple 2D configuration involving a single length parameter (the crack length) under opening mode, such as in [51]. In this section, we provide a detailed overview of more complex configurations and examples to thoroughly demonstrate the full potential of the MA approach.

5.1. *Cases with two lengths involved*

The problem under investigation may involve more than one characteristic length parameter. An emblematic example is the case of crack initiation at the tip of a blunted V-notch [39, 52, 53], including as length parameters both the V-notch radius r_{V} and the crack length ℓ. In such kind of problems, one must choose which parameter will be used for the inner expansion. The correction of the outer expansion will thus be obtained either in the inner domain where the initiation crack length is 1 and the dimensionless V-notch radius is r_{V}/ℓ, or in the inner domain where the V-notch radius is 1 and the dimensionless initiation crack length is ℓ/r_{V}. Either approach is strictly equivalent, so that the final solution is independent of the choice of the normalization parameter. The normalization parameter can thus be chosen for practicality reasons, such as the use of a single (expansion with respect to the V-notch radius) instead of several FE meshes and calculations (expansion with respect to the crack length). Other examples of the MA approach with at least two length parameters include crack initiation at a shallow notch [54], a blunted U-notch [55, 56], or a pore crack initiation [57, 58].

5.2. *Mixed mode loading*

Considering mixed mode loading crack initiation means that the outer and inner expansions involve more than one term in the form $K_j r^{\lambda_j} \underline{u}_j(\theta)$, such as for instance:

$$\underline{U}(r,\theta) = \underline{U}(0,0) + K_a r^{\lambda_a} \underline{u}_a(\theta) + K_b r^{\lambda_b} \underline{u}_b(\theta) + \cdots . \tag{33}$$

This is classically encountered when studying mixed opening and shear mode crack initiation, for instance at a V-notch in 2D [51, 53, 59–61] or in 3D [56, 62]. Higher order terms, such as the T-stress, may also be involved for instance when studying 2D crack deviation [63] or 3D crack front segmentation into facets [64]. In such configurations, the stress field is composed of the sum of the terms corresponding to each mode. The elastic strain energy (and thus the Incremental Energy Release Rate) is the sum of terms corresponding to each mode (in the form $\alpha_j K_j r^{2\lambda_j}$) as well as coupling terms (in the form $\alpha_{jk} K_j K_k r^{\lambda_j+\lambda_k}$). These terms can be computed either by directly prescribing mixed-mode loading boundary conditions in the inner domain, or successively prescribing single-mode loading boundary conditions then using the superposition principle.

5.3. *Interface cracking*

The MA of the CC can be applied to study crack initiation at an interface between two materials, possibly in presence of a singular point [59, 65]. The characteristic exponent and corresponding mode depend on the elastic property contrast and singularity geometry [66, 67]. It may even result in complex characteristic exponents and modes [68], which does not prevent the implementation of the MA approach as the displacement field remains real but may requires the manipulation of complex numbers. Applications of the MA of the CC to interface cracking include bimaterial joint failure [69–72] with the consideration of residual stresses [73], crack initiation in microelectronics structures [74, 75], bond failure of a SiC–SiC brazed assembly [76] and crack deflection in layered ceramics [77] or ceramic matrix composites [78].

5.4. *Comparison with other models*

The MA approach of the CC was compared to other fracture models such as Cohesive Zone Model (CZM), Phase Field (PF) approach for fracture, Thick Level Set (TLS) and Strain Energy Density (SED) approach. It was shown that the MA approach of the CC and Dugdale CZM yielded similar initiation GSIF when applied to predict crack initiation at a V-notch [79, 80], which was a particular case of the more general result that the CZM traction-separation profile corresponding to the CC actually depends on the geometry, the type of loading, the cracking mechanism and the adopted stress criterion [23]. The comparison between the TLS and the matched asymptotic approach of the CC revealed similar apparent strengths for all cases provided the assumptions of the MA approach are satisfied [81], as well as a dependence of the TLS results to the choice of the stress decrease as a function of the crack opening. This dependence can be put in parallel to the traction-separation profile of CZM so that one stress decrease function could be identified in the TLS to retrieve the CC results. Abaza et al. [82] showed that the PF regularization length could be calibrated so that the apparent SIF at crack nucleation were similar to those obtained with the CC. Similar variations of the apparent SIF at crack nucleation in notched ceramic specimens were then obtained for different notch geometries using CC and PF. The SED and CC comparison in the case of a V-notch loaded under in-plane shear revealed that the analytically computed initiation GSIF were proportional to powers of K_{Ic} and σ_{c} for both methods. The proportionality factor was a function of the notch angle for the CC whereas it was a function of the Poisson's ratio for the

SED approach. Basing the control volume over which the strain energy density was averaged, both approaches predicted similar apparent SIF at crack initiation [83].

5.5. *3D*

There is no restriction regarding the 3D implementation of the MA approach [84]. The displacement field is based on 3D William's expansions [85, 86] which takes the same general form as the 2D one. The 3D singular exponent and associated eigenmode can be computed in a similar way to the 2D one [2, 87]. The main difference compared to the 2D case is related to the dual mode. If the primal mode is $r^{\lambda}\underline{u}(\theta,\phi)$, then the dual mode is $r^{-\lambda-1}\underline{u}^{-}_{3D}(\theta,\varphi)$ in 3D instead of $r^{-\lambda}\underline{u}^{-}_{2D}(\theta)$ in 2D. Otherwise, the space coordinates expansion is also performed with respect to a characteristic length parameter, which can be chosen as the crack extension in a given direction [56, 64, 84] or with respect to the square root of the crack surface [62]. Overall, the CC has takes the same form as in 2D and the same contour integral can be used to compute the GSIF [38], except that the integration domain is a 2D surface in the volume encompassing the singular point instead of a 1D curve in a surface. The main difficulty for the 3D CC application is the crack shape determination. A 2D crack can generally be described by its length and angle, but there is an infinite number of possible 3D crack surface. Even assuming a planar crack path, this plane must be determined, which can be done for instance by maximizing the stress criterion [56] or based on both stress and energy requirements by minimizing the initiation loading [64]. Then, in the crack plane there is still an infinite number of 2D curves to describe the crack front. An option to overcome this difficulty is to adopt a parameterized description of the crack shape [62, 64] or derive the crack shapes from the stress isocontours [56].

5.6. *Other applications*

Some works including the MA approach of the CC also cover studying the presence of a process zone or damage zone ahead of a V-notch or a crack [88–90]. It also provided a robust method for small crack detection based on displacement fields measured by digital image correlation [50, 91]. Several works about ceramic failure were also proposed, such as cracking in layered ceramics [92], platelet-based ceramics [41, 93, 94] or surface defects in polycristalline ceramics [95]. Other works concerned brittle fracture size effect [96], strength anisotropy of 3D printed materials [97], multicracking of a stiff inclusion in a soft matrix [98] or elliptical hole-induced crack initiation [99].

6. Conclusions and further developments

Crack initiation is an unsolved problem in Linear Elastic Fracture Mechanics, that does manage correctly to predict crack propagation in diverse material systems. However, crack initiation requires the employment of more complex, computational costly and controversial tools. This review shows how Matched Asymptotics and the Coupled Criterion of the Finite Fracture Mechanics have been combined in the literature to predict crack initiation near stress singularities, such as V-notches or multimaterial corners, or related to, such as U-notches.

The main advantages of this combination are: (i) it allows to obtain predictions with a very low computational cost, where typically only linear models are involved and quasianalytical expressions can be obtained for the load prediction, (ii) The results are easily generalized for variations in material properties and even geometry, (iii) it is physically based, thus results can be interpreted, explained and tailored following a physical reasoning and finally (iv) according to the literature review it presents a good agreement with experiments.

The main disadvantages are (i) the solutions are still limited to crack length at onset that has to be very small compared with the characteristic lengths of the problem and (ii) it is necessary to introduce special assumptions when nonlinearities are involved.

Other methods have been used to predict crack initiation in the stress singularities or in the problems target of the combination of matched asymptotics and finite fracture mechanics: Cohesive Zone Models (CZM) prescribe a cohesive law between a pair of surfaces, relating force and separation, see e.g. [80]. This method is very versatile and presents good agreement with experiments, but requires setting crack geometry before initiation and typically involve nonlinear computational models. In the last decades gradient-damage-based models such as that named Phase Field have been extensively developed. These models are based on the regularization of the crack through a regularization length. It has been proven that when this length vanishes, the result of LEFM is recovered. Then, for V-notches and related problems, these models present the same problems as LEFM. To overcome this issue, several strategies have been proposed, such as assuming that the regularization length is a material parameter [100], defining a CZM [101], or understanding this regularization length in the context of the CC [90].

Declaration of interests

The authors do not work for, advise, own shares in, or receive funds from any organization that could benefit from this article, and have declared no affiliations other than their research organizations.

Dedication

The manuscript was written through contributions of all authors. All authors have given approval to the final version of the manuscript.

Acknowledgments

This paper is entirely dedicated to our friend and colleague, Pr. Dominique Leguillon.

SJ-A and IGG acknowledge the funding received from the European Union's Horizon 2020 research and innovation programme under Marie Sklodowska-Curie grant agreement No. 861061-NEWFRAC. SJ-A also acknowledges the Iberdrola Foundation under the Marie Sklodowska-Curie Grant Agreement No 101034297. IGG also acwnoledges the support of Ministerio de Ciencia e Innovación de España (Project PID2020-117001GB-I00/AEI/10.13039/501100011033).

References

[1] M. Van Dyke, *Perturbation Methods in Fluid Mechanics*, Academic Press: New York, 1964.

[2] D. Leguillon and E. Sanchez-Palencia, *Computation of Singular Solutions in Elliptic Problems and Elasticity*, Wiley: USA, 1987.

[3] P. Lagerstrom, *Matched Asymptotic Expansions: Ideas and Techniques*, Applied Mathematical Sciences, Springer: Berlin, 1988.

[4] J. Kevorkian and J. Cole, *Multiple scale and singular perturbation methods*, Springer Science & Business Media: New York, 2012.

[5] R. O'Malley, *The Method of Matched Asymptotic Expansions and Its Generalizations*, Historical Developments in Singular Perturbations, Springer: Cham, 2014.

[6] F. Lene and D. Leguillon, "Homogenized constitutive law for a partialy cohesive composite material", *Int. J. Solids Struct.* **18** (1982), no. 5, pp. 443–458.

[7] A. Bensoussan, L. Lions and G. Papanicolaou, *Asymptotic Analysis for Periodic Structures. Studies in Mathematics and its Application*, North-Holland: Amsterdam, 1978.
[8] D. Leguillon, "Comparison of matched asymptotics, multiple scalings and averages in homogenization of periodic structures", *Math. Models Methods Appl. Sci.* **07** (1997), no. 05, pp. 663–680.
[9] D. Leguillon and E. Sanchez-Palencia, "Approximation of a two dimensional problem of junctions", *Comput. Mech.* **6** (1990), pp. 435–455.
[10] D. Leguillon, "Asymptotic and numerical analysis of a crack branching in non-isotropic materials", *Eur. J. Mech. Solids* **12** (1993), pp. 33–51.
[11] P. Sicsic and J. Marigo, "From gradient damage laws to Griffith's theory of crack propagation", *J. Elast.* **113** (2013), no. 1, pp. 55–74.
[12] J. Cook and J. Gordon, "A mechanism for the control of crack propagation in all-brittle systems", *Proc. R. Soc. A* **282** (1964), pp. 508–520.
[13] D. Leguillon, C. Lacroix and E. Martin, "Interface debonding ahead of a primary crack", *J. Mech. Phys. Solids* **48** (2000), no. 10, pp. 2137–2161.
[14] D. Leguillon, "A method based on singularity theory to predict edge delamination of laminates", *Int. J. Fract.* **100** (1999), no. 1, pp. 105–120.
[15] D. Leguillon and E. Sanchez-Palencia, "On 3D cracks intersecting a free surface in laminated composites", *Int. J. Fract.* **99** (1999), no. 1, pp. 25–40.
[16] D. Leguillon, "Interface crack tip singularity with contact and friction", *C. R. Acad. Sci. IIB* **327** (1999), no. 5, pp. 437–442.
[17] D. Leguillon and R. Abdelmoula, "Mode III near and far fields for a crack lying in or along a joint", *Intl J. Solids Struct.* **37** (2000), no. 19, pp. 2651–2672.
[18] J. Leblond and D. Leguillon, "The stress intensity factors near an angular point on the front of an interface crack", *Eur. J. Mech. A Solids* **18** (1999), no. 5, pp. 837–857.
[19] M. Williams, "Stress singularities resulting from various boundary condition sinangular corners of plates inextension", *J. Appl. Mech.* **19** (1952), pp. 526–528.
[20] D. Leguillon, "A criterion for crack nucleation at a notch in homogeneous materials", *C. R. Acad. Sci. IIB* **329** (2001), no. 2, pp. 97–102.
[21] D. Leguillon, "Strength or toughness? A criterion for crack onset at a notch", *Eur. J. Mech. A Solids* **21** (2002), no. 1, pp. 61–72.
[22] P. Weißgraeber, D. Leguillon and W. Becker, "A review of finite fracture mechanics: crack initiation at singular and non-singular stress raisers", *Arch. Appl. Mech.* **86** (2016), no. 1–2, pp. 375–401.
[23] A. Doitrand, T. Duminy, H. Girard and X. Chen, *A review of the coupled criterion*, preprint, 2024. Online at https://hal.science/hal-04023438.
[24] A. Sapora, A. Torabi, S. Etesam and P. Cornetti, "Finite Fracture Mechanics crack initiation from a circular hole", *Fatigue Fract. Eng. Mater. Struct.* **41** (2018), no. 7, pp. 1627–1636.
[25] P. Cornetti and A. Sapora, "Penny-shaped cracks by Finite Fracture Mechanics", *Int. J. Fract.* **219** (2019), pp. 153–159.
[26] T. Methfessel, C. El Yaakoubi-Mesbah and W. Becker, "Failure analysis of crack-prone joints with Finite Fracture Mechanics using an advanced modeling approach for the adhesive layer", *Int. J. Adhesion Adhesives* **130** (2024), article no. 103608.
[27] M. Kashtalyan, I. García and V. Mantič, "Evolution of crack density in cross-ply laminates—application of a coupled stress and energy criterion", *Key Eng. Mater.* **713** (2016), pp. 262–265.
[28] A. Doitrand, C. Fagiano, N. Carrére, V. Chiaruttini and M. Hirsekorn, "Damage onset modeling in woven composites based on a coupled stress and energy criterion", *Eng. Fract. Mech.* **169** (2017), pp. 189–200.
[29] J. Li, E. Martin, D. Leguillon and C. Dupin, "A finite fracture model for the analysis of multi-cracking in woven ceramic matrix composites", *Composites B* **139** (2018), pp. 75–83.
[30] J. Vereecke, C. Bois, J. Wahl, T. Briand, L. Ballère and F. Lavelle, "Explicit modelling of meso-scale damage in laminated composites—comparison between finite fracture mechanics and cohesive zone model", *Compos. Sci. Technol.* **253** (2024), article no. 110640.
[31] A. Doitrand, G. Molnár, D. Leguillon, E. Martin and N. Carrère, "Dynamic crack initiation assessment with the coupled criterion", *Eur. J. Mech. A Solids* **93** (2022), article no. 104483.
[32] X. Chen, A. Doitrand, N. Godin and C. Fusco, "Dynamic crack initiation in circular hole PMMA plates considering nonlinear elastic material behavior", *Theor. Appl. Fract. Mech.* **124** (2023), article no. 103783.
[33] A. Doitrand, S. Rubeck, S. Meille, J. Chevalier, P. Steyer and S. Gallois-Garreignot, "Influence of debonding and substrate plasticity on thin film multicracking", *Theor. Appl. Fract. Mech.* **131** (2024), article no. 104375.
[34] J. Li, D. Leguillon, E. Martin and X. Zhang, "Numerical implementation of the coupled criterion for damaged materials", *Int. J. Solids Struct.* **165** (2019), pp. 93–103.

[35] A. Griffith, "The theory of rupture", in *First International Congress on Applied Mechanics, Farnborough*, 1924, pp. 55–63.
[36] G. Irwin, "Analysis of stresses and strains near the end of a crack traversing a plate", *J. Appl. Mech.* **24** (1957), no. 3, pp. 361–364.
[37] G. Irwin, *Fracture*, Springer: Berlin, Heidelberg, 1958, pp. 551–590.
[38] A. Doitrand, D. Leguillon and E. Martin, "Computation of generalized stress intensity factors of 3D singularities", *Int. J. Solids Struct.* **190** (2020), pp. 271–280.
[39] D. Leguillon, D. Quesada, C. Putot and E. Martin, "Prediction of crack initiation at blunt notches and cavities—size effects", *Eng. Fract. Mech.* **74** (2007), no. 15, pp. 2420–2436.
[40] P. E. Labossiere and M. L. Dunn, "Stress intensities at interface corners in anisotropic bimaterials", *Eng. Fract. Mech.* **62** (1999), no. 6, pp. 555–576.
[41] T. Duminy, V. Ayyalasomayajula, A. Doitrand and S. Meille, "Influence of elastic and toughness anisotropy on crack initiation", *Int. J. Solids Struct.* **302** (2024), article no. 112950.
[42] M. Herrera-Garrido, V. Mantič and A. Barroso, "Computational semi-analytic code for stress singularity analysis", *Procedia Struct. Integr.* **42** (2022), pp. 958–966. 23 European Conference on Fracture.
[43] M. Herrera-Garrido, V. Mantič and A. Barroso, "A powerful matrix formalism for stress singularities in anisotropic multi-material corners. Homogeneous (orthogonal) boundary and interface conditions", *Theor. Appl. Fract. Mech.* **119** (2022), article no. 103271.
[44] M. Herrera-Garrido, V. Mantič and A. Barroso, "A semi-analytical matrix formalism for stress singularities in anisotropic multi-material corners with frictional boundary and interface conditions", *Theor. Appl. Fract. Mech.* **129** (2024), article no. 104160.
[45] A. Doitrand, D. Leguillon and R. Estevez, "Experimental determination of generalized stress intensity factors from full-field measurements", *Eng. Fract. Mech.* **230** (2020), article no. 106980.
[46] Z. Yosibash and Y. Schapira, "Edge stress intensity functions in polyhedral domains and their extraction by a quasidual function method", *Int. J. Fract.* **136** (2005), pp. 37–73.
[47] Z. Yosibash and Y. Schapira, "Edge stress intensity functions along elliptic and part-elliptic 3D cracks", *Eng. Fract. Mech.* **245** (2021), article no. 107477.
[48] M. Dunn, W. Suwito and S. Cunningham, "Fracture initiation at sharp notches: correlation using critical stress intensities", *Int. J. Solids Struct.* **34** (1997), no. 29, pp. 3873–3883.
[49] P. Lazzarin, F. Berto and M. Zappalorto, "Rapid calculations of notch stress intensity factors based on averaged strain energy density from coarse meshes: theoretical bases and applications", *Int. J. Fatigue* **32** (2010), no. 10, pp. 1559–1567.
[50] D. Leguillon, "Determination of the length of a short crack at a v-notch from a full field measurement", *Int. J. Solids Struct.* **48** (2011), no. 6, pp. 884–892.
[51] Z. Yosibash, E. Priel and D. Leguillon, "A failure criterion for brittle elastic materials under mixed-mode loading", *Int. J. Fract.* **141** (2006), pp. 291–312.
[52] D. Leguillon and Z. Yosibash, "Crack onset at a v-notch. Influence of the notch tip radius", *Int. J. Fract.* **122** (2003), pp. 1–21.
[53] E. Priel, Z. Yosibash and D. Leguillon, "Failure initiation at a blunt V-notch tip under mixed mode loading", *Int. J. Fract.* **149** (2008), pp. 143–173.
[54] P. Cornetti, D. Taylor and A. Carpinteri, "An asymptotic matching approach to shallow-notched structural elements", *Eng. Fract. Mech.* **77** (2010), no. 2, pp. 348–358.
[55] D. Picard, D. Leguillon and C. Putot, "A method to estimate the influence of the notch-root radius on the fracture toughness measurement of ceramics", *J. Eur. Ceram. Soc.* **26** (2006), no. 8, pp. 1421–1427.
[56] A. Doitrand and D. Leguillon, "Numerical modeling of the nucleation of facets ahead of a primary crack under mode I+III", *Int. J. Fract.* **123** (2018), no. 1, pp. 37–50.
[57] D. Leguillon and R. Piat, "Fracture of porous materials—influence of the pore size", *Eng. Fract. Mech.* **75** (2008), no. 7, pp. 1840–1853. Critical Distance Theories of Fracture.
[58] A. Doitrand and D. Leguillon, "Asymptotic analysis of pore crack initiation near a free edge", *Theor. Appl. Fract. Mech.* **116** (2021), article no. 103125.
[59] I. García and D. Leguillon, "Mixed-mode crack initiation at a v-notch in presence of an adhesive joint", *Int. J. Solids Struct.* **49** (2012), no. 15, pp. 2138–2149.
[60] A. Doitrand, E. Martin and D. Leguillon, "Numerical implementation of the coupled criterion: matched asymptotic and full finite element approaches", *Finite Elem. Anal. Des.* **168** (2020), article no. 103344.
[61] P. Cornetti, A. Sapora and A. Carpinteri, "Mode mixity and size effect in V-notched structures", *Int. J. Solids Struct.* **50** (2013), no. 10, pp. 1562–1582.
[62] Z. Yosibash and B. Mittelman, "A 3-D failure initiation criterion from a sharp V-notch edge in elastic brittle structures", *Eur. J. Mech. A Solids* **60** (2016), pp. 70–94.
[63] D. Leguillon and S. Murer, "Crack deflection in a biaxial stress state", *Int. J. Fract.* **150** (2008), pp. 75–90.

[64] A. Doitrand, D. Leguillon, G. Molnár and V. Lazarus, "Revisiting facet nucleation under mixed mode I+III loading with T-stress and mode-dependent fracture properties", *Int. J. Fract.* **242** (2023), pp. 85–106.
[65] V. Tran, D. Leguillon and A. Krishnan, "Interface crack initiation at V-notches along adhesive bonding in weakly bonded polymers subjected to mixed-mode loading", *Int. J. Fract.* **176** (2012), pp. 65–79.
[66] D. Leguillon and E. Martin, "The strengthening effect caused by an elastic contrast—part I: the bimaterial case", *Int. J. Fract.* **179** (2013), pp. 157–167.
[67] D. Leguillon and E. Martin, "The strengthening effect caused by an elastic contrast—part II: stratification by a thin stiff layer", *Int. J. Fract.* **179(1–2)** (2013), pp. 169–178.
[68] D. Leguillon and S. Murer, "A criterion for crack kinking out of an interface", *Key Eng. Mater.* **385-387** (2008), pp. 9–12.
[69] D. Leguillon, J. Laurencin and M. Dupeux, "Failure initiation in an epoxy joint between two steel plates", *Eur. J. Mech. A Solids* **22** (2003), no. 4, pp. 509–524.
[70] A. Moradi, D. Leguillon and N. Carrére, "Influence of the adhesive thickness on a debonding—an asymptotic model", *Eng. Fract. Mech.* **114** (2013), pp. 55–68.
[71] J. Felger, P. Rosendahl, D. Leguillon and W. Becker, "Predicting crack patterns at bi-material junctions: a coupled stress and energy approach", *Int. J. Solids Struct.* **164** (2019), pp. 191–201.
[72] J. Felger, N. Stein, C. Frey and W. Becker, "Scaling laws for the adhesive composite butt joint strength derived by finite fracture mechanics", *Compos. Struct.* **208** (2019), pp. 546–556.
[73] C. Henninger and D. Leguillon, "Adhesive fracture of an epoxy joint under thermal and mechanical loadings", *J. Therm. Stresses* **31** (2007), no. 1, pp. 59–76.
[74] H. Brillet-Rouxel, E. Arfan, D. Leguillon, M. Dupeux, M. Braccini and S. Orain, "Crack initiation in Cu-interconnect structures, Microelectronic Engineering", *Phys. Scr.* **83** (2007), pp. 2297–2302.
[75] J. Schlosser, E. Martin, C. Henninger, et al., "CFC/Cu bond damage in actively cooled plasma facing components", *Phys. Scr.* (2007), pp. 204–209.
[76] L. Nguyen, D. Leguillon, O. Gillia and E. Riviere, "Bond failure of a SiC/SiC brazed assembly", *Mech. Mater.* **50** (2012), pp. 1–8.
[77] D. Leguillon, S. Tariolle, E. Martin, T. Chartier and J. Besson, "Prediction of crack deflection in porous/dense ceramic laminates", *J. Eur. Ceram. Soc.* **26** (2006), no. 3, pp. 343–349.
[78] C. Lacroix, D. Leguillon and E. Martin, "The influence of an interphase on the deflection of a matrix crack in a ceramic-matrix composite", *Compos. Sci. Technol.* **62** (2002), no. 4, pp. 519–523.
[79] C. Henninger, D. Leguillon and E. Martin, "Crack initiation at a V-notch—comparison between a brittle fracture criterion and the Dugdale cohesive model", *C. R. Méc.* **335** (2007), no. 7, pp. 388–393.
[80] S. Murer and D. Leguillon, "Static and fatigue failure of quasi-brittle materials at a V-notch using a Dugdale model", *Eur. J. Mech. A Solids* **29** (2010), no. 2, pp. 109–118.
[81] J. Zghal, K. Moreau, N. Moës, D. Leguillon and C. Stolz, "Analysis of the failure at notches and cavities in quasi-brittle media using the Thick Level Set damage model and comparison with the coupled criterion", *Int. J. Fract.* **211** (2018), pp. 253–280.
[82] A. Abaza, J. Laurencin, A. Nakajo, S. Meille, J. Debayle and D. Leguillon, "Prediction of crack nucleation and propagation in porous ceramics using the phase-field approach", *Theor. Appl. Fract. Mech.* **119** (2022), article no. 103349.
[83] A. Campagnolo, F. Berto and D. Leguillon, "Fracture assessment of sharp V-notched components under Mode II loading: a comparison among some recent criteria", *Theor. Appl. Fract. Mech.* **85** (2016), pp. 217–226.
[84] D. Leguillon, "An attempt to extend the 2D coupled criterion for crack nucleation in brittle materials to the 3D case", *Theor. Appl. Fract. Mech.* **74** (2014), pp. 7–17.
[85] M. Williams, "On the stress distribution at the base of a stationary crack", *ASME J. App. Mech.* **24** (1957), pp. 109–114.
[86] T. Apel, D. Leguillon, C. Pester and Z. Yosibash, "Edge singularities and structure of the 3-D Williams expansion", *C. R. Méc.* **336** (2008), no. 8, pp. 629–635.
[87] D. Leguillon, "Computation of 3d-singularities in elasticity", in *Boundary Value Problems and Integral Equations in Nonsmooth Domains*, Lecture Notes in Pure and Applied Mathematics, Marcel Dekker: Paris, 1995, pp. 161–170.
[88] D. Leguillon, "A damage model based on singular elastic fields", *C. R. Méc.* **336** (2008), no. 3, pp. 283–288.
[89] D. Leguillon and Z. Yosibash, "Failure initiation at V-notch tips in quasi-brittle materials", *Int. J. Solids Struct.* **122–123** (2017), pp. 1–13.
[90] A. Doitrand and G. Molnár, *Understanding regularized crack initiation through the lens of Finite Fracture Mechanics*, preprint, 2024. Online at https://doi.org/10.21203/rs.3.rs-4583166/v1.
[91] R. Romani, M. Bornert, D. Leguillon, R. Le Roy and K. Sab, "Detection of crack onset in double cleavage drilled specimens of plaster under compression by digital image correlation—theoretical predictions based on a coupled criterion", *Eur. J. Mech. A Solids* **51** (2015), pp. 172–182.

[92] D. Leguillon, E. Martin, O. Ševeček and R. Bermejo, "Application of the coupled stress-energy criterion to predict the fracture behaviour of layered ceramics designed with internal compressive stresses", *Eur. J. Mech. A Solids* **54** (2015), pp. 94–104.

[93] S. Jiménez-Alfaro and D. Leguillon, "Modelling of glass matrix composites by the Coupled Criterion and the Matched Asymptotics approach. The role of a single platelet", *Theor. Appl. Fract. Mech.* **122** (2022), article no. 103650.

[94] S. Jiménez-Alfaro and D. Leguillon, "Modelling of glass matrix composites by the Coupled Criterion and the Matched Asymptotic Approach. The effect of residual stresses and volume fraction", *Theor. Appl. Fract. Mech.* **128** (2023), article no. 104112.

[95] D. Leguillon and E. Martin, "Prediction of multi-cracking in sub-micron films using the coupled criterion", *Int. J. Fract.* **209** (2018), pp. 187–202.

[96] S. Jiménez-Alfaro and D. Leguillon, "Finite fracture Mechanics at the micro-scale. Application to bending tests of micro cantilever beams", *Eng. Fract. Mech.* **258** (2021), article no. 108012.

[97] L. Xu and D. Leguillon, "Dual-notch void model to explain the anisotropic strengths of 3D printed polymers", *J. Eng. Mater. Technol.* (2019), article no. 014501.

[98] D. Quesada, D. Leguillon and C. Putot, "Multiple failures in or around a stiff inclusion embedded in a soft matrix under a compressive loading", *Eur. J. Mech. A Solids* **28** (2009), no. 4, pp. 668–679.

[99] J. Felger, N. Stein and W. Becker, "Asymptotic finite fracture mechanics solution for crack onset at elliptical holes in composite plates of finite-width", *Eng. Fract. Mech.* **182** (2017), pp. 621–634.

[100] E. Tanné, T. Li, B. Bourdin, J.-J. Marigo and C. Maurini, "Crack nucleation in variational phase-field models of brittle fracture", *J. Mech. Phys. Solids* **110** (2018), pp. 80–99.

[101] J.-Y. Wu and V. P. Nguyen, "A length scale insensitive phase-field damage model for brittle fracture", *J. Mech. Phys. Solids* **119** (2018), pp. 20–42.

ACADÉMIE DES SCIENCES
INSTITUT DE FRANCE

Comptes Rendus. Mécanique
2025, Vol. 353, p. 1063-1084
https://doi.org/10.5802/crmeca.325

Research article / *Article de recherche*

An incremental variational method to the coupling between gradient damage, thermoelasticity and heat conduction

Une méthode variationnelle incrémentale pour le couplage entre gradient d'endommagement, thermoélasticité et conduction thermique

Banouho Kamagaté [a,b], Long Cheng [c], Radhi Abdelmoula [d], Emile Danho [b] and Djimédo Kondo [*,a]

[a] Institut Jean Le Rond d'Alembert, CNRS UMR7190, Sorbonne Université, 4 place Jussieu, 75005 Paris, France

[b] Laboratoire de Mécanique et Informatique, UFR Mathématique et Informatique, Université Félix Houphouët-Boigny, rue des écoles, Abidjan, Côte d'Ivoire

[c] GeoRessources Laboratory, Université de Lorraine (ENSG), CNRS UMR7359, 54518 Vandoeuvre-lès-Nancy, France

[d] Laboratoire des Sciences des Procédés et des Matériaux, Institut Galilée, Université Sorbonne Paris Nord, CNRS UPR3407, 93430 Villetaneuse, France

E-mail: djimedo.kondo@sorbonne-universite.fr

Abstract. In this work, we propose an incremental variational approach to study the coupling between gradient damage, thermoelasticity and heat conduction phenomena. To this end, we first extend the thermodynamics of linear thermoelasticity to incorporate gradient damage phenomena. After carefully introducing the concept of *kinetic entropy* to describe the interaction between thermoelasticity and heat conduction, this extension is implemented to establish a four-field incremental energy minimization procedure. By considering a suitable *kinetic entropy* approximation, the latter is then consistently reduced to a three-field (displacement, damage, and absolute temperature) dependency, numerically implemented by means of a staggered optimization algorithm. Applications consisting in a study of the cracking of a plate under thermal shocks are considered. The approach is shown to deliver reliable predictions, based on comparison to available experimental observations which is also provided.

Résumé. Dans ce travail, nous proposons une approche variationnelle incrémentale pour étudier le couplage entre les phénomènes d'endommagement non local, thermoélasticité et conduction thermique. À cette fin, nous étendons d'abord le cadre thermodynamique de la thermoélasticité linéaire afin d'y intégrer les phénomènes d'endommagement non local. Après avoir soigneusement introduit le concept d'*entropie cinétique* pour décrire l'interaction entre thermoélasticité et conduction thermique, cette extension est mise en œuvre pour établir une procédure de minimisation de l'énergie incrémentale à quatre champs. En considérant une approximation adaptée de l'*entropie cinétique*, cette procédure est ensuite réduite de manière cohérente à une dépendance en trois champs (déplacement, endommagement et température absolue), mise en œuvre numériquement au moyen d'un algorithme d'optimisation alternée. Des applications sont proposées,

* Corresponding author

consistant en l'étude de la fissuration d'une plaque soumise à des chocs thermiques. L'approche montre sa capacité à fournir des prédictions fiables, une comparaison avec les observations expérimentales disponibles étant également présentée.

Keywords. Gradient damage model, thermoelasticity, heat conduction, thermodynamics-based formulation, incremental variational approach.

Mots-clés. Modèle à gradient d'endommagement, thermoélasticité, conduction thermique, formulation fondée sur la thermodynamique, approche variationnelle incrémentale.

Note. Article submitted by invitation.

Note. Article soumis sur invitation.

Manuscript received 4 May 2025, revised 18 September 2025, accepted 20 September 2025.

1. Introduction

Thermoelasticity theory describes the interaction between deformations and temperature variations in materials and constitutes a fundamental framework in the physics of continuous media. The first variational formulation of coupled linearized thermoelasticity can be traced back to the pioneering work of [1] (see also [2]), which was based on the thermodynamics of irreversible processes and employed Fourier's law for heat conduction. This approach has been later followed and extended by several works, such as [3–8]. These studies contributed to a systematic treatment of the coupled equations governing mechanics and heat conduction. However, most of these approaches do not provide a variational framework; that is, they do not allow for the construction of an energy functional whose minimization allows to rigorously yield the field equations of linear thermoelasticity. As a result, and strictly speaking, models proposed in this framework do not possess a fully variational structure; rather, they fall within the scope of so-called quasi-variational formulations (see for instance [9,10]). An alternative formulation of thermoelasticity has been proposed by [11] who distinguished three types of coupled thermoelasticity models among which Type II which is of particular interest for variational formulation due to the fact that its heat conduction law is dissipationless (at the difference of Fourier law). A systematic analysis of these three Green–Naghdi types of models has been done by [12]. These studies highlight the lack of a truly well-established variational formulation for coupled linear thermoelasticity with Fourier type heat conduction, and they also lack an explicit recognition of the need for thermodynamics-based variational formulations capable of accounting for the coupling between thermoelasticity, heat conduction, and dissipative phenomena.

To address the issue of establishing variational formulations in presence of thermomechanical couplings, [13] proposed an incremental variational approach based on thermodynamics of irreversible processes. Their approach consists in introducing an integration factor that is based on a time rescaling of the dissipation potential (see also [14]). This factor, expressed as the ratio of the external temperature to the equilibrium temperature, must remain equal to one throughout the system at equilibrium. Essentially, the equality of these two temperatures acts as an internal constraint in the variational analysis, which relaxes at equilibrium and enables the incorporation of strong coupling between damage and thermal mechanisms during entropy production. Independently, in the same year, [15] proposed a time-discretization scheme, in a study on shape memory alloys, to obtain solutions to the incremental problem by optimizing the corresponding functional $\mathscr{F}$. Following these works, a series of studies have been proposed in the incremental variational setting. Among them, particular attention can be paid to [14,16,17] and more recently [18–20]. Note also the study by [12] who also attempted to provide an incremental variational formulation for the three types of Green and Naghdi's thermoelasticity models.

Despite their interest, these approaches still need to be extended in order to account for nonlocal dissipative mechanisms such as in plasticity or damage processes. The present study aims

to extend the incremental variational formulation to non local damage models for which there is no equivalent publication, except for [20], in which a four-field mixed variational approach was recently proposed without numerical implementation nor simulation.

Coming to the coupling between gradient damage with thermoelasticity, it has attracted increasing attention, particularly for simulating thermomechanical degradation phenomena such as thermal shock-induced cracking. This has led to a variety of modeling strategies, mainly based on phase-field methods, where the temperature field is often assumed to be known, typically obtained from an independent solution to the heat equation. This simplification allows for a variational formulation restricted to the displacement and damage fields. In this context, one may mention the works of [21–24], in which the evolution of the temperature field is solved independently of the mechanical problem. The resulting thermal field is then used as a prescribed input in the phase-field model. Another class of models, such as those proposed in [25–28], lacks a variational structure and does not rigorously integrate damage within a thermoelastic coupling framework.

In the present study, by taking advantage of thermodynamics of irreversible processes, we aim at developing variational gradient damage models with coupled thermoelasticity. Moreover, based on some experimental data (see for instance [29]) and following [15], the intrinsic contribution of the damage in the heat production could be neglected. In this perspective, the above mentioned integration factor will not be considered in the corresponding variational analysis. Consequently, the variational structure which is preserved and addressed herein corresponds to a so-called moderate coupling between the damage and thermoelasticity. This is of course an approximation but will lead to easier calculations which are expected to yield sufficiently accurate predictions. It is important to emphasize that this moderate coupling framework still accounts for the influence of thermoelasticity on entropy evolution, which remains affected by the presence of damage.

The paper is organized as follows. Based on the framework of thermodynamics of irreversible processes, we develop in Section 2 an incremental variational principle for the coupled problem, which involves four fields: displacement, damage, temperature, and the so-called kinetic entropy.

The latter is then carefully approximated in each increment that allows to reduce and express the incremental variational principle as based on functional of the three former fields. This formulation is further applied in Section 3 to obtain a variational model for the concerned coupled system.

Finally, by making use of a staggered optimization algorithm, we apply the proposed model to simulate cracking of a plate under thermal shocks loadings. A comparison to available experimental observations of [30] is also provided.

2. General formulation of incremental variational principle for the coupled problem

This section deals with a thermodynamics based formulation of an incremental variational framework for gradient damage process coupled with thermoelasticity as well as heat conduction. We assume that the material is subject to infinitesimal strains and small temperature variations.

2.1. *Thermodynamics of the coupling between linearized thermoelasticity and gradient damage*

Let us consider a continuum medium, denoted by Ω, for which the global form of the first and second principles of thermodynamics are classically expressed as:

$$\dot{\mathscr{E}} = -\mathscr{P}_{\text{int}} + \mathscr{P}_{\text{cal}}; \qquad \dot{\mathscr{S}} \geq \int_{\Omega} \frac{r}{T}\,\mathrm{d}\Omega - \int_{\partial\Omega} \frac{\boldsymbol{q}\cdot\boldsymbol{n}}{T}\,\mathrm{d}S \tag{1}$$

where $\mathscr{E}$ is the global internal energy; $\mathscr{P}_{\text{int}}$ accounts for the power of internal work including that of possible microforces; $\mathscr{P}_{\text{cal}}$ symbolizes the calorific power received by the system, which is furnished by the external heat supplies per unit volume, denoted by r, and per unit surface, denoted by $\boldsymbol{q}$; $\mathscr{S}$ gives the global entropy; $\boldsymbol{n}$ is the unit outward normal on the boundary of $\partial\Omega$ and T the local absolute temperature.

In order to incorporate the gradient damage mechanism, we mainly rely on the work of [31] by introducing the internal variables such as the damage, denoted by α, and its gradient $\nabla\alpha$, with the latter characterizing the non-local effect of damage. In this context, the power of interior forces not only requires the classical term $\boldsymbol{\sigma} : \dot{\boldsymbol{\varepsilon}}$, where $\boldsymbol{\sigma}$ denotes the Cauchy stress tensor; $\dot{\boldsymbol{\varepsilon}}$ is the rate of the linearized strain tensor $\boldsymbol{\varepsilon} = \nabla_s \boldsymbol{u}$ (with $\boldsymbol{u}$ the displacement vector and ∇_s the symmetric gradient operator), but also incorporates the microscopic forces associated to damage α and its gradient $\nabla\alpha$, which are respectively denoted by Y_α and $\boldsymbol{Y}_{\nabla\alpha}$. One has then:

$$\mathscr{P}_{\text{int}} = -\int_\Omega \boldsymbol{\sigma} : \dot{\boldsymbol{\varepsilon}}\, \mathrm{d}\Omega - \int_\Omega \left(Y_\alpha \dot{\alpha} + \boldsymbol{Y}_{\nabla\alpha} \cdot \nabla\dot{\alpha} \right) \mathrm{d}\Omega. \tag{2}$$

As classically, let us introduce the Helmholtz free energy per unit volume, denoted by w, a function of the state variables, such that:

$$w := w(\boldsymbol{\varepsilon}, T, \alpha, \nabla\alpha). \tag{3}$$

Note that w is separately convex with respect to $\boldsymbol{\varepsilon}$, α and $\nabla\alpha$, but concave with respect to T.

The state laws which furnish the reversible forces are then derived as (see Appendix A):

$$\boldsymbol{\sigma}^{\text{nd}} = \frac{\partial w}{\partial \boldsymbol{\varepsilon}}; \qquad s = -\frac{\partial w}{\partial T}; \qquad Y_\alpha^{\text{nd}} = \frac{\partial w}{\partial \alpha}; \qquad \boldsymbol{Y}_{\nabla\alpha}^{\text{nd}} = \frac{\partial w}{\partial \nabla\alpha} \tag{4}$$

with s the entropy per unit volume of the solid. The superscripts "nd" denotes the non-dissipative part of the related thermodynamic forces.

Also, the Clausius–Duhem inequality (positivity of the dissipation) can be derived as:

$$\mathscr{D} = \underbrace{\boldsymbol{\sigma} : \dot{\boldsymbol{\varepsilon}} - \dot{w} - s\dot{T} + Y_\alpha \dot{\alpha} + \boldsymbol{Y}_{\nabla\alpha} \cdot \nabla\dot{\alpha}}_{\mathscr{D}_{\text{int}}} \underbrace{- \frac{\nabla T}{T} \cdot \boldsymbol{q}}_{\mathscr{D}_{\text{th}}} \geq 0. \tag{5}$$

This local dissipation $\mathscr{D}$ can be classically decomposed into two parts: the intrinsic dissipation $\mathscr{D}_{\text{int}}$ and the thermal dissipation due to heat conduction $\mathscr{D}_{\text{th}}$.

Since the strain field $\boldsymbol{\varepsilon}$ is non-dissipative in thermoelasticity, it follows that the dissipative component of the associated thermodynamic force vanish, i.e. $\boldsymbol{\sigma}^{\text{d}} = \boldsymbol{\sigma} - \boldsymbol{\sigma}^{\text{nd}} = 0$. Consequently, eq. (5) reduces then to:

$$\mathscr{D} = \underbrace{\boldsymbol{Y}_\alpha^{\text{d}} \dot{\alpha} + \boldsymbol{Y}_{\nabla\alpha}^{\text{d}} \cdot \nabla\dot{\alpha}}_{\mathscr{D}_{\text{int}}} \underbrace{- \frac{\nabla T}{T} \cdot \boldsymbol{q}}_{\mathscr{D}_{\text{th}}} \geq 0 \tag{6}$$

where $\boldsymbol{Y}_\alpha^{\text{d}}$ and $\boldsymbol{Y}_{\nabla\alpha}^{\text{d}}$ are the dissipative thermodynamic forces of α and $\nabla\alpha$, satisfying $Y_\alpha^{\text{d}} = Y_\alpha - Y_\alpha^{\text{nd}}$ and $\boldsymbol{Y}_{\nabla\alpha}^{\text{d}} = \boldsymbol{Y}_{\nabla\alpha} - \boldsymbol{Y}_{\nabla\alpha}^{\text{nd}}$, respectively.

To characterize the evolution of dissipative systems in the context of Generalized Standard Materials (GSM) framework [32], one can resort to the dissipation potential, denoted by φ. Following [13], and in the case of a coupling between thermoelasticity and gradient damage, a joint form can be adopted:

$$\varphi\left(\dot{\alpha}, \nabla\dot{\alpha}, -\frac{\nabla T}{T}; \alpha, \nabla\alpha, T\right) = \varphi^M(\dot{\alpha}, \nabla\dot{\alpha}; \alpha, \nabla\alpha) - \varphi^T\left(-\frac{\nabla T}{T}; T\right) \tag{7}$$

where φ^M and φ^T respectively correspond to the damage dissipation and that of heat conduction. The latter owns the positiveness of the dissipation associated with heat conduction. Note that

both φ^M and φ^T are convex with respect to their respective arguments. It follows from eq. (7) that φ is convex with respect to $\dot{\alpha}$ and $\nabla\dot{\alpha}$, but concave with respect to $-\nabla T/T$. One has:[1]

$$Y_\alpha^{\mathrm{d}} = \frac{\partial\varphi}{\partial\dot{\alpha}}; \qquad \boldsymbol{Y}_{\nabla\alpha}^{\mathrm{d}} = \frac{\partial\varphi}{\partial\nabla\dot{\alpha}}; \qquad \boldsymbol{q} = \frac{\partial\varphi^T}{\partial\left(-\frac{\nabla T}{T}\right)} \tag{8}$$

Concerning the dissipative processes, we recall that the corresponding dissipation potential is assumed to take a joint form (see eq. (7)), wherein the damage dissipation potential φ^M and that of the thermal conduction φ^T are combined but remain decoupled. Since this study aims to provide a first attempt at formulating an incremental variational framework for modeling gradient damage mechanisms coupled with thermoelasticity and heat conduction, a *moderate* coupling framework, as mentioned in Section 1, is adopted, in which the damage process affects the entropy evolution only through the thermoelastic potential.

For more details on the thermodynamic formulations presented above, readers are referred to Appendix A. In the following part of this section, inspired by [13] (see also [14]), a rate form of the total energy functional which involves the two above potentials will be proposed. Its integral over the time increment will allow to construct an incremental energy functional. Stationarity of the latter will allow to establish the solution of the concerned coupled problem.

2.2. *Incremental variational principle*

Let us consider a system subjected to some mechanical and/or external thermal actions. Specifically, the mechanical loads could be composed of surface forces $\boldsymbol{T}$ applied on the Neumann boundary $\partial_{\boldsymbol{T}}\Omega$ and an external displacement $\overline{\boldsymbol{u}}$ on the Dirichlet part $\partial_{\boldsymbol{u}}\Omega$, where $\partial_{\boldsymbol{T}}\Omega \cup \partial_{\boldsymbol{u}}\Omega = \partial\Omega$ and $\partial_{\boldsymbol{T}}\Omega \cap \partial_{\boldsymbol{u}}\Omega = \emptyset$. Concerning the external thermal charge, the boundary of the medium could be subjected to a heat supply Q on its Neumann surface $\partial_Q\Omega$ and prescribed temperature $\overline{T}$ on the Dirichlet border $\partial_T\Omega$, for which we have $\partial_Q\Omega \cup \partial_T\Omega = \partial\Omega$ and $\partial_Q\Omega \cap \partial_T\Omega = \emptyset$. Furthermore, a body force per unit volume, denoted by $\boldsymbol{F}$, can be considered. It follows that the external power functional reads (see also [13]):

$$P_{\mathrm{ext}} := \int_\Omega \boldsymbol{F}\cdot\dot{\boldsymbol{u}}\,\mathrm{d}\Omega + \int_{\partial_{\boldsymbol{T}}\Omega} \boldsymbol{T}\cdot\dot{\boldsymbol{u}}\,\mathrm{d}S + \int_{\partial_Q\Omega} Q\log\frac{T}{T_0}\,\mathrm{d}S. \tag{9}$$

Since we consider the Helmholtz free energy, it may be more appropriate to consider the temperature field to be in equilibrium at any given time t. Yet, due to thermal diffusion, heat tends to enter the material point and alter its entropy, which corresponds to some kinetic behaviors. To describe this process, we assume that the entropy change occurs at a non-equilibrium state, denoted as time t^-. In this perspective and inspired by recent work by [33] on the coupling between gradient damage, poroelasticity, and fluid flow in porous media, we distinguish between equilibrium entropy s and a so-called *kinetic entropy*, denoted by $\hat{s}$, which must be equivalent at equilibrium states at time t. Furthermore, the reversible process of the concerned open system is described by the power $\dot{w} + \hat{s}\dot{T}$. Following [13,14], and inspired by [34] for elasto(visco)-plasticity, [35,36] for gradient plasticity, or [37], etc., let us introduce the rate form of total energy functional for damage coupled with thermoelastic behavior:

$$\Pi(\dot{\boldsymbol{u}}, \dot{T}, s, \dot{\alpha}; T) = \int_\Omega \dot{w}(\dot{\boldsymbol{\varepsilon}}, \dot{T}, \dot{\alpha}, \nabla\dot{\alpha}) + \hat{s}\dot{T} + \varphi\left(\dot{\alpha}, \nabla\dot{\alpha}, -\frac{\nabla T}{T}; \alpha, \nabla\alpha, T\right)\mathrm{d}\Omega - P_{\mathrm{ext}}. \tag{10}$$

Remark 1. Regarding the concept of *kinetic entropy*, note that the overall system is thermodynamically open due to the presence of external heat sources and/or fluxes. At the local scale, each

[1] In the case where the potential φ is not differentiable, one should refer to the notion of subdifferential $\partial\varphi$, e.g. the evolution law for α then taking the form: $\mathscr{A}_\alpha \in \partial_{\dot{\alpha}}\varphi$. The irreversible force $\mathscr{A}_\alpha$ is said to belong to the sub-gradient of φ at the considered point.

material point is assumed to be in a thermodynamically non-equilibrium state at time t^- due to the thermal diffusion, whereby heat tends to enter the point and modify its entropy. The same material point is then considered to reach equilibrium at time t. The characterization of this kinetic entropy will be done in the following by considering eqs. (12) and (13) in the variational point of view.

We now proceed to establish an incremental variational problem in order to reduce the time-dependent nature such that the solution is expected to be given by the optimization of an incremental total energy functional. Specifically, the total time path $[t_0, t_f]$ is discretized into a sequence of time steps: $t_0 = 0, \ldots, t_n, t_{n+1}, \ldots, t_N = t_f$. The state at each step is determined by consistently optimizing within each time interval $[t_n, t_{n+1}]$. Given the known state $(\boldsymbol{\varepsilon}_n, T_n, \hat{s}_n, \alpha_n)$ at time t_n, we seek to find the corresponding unknown state $(\boldsymbol{\varepsilon}_{n+1}, T_{n+1}, \hat{s}_{n+1}, \alpha_{n+1})$ at t_{n+1}. In this context, we define the following functional to characterize the incremental evolution:

$$I_n(\boldsymbol{\varepsilon}_{n+1}, T_{n+1}, \hat{s}_{n+1}, \alpha_{n+1}) = \int_{t_n}^{t_{n+1}} \Pi(\dot{\boldsymbol{u}}, \dot{T}, \hat{s}, \dot{\alpha}; T)\, \mathrm{d}t. \tag{11}$$

Taking variation of eq. (11) respectively respect to $\boldsymbol{u}$, T and α, and enforcing the stationarities t_{n+1} yield (see Appendix B for details):

$$\begin{cases} \operatorname{div}\boldsymbol{\sigma}_{n+1} + \boldsymbol{F}_{n+1} = \boldsymbol{0}; & \forall\, \boldsymbol{x} \in \Omega \\ \boldsymbol{\sigma}_{n+1} \cdot \boldsymbol{n} = \boldsymbol{T}_{n+1}; & \forall\, \boldsymbol{x} \in \partial_{\boldsymbol{T}}\Omega \\ \hat{s}_{n+1} = s_{n+1}; & \forall\, \boldsymbol{x} \in \Omega \\ Y_\alpha|_{n+1} - \operatorname{div}\boldsymbol{Y}_{\nabla\alpha}|_{n+1} = 0; & \forall\, \boldsymbol{x} \in \Omega \\ \boldsymbol{Y}_{\nabla\alpha}|_{n+1} \cdot \boldsymbol{n} = 0; & \forall\, \boldsymbol{x} \in \partial\Omega \end{cases} \tag{12}$$

and in the interval $[t_n, t_{n+1}]$:

$$\begin{cases} \dot{\hat{s}} + \operatorname{div}\dfrac{\boldsymbol{q}}{T} = 0; & \forall\, \boldsymbol{x} \in \Omega \\ \boldsymbol{q} \cdot \boldsymbol{n} = Q; & \forall\, \boldsymbol{x} \in \partial_Q\Omega \\ \left[\dfrac{\partial\varphi}{\partial\alpha} - \dfrac{\mathrm{d}}{\mathrm{d}t}\left(\dfrac{\partial\varphi}{\partial\dot{\alpha}}\right)\right] - \operatorname{div}\left[\dfrac{\partial\varphi}{\partial\nabla\alpha} - \dfrac{\mathrm{d}}{\mathrm{d}t}\left(\dfrac{\partial\varphi}{\partial\nabla\dot{\alpha}}\right)\right] = 0; & \forall\, \boldsymbol{x} \in \Omega \\ \left[\dfrac{\partial\varphi}{\partial\nabla\alpha} - \dfrac{\mathrm{d}}{\mathrm{d}t}\left(\dfrac{\partial\varphi}{\partial\nabla\dot{\alpha}}\right)\right] \cdot \boldsymbol{n} = 0; & \forall\, \boldsymbol{x} \in \partial\Omega \\ \dot{T} = 0; & \forall\, \boldsymbol{x} \in \Omega \end{cases} \tag{13}$$

eqs. (12) furnish the Euler–Lagrange equations of I_n and the Neumann boundary conditions at t_{n+1}, while eqs. (13) allow to determine the optimization path. Their derivation is presented in detail in Appendix B. All of them are expressed thanks to the thermodynamics potentials allowing to take into account the non-local damage effects. Essentially, these equations make I_n to be stationary in $[t_n, t_{n+1}]$. Let us suppose the thermodynamics potentials as classically being quadratic, and recall their convexity as discussed in Section 2.1. It follows that I_n must be convex with respect to u_{n+1} and α_{n+1} but concave with respect to T_{n+1}. We can hence establish the following incremental variational principle:

$$(\boldsymbol{u}_{n+1}, T_{n+1}, \hat{s}_{n+1}, \alpha_{n+1}) = \operatorname{Arg} \inf_{\boldsymbol{u}'_{n+1}, \alpha'_{n+1}} \operatorname{stat}_{T'_{n+1}, \hat{s}'_{n+1}} \left\{ I_n(\boldsymbol{u}'_{n+1}, T'_{n+1}, \hat{s}'_{n+1}, \alpha'_{n+1}) \right\} \tag{14}$$

with $(\boldsymbol{u}_{n+1}, T_{n+1}, \hat{s}_{n+1}, \alpha_{n+1})$ henceforth the estimate of the expected solution and $(\boldsymbol{u}'_{n+1}, T'_{n+1}, \hat{s}'_{n+1}, \alpha'_{n+1})$ denoting the admissible fields of the displacement, the absolute temperature, the *kinetic entropy* as well as that of the damage, respectively.

2.3. *A reduced form of the variational scheme*

As demonstrated above, the application of the incremental variational principle (14) necessitates the calculation of the optimization path, whose numerical implementation might be performed via a fully implicit algorithm. However, as discussed in [38] (see also [13,33]), this path calculation could be treated as avoidable except for some particular case. Instead, a *weak* quantification of I_n that aligns with the field equations at t_{n+1} could be sufficient. From this perspective, we employ backward Euler approximations for the following rate fields:

$$\dot{\boldsymbol{u}} \simeq \frac{\boldsymbol{u}_{n+1}-\boldsymbol{u}_n}{\Delta t}; \qquad \dot{\alpha} \simeq \frac{\alpha_{n+1}-\alpha_n}{\Delta t}; \qquad \dot{T} \simeq \frac{T_{n+1}-T_n}{\Delta t}; \tag{15}$$

where $\Delta t = t_{n+1} - t_n$.

Recall that, as aforementioned, the entropy simultaneously presents some *equilibrium* and *kinetic* behaviors at any given time.[2] In this perspective and in the context of incremental variational framework, we assume that the entropy is considered to be in a non-equilibrium (i.e., kinetic) state at time t_n, and it relaxes to an equilibrium state at t_{n+1}. The continuity of $\hat{s}$ in time dimension makes:

$$\hat{s} \simeq s_n = -\frac{\partial w}{\partial T}(\boldsymbol{u}_n, T_n, \alpha_n, \nabla\alpha_n). \tag{16}$$

This expression actually corresponds to an optimization of the kinetic entropy over the previous increment. Indeed, as shown for instance in [39], the kinetic entropy $\hat{s}$ can be approximated at any time within the interval $[t_n, t_{n+1})$, except at the final time t_{n+1}, which is considered here as the stationary state to be determined. In summary, this type of approximation, as will be demonstrated in the following, ensures a consistent representation of the coupled constitutive relations and guarantees satisfactory convergence as $\Delta t \to 0$. By considering eqs. (3), (7), (15) and (16) and making use of the rectangular rule for the time integration of φ as well as the term of thermal boundary condition, the incremental energy I_n can be calculated as:

$$\begin{aligned} I_n(\boldsymbol{u}_{n+1}, T_{n+1}, \alpha_{n+1}) \simeq & \int_\Omega (w_{n+1} - w_n) + s_n(T_{n+1} - T_n)\,\mathrm{d}\Omega + \Delta t \int_\Omega (\varphi^M_{n+1} - \varphi^T_{n+1})\,\mathrm{d}\Omega \\ & - \int_\Omega \boldsymbol{F}_{n+1}\cdot(\boldsymbol{u}_{n+1}-\boldsymbol{u}_n)\,\mathrm{d}\Omega - \int_{\partial_{\boldsymbol{T}}\Omega} \boldsymbol{T}_{n+1}\cdot(\boldsymbol{u}_{n+1}-\boldsymbol{u}_n)\,\mathrm{d}S - \Delta t \int_{\partial_Q\Omega} Q_{n+1}\log\frac{T_{n+1}}{T_n}\,\mathrm{d}S. \end{aligned} \tag{17}$$

Let us compute the variation of eq. (17) with respect to $\boldsymbol{u}_{n+1}, T_{n+1}, \alpha_{n+1}$; the stationarity gives:

$$\begin{cases} \operatorname{div}\dfrac{\partial w_{n+1}}{\partial \boldsymbol{\varepsilon}_{n+1}} + \boldsymbol{F}_{n+1} = 0; & \forall\, \boldsymbol{x} \in \partial\Omega \\ \dfrac{\partial w_{n+1}}{\partial \boldsymbol{\varepsilon}_{n+1}}\cdot\boldsymbol{n} - \boldsymbol{T}_{n+1} = 0; & \forall\, \boldsymbol{x} \in \partial_{\boldsymbol{T}}\Omega \\ T_{n+1}\dfrac{-\frac{\partial w_{n+1}}{\partial T_{n+1}} - s_n}{\Delta t} + \operatorname{div}\dfrac{\partial \varphi^T_{n+1}}{\partial\left(-\frac{\nabla T_{n+1}}{T_{n+1}}\right)} = 0; & \forall\, \boldsymbol{x} \in \Omega \\ \dfrac{\partial \varphi^T_{n+1}}{\partial\left(-\frac{\nabla T_{n+1}}{T_{n+1}}\right)}\cdot\boldsymbol{n} - Q_{n+1} = 0; & \forall\, \boldsymbol{x} \in \partial_Q\Omega \\ \left(\dfrac{\partial w_{n+1}}{\partial \alpha_{n+1}} + \dfrac{\partial \varphi^M_{n+1}}{\partial \dot{\alpha}_{n+1}}\right) - \operatorname{div}\dfrac{\partial w_{n+1}}{\partial \nabla\alpha_{n+1}} + \dfrac{\partial \varphi^M_{n+1}}{\partial \nabla\dot{\alpha}_{n+1}} = \mathcal{O}(\Delta t); & \forall\, \boldsymbol{x} \in \Omega \\ \left(\dfrac{\partial w_{n+1}}{\partial \nabla\alpha_{n+1}} + \dfrac{\partial \varphi^M_{n+1}}{\partial \nabla\dot{\alpha}_{n+1}}\right)\cdot\boldsymbol{n} = \mathcal{O}(\Delta t); & \forall\, \boldsymbol{x} \in \partial\Omega. \end{cases} \tag{18}$$

[2] Specifically, the entropy is kinetic at the non-equilibrium state t^- and equilibrium at t.

Furthermore, by considering eqs. (4) and (8), (18) can be readily recast into:

$$\begin{cases} \operatorname{div}\boldsymbol{\sigma}_{n+1} + \boldsymbol{F}_{n+1} = 0; & \forall\, \boldsymbol{x} \in \Omega \\ \boldsymbol{\sigma}_{n+1} \cdot \boldsymbol{n} - \boldsymbol{T}_{n+1} = 0; & \forall\, \boldsymbol{x} \in \partial_{\boldsymbol{T}}\Omega \\ T_{n+1}\dfrac{s_{n+1} - s_n}{\Delta t} + \operatorname{div}\boldsymbol{q}_{n+1} = 0; & \forall\, \boldsymbol{x} \in \Omega \\ \boldsymbol{q}_{n+1} \cdot \boldsymbol{n} - Q_{n+1} = 0; & \forall\, \boldsymbol{x} \in \partial_Q\Omega \\ Y_\alpha|_{n+1} - \operatorname{div}\boldsymbol{Y}_{\nabla\alpha}|_{n+1} = \mathcal{O}(\Delta t); & \forall\, \boldsymbol{x} \in \Omega \\ \boldsymbol{Y}_{\nabla\alpha}|_{n+1} \cdot \boldsymbol{n} = \mathcal{O}(\Delta t); & \forall\, \boldsymbol{x} \in \partial\Omega \end{cases} \tag{19}$$

which are the governing equations (equilibrium, heat equations, damage criterion) and Neumann boundary conditions associated to $\boldsymbol{u}_{n+1}, T_{n+1}, \alpha_{n+1}$, respectively.

Recalling the convexity of $I_n(\boldsymbol{u}_{n+1}, T_{n+1}, \alpha_{n+1})$ with respect to $\boldsymbol{u}_{n+1}$ and α_{n+1} and the concavity with respect to T_{n+1}, the incremental variational principle of eq. (14) could be reduced into the following form as three fields dependent, such that:

$$(\boldsymbol{u}_{n+1}, T_{n+1}, \alpha_{n+1}) = \operatorname{Arg} \inf_{\boldsymbol{u}_{n+1}', \alpha_{n+1}'} \sup_{T_{n+1}'} \left\{ I_n(\boldsymbol{u}'_{n+1}, T'_{n+1}, \alpha'_{n+1}; \hat{s}) \right\} \tag{20}$$

$\hat{s}$ being aforehand identified in the current increment.

3. A variational model for coupled thermoelasticity with gradient damage

This section aims to apply the established incremental variational principle to a gradient damage model coupled with thermoelasticity and heat conduction. As mentioned before, we assume the material undergoes infinitesimal deformations and small temperature variations. Accordingly, the formulation of the variational model will rely on the choice of a suitable Helmholtz free energy, a damage dissipation potential, and the Fourier potential for heat conduction.

3.1. *Helmholtz free energy and dissipation potentials*

We propose as:

Helmholtz free energy for linear thermoelasticity:

$$w(\boldsymbol{\varepsilon}, T, \alpha) = \frac{1}{2}\boldsymbol{\varepsilon} : \mathbb{C}(\alpha) : \boldsymbol{\varepsilon} - s_0 T - (T - T_0)\boldsymbol{\beta}(\alpha) : \boldsymbol{\varepsilon} - \frac{c(\alpha)}{2T_0}(T - T_0)^2 \tag{21}$$

where $\mathbb{C}(\alpha)$, $\boldsymbol{\beta}(\alpha)$, $c(\alpha)$ are respectively the stiffness tensor, the second order tensor of linear thermal expansion and the heat capacity. A priori, all these material parameters are affected by the damage.

Next, the reversible thermodynamic forces obtained from the state laws read:

$$\begin{aligned} &\boldsymbol{\sigma} = \mathbb{C}(\alpha) : \boldsymbol{\varepsilon} - (T - T_0)\boldsymbol{\beta}(\alpha); \\ &s - s_0 = \boldsymbol{\beta}(\alpha) : \boldsymbol{\varepsilon} + \frac{c(\alpha)}{T_0}(T - T_0); \\ &Y_\alpha^{\mathrm{nd}} = \frac{\partial w}{\partial \alpha}; \\ &\boldsymbol{Y}_{\nabla\alpha}^{\mathrm{nd}} = \boldsymbol{0}. \end{aligned} \tag{22}$$

Dissipation potential: Let us recall that the dissipation potential is considered as in a joint form of the damage dissipation potential φ^M and that for thermal conduction φ^T (see eq. (7)). Following [33,40], the dissipation potential φ^M is chosen:

$$\varphi^M(\dot{\alpha}, \nabla\dot{\alpha}; \alpha, \nabla\alpha) = Y_c(\alpha)\dot{\alpha} + 2l_0^2 w_1 \nabla\alpha \cdot \nabla\dot{\alpha} \tag{23}$$

where $Y_c(\alpha)$ denotes the critical damage energy at current state, l_0 is the material internal length and w_1 the first threshold in energy release rate that can be identified from different damage descriptions (e.g. [41] for AT1 model and [42] for AT2 model).

In addition to satisfying the classical requirements (being a positive scalar-valued function, convex with respect to its arguments, and minimal when the arguments vanish), φ^M is positively homogeneous of degree 1 and have the following remarkable property. Indeed, it corresponds to the so-called *simple dissipative systems*,[3] for which the total dissipated energy until the current time is function only of the current value of internal variables.

Owing to this property, it readily follows that:

$$\int_{t_n}^{t_{n+1}} \varphi^M(\dot{\alpha}, \nabla\dot{\alpha}; \alpha, \nabla\alpha)\,\mathrm{d}t = w_1 l_0 \left[\frac{\omega(\alpha_{n+1}) - \omega(\alpha_n)}{l_0} + l_0\big(\| \nabla\alpha_{n+1} \|^2 - \| \nabla\alpha_n \|^2\big)\right]. \tag{24}$$

It is worthy to note here that eq. (24) allows to obtain a closed-form expression of the related incremental dissipation due to the simple dissipative process without the approximation made in eq. (17). Nevertheless, the incremental variational method proposed in Section 2 remains applicable to more general cases.

Coming now to the dissipation potential φ^T corresponding to thermal dissipation, we assume the validity of the Fourier potential to describe heat conduction:

$$\varphi^T\left(-\frac{\nabla T}{T}; T\right) = \frac{T}{2}\left(-\frac{\nabla T}{T}\right)\cdot \boldsymbol{k} \cdot \left(-\frac{\nabla T}{T}\right) = \frac{\nabla T \cdot \boldsymbol{k} \cdot \nabla T}{2T} \tag{25}$$

where $\boldsymbol{k}$ is the isotropic thermal conductivity tensor that is assumed here as constant.

Since small temperature variations are considered, the force term in the Fourier potential can be approximated as (see for instance [14]):

$$-\frac{\nabla T}{T} \simeq -\frac{\nabla T}{T_r} \tag{26}$$

with T_r a reference temperature that is supposed to be the initial temperature T_0. Additionally, we consider that φ^T is parametrically affected by T_0. Then, eq. (25) can be readily reduced as:

$$\varphi^T\left(-\frac{\nabla T}{T_0}; T_0\right) = \frac{T_0}{2}\left(-\frac{\nabla T}{T_0}\right)\cdot \boldsymbol{k} \cdot \left(-\frac{\nabla T}{T_0}\right) = \frac{\nabla T \cdot \boldsymbol{k} \cdot \nabla T}{2T_0}. \tag{27}$$

3.2. *Derivation of the incremental functional I_n for the proposed variational model*

As discussed in Section 2, the non-dissipative process of the concerned system is described by $\dot{w} + \hat{s}\dot{T}$, in which the kinetic entropy was approximated as $\hat{s} \simeq s_n$. From this assumption, one has:

$$\hat{s} \simeq -\frac{\partial w}{\partial T}(\boldsymbol{\varepsilon}_n, T_n, \alpha_n) = s_0 + \boldsymbol{\beta}(\alpha_n) : \boldsymbol{\varepsilon}_n + \frac{c(\alpha_n)}{T_0}(T_n - T_0)$$

which can be reported as s_n in the incremental energy functional (17).

As mentioned before, this choice $\hat{s} \simeq s_n$ is one of the possible approximations for describing the kinetic entropy. In order to well incorporate the effect of damage on the thermoelastic degradation during the variational calculation, we assume henceforward that the dependence of $\beta(\alpha)$ and $c(\alpha)$ on the damage field α in the current increment is incorporated through a semi-implicit scheme, such that:

$$\hat{s} \simeq s_0 + \boldsymbol{\beta}(\alpha_{n+1}) : \boldsymbol{\varepsilon}_n + \frac{c(\alpha_{n+1})}{T_0}(T_n - T_0) \tag{28}$$

[3] See [43] for an account of simple dissipative systems.

which also corresponds to

$$w_n \simeq \frac{1}{2}\boldsymbol{\varepsilon}_n : \mathbb{C}(\alpha_n) : \boldsymbol{\varepsilon}_n - s_0 T_n - (T_n - T_0)\boldsymbol{\beta}(\alpha_{n+1}) : \boldsymbol{\varepsilon}_n - \frac{c(\alpha_{n+1})}{2T_0}(T_n - T_0)^2. \tag{29}$$

It is important to note here that this approximation is variationally consistent.

In the increment $[t_n, t_{n+1}]$, these two equations lead to:

$$\hat{s}\dot{\hat{T}} \simeq \hat{s}\frac{T_{n+1} - T_n}{\Delta t} = \frac{T_{n+1} - T_n}{\Delta t}\left[s_0 + \boldsymbol{\beta}(\alpha_{n+1}) : \boldsymbol{\varepsilon}_n + \frac{c(\alpha_{n+1})}{T_0}(T_n - T_0)\right] \tag{30}$$

and

$$\begin{aligned} w_{n+1} - w_n \simeq{}& \frac{1}{2}\boldsymbol{\varepsilon}_{n+1} : \mathbb{C}(\alpha_{n+1}) : \boldsymbol{\varepsilon}_{n+1} - \frac{1}{2}\boldsymbol{\varepsilon}_n : \mathbb{C}(\alpha_n) : \boldsymbol{\varepsilon}_n - (T_{n+1} - T_n)s_0 \\ & - \boldsymbol{\beta}(\alpha_{n+1}) : \left[(T_{n+1} - T_0)\boldsymbol{\varepsilon}_{n+1} - (T_n - T_0)\boldsymbol{\varepsilon}_n\right] - \frac{c(\alpha_{n+1})}{2T_0}(T_{n+1} - T_n)(T_{n+1} + T_n - 2T_0) \end{aligned} \tag{31}$$

Still in the context of small temperature variations, the external power functional expressed in eq. (9) can be reduced into:

$$P_{\text{ext}} := \int_\Omega \boldsymbol{F}\cdot\dot{\boldsymbol{u}}\,\mathrm{d}\Omega + \int_{\partial_T\Omega} \boldsymbol{T}\cdot\dot{\boldsymbol{u}}\,\mathrm{d}S + \int_{\partial_Q\Omega} Q\frac{T - T_0}{T_0}\,\mathrm{d}S. \tag{32}$$

Gathering eqs. (23), (24), (27), (30), (31) and (32), the incremental energy functional given by (17) can be recast in the form:

$$\begin{aligned} I_n(\boldsymbol{\varepsilon}_{n+1}, \alpha_{n+1}, T_{n+1}) = {}& \int_\Omega \left[\frac{1}{2}\boldsymbol{\varepsilon}_{n+1} : \mathbb{C}(\alpha_{n+1}) : \boldsymbol{\varepsilon}_{n+1} - (T_{n+1} - T_0)\boldsymbol{\beta}(\alpha_{n+1}) : (\boldsymbol{\varepsilon}_{n+1} - \boldsymbol{\varepsilon}_n)\right. \\ & \left. - \frac{c(\alpha_{n+1})}{2T_0}(T_{n+1} - T_n)^2\right]\mathrm{d}\Omega \\ & + \int_\Omega w_1 l_0\left[\frac{\omega(\alpha_{n+1}) - \omega(\alpha_n)}{l_0} + l_0\left(\| \nabla\alpha_{n+1} \|^2 - \| \nabla\alpha_n \|^2\right)\right]\mathrm{d}\Omega \\ & - \Delta t\int_\Omega \frac{\nabla T_{n+1}\cdot\boldsymbol{k}\cdot\nabla T_{n+1}}{2T_0}\,\mathrm{d}\Omega - \int_\Omega \boldsymbol{F}_{n+1}\cdot(\boldsymbol{u}_{n+1} - \boldsymbol{u}_n)\,\mathrm{d}\Omega \\ & - \int_{\partial_T\Omega} \boldsymbol{T}_{n+1}\cdot(\boldsymbol{u}_{n+1} - \boldsymbol{u}_n)\,\mathrm{d}S - \Delta t\int_{\partial_Q\Omega} Q_{n+1}\frac{T_{n+1} - T_0}{T_0}\,\mathrm{d}S. \end{aligned} \tag{33}$$

Note that in the context of variational optimization, the quantities that depend only on the state at t_n can be treated as constants in the above equation. Moreover, due to the form of the state and dissipation potentials expressed by (21), (23) and (27), it can be readily understood that this incremental energy functional is quadratic in each of its arguments and convex with respect to $\boldsymbol{u}_{n+1}$ and α_{n+1}, but concave with respect to T_{n+1}. Hence, the resolution of the concerned problem can be achieved by applying the incremental variational principle (20). We provide below the governing equations and corresponding boundary conditions, which are obtained based on the variational calculus of eq. (33) with respect to $\boldsymbol{u}_{n+1}$, T_{n+1} and α_{n+1}:

$$\begin{cases} \operatorname{div}\left[\mathbb{C}(\alpha_{n+1}) : \boldsymbol{\varepsilon}_{\boldsymbol{n+1}} - (T_{n+1} - T_0)\boldsymbol{\beta}(\alpha_{n+1})\right] + \boldsymbol{F}_{n+1} = \boldsymbol{0}; & \forall\, \boldsymbol{x} \in \Omega \\ \left[\mathbb{C}(\alpha_{n+1}) : \boldsymbol{\varepsilon}_{n+1} - (T_{n+1} - T_0)\boldsymbol{\beta}(\alpha_{n+1})\right]\cdot\boldsymbol{n} - \boldsymbol{T}_{n+1} = \boldsymbol{0}; & \forall\, \boldsymbol{x} \in \partial_T\Omega \\ c(\alpha_{n+1})\dfrac{T_{n+1} - T_n}{\Delta t} + T_0\boldsymbol{\beta}(\alpha_{n+1}) : \dfrac{\boldsymbol{\varepsilon}_{n+1} - \boldsymbol{\varepsilon}_n}{\Delta t} - \operatorname{div}\boldsymbol{k}\cdot\nabla T_{n+1} = 0; & \forall\, \boldsymbol{x} \in \Omega \\ (-\boldsymbol{k}\cdot\nabla T_{n+1})\cdot\boldsymbol{n} + Q_{n+1} = 0; & \forall\, \boldsymbol{x} \in \partial_Q\Omega \\ \dfrac{\partial w_{n+1}}{\partial\alpha_{n+1}} + w_1\dfrac{\partial\omega(\alpha_{n+1})}{\partial\alpha_{n+1}} - 2w_1 l_0^2\nabla^2\alpha_{n+1} = 0; & \forall\, \boldsymbol{x} \in \Omega \\ (2w_1 l_0^2\nabla\alpha_{n+1})\cdot\boldsymbol{n} = 0; & \forall\, \boldsymbol{x} \in \partial\Omega \end{cases} \tag{34}$$

with ∇^2 the Laplacian operator.

4. Numerical implementation and application

In this section, we deal with a numerical implementation procedure for the proposed variational model coupling gradient damage, thermoelasticity and heat conduction. Since its total energy functional (33) includes a quadratic term of the product between ∇u and α, I_n is hence separately but not globally convex with respect to them. This makes the corresponding global minimization unachievable. However, this issue does not arise between the displacement $\boldsymbol{u}$ and the temperature field T. For this reason, the variational optimization is performed through a semi-staggered algorithm, which is implemented in this work with the open-source computing platform FEniCS [44]. This approach is then applied to the study of plate cracking under thermal shocks in quasi-static conditions.

4.1. *Numerical algorithm*

In order to make the above mentioned semi-staggered optimization in the current increment $[t_n, t_{n+1}]$, we first switch off the damage variation, such that $\alpha := \alpha_n$, and solving the following stationary problem where the thermoelasticity and heat conduction process are coupled:

$$(\boldsymbol{u}_{n+1}, T_{n+1}) = \operatorname{Arg\,stat}\, \boldsymbol{u}'_{n+1}, T'_{n+1}\{I_n^{\text{th}}(\boldsymbol{u}'_{n+1}, T'_{n+1}; \alpha_n)\}. \tag{35}$$

By considering eq. (33) and neglecting the constant terms, I_n^{th} can be explicitly expressed as:

$$\begin{aligned} I_n^{\text{th}}(\boldsymbol{\varepsilon}_{n+1}, T_{n+1}; \alpha_n) = \int_\Omega \Big[& \frac{1}{2}\boldsymbol{\varepsilon}_{n+1} : \mathbb{C}(\alpha_n) : \boldsymbol{\varepsilon}_{n+1} - (T_{n+1} - T_0)\boldsymbol{\beta}(\alpha_n) : (\boldsymbol{\varepsilon}_{n+1} - \boldsymbol{\varepsilon}_n) \\ & - \frac{c(\alpha_n)}{2T_0}(T_{n+1} - T_n)^2 \Big] \mathrm{d}\Omega - \Delta t \int_\Omega \frac{\nabla T_{n+1} \cdot \boldsymbol{k} \cdot \nabla T_{n+1}}{2T_0} \mathrm{d}\Omega - \int_\Omega \boldsymbol{F}_{n+1} \cdot (\boldsymbol{u}_{n+1} - \boldsymbol{u}_n) \mathrm{d}\Omega \\ & - \int_{\partial_T \Omega} \boldsymbol{T}_{n+1} \cdot (\boldsymbol{u}_{n+1} - \boldsymbol{u}_n) \mathrm{d}S - \Delta t \int_{\partial_Q \Omega} Q_{n+1} \frac{T_{n+1} - T_0}{T_0} \mathrm{d}S. \end{aligned} \tag{36}$$

Next, we estimate the damage solution α_{n+1} from the following minimizer:

$$\alpha_{n+1} = \operatorname{Arg\,min}\, \alpha'_{n+1}\{I_n^{\text{dam}}(\alpha'_{n+1})\} \tag{37}$$

where

$$\begin{aligned} I_n^{\text{dam}}(\alpha_{n+1}) = \int_\Omega \Big[& \frac{1}{2}\bar{\boldsymbol{\varepsilon}}_{n+1} : \mathbb{C}(\alpha_{n+1}) : \bar{\boldsymbol{\varepsilon}}_{n+1} - (\overline{T}_{n+1} - T_0)\boldsymbol{\beta}(\alpha_{n+1}) : (\boldsymbol{\varepsilon}_{n+1} - \boldsymbol{\varepsilon}_n) \\ & - \frac{c(\alpha_{n+1})}{2T_0}(\overline{T}_{n+1} - T_n)^2 + w_1 l_0 \left(\frac{\omega(\alpha_{n+1})}{l_0} + l_0 \parallel \nabla \alpha_{n+1} \parallel^2 \right) \Big] \mathrm{d}\Omega \end{aligned} \tag{38}$$

where the bar superscript denotes the optimization of $\boldsymbol{u}_{n+1}$ and T_{n+1} computed from eq. (35).

Specifically, eq. (35) is solved by using the *NonlinearVariationalSolver* module in the open-source DOLFIN [45], which allows an automatic iteration in each time increment with user-defined tolerances of absolute and relative errors as well as the maximal number of iterations, etc. Moreover, mixed finite elements of Lagrange type, i.e. CG1 and CG2 elements, are adopted to discretize the corresponding mixed function space that includes the temperature and the displacement fields. For the damage minimization problem (37), linear Lagrange finite elements (i.e. CG1 elements) and the *PETScTAOSolver* of DOLFIN are utilized. Note that the latter allows to numerically enforce the damage irreversibility condition, i.e. $\dot{\alpha} \geq 0$, by uploading its lower bound at each endpoint of increment, such that $\alpha \in [\alpha_{\min}, 1]$ with $\alpha_{\min} \leftarrow \alpha_{n+1}$. The whole numerical procedure is shown in Algorithm 1.

Algorithm 1: Semi-staggered algorithm proposed and implemented for the model in $[t_0, t_f]$

Input: $\{\boldsymbol{u}_0, \alpha_0, T_0\}$ at t_0
Output: $\{\boldsymbol{u}_n, \alpha_n, T_n\}$ at $t = t_1, \ldots, t_n, t_{n+1}, \ldots, t_N = t_f$
Set initial and boundary conditions;
Initialize $t = t_0$; set final time t_f, absolute tolerance err_{tol} and calculate the constant time increment $\Delta t = \frac{t_f - t_0}{N}$;
Initialize the increment counter with $n = 0$;
while $t \leq t_f$ **do**
  $t = t_{n+1} = t_0 + (n+1)\Delta t$;
  Initialize an iteration counter with $i = 0$; set $(\boldsymbol{u}^0_{n+1}, \alpha^0_{n+1}, T^0_{n+1}) := (\boldsymbol{u}_n, \alpha_n, T_n)$;
  repeat
    Compute $(\boldsymbol{u}^{i+1}_{n+1}, T^{i+1}_{n+1})$ with $(\boldsymbol{u}^i_{n+1}, T^i_{n+1})$ by solving eq. (35)
    Compute α^{i+1}_{n+1} with α^i_{n+1} from minimization of eq. (37)
    $i = i + 1$;
  until $\|\boldsymbol{u}^{i+1}_{n+1} - \boldsymbol{u}^i_{n+1}\|_2 < \text{err}_{\text{tol}}$ ***and*** $\|T^{i+1}_{n+1} - T^i_{n+1}\|_2 < \text{err}_{\text{tol}}$ ***and*** $\|\boldsymbol{\alpha}^{i+1}_{n+1} - \boldsymbol{\alpha}^i_{n+1}\|_2 < \text{err}_{\text{tol}}$;
  update $(\boldsymbol{u}_n, \alpha_n, T_n) \leftarrow (\boldsymbol{u}_{n+1}, \alpha_{n+1}, T_{n+1})$;
  update the lower bound of phase field $\alpha_{\min} = \alpha_{n+1}$.
end

4.2. *Application to plate cracking under thermal shocks*

This section is devoted to the numerical simulation of plate cracking under thermal shock conditions. For application purpose, we consider, as classically $\mathbb{C}(\alpha) = g(\alpha)\mathbb{C}^0$ with $g(\alpha)$ the degradation function that is taken as $g(\alpha) = (1-\alpha)^2$ and $\mathbb{C}^0$ the stiffness tensor of the sound solid. Having in hand this expression, the dilatation tensor can be computed as $\boldsymbol{\beta}(\alpha) = \mathbb{C}(\alpha) : \boldsymbol{a}$ with $\boldsymbol{a}$ the constant tensor of linear thermal expansion (thermal strain tensor). The heat capacity c is also taken constant. As studied in [28] (see also Figure 1), we consider a rectangular plate with a length $L = 25\,\text{mm}$ and a height $H = 9.8\,\text{mm}$. The plate is initially at a temperature, denoted by T_0, whose value depends on the specific test conditions. The right edge of the plate is constrained with zero horizontal displacement to account for the symmetry of the problem, while the other boundaries remain free of stress. A temperature $T_B = 300\,\text{K}$ is applied to these free boundaries to induce the thermal shock process with a temperature drop, such that $\Delta T = T_0 - T_B$.

The material parameters are summarized in Table 1 which can also be found in [28].

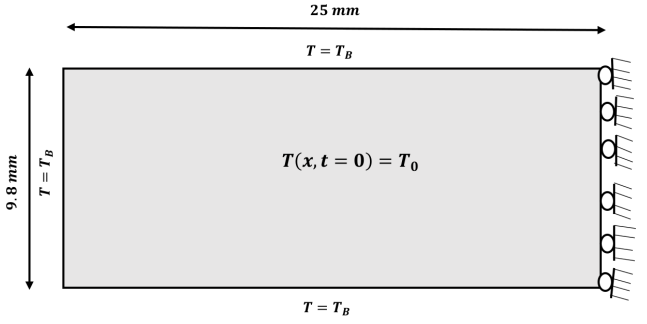

Figure 1. Geometry and boundary conditions of the quenching test on ceramics [30].

Table 1. Material parameters for numerical quenching test reported by [28].

Parameter	Name	Value	Unit
E	Young's modulus	340	GPa
ν	Poisson coefficient	0,22	–
G_c	Critical fracture energy	42.47	J/m^2
κ	Thermal conductivity	300	W(m K)
c	Specific heat capacity	0.775	J/(kg K)
a	Thermal expansion coefficient	$8 \cdot 10^{-6}$	K^{-1}
l_0	Internal length of damage	0.092	mm

4.2.1. *AT1-type gradient damage model applied to the quenching test*

Numerical simulations are carried out by employing the AT1-type damage model. This model is defined by a linear damage function $\omega(\alpha) = \alpha$, and an elastic energy density given by $w_1 = \frac{3G_c}{8l_0}$. To investigate the impact of thermal loading on crack nucleation and propagation, we perform numerical simulations for two initial temperatures $T_0 = 550\,\text{K}$ and 880 K, corresponding to $\Delta T = 250\,\text{K}$ and $\Delta T = 580\,\text{K}$ on the stress free boundaries, respectively.

Figure 2 shows the temperature field T as well as damage field α at times $t = 1\,\mu$s and $t = 10\,\mu$s for $\Delta T = 250\,\text{K}$. It is observed that the temperature field evolves more rapidly near the boundaries of the plate due to a high thermal gradient. This phenomenon leads to a progressive cooling of the plate, starting at the thermal shock boundaries and propagating inward. Concerning cracking (represented by strongly localized damage zone with $\alpha = 1$), it occurs at the boundaries subjected to thermal shock and logically propagates inward. Smaller cracks appear between larger ones, and their propagation is hindered by the presence of the latter.

Figure 3 illustrates the different fields at $t = 10\,\mu$s for another temperature variation $\Delta T = 580\,\text{K}$.

By comparing with Figure 2, the localized damage zone is shown to be more pronounced. It is also observed that cracks, particularly smaller cracks, become more numerous when the temperature variation $\Delta T = 580\,\text{K}$. This is due to a more intense thermal effect at this time $t = 10\,\mu$s in the plate (see Figure 3(a)). Moreover, we show in Figure 4 the contour of the horizontal displacement, denoted by u_x, at $t = 10\,\mu$s respectively for $\Delta T = 250\,\text{K}$ and 580 K. These horizontal displacement fields show jump at the location of vertical cracks. Note that the amplitude of the displacement is different for the two thermal shock conditions.

Finally, it is worth noting that at a sufficiently early time (e.g., $t = 0.01\,\mu$s), no crack appears under the thermal shock load of $\Delta T = 250\,\text{K}$. In contrast, at the same time, cracks are already nucleated under the higher thermal load $\Delta T = 580\,\text{K}$, which induce displacement discontinuities on the two sides of them. Readers are referred to Appendix C for more details about this effect.

4.2.2. *Comparison to experimental observations*

In this section, for comparison purpose, we present numerical predictions by the developed model to experimental data reported by [30]. To this end, we adopt the AT2 model (dissipation function $\omega(\alpha) = \alpha^2$ and $\omega_1 = \frac{G_c}{2\ell_0}$). This choice is justified only by the fact that the thermoelastic parameters considered for the simulations are taken from [28], who also used an AT2-type model to compare their numerical results with the same experimental observations.

The configuration chosen is the same as that previously considered with the AT1 model. The temperature imposed on the edges is: $T_B = 300\,\text{K}$. The initial temperatures are set to $T_0 = 550\,\text{K}$, 680 K and 880 K. These values respectively correspond to temperature variations of $\Delta T = 250\,\text{K}$, 380 K and 580 K on the hole boundary subjected to thermal shock.

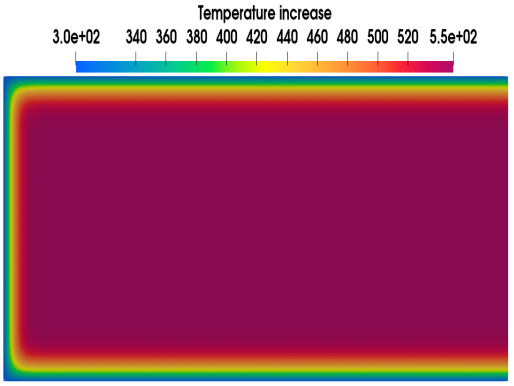

(a) T at $t = 1\,\mu$s

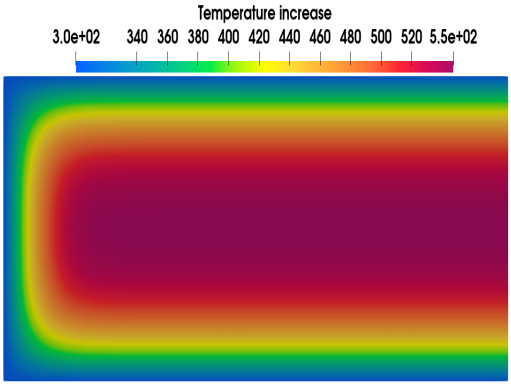

(b) T at $t = 10\,\mu$s

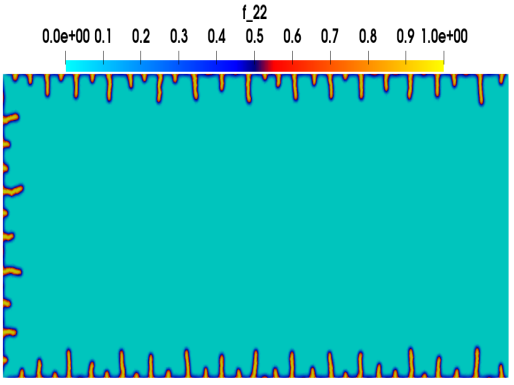

(c) α at $t = 1\,\mu$s

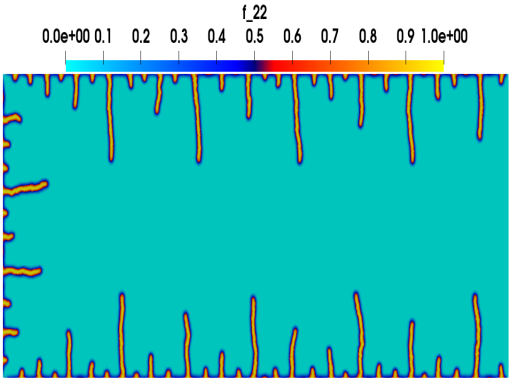

(d) α at $t = 10\,\mu$s

Figure 2. Contours of temperature T and damage fields α at $t = 1\,\mu$s and $10\,\mu$s with $\Delta T = 250\,$K.

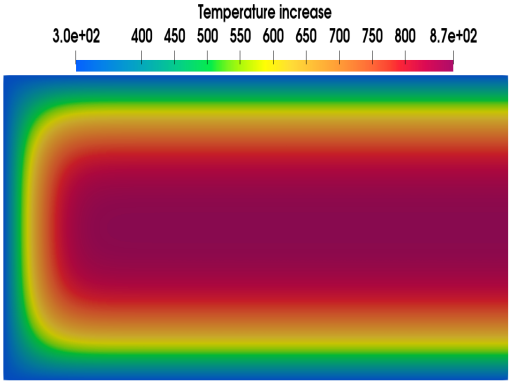

(a) T at $t = 10\,\mu$s

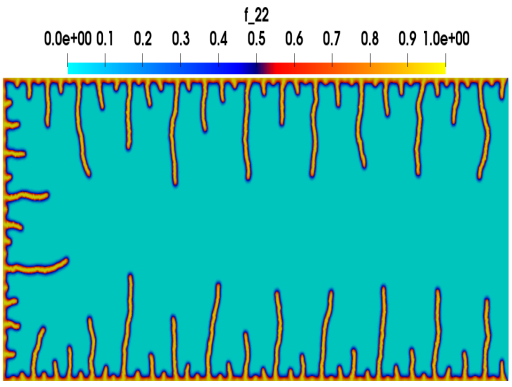

(b) α at $t = 10\,\mu$s

Figure 3. Contours of temperature T and damage fields α at $10\,\mu$s with $\Delta T = 580\,$K.

Figures 5, 6, and 7 illustrate the evolution of the damage pattern α at $t = 10\,\mu$s for different thermal shock amplitudes, as well as the comparison with the experimental results reported

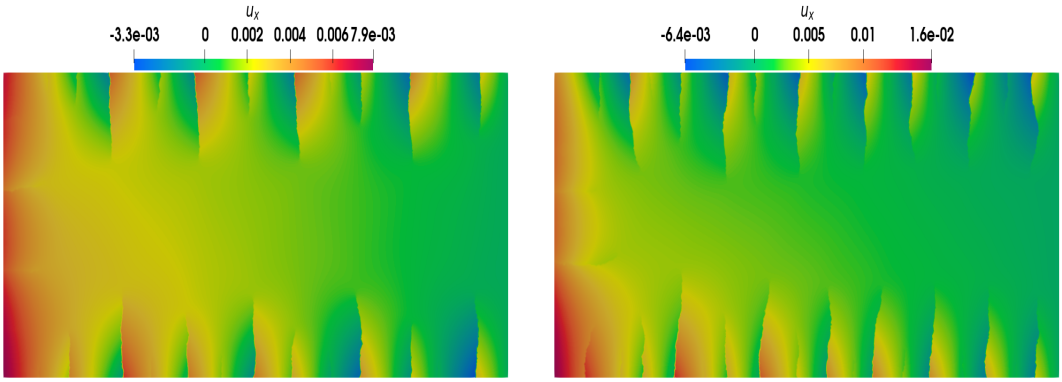

(a) u_x at $t = 10\,\mu$s with $\Delta T = 250\,$K **(b)** u_x at $t = 10\,\mu$s with $\Delta T = 580\,$K

Figure 4. Contours of horizontal displacement (denoted by u_x) at $10\,\mu$s with $\Delta T = 250\,$K and $580\,$K, respectively.

by [30]. The contours of the predicted damage field show good qualitative agreement with the experimental observations. This confirms the ability of the proposed model to realistically reproduce the cracking phenomena induced by transient thermal stress. As previously observed for the AT1 model, cracks develop nucleate from the boundary exposed to thermal shock and propagate towards the interior of the plate. A gradual increase in crack density is also observed as the amplitude of the thermal shock is high, which is in agreement with the experimental results. During the propagation process, numerous short and parallel cracks appear, among which some stop while others continue to propagate. Finally, it can be observed from Figure 8 that increasing ΔT results in a larger number of cracks.

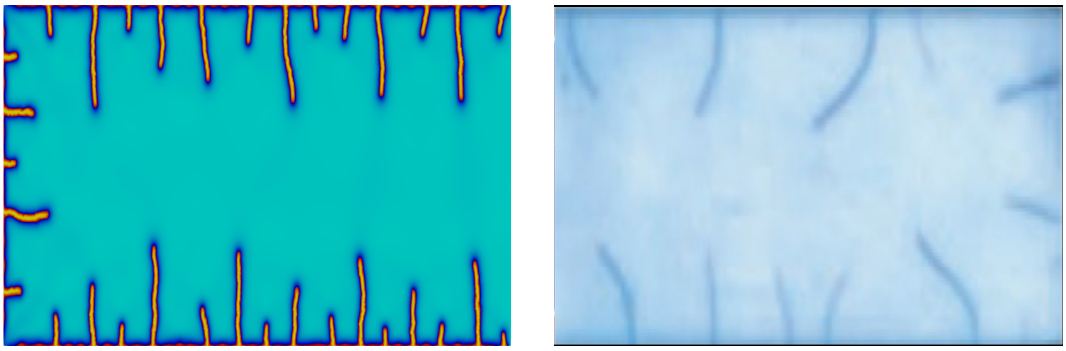

(a) α at $t = 10\,\mu$s **(b)** α at $t = 10\,\mu$s (experimental result)

Figure 5. Predicted damage field α (a) and the corresponding experimental result (b) at $10\,\mu$s with $\Delta T = 250\,$K.

5. Conclusion

In this work, we developed an incremental variational approach for gradient damage coupled with thermoelasticity and heat conduction. This was formulated by relying on the Generalized Standard Materials framework with a particular account of the non local damage. The proposed

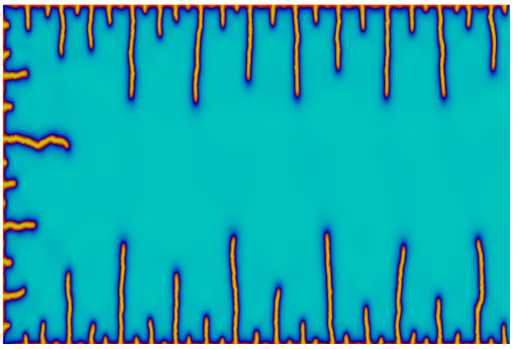

(a) α at $t = 10\,\mu$s

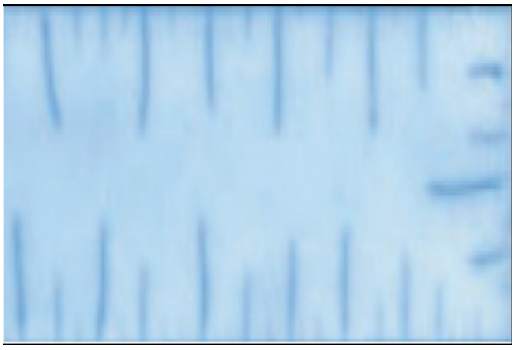

(b) α at $t = 10\,\mu$s (experimental result)

Figure 6. Predicted damage field α (a) and the corresponding experimental result (b) at $10\,\mu$s with $\Delta T = 380\,$K.

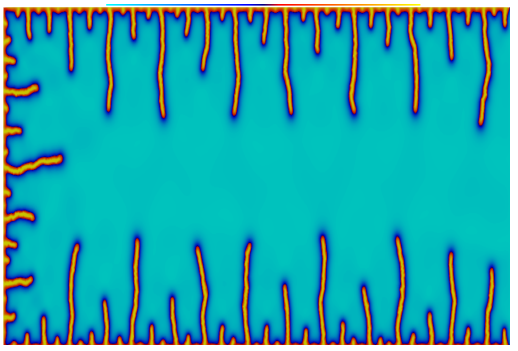

(a) α at $t = 10\,\mu$s

(b) α at $t = 10\,\mu$s (experimental result)

Figure 7. Predicted damage field α (a) and the corresponding experimental result (b) at $10\,\mu$s with $\Delta T = 580\,$K.

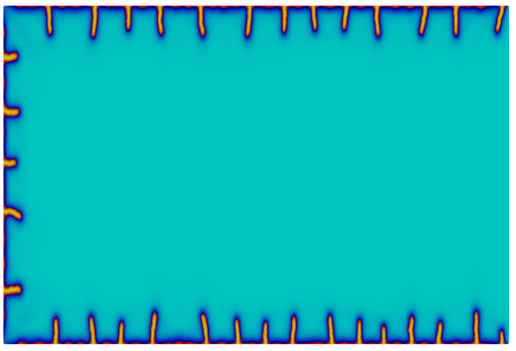

(a) α at $t = 1\,\mu$s with $\Delta T = 250\,$K

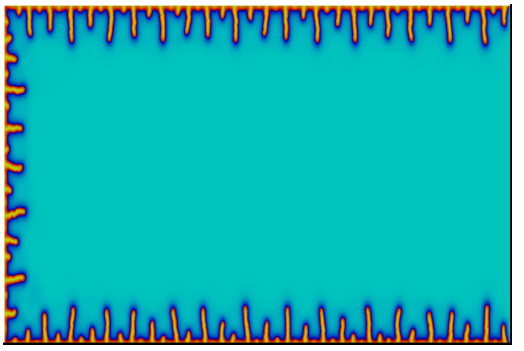

(b) α at $t = 1\,\mu$s with $\Delta T = 580\,$K

Figure 8. Predicted damage field α for AT2 at $1\,\mu$s with $\Delta T = 250\,$K and $580\,$K, respectively.

incremental variational principle consists in the minimization of a four-fields incremental energy functional, in which the consideration of a *kinetic entropy* is required for an appropriate descrip-

tion of the coupling between the heat conduction and the thermoelastic deformations. More specifically, the irreversible process is quantified via a dissipation potential that is expressed in a joint form between the damage dissipation and the heat conduction. By simultaneously considering a suitable dissipation potential together with a Helmholtz free energy we succeed to establish a total energy functional. The incremental form of the latter is dependent on the displacement, the damage, the absolute temperature fields as well as on the *kinetic entropy*. It was then demonstrated that the corresponding weak forms lead to the appropriate Euler–Lagrange equations and boundary conditions for the concerned coupled system. An incremental variational principle was hence proposed. With a suitable kinetic entropy approximation, the variational procedure is reduced to a three-field dependency: displacement, damage, and temperature fields.

This has led to the variational formulation of a complete thermoelastic-gradient damage model, whose numerical implementation has been carried out through a semi-staggered algorithm by using the open-source platform FEniCS. For illustration purpose, the model has been applied to the simulate the fracturing process of a plate under thermal shocks. A comparison with available experimental data of [30] has shown qualitatively good agreements.

Finally, it should be noted that some extensions/improvements of the proposed variational approach are possible. We are particularly interested by:

- consideration of a strong coupling between the thermoelasticity and the gradient damage: this could be achieved by introducing an integration factor (proposed by [13]) in the dissipation potential of gradient damage in order to well incorporate its contribution to entropy production;
- an extension of the present study to the context thermo-poroelastic couplings for which a thermodynamic basis is already available (see for instance [46]): note that this type of coupling has been recently investigated by [47] in the context of phase-fields methods.

Another interesting point could consist in comparing predictions of fracture nucleation under thermal shocks to that which can be established by considering the coupled criterion proposed by D. Leguillon and coauthors [48,49] (see several papers in the present issue).

Appendix A. Thermodynamics formulation for the coupling between gradient damage and thermoelasticity

Thermodynamics provides a theoretical and essential framework allowing to rigorously describe the evolution of a multiphysical system depending on all forms of energy. In this section, we formulate a suitable thermodynamic description of thermoelasticity with heat conduction coupled to gradient damage. Given the continuum medium Ω, the global internal energy $\mathscr{E}$, the global entropy $\mathscr{S}$ and the calorific power are classically expressed as:

$$\mathscr{E} = \int_\Omega e \,\mathrm{d}\Omega; \qquad \mathscr{S} = \int_\Omega s \,\mathrm{d}\Omega; \qquad \mathscr{P}_{\mathrm{cal}} = \int_\Omega r \,\mathrm{d}\Omega - \int_{\partial\Omega} \boldsymbol{q}\cdot\boldsymbol{n}\,\mathrm{d}S \tag{39}$$

where e is the density of internal energy per unit volume.

Introducing eqs. (39) and (2) into (1) yields the following local energy balance equation and the Clausius–Duhem inequality for a thermomechanical medium with gradient damage effects:

$$\begin{aligned} &\dot{e} = \boldsymbol{\sigma} : \dot{\boldsymbol{\varepsilon}} + r - \mathrm{div}\,\boldsymbol{q} + Y_\alpha \dot{\alpha} + \boldsymbol{Y}_{\nabla\alpha}\cdot\nabla\dot{\alpha}, \\ &\mathscr{D} = \boldsymbol{\sigma} : \dot{\boldsymbol{\varepsilon}} - \dot{e} + T\dot{s} + Y_\alpha \dot{\alpha} + \boldsymbol{Y}_{\nabla\alpha}\cdot\nabla\dot{\alpha} - \frac{\nabla T}{T}\cdot\boldsymbol{q} \geq 0. \end{aligned} \tag{40}$$

Yet, since the entropy s is less "controllable", it would be more appropriate to adopt its conjugate variable, i.e. the absolute temperature T, as an external state variable. In this context, it can be

preferable to consider the Helmholtz free energy per unit volume w, which satisfies the following partial Legendre transform:

$$-w = Ts - e. \tag{41}$$

It is convenient to emphasize here that e is convex with respect to all of its arguments. It follows by duality that w is a concave function of the temperature field T, while its convexity with respect to other variables still holds. Substituting eq. (41) into (40) yields eq. (5), namely:

$$\mathscr{D} = \underbrace{\boldsymbol{\sigma} : \dot{\boldsymbol{\varepsilon}} - \dot{w} - s\dot{T} + Y_\alpha \dot{\alpha} + \boldsymbol{Y}_{\nabla\alpha} \cdot \nabla\dot{\alpha}}_{\mathscr{D}_{\text{int}}} \underbrace{- \frac{\nabla T}{T} \cdot \boldsymbol{q}}_{\mathscr{D}_{\text{th}}} \geq 0$$

where $\mathscr{D}_{\text{int}}$ is the intrinsic dissipation and $\mathscr{D}_{\text{th}}$ the dissipation of the heat conduction.

Moreover, through a straightforward rearrangement of the expression of $\mathscr{D}_{\text{int}}$, the following equality can be readily obtained:

$$\dot{w} = \left[(\boldsymbol{\sigma} : \dot{\boldsymbol{\varepsilon}} + Y_\alpha \dot{\alpha} + \boldsymbol{Y}_{\nabla\alpha} \cdot \nabla\dot{\alpha}) - \mathscr{D}_{\text{int}} \right] - s\dot{T}. \tag{42}$$

From a similar perspective as presented in [50] in the case without gradient damage, the above equation reveals that the variation of w can be divided into two parts: the first one in the bracket corresponds to the isothermal and non-dissipative mechanical work ; the other, i.e. $-s\dot{T}$, accounts for variations of w when all other parameters hold constant and is obviously associated with the temperature variation. Hence, one can define w as a function of $\boldsymbol{\varepsilon}$, α, $\nabla\alpha$ and T, which has been given by eq. (3), namely:

$$w := w(\boldsymbol{\varepsilon}, T, \alpha, \nabla\alpha).$$

Since the state variables are independent, eq. (42) can be reformulated as:

$$\dot{w} = \frac{\partial w}{\partial \boldsymbol{\varepsilon}} : \dot{\boldsymbol{\varepsilon}} + \frac{\partial w}{\partial \alpha}\dot{\alpha} + \frac{\partial w}{\partial \nabla\alpha} \cdot \nabla\dot{\alpha} + \frac{\partial w}{\partial T}\dot{T} = \left[(\boldsymbol{\sigma} : \dot{\boldsymbol{\varepsilon}} + Y_\alpha \dot{\alpha} + \boldsymbol{Y}_{\nabla\alpha} \cdot \nabla\dot{\alpha}) - \mathscr{D}_{\text{int}} \right] - s\dot{T} \tag{43}$$

which allows to identify the following non-dissipative thermodynamic forces (denoted with superscript "nd") as the state laws given by eq. (4). Inserting the latter into (5) yields the local dissipation $\mathscr{D}$ described by eq. (6).

Finally, as mentioned in Section 2, the evolution laws are described through a joint dissipation potential φ, i.e. eq. (7). It is worthy to point out that the in the dissipation potential, φ^M is supposed as a function of the rate of the internal state variables (i.e., $\dot{\alpha}$ and $\nabla\dot{\alpha}$) and parametrically depends on its current state variables. For φ^T, and in link to the definition of the thermal dissipation $\mathscr{D}_{\text{th}}$ (see eq. (6)), the simplest form could be the Fourier potential, which is defined as function of an *additional* variable $-\nabla T/T$ and parametrically depends on T.

Appendix B. Variational analysis of the incremental total energy functional I_n

Having in hand eq. (11), along with the integral of the exact differential of $\dot{w}$ and the substitution eqs. (3), (7), and (9) into (11), we obtain:

$$\begin{aligned} I_n(\boldsymbol{u}_{n+1}, T_{n+1}, \hat{s}_{n+1}, \alpha_{n+1}) = &\int_\Omega w_{n+1}(\boldsymbol{u}_{n+1}, T_{n+1}, \alpha_{n+1}, \nabla\alpha_{n+1}) - w_n(\boldsymbol{u}_n, T_n, \alpha_n, \nabla\alpha_n)\,\mathrm{d}\Omega \\ &+ \int_{t_n}^{t_{n+1}} \int_\Omega \hat{s}\dot{T} + \varphi\left(\dot{\alpha}, \nabla\dot{\alpha}, -\frac{\nabla T}{T}; \alpha, \nabla\alpha\right) \mathrm{d}\Omega\,\mathrm{d}t - \int_{t_n}^{t_{n+1}} \int_{\partial_Q\Omega} Q \log\frac{T}{T_0}\,\mathrm{d}S\,\mathrm{d}t \\ &- \int_\Omega \boldsymbol{F}_{n+1} \cdot (\boldsymbol{u}_{n+1} - \boldsymbol{u}_n)\,\mathrm{d}\Omega - \int_{\partial_T\Omega} \boldsymbol{T}_{n+1} \cdot (\boldsymbol{u}_{n+1} - \boldsymbol{u}_n)\,\mathrm{d}S\,\mathrm{d}t. \end{aligned} \tag{44}$$

Taking variation of eq. (44) with respect to T and simultaneously considering (4) and (8) gives the related weak form:

$$-\int_\Omega s_{n+1}\,\delta T_{n+1}\,\mathrm{d}\Omega + \int_{t_n}^{t_{n+1}} \int_\Omega \left(\hat{s}\,\delta\dot{T} + \frac{\boldsymbol{q}}{T} \cdot \nabla\delta T\right) \mathrm{d}\Omega\,\mathrm{d}t - \int_{t_n}^{t_{n+1}} \int_{\partial_Q\Omega} Q\frac{\delta T}{T}\,\mathrm{d}S\,\mathrm{d}t = 0 \tag{45}$$

whose integration by parts with respect to time and space yields:

$$\int_\Omega (-s_{n+1}+\hat{s}_{n+1})\delta T_{n+1}\mathrm{d}\Omega - \int_{t_n}^{t_{n+1}}\int_\Omega \left[\dot{\hat{s}}+\operatorname{div}\frac{\boldsymbol{q}}{T}\right]\delta T\,\mathrm{d}\Omega\,\mathrm{d}t + \int_{t_n}^{t_{n+1}}\int_{\partial_Q\Omega}(\boldsymbol{q}\cdot\boldsymbol{n}-Q)\frac{\delta T}{T}\mathrm{d}S\,\mathrm{d}t = 0. \quad (46)$$

Ensuring stationarity yields at $t = t_{n+1}$:

$$\hat{s}_{n+1} = s_{n+1}; \qquad \forall\, \boldsymbol{x}\in\Omega \quad (47)$$

and in the time interval $[t_n, t_{n+1}]$

$$\dot{\hat{s}}+\operatorname{div}\frac{\boldsymbol{q}}{T}=0; \qquad \forall\, \boldsymbol{x}\in\Omega, \quad (48)$$

$$\boldsymbol{q}\cdot\boldsymbol{n} = Q; \qquad \forall\, \boldsymbol{x}\in\partial_Q\Omega. \quad (49)$$

It follows from eq. (47) that the *kinetic entropy* $\hat{s}_{n+1}$ is optimized at time t_{n+1} as equal to the *equilibrium entropy* s_{n+1}, which indicates that the material point reaches the local thermodynamic equilibrium at t_{n+1}. Also, eq. (48) reveals that the evolution of *kinetic entropy* satisfies the heat equation in $[t_n, t_{n+1}]$ with the corresponding Neumann boundary condition on $\partial_Q\Omega$ given by (49).

Similarly, by taking variations of eq. (44) with respect to the other variables and considering (4) and (8), the corresponding weak forms for $\boldsymbol{u}$, α and $\hat{s}$ can be derived as follows:

$$-\int_\Omega \left[\operatorname{div}\boldsymbol{\sigma}_{n+1}+\boldsymbol{F}_{n+1}\right]\cdot\delta\boldsymbol{u}_{n+1}\,\mathrm{d}\Omega + \int_{\partial_T\Omega}\left(\boldsymbol{\sigma}_{n+1}\cdot\boldsymbol{n}-\boldsymbol{T}_{n+1}\right)\cdot\delta\boldsymbol{u}_{n+1}\,\mathrm{d}S = 0, \quad (50)$$

$$\begin{aligned}&\int_\Omega \left[Y_\alpha|_{n+1} - \operatorname{div}\boldsymbol{Y}_{\nabla\alpha}|_{n+1}\right]\delta\alpha_{n+1}\,\mathrm{d}\Omega + \int_{\partial\Omega}\left(\boldsymbol{Y}_{\nabla\alpha}|_{n+1}\cdot\boldsymbol{n}\right)\delta\alpha_{n+1}\,\mathrm{d}S\\ &\quad+\int_{t_n}^{t_{n+1}}\int_\Omega\left\{\left[\frac{\partial\varphi}{\partial\alpha}-\frac{\mathrm{d}}{\mathrm{d}t}\left(\frac{\partial\varphi}{\partial\dot{\alpha}}\right)\right]-\operatorname{div}\left[\frac{\partial\varphi}{\partial\nabla\alpha}-\frac{\mathrm{d}}{\mathrm{d}t}\left(\frac{\partial\varphi}{\partial\nabla\dot{\alpha}}\right)\right]\right\}\delta\alpha\,\mathrm{d}\Omega\,\mathrm{d}t\\ &\quad+\int_{t_n}^{t_{n+1}}\int_{\partial\Omega}\left\{\left[\frac{\partial\varphi}{\partial\nabla\alpha}-\frac{\mathrm{d}}{\mathrm{d}t}\left(\frac{\partial\varphi}{\partial\nabla\dot{\alpha}}\right)\right]\cdot\boldsymbol{n}\right\}\delta\alpha\,\mathrm{d}S\,\mathrm{d}t = 0,\end{aligned} \quad (51)$$

$$\int_{t_n}^{t_{n+1}}\int_\Omega \dot{T}\,\delta\hat{s}\,\mathrm{d}\Omega\,\mathrm{d}t = 0, \quad (52)$$

where $\cdot|_{n+1}$ symbolizes the estimate of considered quantity at time t_{n+1}.

Appendix C. Damage and displacement fields at $t = 0.01\,\mu$s and $0.1\,\mu$s with $\Delta T = 250\,$K

In this section, we display the damage field (i.e. α) as well as the horizontal and vertical displacements (i.e. u_x and u_y) fields respectively at $t = 0.01\,\mu$s and $0.1\,\mu$s under the thermal shock loads $\Delta T = 250\,$K. The primary objective is to show the transition from damage processes at early stage to occurence cracks. It can be observed in Figure 9(a) that at $t = 0.01\,\mu$s, damage starts on the thermal loading boundaries without any strongly localized field (i.e. smeared cracks) such that $\alpha < 1$. While at $t = 0.1\,\mu$s (see Figure 9(b)), the damage has already been localized leading to the propagation of the diffused cracks. In addition, it is very interesting to note that displacement jumps are observed (in Figures 9(c)–(f)) at $t = 0.1\,\mu$s for horizontal (resp. vertical) displacements on the top and bottom (resp. left) boundaries, which somehow represent the opening of these smeared cracks during the damage evolution.

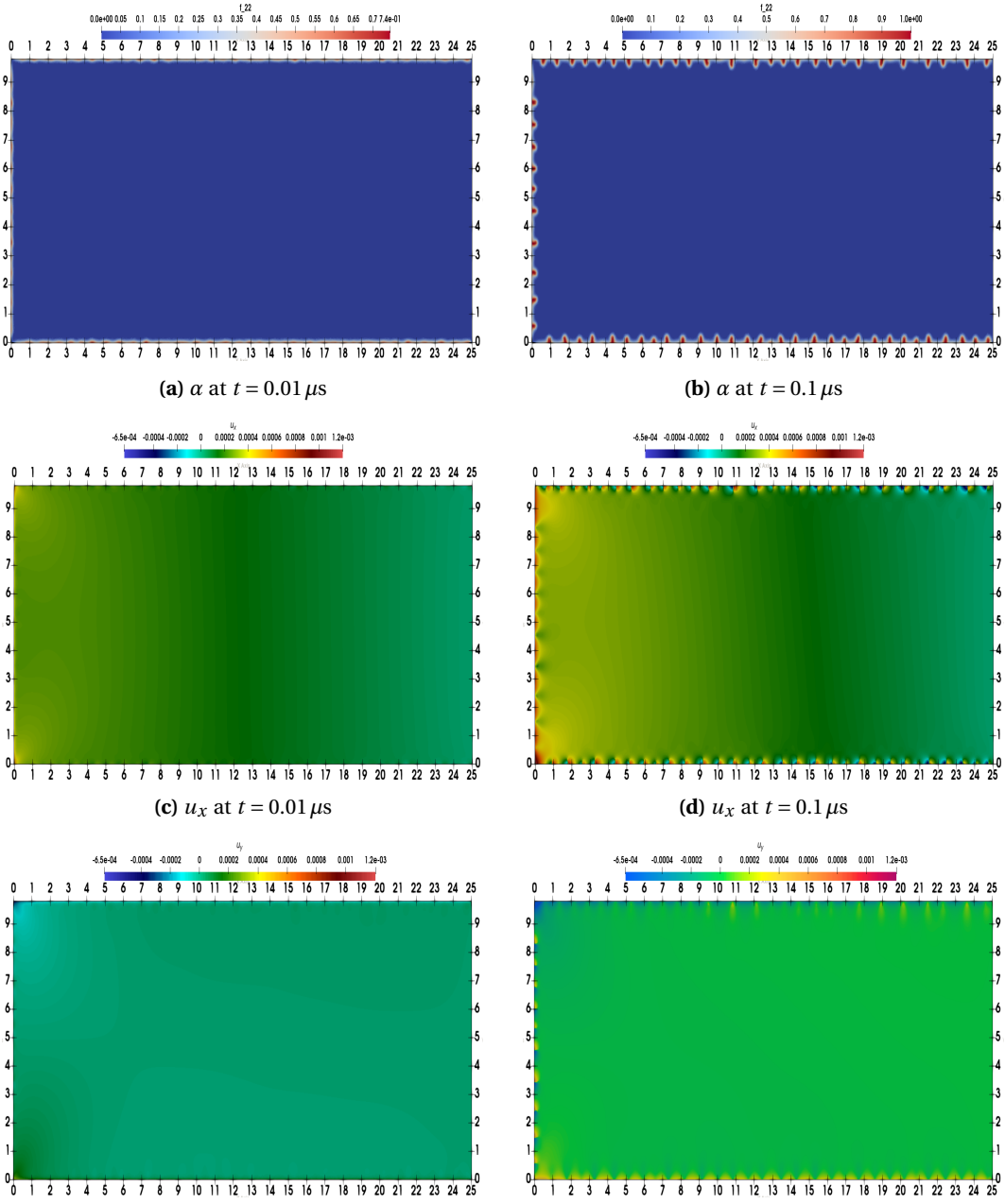

(a) α at $t = 0.01\,\mu$s

(b) α at $t = 0.1\,\mu$s

(c) u_x at $t = 0.01\,\mu$s

(d) u_x at $t = 0.1\,\mu$s

(e) u_y at $t = 0.01\,\mu$s

(f) u_y at $t = 01\,\mu$s

Figure 9. Contours of damage α, horizontal displacement u_x and vertical displacement u_y and at $t = 0.011\,\mu$s and $0.1\,\mu$s with $\Delta T = 250\,$K.

Declaration of interests

The authors do not work for, advise, own shares in, or receive funds from any organization that could benefit from this article, and have declared no affiliations other than their research organizations.

References

[1] M. A. Biot, "Thermoelasticity and irreversible thermodynamics", *J. Appl. Phys.* **27** (1956), no. 3, pp. 240–253.

[2] M. A. Biot, "New methods in heat flow analysis with application to flight structures", *J. Aeronaut. Sci.* **24** (1957), no. 12, pp. 857–873.

[3] B. A. Boley and J. H. Weiner, *Theory of thermal stresses*, John Wiley & Sons, 1962.

[4] M. Ben-Amoz, "On a variational theorem in coupled thermoelasticity", *J. Appl. Mech.* **32** (1965), pp. 943–945.

[5] G. Herrmann, "On variational principles in thermoelasticity and heat conduction", *Q. Appl. Math.* **21** (1963), no. 2, pp. 151–155.

[6] W. Nowacki, "Thermal stresses in anisotropic bodies", in *Thermomechanics in solids. A symposium held at CISM, Udine, July 1974* (W. Nowacki and I. N. Sneddon, eds.), CISM International Centre for Mechanical Sciences, vol. 223, Springer, 1977, pp. 25–54.

[7] W. Nowacki, *Thermoelasticity*, 2nd edition, Elsevier, 1986.

[8] G. Batra, "On a principle of virtual work for thermo-elastic bodies", *J. Elasticity* **21** (1989), no. 2, pp. 131–146.

[9] B. A. Finlayson and L. E. Scriven, "On the search for variational principles", *Int. J. Heat Mass Transfer* **10** (1967), no. 6, pp. 799–821.

[10] G. Lebon and P. Perzyna, "Variational principles in thermomechanics", in *Recent developments in thermomechanics of solids*, CISM International Centre for Mechanical Sciences, vol. 262, Springer, 1980, pp. 221–396.

[11] A. E. Green and P. M. Naghdi, "Thermoelasticity without energy dissipation", *J. Elasticity* **31** (1993), no. 3, pp. 189–208.

[12] S. Bargmann and P. Steinmann, "Theoretical and computational aspects of non-classical thermoelasticity", *Comput. Methods Appl. Mech. Eng.* **196** (2006), no. 1-3, pp. 516–527.

[13] Q. Yang, L. Stainier and M. Ortiz, "A variational formulation of the coupled thermo-mechanical boundary-value problem for general dissipative solids", *J. Mech. Phys. Solids* **54** (2006), pp. 401–424.

[14] L. Stainier, "Chapter Two — A variational approach to modeling coupled thermo-mechanical nonlinear dissipative behaviors", *Adv. Appl. Mech.* **46** (2013), pp. 69–126.

[15] M. Peigney, "A time-integration scheme for thermomechanical evolutions of shape-memory alloys", *C. R. Méc.* **334** (2006), no. 4, pp. 266–271.

[16] M. Peigney and J.-P. Seguin, "An incremental variational approach to coupled thermo-mechanical problems in anelastic solids. Application to shape-memory alloys", *Int. J. Solids Struct.* **50** (2013), no. 24, pp. 4043–4054.

[17] L. Stainier and M. Ortiz, "Study and validation of a variational theory of thermo-mechanical coupling in finite visco-plasticity", *Int. J. Solids Struct.* **47** (2010), no. 5, pp. 705–715.

[18] A. Bartels, T. Bartel, M. Canadija and J. Mosler, "On the thermomechanical coupling in dissipative materials: a variational approach for generalized standard materials", *J. Mech. Phys. Solids* **82** (2015), pp. 218–234.

[19] I. Romero, E. M. Andrés and Á. Ortiz-Toranzo, "Variational updates for general thermo-chemo-mechanical processes of inelastic solids", *Comput. Methods Appl. Mech. Eng.* **385** (2021), article no. 114013 (23 pages).

[20] S. Teichtmeister and M.-A. Keip, "A variational framework for the thermomechanics of gradient-extended dissipative solids—with applications to diffusion, damage and plasticity", *J. Elasticity* **148** (2022), no. 1, pp. 81–126.

[21] B. Bourdin, J.-J. Marigo, C. Maurini and P. Sicsic, "Morphogenesis and propagation of complex cracks induced by thermal shocks", *Phys. Rev. Lett.* **112** (2014), no. 1, article no. 014301 (5 pages).

[22] P. Sicsic, J.-J. Marigo and C. Maurini, "Initiation of a periodic array of cracks in the thermal shock problem: a gradient damage modeling", *J. Mech. Phys. Solids* **63** (2014), pp. 256–284.

[23] T. K. Mandal, V. P. Nguyen, J.-Y. Wu, C. Nguyen-Thanh and A. de Vaucorbeild, "Fracture of thermo-elastic solids: phase-field modeling and new results with an efficient monolithic solver", *Comput. Methods Appl. Mech. Eng.* **376** (2021), article no. 113648.

[24] M. Dhahri, R. Abdelmoula, J. Li and Y. Maalej, "Thermal shock cracking in thin plate specimens using a gradient damage model", *J. Mech. Mater. Struct.* **18** (2023), no. 1, pp. 19–38.

[25] D. Chu, X. Li and Z. Liu, "Study the dynamic crack path in brittle material under thermal shock loading by phase field modeling", *Int. J. Fract.* **208** (2017), no. 1, pp. 115–130.

[26] J.-H. Zheng, Z. Zhong and C.-Y. Jiang, "Coupled thermoelastic theory and associated variational principles based on decomposition of internal energy", *Acta Mech. Sin.* **36** (2020), no. 1, pp. 107–115.

[27] T. Zhang, T. Q. Bui, T. Yu, Y. Li and S. Natarajan, "Quasi-static thermoelastic fracture: Adaptive phase-field modeling with variable-node elements", *Theor. Appl. Fract. Mech.* **124** (2023), article no. 103811.

[28] Y. Li, T. Yu, C. Xing and S. Natarajan, "Modeling quasi-static and dynamic thermo-elastic coupled brittle fracture using an adaptive isogeometric hybrid phase-field method", *Finite Elem. Anal. Des.* **224** (2023), article no. 103993.

[29] A. Chrysochoos, C. Licht and R. Peyroux, "A one-dimensional thermomechanical modeling of phase change front propagation in a SMA polycrystal", *C. R. Méc.* **331** (2003), pp. 25–32.

[30] Y. Shao, Y. Zhang, X. Xu, Z. Zhou, W. Li and B. Liu, "Effect of crack pattern on the residual strength of ceramics after quenching", *J. Am. Ceram. Soc.* **94** (2011), no. 9, pp. 2804–2807.

[31] M. Frémond and B. Nedjar, "Damage, gradient of damage and principle of virtual power", *Int. J. Solids Struct.* **33** (1996), no. 8, pp. 1083–1103.
[32] B. Halphen and Q.-C. Nguyen, "Sur les matériaux standards généralisés", *J. Méc., Paris* **14** (1975), no. 1, pp. 39–63.
[33] X.-D. Zhang, L. Cheng, D. Kondo and A. Giraud, "Incremental variational approach to gradient damage coupled with poroelasticity of saturated media", *J. Mech. Phys. Solids* **187** (2024), article no. 105614.
[34] M. Ortiz and L. Stainier, "The variational formulation of viscoplastic constitutive updates", *Comput. Methods Appl. Mech. Eng.* **171** (1999), no. 3-4, pp. 419–444.
[35] W. Han, S. Jensen and B. D. Reddy, "Numerical approximations of problems in plasticity: error analysis and solution algorithms", *Numer. Linear Algebra Appl.* **4** (1997), no. 3, pp. 191–204.
[36] Q.-S. Nguyen, "Quasi-static responses and variational principles in gradient plasticity", *J. Mech. Phys. Solids* **97** (2016), pp. 156–167.
[37] H. Petryk, "Incremental energy minimization in dissipative solids", *C. R. Méc.* **331** (2003), no. 7, pp. 469–474.
[38] M. Ortiz and J. B. Martin, "Symmetry — preserving return mapping algorithms and incrementally external paths: a unification of concepts", *Int. J. Numer. Methods Eng.* **28** (1989), pp. 1839–1853.
[39] T. Heuzé and L. Stainier, "A variational formulation of thermomechanical constitutive update for hyperbolic conservation laws", *Comput. Methods Appl. Mech. Eng.* **394** (2022), article no. 114893.
[40] K. Kpotufe, *Modèles à gradient d'endommagement : cadre thermodynamique, formulation variationnelle et applications*, PhD thesis, Sorbonne Université (France) and Université de Lomé (Togo), 2021.
[41] K. Pham, H. Amor, J.-J. Marigo and C. Maurini, "Gradient damage models and their use to approximate brittle fracture", *Int. J. Damage Mech.* **20** (2011), no. 4, pp. 618–652.
[42] B. Bourdin, G. A. Francfort and J.-J. Marigo, "Numerical experiments in revisited brittle fracture", *J. Mech. Phys. Solids* **48** (2000), no. 4, pp. 797–826.
[43] A. Ehrlacher and B. Fedelich, "Stability and bifurcation of simple dissipative systems: application to brutal damage", in *Cracking and damage. Strain localization and size effect* (Z. P. Bazant and J. Mazars, eds.), Taylor & Francis, 1989, pp. 221–227.
[44] M. S. Alnaes et al., "The FEniCS Project Version 1.5", *Arch. Numer. Soft.* **3** (2015), no. 100, pp. 9–23.
[45] A. Logg, K.-A. Mardal and G. N. Wells (eds.), *Automated solution of differential equations by the finite element method*, Lecture Notes in Computational Science and Engineering, vol. 84, Springer, 2012.
[46] O. Coussy, *Poromechanics*, Wiley Publishing, 2004.
[47] Y. Liu, K. Yoshioka, T. You, H. Li and F. Zhang, "A phase-field fracture model in thermo-poro-elastic media with micromechanical strain energy degradation", *Comput. Methods Appl. Mech. Eng.* **429** (2024), article no. 117165.
[48] D. Leguillon, "A simple model of thermal crack pattern formation using the coupled criterion", *C. R. Méc.* **341** (2013), no. 6, pp. 538–546.
[49] L. F. F. Ricardo, D. Leguillon, G. Parry and A. Doitrand, "Modeling the thermal shock induced cracking in ceramics", *J. Eur. Ceram. Soc.* **40** (2020), no. 4, pp. 1513–1521.
[50] H. Maitournam, *Mécanique des structures anélastiques*, Éditions de l'École polytechnique, 2013.

ACADÉMIE DES SCIENCES
INSTITUT DE FRANCE

Comptes Rendus. Mécanique
2025, Vol. 353, p. 79-89
https://doi.org/10.5802/crmeca.268

Research article / *Article de recherche*

Closed-form analysis of a thermally loaded single-layer system on a rigid foundation

Analyse de forme fermée d'un système monocouche thermiquement chargé sur une fondation rigide

Debora Linn [*,a] **and Wilfried Becker** [a]

[a] Technical University of Darmstadt, Institute of Applied Dynamics,
Otto-Berndt-Str. 2, 64287 Darmstadt, Germany
E-mails: linn@ad.tu-darmstadt.de (D. Linn), becker@fsm.tu-darmstadt.de (W. Becker)

Abstract. A closed-form analytical model of a single layer with a linear elastic material behavior on a rigid foundation subjected to thermal loading is investigated. The closed-form analytical model is based on a higher-order displacement approach that takes the singularity exponent into account. Two applications are considered in this work. First, the interlaminar stresses are analyzed at the interface between the substrate and the material layer. These stresses are an indicator of the formation of interlaminar cracks, which cause the individual layer to peel off. Based on the interlaminar stresses, the closed-form analytical approach, which considers the singularity exponent in the displacement approach, is compared to a model with a second order displacement approach and a FEM model. In the second part, the development of transversal cracks is considered within the framework of Finite Fracture Mechanics, using a coupled stress and energy criterion. Transverse cracks often occur in thin brittle layers such as ceramic coatings and form in periodic patterns. In this work, a representative unit cell is considered – i.e. the material layer between two cracks. This unit cell is used to determine the cooling temperature at which transverse cracks develop. Furthermore, the resulting distance between two cracks can be determined when larger cooling temperatures are applied.

Résumé. Un modèle analytique de forme fermée d'une couche unique avec un comportement de matériau élastique linéaire sur une fondation rigide soumise à une charge thermique est étudié. Le modèle analytique de forme fermée est basé sur une approche de déplacement d'ordre supérieur qui prend en compte l'exposant de singularité. Deux applications sont considérées dans ce travail. Premièrement, les contraintes interlaminaires sont analysées à l'interface entre le substrat et la couche de matériau. Ces contraintes sont un indicateur de la formation de fissures interlaminaires, qui entraînent le décollement de la couche individuelle. Sur la base des contraintes interlaminaires, l'approche analytique de forme fermée, qui prend en compte l'exposant de singularité dans l'approche de déplacement, est comparée à un modèle avec une approche de déplacement du second ordre et à un modèle FEM. Dans la deuxième partie, le développement de fissures transversales est étudié dans le cadre de la mécanique de la rupture finie, en utilisant un critère couplé de contrainte et d'énergie. Les fissures transversales se produisent souvent dans des couches fragiles minces

* Corresponding author

telles que les revêtements céramiques et se forment selon des schémas périodiques. Dans ce travail, une cellule unitaire représentative est considérée – c'est-à-dire la couche de matériau entre deux fissures. Cette cellule unitaire est utilisée pour déterminer la température de refroidissement à laquelle les fissures transversales se développent. En outre, la distance résultante entre deux fissures peut être déterminée lorsque des températures de refroidissement plus élevées sont appliquées.

Keywords. Analytical model, Stress prediction, Interlaminar stresses, Transversal cracks, Crack pattern.

Mots-clés. Modèle analytique, prédiction des contraintes, contraintes interlaminaires, fissures transversales, schéma de fissuration.

Manuscript received 28 June 2024, revised 12 September 2024, accepted 16 September 2024.

1. Introduction

In the field of engineering, there are many applications in which an adhesive bonding is used to join two components. There is great interest in understanding the mechanics behind such adhesive joints in order to design them better and find parameters to improve joint strength. In civil engineering, for example, concrete structures to which a patch of finite size is bonded are analyzed. If concrete structures are damaged due to age or environmental impact, patches can be glued onto the concrete surface to repair or generally reinforce the structure. These patches typically have a high strength and are made of carbon fiber reinforced plastic (CFRP), for example. Frhaan et al. give an overview of the reinforcement of concrete structures with CFRP patches in [1]. Various bonding methods of concrete beam structures are examined by Martinelli et al. in [2, 3]. On the one hand, the CFRP reinforcement bars are bonded directly to the concrete surface and on the other hand, grooves are inserted into the concrete before the CFRP bars are applied, providing a form of anchoring. The detachment behavior of these reinforcement patches is investigated experimentally and numerically. Steel reinforcement patches are also conceivable. Awassa et al. tested shafts reinforced with steel rods from the underground core network in a 4-point bending test in [4]. The typical mode of failure that appears in such a configuration of patch and substrate is the delamination of the patch. Due to the geometry and the different material properties, very high stress concentrations occur locally in the area of the free edges. Calculations of these stresses are essential in order to be able to design such configurations more precisely with regard to their safety.

In the field of structural mechanics, many models for the analysis of bonded joints are presented. A good overview and comparison is given by da Silva et al. in [5, 6]. The modeling developed in this paper is similar to that of Methfessel and Becker, which is described in [7, 8]. There, a closed-form analytical model is presented, which is based on the generalized model of Bigwood and Crocombe [9] and has been extended. In view of a simple and pragmatic model of Methfessel and Becker ([7, 8]) only the overlap area is considered, in which the internal forces and moments and displacements are applied at the edges, depending on the load case. First-order displacement approaches are used for modeling the adherends. Similar to the work of Ojalvo and Eidinoff in [10], the displacements in the adhesive layer are composed of the displacements of the adherends, but, unlike in [10], are extended by higher-order terms. In the current work a higher order displacement approach using the singularity exponent of the system is considered.

The second part of this work focuses on the formation of transverse cracks in thin layers.Thin layers of a solid, brittle material are often applied to protect a component surface. For example, brittle coatings made of a ceramic material on a flexible polymer are used for electronic devices. Another example are automobile catalytic converters, to which γ-alumina layers are applied as catalytic support. A typical failure mode that occurs in such coatings is the formation of transverse cracks that appear in crack patterns. In some cases, such cracks in thickness direction

lead to a loss of stiffness or even delamination of the layer. All in all, this leads to a loss of functionality of the coating. In [11], Leguillon et al. modeled a γ-alumina layer on a rigid substrate and analyzed the formation of transverse cracks using a coupled stress and energy criterion [12]. A coupled stress and energy criterion is also used in [13–15] by Leguillon et al. to predict crack initiation in thickness direction. There are some more publications that are studying the formation of transversal cracks like [16], where Bahr et al. investigated the crack growth or scaling behavior during shrinkage processes, such as cooling or drying, using a fracture mechanics bifurcation analysis with two plausible scaling assumptions. Another investigation that is worth mentioning is [17]. There, Jenkins considered a material layer that solidifies starting from a liquid. The solidification process causes the layer to shrink until cracks form in the layer due to excessive internal stresses. The distance between the cracks is then determined using energy minimization. In [18], Shao et al. carried out experimental tests with ceramic plates and ceramic slabs in which crack patterns form under thermal shock (quenching).

2. Generic model

2.1. *Mechanical situation*

Before focusing on a special material and application, this section will begin by considering a generic model where a thin layer of thickness t is perfectly attached to a substrate and subjected to an external thermal loading ΔT. To keep the model simple there are some assumptions made. First, linear elastic, isotropic material behavior of the layer with Young's modulus E, Poisson's ratio ν and thermal expansion coefficient α_{th} is supposed. Second, the substrate is idealized as a rigid body. The model is shown in Figure 1. Due to the fact that geometry and loading do not change in y-direction plane-strain behavior is assumed. Thus the displacement $u_y = v$ in y-direction vanishes and it is possible to reduce the system to a two-dimensional model with length l. Later, two applications are analyzed where specific parameters are chosen (see Section 3).

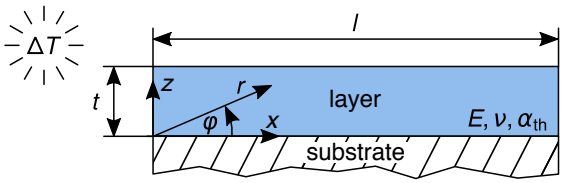

Figure 1. Mechanical model of the thin layer on a rigid substrate

2.2. *Singularity exponent*

Before the analytical model is derived, a pre-study is performed. Looking more closely at the situation at hand, it can be seen that stress singularities occur at the free edges at the layer substrate interface. In order to understand these singularities more precisely a pre-study is carried out using the method of complex potentials. This method in essence was formulated by Kolosow [19], and was later expanded and widely described by Muschelišvili [20]. With this method of complex potentials it is possible to determine the singularity exponent. The basic idea is to represent the real field quantities by means of two complex potentials Φ and Ψ depending on the complex variable $\zeta = x + iz$. The decisive benefit then is the automatic fulfillment of the

equilibrium conditions, kinematics and Hooke's law when the stresses and displacements are represented in the following manner (Kolosow's equations):

$$\sigma_\varphi + i\tau_{r\varphi} = \Phi'(\zeta) + \overline{\Phi'(\zeta)} + \zeta\Phi''(\zeta) + \frac{\zeta}{\bar{\zeta}}\Psi'(\zeta)\,, \tag{1}$$

$$u_r + i\,u_{r\varphi} = \frac{\mathrm{e}^{-i\varphi}}{2G}\left(\kappa\Phi(\zeta) - \zeta\overline{\Phi'(\zeta)} - \overline{\Psi(\zeta)}\right), \quad \text{with:} \quad \kappa = 3-4\nu \text{ (plane strain)}\,. \tag{2}$$

The first line contains the relation for the stresses σ_φ and $\tau_{r\varphi}$, and the second line contains the relation for the displacements. ζ is the complex coordinate $\zeta = r\mathrm{e}^{i\varphi}$ (see also Figure 1) and $\Phi(\zeta)$ and $\Psi(\zeta)$ are the complex potentials for which in the present case the following representations are chosen.

$$\Phi(\zeta) = (a_1 + i\,a_2)\,\zeta^\lambda\,; \quad \Psi(\zeta) = (b_1 + i\,b_2)\,\zeta^\lambda \tag{3}$$

a_1, a_2, b_1 and b_2 are real constants and λ is the singularity exponent which is to be determined. When inserting the chosen representations into the equations (1) and (2) from the given boundary conditions an algebraic equation system is obtained. Namely for the free edge on the left ($\varphi = \pi/2$ no traction applied) the stresses must be zero and for the bottom edge ($\varphi = 0$ rigid substrate) the displacements must be zero. Evaluating these boundary conditions and separating real and imaginary parts leads to a homogeneous system of equations. For a non-trivial solution of this system the determinant of the coefficient matrix has to be equal zero. This results in the characteristic polynomial:

$$-4\lambda^2 + 2\kappa\cos(\pi\lambda) + \kappa + 1 = 0\,. \tag{4}$$

From this characteristic polynomial the singularity exponent λ can be obtained. For the special case of a γ-alumina layer with a Poisson's ratio of $\nu = 0.2$ for instance a singularity exponent of $\lambda = 0.7811$ can be calculated. This means that the displacements locally (for very small radii r) behave like $r^{0.7811}$ and the strains and stresses behave like $r^{-0.2789}$. So there are relatively strong stress singularities, which should be taken into account in some way in further investigations.

2.3. *Approximate displacement approach*

For the given mechanical situation now an approximate displacement approach is suggested. Goal is to get an approximate closed-form analytical description of the deformation, strain and stress field. Therefore the displacements u in horizontal and w in vertical direction within the layer are described with a second-order approach extended with an additional term. In this additional term the singularity exponent of the free edges is taken into account. This additional term is used to describe the displacements and stresses more precisely, especially at the ends of the layer, as will be shown later in a comparison of the interlaminar stresses calculated using simpler approaches. With this motivation the horizontal and vertical displacements in the layer are represented as follows

$$u(x,z) = u_1(x)z + u_2(x)z^2 + u_3(x)z^\lambda\,, \tag{5}$$

$$w(x,z) = w_1(x)z + w_2(x)z^2 + w_3(x)z^\lambda\,. \tag{6}$$

Herein $u_1(x)$, $u_2(x)$, $u_3(x)$, $w_1(x)$, $w_2(x)$ and $w_3(x)$ are unknown functions of only the coordinate x and have to be determined in such a way that representations (5) and (6) are a good approximation of the real deformations. Next step is to determine the unknown displacement functions. For a simpler description, the arguments x and z of the displacement functions are omitted in the following. To determine the unknown displacement functions dependent on x the minimum total energy principle is used

$$\Pi = \Pi_{\text{int}} + \Pi_{\text{ext}} = \min\,, \tag{7}$$

which means that the total energy, consisting of the internal potential Π_{int} and the external potential Π_{ext}, is required to become minimal. As we only consider thermal and no mechanical loads the external potential is equal zero and the potential energy only consists of the internal energy (which means the total thermally induced elastic strain energy):

$$\begin{aligned}\Pi &= \frac{1}{2}\int_V \boldsymbol{\sigma} : \boldsymbol{\varepsilon}\, \mathrm{d}V \\ &= \frac{1}{2}\int_0^l \int_0^h \left[\sigma_x\left(\varepsilon_x - \alpha_{\text{th}}\Delta T\right) + \sigma_y\left(-\alpha_{\text{th}}\Delta T\right) + \sigma_z\left(\varepsilon_z - \alpha_{\text{th}}\Delta T\right) + \tau_{xz}\gamma_{xz}\right] \mathrm{d}z\mathrm{d}x\,.\end{aligned} \tag{8}$$

This minimum total energy principle postulates that a system is in equilibrium when the potential energy Π becomes minimal.

$$\delta\Pi = 0\,. \tag{9}$$

Using the kinematic relations

$$\varepsilon_x = \frac{\partial u}{\partial x} = {u_1}'z + {u_2}'z^2 + {u_3}'z^\lambda\,, \tag{10}$$

$$\varepsilon_z = \frac{\partial w}{\partial z} = w_1 + 2w_2 z + \lambda w_3 z^{\lambda-1}\,, \tag{11}$$

$$\gamma_{xz} = \frac{\partial u}{\partial z} + \frac{\partial w}{\partial x} = u_1 + 2u_2 z + \lambda u_3 z^{\lambda-1} + {w_1}'z + {w_2}'z^2 + {w_3}'z^\lambda\,, \tag{12}$$

$$\varepsilon_y = \gamma_{xy} = \gamma_{yz} = 0\,, \tag{13}$$

Hooke's law

$$\begin{pmatrix}\sigma_x\\ \sigma_y\\ \sigma_z\\ \tau_{xz}\end{pmatrix} = \frac{E}{2(1+\nu)(1-2\nu)}\begin{pmatrix}1-\nu & \nu & \nu & 0\\ \nu & 1-\nu & \nu & 0\\ \nu & \nu & 1-\nu & 0\\ 0 & 0 & 0 & \frac{1-2\nu}{2}\end{pmatrix}\begin{pmatrix}\varepsilon_x - \alpha_{\text{th}}\Delta T\\ -\alpha_{\text{th}}\Delta T\\ \varepsilon_z - \alpha_{\text{th}}\Delta T\\ \gamma_{xz}\end{pmatrix}, \tag{14}$$

and applying the variation for all displacement variables u_1, u_2, u_3, w_1, w_2, w_3, we get a non-homogeneous differential equation system of second order (see Appendix A). Next step is solving this differential equation system. Therefore we have to reduce it to a system of first order of the following kind:

$$\boldsymbol{A}\boldsymbol{\phi} + \boldsymbol{B}\dot{\boldsymbol{\phi}} = \boldsymbol{b}\,. \tag{15}$$

where the vector $\boldsymbol{\phi}$ contains all displacement functions and their derivatives which are all dependent on x.

$$\boldsymbol{\phi} = \left(u_1, u_2, u_3, w_1, w_2, w_3, u_1', u_2', u_3', w_1', w_2', w_3'\right)^{\mathrm{T}} \tag{16}$$

As the system is non-homogeneous, the general solution consists of a homogeneous part $\boldsymbol{\phi}_{\text{h}}$ and a particular part $\boldsymbol{\phi}_{\text{p}}$.

$$\boldsymbol{\phi} = \boldsymbol{\phi}_{\text{h}} + \boldsymbol{\phi}_{\text{p}}\,. \tag{17}$$

While the particular solution can be obtained using the method of undetermined coefficients,

$$\boldsymbol{\phi}_{\text{p}} = \boldsymbol{A}^{-1}\boldsymbol{b}\,, \tag{18}$$

the homogeneous solution is derived from solving an eigenvalue problem. For the homogeneous solution the equation system is transformed to this form,

$$\dot{\boldsymbol{\phi}}_{\text{h}} = -\boldsymbol{B}^{-1}\boldsymbol{A}\boldsymbol{\phi}_{\text{h}}\,, \tag{19}$$

where $-\boldsymbol{B}^{-1}\boldsymbol{A}$ is the new system matrix. By inserting the general exponential representation $\boldsymbol{v}\mathrm{e}^{\mu x}$ into the system of differential equations an eigenvalue system is obtained. Consequently, the 12 eigenvalues $\mu_{1\ldots12}$ can be determined by setting the coefficient determinant equal to zero. Thus eventually with the corresponding eigenvectors $\boldsymbol{v}_{1\ldots12}$ the general solution can be written as follows

$$\boldsymbol{\phi} = C_1\mathrm{e}^{\mu_1 x}\boldsymbol{v}_1 + C_2\mathrm{e}^{\mu_2 x}\boldsymbol{v}_2 + \cdots + C_{12}\mathrm{e}^{\mu_{12} x}\boldsymbol{v}_{12} + \boldsymbol{A}^{-1}\boldsymbol{b}\,. \tag{20}$$

$C_{1\ldots12}$ describe the 12 still unknown constants, which in the next step are determined by using the 12 boundary conditions. The following six equations result from the variation approach and are evaluated once at the left edge ($x = 0$) and once at the right edge ($x = l$) and in total form a linear system of equations with 12 equations for the 12 unknown constants $C_{1\ldots12}$.

$$3(1-\nu)\left(\frac{2}{3}h^2u_1' + \frac{1}{2}h^3u_2' + \frac{2}{\lambda+2}h^{\lambda+1}u_3\prime\right) + 3h\nu w_1 + 4h^2\nu w_2 + \frac{6\lambda}{\lambda+1}h^\lambda\nu w_3 = 3(1+\nu)\Delta T\alpha_{\text{th}}h \quad (21)$$

$$3(1-\nu)\left(\frac{1}{2}h^2u_1' + \frac{2}{5}h^3u_2' + \frac{2}{\lambda+3}h^{\lambda+1}u_3'\right) + 2h\nu w_1 + 3h^2\nu w_2 + \frac{6\lambda}{\lambda+2}h^\lambda\nu w_3 = 2(1+\nu)\Delta T\alpha_{\text{th}}h \quad (22)$$

$$(1-\nu)\left(\frac{2h^2}{\lambda+2}u_1' + \frac{2h^3}{\lambda+3}u_2' + \frac{2h^{\lambda+1}}{2\lambda+1}u_3'\right) + \frac{2h\nu}{\lambda+1}w_1 + \frac{4h^2\nu}{\lambda+2}w_2 + h^\lambda\nu w_3 = \frac{2}{\lambda+1}(1+\nu)\Delta T\alpha_{\text{th}}h \quad (23)$$

$$hu_1 + \frac{4}{3}h^2u_2 + \frac{2\lambda}{\lambda+1}h^\lambda u_3 + \frac{2}{3}h^2w_1' + \frac{1}{2}h^3w_2' + \frac{2}{\lambda+2}h^{\lambda+1}w_3' = 0 \quad (24)$$

$$\frac{2}{3}hu_1 + h^2u_2 + \frac{2\lambda}{\lambda+2}h^\lambda u_3 + \frac{1}{2}h^2w_1' + \frac{2}{5}h^3w_2' + \frac{2}{\lambda+3}h^{\lambda+1}w_3' = 0 \quad (25)$$

$$\frac{2}{\lambda+1}hu_1 + \frac{4}{\lambda+2}h^2u_2 + h^\lambda u_3 + \frac{2}{\lambda+2}h^2w_1' + \frac{2}{\lambda+3}h^3w_2' + \frac{2}{2\lambda+1}h^{\lambda+1}w_3' = 0 \quad (26)$$

Solving this system of equations provides the unknown constants, which can be inserted into the displacement functions. The displacement field is thus determined and the stresses are also available via the kinematics and the constitutive law.

2.4. *Finite Element Model*

To compare and validate the analytical solution, a numerical model is created using the finite element method in Simulia Abaqus. The model is discretized in a way that at the lower left region, where the stress singularity is expected, the mesh is the finest (see Figure 2). In this area, square elements with an edge length of $2 * 10^{-4}$ mm are chosen, for comparison the layer thickness is 0.1 mm. Starting from this area, the mesh becomes coarser towards the other edges. The model uses quadratic basis functions and has about 410,000 degrees of freedom.

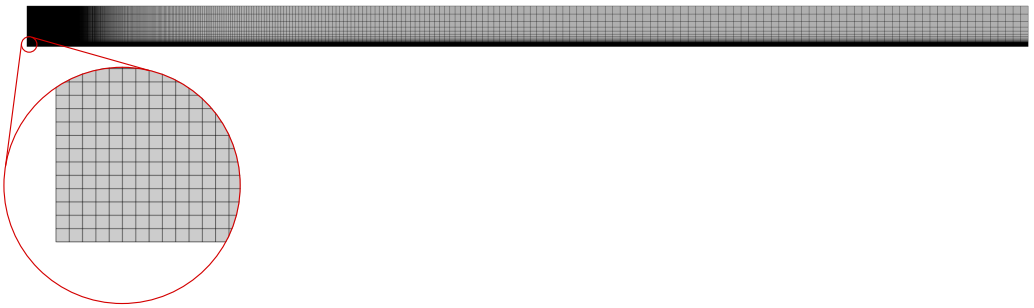

Figure 2. Finite Element Model

Table 1. Model parameters of the γ-alumina layer on the substrate

Parameter	Value	Unit
Layer thickness t	0.1	mm
Length l	5.0	mm
Elastic modulus E	250,000	MPa
Poisson's ration ν	0.2	-
Thermal expansion coefficient α_{th}	$6 * 10^{-6}$	K^{-1}
Thermal loading ΔT	-200	K
Singularity exponent λ	0.7811	–

3. Applications

Based on the model for a single layer of material on a rigid substrate under a temperature load, two cases are considered in the following. Firstly, the interlaminar stresses along the interface between the layer and the substrate are analyzed. These stresses are of particular interest as they may lead to the formation of interlaminar cracks and consequently delamination of the layer. In the second part, the development of transverse cracks is considered. In both cases, a thin γ-alumina layer with Young's modulus $E = 250,000$ MPa, Poisson's ratio $\nu = 0.2$ and thermal expansion coefficient $\alpha_{\text{th}} = 6 * 10^{-6}$ K^{-1} is considered. The layer is modeled with a thickness of $t = 0.1$ mm and length $l = 5$ mm. It is perfectly bonded to the rigid base and subjected to an external thermal loading of $\Delta T = -200$ K. The model is shown in Figure 1 and all parameters are summarized in Table 1.

3.1. *Analysis of interlaminar stresses*

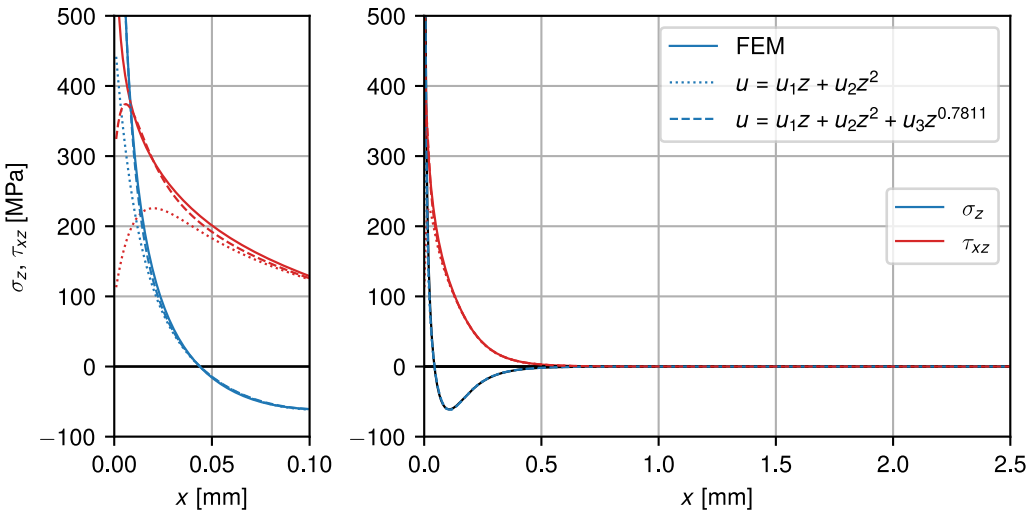

Figure 3. Interlaminar stresses σ_z and τ_{xz} along the interface between layer and substrate

The interlaminar stresses along the interface between layer and substrate are now evaluated. Figure 3 on the right side shows the interlaminar peel stress σ_z and the shear stress τ_{xz} up to the center of the model, and on the left side the region of the edge where the stress singularity is expected in detail. Now the stress distribution resulting from the analytical model when

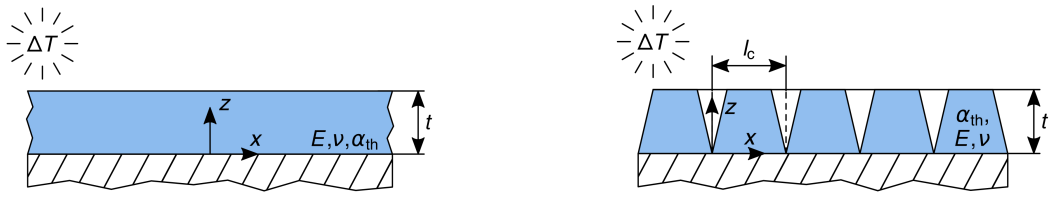

(a) **(b)**

Figure 4. (a): Single layer with infinite length without cracks. (b): Model of the formation of transversal cracks in pattern

the singularity exponent is considered can be compared with the numerical model and the analytical model that uses only a second order polynomial approach for the displacements. It can be seen that the expected stress singularity at the free edge is approximated better with the new displacement approach than with the second order approach. Further it shows a better agreement to the calculation with the FEM. Especially the interlaminar peel stress σ_z shows an almost perfect agreement between the new displacement approach and the FEM.

3.2. *Formation of transversal cracks*

Beside the delamination of the layer there is another failure mode that can be mentioned. This is the formation of transverse cracks in thin, brittle layers like the γ-alumina layer. For this purpose, a thin γ-alumina layer is first considered as infinitely extended in the longitudinal direction and is loaded with a temperature load ΔT (see Figure 4(a)). Now, failure is considered to be the formation of two cracks in the thickness direction, which have a characteristic distance l_c between them (see Figure 4(b)). If just the section of layer between two cracks with the distance l_c is considered, the generic initial situation is given again (see Figure 1).

Namely, a layer with linear elastic properties on a rigid substrate with length l_c and thickness t. Consequently, the displacement field is determined using the previously described approach and the stress field within the layer can be derived using kinematic relations and the constitutive law. The failure prediction can be performed with Finite Fracture Mechanics using a coupled stress and energy criterion. Here, a quadratic stress criterion

$$f(\sigma_x, \sigma_c) = \left(\frac{\sigma_x}{\sigma_c}\right)^2 \geq 1\,, \tag{27}$$

is used, where the stress σ_x is used at the center of the infinitely extended layer. The present structural situation is modeled in plane elasticity (plane strain), so the stress σ_x can be expressed as follows:

$$\sigma_x = \frac{E}{(1-\nu)^2}\alpha_{th}\Delta T\,. \tag{28}$$

According to this term, the stress and consequently the stress criterion depend only on the temperature change ΔT. Consequently, the evaluation of the stress criterion results in a constant failure temperature change, which is independent of the layer thickness.

For the energy criterion the following linear criterion is used:

$$g(\overline{G}_I, G_c) = \frac{\overline{G}_I}{G_c} \geq 1 \quad \text{with:} \quad \overline{G}_I = \frac{1}{t}\int_0^t \sigma_x u_x \,\mathrm{d}z\,. \tag{29}$$

Herein the quantity $\overline{G}_I$ is the so-called incremental energy release rate and the quantity G_c is the fracture toughness of the given material. The coupled criterion postulates the formation of a crack through the total layer thickness t if both criteria for this length are fulfilled.

The coupled criterion is now evaluated, so that the critical temperature change ΔT_c can be calculated for different layer thicknesses. This situation has also been investigated by Leguillon [11], so that a comparison of the results can be drawn (see Figure 5 (left)).

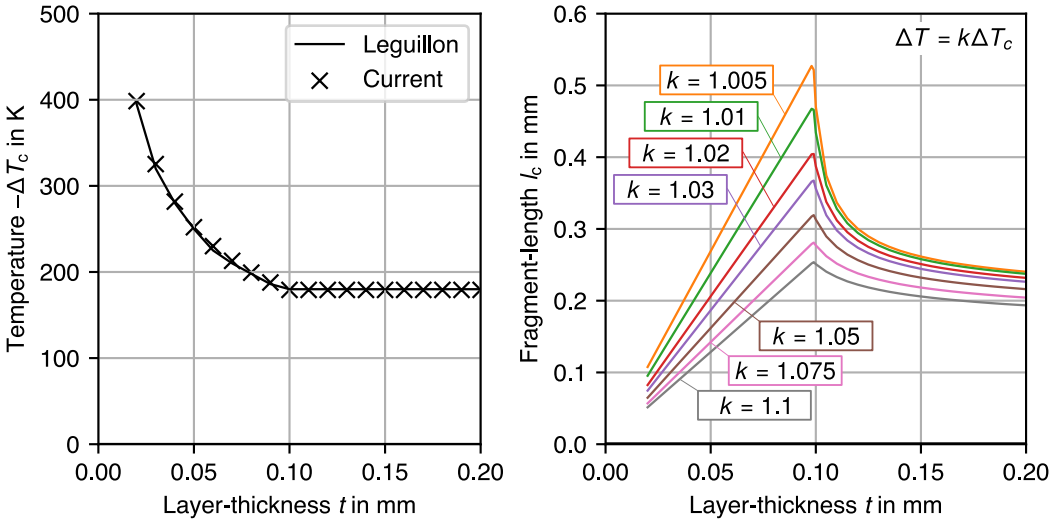

Figure 5. Critical temperature reduction (left) and fragment-length (right) for different layer-thicknesses

For layer thicknesses below 0.1 mm, the energy criterion is decisive, that means the critical cooling increases with thinner layer thickness. For layer thicknesses larger than 0.1 mm, the stress criterion is governing failure and cracks develop at a cooling of 179 K. For layer thicknesses of exactly 0.1 mm, both criteria return a critical load of −179 K. When comparing the results to the investigations of Leguillon, extremely good agreements can be seen. Both curves match each other almost perfectly, even the transition to a constant failure temperature occurs with both at a layer thickness of 0.1 mm.

In the following, the layer is loaded with temperature loads that are k times larger than the critical temperature load ΔT_c so that the resulting fragment length l_c, which is the characteristic distance between two cracks is determined. These fragment lengths are plotted in Figure 5 (right) for different layer thicknesses. A comparison of the curves for different temperature loads shows that smaller fragment lengths occur with higher temperature loads (i.e. with a higher factor k). Qualitatively, the curves are the same for different temperature loads: For layer thicknesses up to 0.1 mm, the fragment length increases with increasing layer thickness and at layer thicknesses larger than 0.1 mm, the fragment length is decreasing with increasing layer thickness.

4. Conclusion

In this work, a single layer with elastic material behavior on a rigid substrate has been modeled under temperature loading. An analytical model has been derived to describe the displacement and stress field in an approximate closed-form. Thereby the singularity exponent is taken into account in the displacement approach. One advantage over calculations with the FEM is that parameter studies can be carried out much more quickly and easily. In order to evaluate the accuracy of the closed-form analytical model, a comparison of the interlaminar stresses calculated with different displacement approaches and FEM has been carried out. It has been

shown that the results are in better agreement with the approach that takes the singularity exponent into account than with a simple second-order approach. Another important point that should be mentioned is that very high stresses occur at the free edge. These high interlaminar stresses are a cause for the development of interlaminar cracks that lead to a delamination of the layer. An analysis of the development of such interlaminar cracks is a necessary future work and could be performed for example by Finite Fracture Mechanics. The second application investigated in this work is the prediction of transverse cracks, i.e. cracks in the thickness direction that form in a pattern. In this analysis, the coupled criterion has been used to predict the failure temperature change and the fragment length. Although a very simple model is used, the results show good agreement with Leguillon's findings.

Conflicts of interest

The authors declare no competing financial interest.

Dedication

The manuscript was written through contributions of all authors. All authors have given approval to the final version of the manuscript.

Appendix A. Differential equation system

$$(2\nu-1)\left(hu_1+h^2u_2+h^\lambda u_3\right)+\left(2\nu-\frac{1}{2}\right)h^2w_1'+\left(2\nu-\frac{1}{3}\right)h^3w_2'+\left(2\nu-\frac{1}{\lambda+1}\right)h^{\lambda+1}w_3' - (\nu-1)\left(\frac{2}{3}h^3u_1''+\frac{1}{2}h^4u_2''+\frac{2}{\lambda+2}h^{\lambda+2}u_3''\right)=0 \quad (30)$$

$$(2\nu-1)\left(h^2u_1+\frac{4}{3}h^3u_2+\frac{2\lambda}{\lambda+1}h^{\lambda+1}u_3\right)+2\left(\nu-\frac{1}{3}\right)h^3w_1'+2\left(\nu-\frac{1}{4}\right)h^4w_2'+2\left(\nu-\frac{1}{\lambda+2}\right)h^{\lambda+2}w_3' - (\nu-1)\left(\frac{1}{2}h^4u_1''+\frac{2}{5}h^5u_2''+\frac{2}{\lambda+3}h^{\lambda+3}u_3''\right)=0 \quad (31)$$

$$(2\nu-1)\left(h^\lambda u_1+\frac{2\lambda}{\lambda+1}h^{\lambda+1}u_2+\frac{\lambda^2}{2\lambda-1}h^{2\lambda-1}u_3\right)+\left(2\nu-\frac{\lambda}{\lambda+1}\right)h^{\lambda+1}w_1'+\left(2\nu-\frac{\lambda}{\lambda+2}\right)h^{\lambda+2}w_2' + \left(2\nu-\frac{1}{2}\right)h^{2\lambda}w_3'-2(\nu-1)\left(\frac{1}{\lambda+2}h^{\lambda+2}u_1''+\frac{1}{\lambda+3}h^{\lambda+3}u_2''+\frac{1}{2\lambda+1}h^{2\lambda+1}u_3''\right)=0 \quad (32)$$

$$2(\nu+1)\left(hw_1+h^2w_2+h^\lambda w_3\right)+\left(2\nu-\frac{1}{2}\right)h^2u_1'+2\left(\nu-\frac{1}{3}\right)h^3u_2'+\left(2\nu-\frac{1}{\lambda+1}\right)h^{\lambda+1}u_3' + (2\nu-1)\left(\frac{1}{3}h^3w_1''+\frac{1}{4}h^4w_2''+\frac{1}{\lambda+2}h^{\lambda+2}w_3''\right)=2(\nu+1)\Delta T\alpha_{\text{th}} \quad (33)$$

$$-2(\nu-1)\left(h^2w_1+\frac{4}{3}h^3w_2+\frac{2\lambda}{\lambda+1}h^{\lambda+1}w_3\right)+\left(2\nu-\frac{1}{3}\right)h^3u_1'+\left(2\nu-\frac{1}{2}\right)h^4u_2'+\left(2\nu-\frac{1}{\lambda+2}\right)h^{\lambda+2}u_3' + (2\nu-1)\left(\frac{1}{4}h^4w_1''+\frac{1}{5}h^5w_2''+\frac{1}{\lambda+3}h^{\lambda+3}w_3''\right)=-2(\nu-1)h^2\Delta T\alpha_{\text{th}} \quad (34)$$

$$-2(\nu-1)\left(h^{\lambda}w_1+\frac{2\lambda}{\lambda+1}h^{\lambda+1}w_2+\frac{\lambda^2}{2\lambda-1}h^{2\lambda-1}w_3\right)+\left(2\nu-\frac{1}{\lambda+1}\right)h^{\lambda+1}u_1'+2\left(\nu-\frac{1}{\lambda+2}\right)h^{\lambda+2}u_2'$$
$$+\left(2\nu-\frac{1}{2}\right)h^{2\lambda}u_3'+2\left(\nu-\frac{1}{2}\right)\left(\frac{1}{\lambda+2}h^{\lambda+2}w_1''+\frac{1}{\lambda+3}h^{\lambda+3}w_2''+\frac{1}{2\lambda+1}h^{2\lambda+1}w_3''\right)$$
$$=2(\nu+1)\,h^{\lambda}\Delta T\alpha_{\mathrm{th}} \quad (35)$$

Declaration of interests

The authors do not work for, advise, own shares in, or receive funds from any organization that could benefit from this article, and have declared no affiliations other than their research organizations.

References

[1] W. Frhaan, B. H. Bakar, N. Hilal and A. Al-Hadithi, "CFRP for strengthening and repairing reinforced concrete: A review", *Innov. Infrastruct. Solut.* **6** (2021), no. 49, pp. 1–13.

[2] E. Martinelli, M. Breveglieri, C. Czaderski and N. Moshiri, *EBR vs EBROG for FRP Strengthening of RC Slabs: Experimental and numerical Modelling*, Zenodo, 2023.

[3] E. Martinelli, M. Breveglieri, N. Moshiri and C. Czaderski, *Numerical Simulation of lap-shear and prestress Force release tests of FRP Strips glued on Concrete: Considerations about the role of mixed-mode Fracture Processes*, Zenodo, 2023.

[4] O. Awassa, R. El-Hacha and K. Falkenberg, *Strengthening Underground reinforced Concrete Structures using externally bonded carbon fibre-Reinforced polymer sheets*, Zenodo, 2023.

[5] L. F. M. da Silva, P. J. C. das Neves, R. D. Adams and J. K. Spelt, "Analytical models of adhesively bonded joints—Part I: Literature survey", *Int. J. Adhes. Adhes.* **29** (2009), no. 3, pp. 319–330.

[6] L. F. M. da Silva, P. J. C. das Neves, R. D. Adams, A. Wang and J. K. Spelt, "Analytical models of adhesively bonded joints—Part II: Comparative study", *Int. J. Adhes. Adhes.* **29** (2009), no. 3, pp. 331–341.

[7] T. S. Methfessel and W. Becker, "A generalized model for predicting stress distributions in thick adhesive joints using a higher-order displacement approach", *Compos. Struct* **291** (2022), article no. 115556.

[8] T. S. Methfessel and W. Becker, *Debonding prediction of a reinforcing CFRP patch on concrete structures*, Zenodo, 2023.

[9] D. A. Bigwood and A. D. Crocombe, "Elastic analysis and engineering design formulae for bonded joints", *Int. J. Adhes. Adhes.* **9** (1989), no. 4, pp. 229–242.

[10] I. U. Ojalvo and H. L. Eidinoff, "Bond Thickness Effects upon Stresses in Single-Lap Adhesive Joints", *AIAA J.* **16** (1978), no. 3, pp. 204–211.

[11] D. Leguillon, O. Haddad, M. Adamowska and P. Da Costa, "Cracks Pattern Formation and Spalling in Functionalized Thin Films", *Procedia Mater. Sci.* **3** (2014), pp. 104–109. 20th European Conference on Fracture.

[12] D. Leguillon, "Strength or toughness? A criterion for crack onset at a notch", *Eur. J. Mech. A/Solids* **21** (2002), no. 1, pp. 61–72.

[13] D. Leguillon, "A simple model of thermal crack pattern formation using the coupled criterion", *C. R. Méc. Acad. Sci. Paris* **341** (2013), no. 6, pp. 538–546.

[14] D. Leguillon, J. Li and E. Martin, "Multi-cracking in brittle thin layers and coatings using a FFM model", *Eur. J. Mech. A/Solids* **63** (2017), pp. 14–21.

[15] D. Leguillon and E. Martin, "Prediction of multi-cracking in sub-micron films using the coupled criterion", *Int. J. Fract.* **209** (2018), pp. 187–202.

[16] H.-A. Bahr, H.-J. Weiss, U. Bahr, M. Hofmann, G. Fischer, S. Lampenscherf and H. Balke, "Scaling behavior of thermal shock crack patterns and tunneling cracks driven by cooling or drying", *J. Mech. Phys. Solids* **58** (2010), no. 9, pp. 1411–1421.

[17] D. R. Jenkins, "Determination of crack spacing and penetration due to shrinkage of a solidifying layer", *Int. J. Solids Struct.* **46** (2009), no. 5, pp. 1078–1084.

[18] Y. Shao, X. Xu, S. Meng, G. Bai, C. Jiang and F. Song, "Crack Patterns in Ceramic Plates after Quenching", *J. Am. Ceram. Soc.* **93** (2010), no. 10, pp. 3006–3008.

[19] G. W. Kolosow, *Über eine Anwendung der komplexen Funktionentheorie auf das ebene Problem der mathematischen Elastizitätstheorie*, PhD thesis, 1909. Jurievi Egyetem, in russian.

[20] N. I. Muschelišvili, *Einige Grundaufgaben zur mathematischen Elastizitätstheorie*, Carl Hanser Verlag: München, 1971.

ACADÉMIE DES SCIENCES
INSTITUT DE FRANCE

Comptes Rendus. Mécanique
2025, Vol. 353, p. 91-111
https://doi.org/10.5802/crmeca.280

Review article / *Article de synthèse*

A review of characteristic lengths in the coupled criterion framework and advanced fracture models

Une revue des longueurs caractéristiques dans le cadre du critère couplé et dans les modèles de fracture avancés

Gergely Molnár[a,*], **Aurélien Doitrand**[b,*], **Rafael Estevez**[c] **and Anthony Gravouil**[d]

[a] CNRS, INSA Lyon, LaMCoS, UMR5259, 69621 Villeurbanne, France

[b] Université Lyon, INSA-Lyon, UCBL, CNRS, MATEIS, UMR5510, F-69621 Villeurbanne, France

[c] Univ. Grenoble Alpes, CNRS, Grenoble INP, SIMAP, F-38000 Grenoble, France

[d] Univ Lyon, CNRS, INSA Lyon, LaMCoS, UMR5259, 69621 Villeurbanne, France

E-mails: gergely.molnar@insa-lyon.fr (G. Molnár), aurelien.doitrand@insa-lyon.fr (A. Doitrand), rafael.estevez@grenoble-inp.fr (R. Estevez), anthony.gravouil@insa-lyon.fr (A. Gravouil)

Abstract. The review paper explores the significance of characteristic lengths in fracture mechanics, focusing on the Coupled Criterion framework. It addresses limitations in traditional Linear Elastic Fracture Mechanics, which struggle to predict small-scale crack behaviors, and highlights the need for models that allow characteristic lengths to emerge from material properties and geometry rather than being predefined inputs.

The review covers two main characteristic lengths: the initiation crack length and Irwin's length, examining their interactions with lengths used in other fracture approaches such as Phase-Field methods, Cohesive Zone Models, and atomic-scale simulations. The findings show that Irwin's length consistently appears in models that combine stress and energy criteria, indicating its fundamental role in fracture prediction.

The study identifies limitations in current models, especially in cases involving strong singularities or where the energy condition dominates, and suggests improvements by incorporating process zone descriptions or regularization techniques from Phase-Field models. These enhancements could better capture the complex behaviors at smaller scales.

The paper concludes by advocating for a combined approach that integrates various fracture models, which could provide a more comprehensive understanding of crack initiation and propagation across different scales. This integrative strategy would allow for more accurate predictions and a deeper insight into the mechanics of fracture.

Résumé. Cet article de revue explore l'importance des longueurs caractéristiques en mécanique de la rupture, en se concentrant sur le cadre du Critère Couplé. Il met en lumière les limites des approches traditionnelles de la mécanique de la rupture élastique linéaire, qui peinent à prédire les comportements des fissures à petite échelle, et souligne le besoin de modèles permettant aux longueurs caractéristiques d'émerger des propriétés des matériaux et de la géométrie, plutôt que d'être définies a priori.

* Corresponding authors

La revue couvre deux longueurs caractéristiques principales : la longueur de fissure d'initiation et la longueur d'Irwin, en examinant leurs interactions avec les longueurs utilisées dans d'autres approches de rupture, telles que les méthodes de champ de phase, les modèles de zone cohésive et les simulations à l'échelle atomique. Les résultats montrent que la longueur d'Irwin apparaît systématiquement dans les modèles combinant des critères de contrainte et énergétique, soulignant son rôle fondamental dans la prédiction de la rupture.

L'étude identifie les limites des modèles actuels, en particulier dans les cas impliquant des singularités fortes ou lorsque la condition énergétique domine, et propose des améliorations en incorporant des descriptions de zone de processus ou des techniques de régularisation issues des modèles de champ de phase. Ces améliorations pourraient mieux capturer les comportements complexes à des plus petites échelles.

L'article conclut en prônant une approche combinée intégrant divers modèles de rupture, ce qui pourrait offrir une compréhension plus complète de l'initiation et de la propagation des fissures à différentes échelles. Cette stratégie intégrative permettrait des prédictions plus précises et une compréhension approfondie des mécanismes de la rupture.

Keywords. Finite fracture mechanics, Coupled criterion, Characteristic length, Crack initiation, Irwin's length.

Mots-clés. Mécanique de la rupture finie, Critère couplé, Longueur caractéristique, Initiation de fissure, Longueur d'Irwin.

Manuscript received 31 October 2024, revised 5 December 2024, accepted 6 December 2024.

1. Introduction

Linear Elastic Fracture Mechanics (LEFM), introduced by Griffith [1, 2], addresses the limitations of traditional mechanics in predicting failure in structures containing sharp defects. Stress-based methods suffice for smooth, flaw-free materials, but they fail around cracks, where stresses theoretically peak to infinity. Griffith's energy-based approach relies on the energy release rate to predict crack growth, thus avoiding the consideration of stress singularities. However, LEFM assumes a defect large enough to disregard smaller-scale phenomena near the crack tip, leading to the concept of a non-linear transition length scale, which defines the boundary between the linear elastic region and more complex fracture processes like plasticity or other dissipative mechanisms.

Despite its effectiveness for large cracks, LEFM cannot fully capture behaviors at this smaller scale. Additionally, most structures are not designed with pre-existing macroscopic cracks, making Griffith's theory impractical in such cases, where it would predict an unrealistic infinite load-bearing capacity. As a result, engineering standards continue to predominantly rely on stress-based criteria for materials where significant defects are not anticipated.

The first empirical observations of the size effect date back to Leonardo da Vinci [3, 4], who noticed that shorter cable segments were stronger than longer ones, though he did not provide a practical explanation for this phenomenon. It was Galileo Galilei who later formulated the correct scaling laws for materials under tension and bending [5], emphasizing how size effects limit the structural integrity of large natural and man-made structures. Centuries later, as iron and steel became more widely used, concerns about brittle fracture grew, prompting early material failure testing [6]. Around the same time, Mariotte [7], through extensive experimentation, suggested that the size effect observed by da Vinci was likely due to internal faults, concluding that larger structural elements have a higher probability of containing weak spots, thus reducing their overall strength.

Alongside the development of fracture mechanics, researchers began exploring statistical theories to explain the power-law scaling observed in experimental data. Peirce [8] introduced the weakest-link model for chains, building on extreme value statistics by Tippett [9]. This line of work reached a milestone with Weibull [10, 11], who developed the Weibull distribution to

model failure probability based on low-strength extremes, establishing a power-law relationship between material strength and failure probability, especially in materials with microscopic flaws or microcracks [12]. This statistical approach has since been applied across various materials and fracture phenomena [13–16]. While widely accepted, in this paper, we focus on a physically-based deterministic approach, recognizing that a combined statistical-deterministic framework can provide a more comprehensive view of material failure across scales.

The non-linear scaling law, first documented by Irwin in the 1950s [17], was initially overlooked or considered a statistical anomaly. Motivated by the observation that large concrete structures (such as dams and bridges) behave differently from small laboratory specimens, Bažant conducted a series of experiments [18]. He eventually published his theoretical explanation in 1986, describing a non-linear scaling law in fracture mechanics [19]. Bažant emphasized the need for non-linear analysis to account for the significant size effects observed in various engineering structures. This phenomenon has since become critical for the design of large-scale composite structures such as ship hulls or structural fuselages, as well as in fields like geotechnical and arctic engineering. For example, evaluating fault slip stability in the Earth's crust involves scale transitions that span multiple orders of magnitude.

Bažant [20] further showed that fracture resistance in many materials deviates from the power-law predictions of linear elastic fracture mechanics, especially when the initial flaw size is smaller than a critical value. In such cases, stress-based criteria should be applied. The existence of this critical length scale has since been demonstrated in various materials, including ceramics [21–24], polymers [25, 26], silica glass [27], silicon carbide [28], fiber composite laminates [29], wood [30], concrete, rock [31], spider silk [32] and even sea ice [33]. However, experimentally demonstrate this non-linear scale transition is challenging, as it requires testing specimens across multiple size ranges.

The transition length scale is often compared to the size of the fracture process zone (FPZ), a region around a crack tip where complex, nonlinear deformation occurs. The FPZ, characterized by a transition from elastic to inelastic behavior, plays a critical role in fracture mechanics. In the 1950s, Irwin [34] and Orowan [35] used X-ray measurements to demonstrate that even in brittle materials, there is evidence of regularization along crack surfaces. They independently concluded that the true critical energy release rate should be several orders of magnitude larger than Griffith's original proposal. Later, Barenblatt [36] and Dugdale [37] theorized that material near the crack yields, and this local cohesive traction limits the otherwise infinite stress peak.

Since then, numerous experimental techniques [38–47] have been developed to measure the size and shape [48] of the FPZ in brittle materials. These studies commonly assume that the FPZ is a damaged region around the crack tip linked to irreversible microstructural changes. The FPZ has been observed in materials such as concrete [49], granite [38], natural faults [50], wood [51], model materials [52], and silica glass [53]. A comprehensive review of the FPZ can be found in the thesis of Brooks [54]. Today, digital image correlation [55] is the primary technique used to quantify the FPZ, although other methods exist for transparent materials like polycarbonate [56] or for X-ray measurement in concrete [45]. Döll and Könczöl [57, 58] used optical interferometry to measure crack tip opening displacement in polymethyl methacrylate, polystyrene, and polycarbonate. Their findings indicate that, for these materials, the experimentally measured opening profile aligns well with predictions from an appropriate Dugdale model.

While the non-linear scaling law is widely accepted, its underlying cause remains a topic of active debate. This is particularly important given the rise of advanced manufacturing techniques that allow the creation of architected materials with structural elements smaller than the critical length scale of bulk materials, resulting in exceptionally strong overall responses [59].

In this review paper, we will explore recent methods and theories that effectively account for this non-linear length scale. This length scale can either be explicitly incorporated as a material parameter or arise through the coupling of different criteria.

Even if well-described by various fracture mechanics models through numerical experiments, it is not always straightforward to explain this transition between strength-based and energy-based descriptions of fracture. This transition is clearly understood using the Coupled Criterion (CC) concept [60], that was proposed to rationalize transverse cracking experiments in laminated composites by Parvizi, Garrett, and Bailey [61]. Their results showed two distinct regimes: for sufficiently thick plies, the strain at crack initiation remained constant, whereas it increased with decreasing ply thickness for thin plies. A criterion based solely on critical stress or strain—first introduced by Lamé and Clapeyron [62]—could only account for the failure of thick plies. Extending this approach to a non-local stress evaluation, either averaged over a finite volume [63] or at a specific distance [64–66]—known as the Theory of Critical Distances [67]—did not explain the increase in strain at failure for thin plies. Since Griffith's energy approach cannot predict crack initiation, an energy-based criterion applied to a finite crack surface increment was introduced, representing crack initiation across the full ply thickness. This idea was already suggested in Aveston and Kelly's model [68] and was later formalized as Finite Fracture Mechanics (FFM) by Hashin [69] and then by Nairn [70], successfully explaining the size effect in thin ply fracture. However, it underestimated the load level for crack initiation in thick plies. Dominique Leguillon [60] eventually proposed combining a non-local stress criterion with an energy criterion applied to a finite crack surface increment, asserting that both conditions must be met simultaneously for crack initiation. This approach effectively explains the transition from tensile strength-driven failure in thick plies to energy release rate-driven failure in thin plies.

The CC highlights that the nonlinear fracture resistance scaling is driven by the ratio between the initial flaw size and the Irwin's length. It results from the initiation length emerging from the coupling between the strength-based and energy-based criteria. Our primary focus will thus be on the CC [60], one of the earliest approaches to offer a mechanics-based explanation for the emergence of a process zone. We will then relate macroscopic theories, such as the theory of critical distances, the Phase-Field method, and the Cohesive Zone Model, to the fundamental concept of the Coupled Criterion. We also demonstrate how approaches that model atomic-scale behavior can bridge the gap between the continuum scale and the actual material properties.

The paper is structured as follows. First, in Section 2 the basics of the Coupled Criterion is presented with particular attention to the emerging length scale. Then in Section 3, we summarize the literature comparing the results of the Coupled Criterion with other theories and numerical methods with allow us to have a length scale explicitly or by emergence. In Section 4, we compare and contrast the results obtained with the methods, highlighting their similarities and differences. Finally, in Section 5, we draw conclusions based on our findings.

2. The characteristic lengths in the Coupled Criterion

The Coupled Criterion (CC) [60] is an approach in fracture mechanics that enables us to study fracture analysis in a wide range of applications [71, 72]. The underlying concept of the CC is that crack initiation occurs when two conditions are simultaneously met. The first condition arises from an energy equilibrium between the states before and after crack initiation over a specified surface S. This allows for the definition of the incremental energy release rate (IERR), given linear elastic material behavior and negligible inertial effects, as $\mathcal{G}_{\text{inc}} = (\delta W_{\text{ext}} - \delta W_{\text{el}})/S$, where W_{ext} represents the work done by external forces, W_{el} the elastic strain energy, and S the crack surface area. The IERR approaches the energy release rate (ERR) $\mathcal{G}$ as the crack surface area approaches zero. The CC model is thus consistent with Linear Elastic Fracture Mechanics

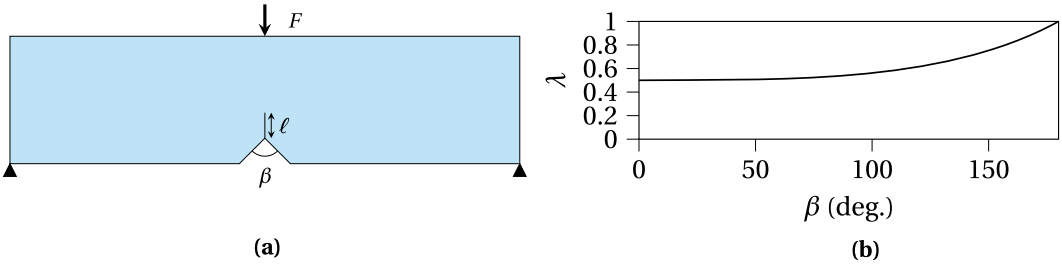

Figure 1. (a) Three-point bending of a specimen with a V-notch. (b) Characteristic exponent of the singularity λ corresponding to the opening mode as a function of β, the angle of the V-notch.

(LEFM) for sufficiently long cracks (under LEFM assumptions), while also enabling the study of crack initiation, which LEFM cannot handle as $\mathscr{G}$ tends toward zero when the crack surface tends toward zero. The energy condition for the CC is expressed as:

$$\mathscr{G}_{\text{inc}} \geqslant \mathscr{G}_{\text{c}}, \tag{1}$$

where $\mathscr{G}_{\text{c}}$ is the material's critical ERR.

The second condition of the CC states that the stress along the prospective crack path must be sufficiently large. This introduces a non-local stress criterion, which can be expressed as a function of the stress tensor components and the material strength surface. For a material adhering to a Rankine's strength surface [73], it is given by:

$$\sigma_{\text{nn}}(\mathbf{x}) \geqslant \sigma_{\text{c}} \forall \mathbf{x} \quad \text{in } \Gamma, \tag{2}$$

where σ_{nn} is the stress normal to the crack path Γ before initiation, and σ_{c} is the material's tensile strength.

Applying the CC involves combining both the stress and energy conditions to determine the minimum load magnitude at which both criteria are simultaneously met for at least one given crack surface.

An emblematic illustration of the CC is the initiation of a crack at the tip of a V-notch, where the free surfaces form an angle β, as seen in a notched specimen under bending, illustrated in Figure 1.

The case $\beta = 0°$ corresponds to an initial crack and reverts to LEFM (i.e., crack propagation based solely on energy) provided the crack is sufficiently long [74]. The case $\beta = 180°$ corresponds to a straight edge with no notch; here, the stress is homogeneous, allowing a criterion based on material tensile strength if the specimen is large enough [60, 75]. An asymptotic approach yields the stress normal to the crack path before initiation σ_{nn} and the IERR for a crack of length ℓ at the notch tip [76]:

$$\begin{cases} \sigma_{\text{nn}}(r, \theta = 0) = K \ell^{\lambda - 1}, \\ \mathscr{G}_{\text{inc}}(\ell) = \dfrac{K^2}{E} \ell^{2\lambda - 1} A_\beta, \end{cases} \tag{3}$$

where r and θ are the polar coordinates, E is Young's modulus, and λ is an exponent characterizing the singularity, varying between 0.5 for a crack ($\beta = 0°$) and 1 for a straight edge ($\beta = 180°$). In-between cases are presented in Figure 1b. The dimensionless function A_β depends on the problem's geometry (notably the notch angle β) and the local loading at the singular point, represented by the generalized stress intensity factor (GSIF) K. The GSIF drives the magnitude of the local stress field variation near the V-notch tip. It is a characteristic parameter that can be used to study the nucleation of a crack, i.e., crack initiation occurs when a critical GSIF is reached. It is

calculated based on a path-independent contour integral [76, 77]. Under a linear elastic framework and assuming small deformations, the GSIF is proportional to the applied load F, shown in Figure 1a.

If $0 < \beta < 180°$, the stress tends to infinity as r approaches 0, making a stress-based criterion alone ineffective, as it predicts crack initiation under an infinitesimal load. Conversely, the IERR approaches 0 as the crack length approaches 0, meaning an energy-based criterion alone does not predict crack initiation either. This indicates a missing element in crack initiation studies: a *length scale*. One approach is to introduce this length as an additional input parameter to the stress criterion (yielding the Theory of Critical Distances [67]) or in conjunction with the energy criterion, resulting in an incremental energy approach within Finite Fracture Mechanics [69, 70].

Another possibility is to use the CC, i.e., to combine the stress criterion and the energy criterion, which are already valid for the two extreme cases ($\beta = 0°$ and $\beta = 180°$). We then look for the minimum loading level and the corresponding crack length for which both criteria are met. The combination of the two criteria introduces a characteristic length into the problem, which is not an input parameter but rather the result of this coupling. We then obtain the initiation crack length ℓ_i and the GSIF K_i at initiation [60, 78]:

$$\begin{cases} \ell_\mathrm{i} = \dfrac{E\mathscr{G}_\mathrm{c}}{A_\beta \sigma_\mathrm{c}^2} = \dfrac{\ell_\mathrm{mat}}{A_\beta}, \\ K_\mathrm{i} = \left(\dfrac{E\mathscr{G}_\mathrm{c}}{A_\beta}\right)^{1-\lambda} (\sigma_\mathrm{c})^{2\lambda-1}. \end{cases} \tag{4}$$

We note that the GSIF is homogeneous to the product of a stress and a length to the power $(1-\lambda)$. For a straight edge, $\lambda = 1$ and the GSIF at initiation becomes $K_\mathrm{i} = \sigma_\mathrm{c}$ (K_i is then homogeneous to a stress), thus reducing to a stress criterion. In the case of a crack, $\lambda = 1/2$ and we return to Irwin's criterion $K_\mathrm{i} = K_\mathrm{Ic} = \sqrt{E\mathscr{G}_\mathrm{c}/A_\beta}$ (K_i is then homogeneous to a critical stress intensity factor). LEFM is therefore included within the CC formulation, allowing for the study of both crack initiation and the propagation of an existing crack. The proposed formulation remains general, as it can address crack initiation with or without a singularity.

In addition to the initiation length, the combination of the two criteria introduces another characteristic length, Irwin's length $\ell_\mathrm{mat} = E\mathscr{G}_\mathrm{c}/\sigma_\mathrm{c}^2$ [17], which is intrinsic to the material since it depends only on its elastic and fracture properties. The asymptotic approach reveals that the initiation length is actually related to Irwin's length through the dimensionless coefficient A_β, which depends on (i) the geometry (here the V-notch angle) and (ii) the loading (here the GSIF) [24, 77]. In the following, we examine how these two lengths in the CC formulation (i.e., the initiation length and Irwin's length) correspond to other characteristic lengths encountered in various fracture mechanics approaches.

3. Correlation with lengths involved in other fracture approaches

In this section, we focus on different approaches able to describe the nonlinear fracture resistance scaling, similarly to the CC. Even if based on different fracture description and involving different input parameters, we thus provide an insight on how the characteristic and intrinsic length scales involved in these approaches are related to the one obtained in the CC: the initiation length and Irwin's length.

Figure 2 illustrates schematically how various major techniques facilitate the emergence of a characteristic length scale, which subsequently aids in describing the nonlinear scaling observed in experiments.

For the Coupled Criterion (CC), a characteristic length emerges as the distance where both energy and stress criteria are simultaneously satisfied. This length can consistently be correlated

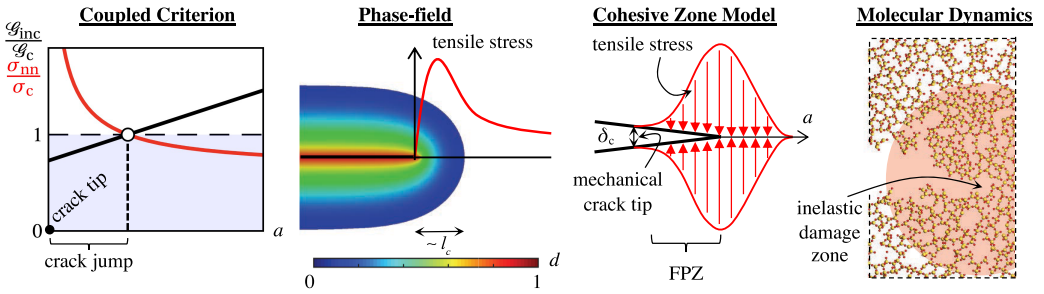

Figure 2. Summary of the key methods discussed, highlighting how each technique integrates material length scales into its framework and how these are reflected in simulation outcomes. In the figure d represents damage, l_c is the phase-field length scale, a is the crack length and δ_c is the critical separation when the crack is fully open.

to Irwin's fundamental metric. Notably, studies have shown that if the initial crack is sufficiently sharp and large compared to the material's intrinsic scale, the resulting length remains constant [74]. This observation provides a possible explanation for the effectiveness of the Theory of Critical Distances (TCD): evaluating the stress at a fixed distance produces results comparable to more advanced criteria.

In smeared damage approaches, such as the Phase-Field (PF) and Thick Level Set (TLS) methods, a regularization length is inherently introduced. This regularization modifies the stress profile, resulting in a slight alteration not only near the crack tip but also in the tail of the theoretically elastic stress response for the same macroscopic equilibrium. This phenomenon raises an important question: at what distance does the calculation of experimental toughness, based on a fit to the singular solution, remain valid?

The Cohesive Zone Model (CZM) operates in a manner similar to smeared damage methods, defining the tension–separation law as an input parameter. However, CZM offers greater flexibility by allowing the critical separation to be specified, which results in a certain damage diffusion length representing the process zone ahead of the crack tip. The latter also depends on the geometry, boundary conditions and local stress state. Despite this advantage, the technique suffers from a significant limitation: it requires prior knowledge of the crack path.

Finally, particle-based methods, such as molecular dynamics (MD) and peridynamics, treat the material as a discrete system of particles. In peridynamics, the horizon explicitly defines the characteristic length scale. In atomic-scale simulations, the interaction between interatomic potentials and the realistic atomic structure leads to the emergence of a localized, inelastic zone around the crack tip [53].

This section discusses these various methods and evaluates their potential for comparison with the Coupled Criterion. We will highlight results from the literature that address the nonlinear scaling transition and examine the underlying mechanisms involved.

3.1. *Theory of critical distances*

The approaches based on the Theory of Critical Distances (TCD) are commonly used for engineering failure prediction [67, 79]. Since a local maximum stress criterion is unsuitable for predicting the experimentally observed size effect, even for non-singular stress fields [80], TCD compares the stress at a specified distance from a stress concentration or singular point to the material tensile strength.

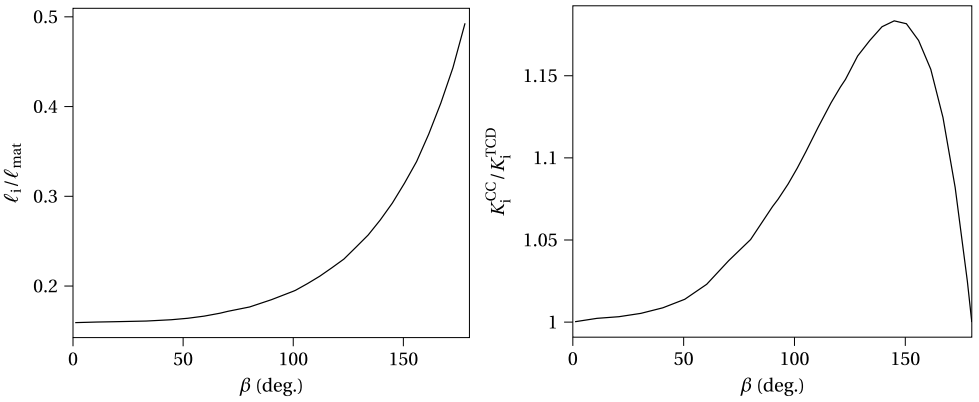

Figure 3. (a) Initiation length normalized by Irwin's length as a function of the V-notch angle predicted using the CC for a V-notch in an infinite medium. (b) Ratio between the GSIF obtained using either the CC (K_i^{CC}) or the TCD (K_i^{TCD}) as a function of the V-notch angle.

The CC and the TCD have been compared in various configurations, e.g., to study the fatigue limit of V-notch specimens [81]. Regardless of the notch radius, the critical distance remains constant in the TCD, whereas it decreases with increasing notch radius in the CC. By basing the TCD critical distance on Irwin's length, a relationship between the critical crack advance for both approaches—independent of material parameters—was derived. This result aligns with the fact that the initiation crack length in the CC is proportional to Irwin's length [24, 77].

Chao Correas et al. [80] demonstrated that both the CC and TCD describe the gradual transition between two stress-driven solutions for crack initiation at a spherical void (for small and large void radii, respectively). The transition between these regimes falls within the same range of void radii relative to the material characteristic length.

Campagnolo et al. [82] compared the CC to the Strain Energy Density (SED) approach for crack initiation at a V-notch under in-plane shear loading. The SED model considers the strain energy density over a control volume around the crack initiation site as the critical parameter. Both methods showed that the apparent SIF at crack initiation is proportional to powers of K_{Ic} and σ_c, differing only in the proportionality factor, which depends on the notch angle in the CC and Poisson's ratio in the SED approach. Both methods predicted similar apparent SIFs at crack initiation for this configuration, with the control volume radius based on Irwin's length [82, 83].

The primary distinction between the TCD and CC is that in TCD, the characteristic length is an input parameter, while in CC it is an output derived from combining the stress and energy conditions. Several ways of nonlocal stress evaluation exist, such as integration over a volume or the use of pure nonlocal functions [84, 85]. One of the first method proposed was to evaluate the stress at a given distance from a singular point. For example, applying the TCD as a point stress criterion at a distance equal to Irwin's length ($\sigma_{nn}(\ell_{mat}) = \sigma_c$) yields:

$$K_i = (E'\mathcal{G}_c)^{1-\lambda}\sigma_c^{2\lambda-1}. \tag{5}$$

This expression only differs from the one obtained using the CC by the coefficient A_β (see Equation (4)), reflecting that the TCD disregards geometry, whereas the CC accounts for it through A_β. Figure 3 illustrates the differences between the TCD and CC in predicting crack initiation at a sharp V-notch.

The normalized initiation length obtained using the CC for different V-notch angles is shown in Figure 3a. It indicates that the initiation length using the CC is generally smaller than Irwin's length and depends on the geometry. In addition, Figure 3b shows the ratio between the GSIF obtained using the CC or the TCD as a function of the V-notch angle. Based on Equations (4) and (5), this ratio is given by $K_{\mathrm{I}}^{\mathrm{CC}}/K_{\mathrm{I}}^{\mathrm{TCD}} = A_{\beta}^{\lambda-1}$. Using LEFM normalization of displacement fields, a ratio of 1 is achieved for $\beta = 0°$ and $\beta = 180°$, with a non-monotonic trend as β increases. Specifically, $A_{\beta} = 1$ for $\beta = 0$, decreasing with increasing β, while λ increases from 1/2 ($\beta = 0°$) to 1 ($\beta = 180°$). Overall, differences of less than 20% can be expected between the CC and TCD in predicting crack initiation at a V-notch in an infinite medium.

Since the TCD disregards the overall specimen geometry, questions arise about its application for small-scale specimens, where size may be smaller than Irwin's length. This method may also be unsuitable for initiation configurations driven by the energy criterion, such as transverse cracking in thin composite laminates [60, 86, 87].

3.2. *Phase-field*

Fracture Phase-Field (PF) models [88, 89] approximate crack discontinuities through a smeared damage field controlled by a length scale parameter (l_{c}), which defines the extent of damage. These models balance elastic energy with diffused fracture energy to identify the energetically favorable crack front, using fracture toughness ($\mathscr{G}_{\mathrm{c}}$) and the regularization length (l_{c}) as primary inputs.

Both the CC and PF approaches use the critical energy release rate ($\mathscr{G}_{\mathrm{c}}$) as an input parameter, but they differ in how they handle tensile strength: CC explicitly incorporates it, while PF replaces it with the regularization length (l_{c}). In simulations of notched thin ply laminate fractures, Reinoso et al. [90] showed that the CC method effectively captures the size effect and accurately predicts failure stress, whereas the PF approach slightly underestimates failure stress, with l_{c} chosen to match the experimentally measured displacement around stress concentrators.

Early studies comparing CC and PF results [91] found good correspondence between the two methods, although the choice of l_{c} was often based on matching maximum tensile stress under uniaxial loading to the material's tensile strength. Strobl et al. [92, 93] simulated Hertzian indentation-induced fractures using both CC and PF, noting consistent trends in crack location and critical displacement, with l_{c} determined using the homogeneous Phase-Field solution under uniaxial tension.

Kumar et al. [94] addressed PF's tendency to overestimate critical loads at the onset of damage by explicitly incorporating a stress criterion, effectively creating a CC-inspired PF approach. Similarly, Abaza et al. [95] calibrated l_{c} in PF models for notched ceramic specimens to match apparent stress intensity factors at crack nucleation with those obtained using CC. Jimenez et al. [96] demonstrated that for small-scale specimens, critical displacements or forces largely depend on $\mathscr{G}_{\mathrm{c}}$, using CC to guide the load range selection in PF models and suggesting PF as a preliminary step for CC when the crack path is not known a priori.

A comprehensive comparison of CC and PF approaches was provided in Ref. [74], which studied tensile opening and in-plane shear fractures, proposing a correlation between tensile strength and l_{c} that depends on the stress state:

$$\sigma_{\mathrm{c}} \simeq \sigma_{\max} = \eta\left(\nu, \frac{\sigma_2}{\sigma_1}, \frac{\sigma_3}{\sigma_1}\right)\sqrt{\frac{E\mathscr{G}_{\mathrm{c}}}{l_{\mathrm{c}}}}, \tag{6}$$

where η accounts for the stress state. This work was later extended to antiplane shear [97]. In these studies, different aspects were compared, such as critical initiation load in tension, branching angle in simple shear, and facet spacing in antiplane shear.

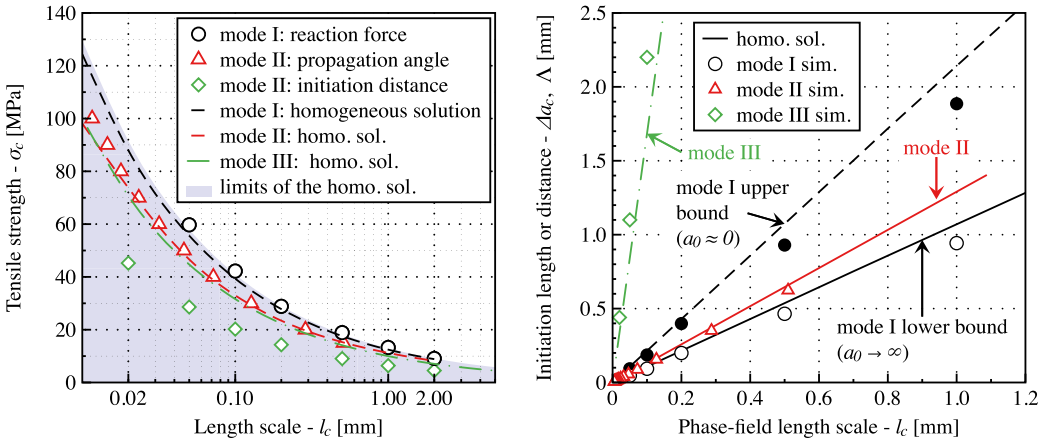

Figure 4. (a) Summarized correlations between the tensile strength (σ_c) and the internal length scale (l_c). The blue shade represents the accessible space based on the homogeneous solution. (b) Correlation between l_c and the initiation lengths and characteristic distances.

The results are summarized in Figure 4. The correlations for tensile opening, in-plane, and antiplane shear fracture modes show a general trend: as the regularization length (l_c) decreases, the material strength (σ_c) increases. However, this relationship cannot be captured by a single master curve; instead, it forms a failure surface varying within the range defined by Equation (6), shown by the shaded area in Figure 4a. Although the initiation length Δa_c does not explicitly appear in the PF, it is crucial for determining where the stress and energy criteria are satisfied simultaneously, with its correlation to l_c being linear across different fracture modes.

The results suggest that l_c serves as an intermediate parameter between Irwin's intrinsic length and the actual process zone size, though it cannot fully account for the effects of macroscopic geometry. This raises the question of whether materials have a single tensile strength (as per Rankine's theory [73]) or if the maximum tensile strength is influenced by the stress state (corresponding to another strength surface in the principal stress space).

Furthermore, studies [74, 98] showed that, similar to the CC, the PF method satisfies both energy and stress criteria due to an indirect correlation between the maximum tensile stress and l_c. As l_c increases, the process zone enlarges, resulting in lower maximum stress and an earlier satisfaction of Griffith's criterion. Thus, higher l_c values correlate with lower maximum tensile stresses needed for fracture.

Additionally, in the PF technique, the stress field is non-singular, requiring the stress tail to be slightly higher than the singular solution used in the CC to maintain equilibrium. The study of antiplane shear highlighted the need for an enhanced CC model incorporating a regularized stress field inspired by PF regularization, which would allow the CC to better address three-dimensional antiplane cracking by introducing a third parameter to account for the crack geometry, as suggested in Ref. [99].

3.3. *Cohesive zone*

When used in fracture mechanics, a Cohesive Zone Model (CZM) [36, 37] is designed to describe the formation and evolution of both the crack (corresponding to the traction-free region) and

the process zone ahead of the crack tip. Given, as input parameters, the material tensile and shear strengths and critical energy release rate, the CZM defines the traction–separation behavior between two surfaces.

The cohesive response is triggered once a local critical traction is reached, leading to separation and a discontinuity in the displacement field across the surfaces, governed by a distribution of traction. The traction–separation profile mechanically replicates the underlying failure mechanisms and remains active until a critical separation δ_c is reached, at which point a crack nucleates locally. This critical separation δ_c provides an intrinsic length scale that characterizes the failure process. As the separation between the two surfaces increases, the traction–separation behavior progresses to this critical point, defining a characteristic length associated with the displacement jumps necessary for crack formation.

As an example, considering only the opening mode and a bilinear traction–separation profile in a linear elastic isotropic material, the critical displacement jump is given by:

$$\delta_c = \frac{2\mathscr{G}_c}{\sigma_c} = \frac{2\sigma_c}{E}\ell_{mat} = 2\varepsilon_c\ell_{mat}, \tag{7}$$

where ε_c is the material tensile strain at failure. The critical displacement jump is thus related to the material's Irwin's length and critical strain, making it an intrinsic material property.

In addition, to this characteristic length, another length is involved in CZM which is the extent of the process zone ahead of the crack. Indeed, the CZM and the CC mainly differ concerning the description of the cracking process. While the CC relies on a binary description of fracture considering two possible states, namely undamaged or cracked material, the CZM defines an intermediate state: the process zone through the description of a traction–separation profile. This process zone induces another main difference between both approaches since the stress can locally be larger than the material tensile strength in the CC whereas in CZM, the stress is always bounded by the material strength within the process zone. The process zone length depends on the Irwin's length [100, 101], but contrary to the critical displacement jump, it is not an intrinsic material property as it also depends on the specimen geometry and boundary conditions. Cornetti et al. [102] observed that for an initial crack in infinite medium or at a V-notch, the CZM process zone length was significantly different from the initiation length obtained using the CC, even if both length variations followed almost identical trends with respect to the normalized initial crack length. This analysis was then refined [103] by introducing a weight function in the stress condition of the CC in order to match the CZM. The CZM with cohesive laws exhibiting earlier softening showed satisfactory correspondence with the CC stress conditions, modified by weight functions that were elevated near the crack tip and tapered off with distance. Actually, it was shown that the difference between the failure load predicted by the CC and the CZM differs as the critical separation (and equivalently the Irwin's length) increases [104].

Nevertheless, an equivalence may possibly be determined between the CC and a given traction–separation CZM profile. Summarizing previous works aiming at the comparison between the CC and CZM [80, 105–115], it appears that there is not a unique CZM traction–separation profile that enables retrieving the failure loading and crack length predicted using the CC. The CZM traction–separation profile corresponding to the CC actually depends on the geometry, the type of loading, the cracking mechanism and thus has to be identified for a given configuration. A further comparison between the CC and the CZM was established based on another extrinsic length, i.e., the length of the crack after the unstable propagation following initiation [114]. It was shown that the range of crack lengths after unstable propagation obtained with various traction–separation profiles respectively comprised the crack length lower bound obtained using the CC, and that crack lengths similar to those obtained using the CC were obtained using a bilinear traction–separation profile in that case.

3.4. *Atomic scale simulations*

At the smallest scales currently accessible through computational resources to study fracture, molecular dynamics (MD) simulations [53] offer valuable insights into crack propagation by using interatomic potentials and detailed atomic structures, thus avoiding the need for additional numerical parameters. Recent studies [116, 117] have advanced our understanding of finite-size effects, revealing a critical transition in wear mechanisms at the atomic scale. Specifically, atomistic simulations show that when asperity contact junctions surpass a critical size, fracture-induced debris formation occurs, while smaller junctions result in a gradual smoothing through plastic deformation. This non-linear behavior highlights the crucial role of length scale in determining whether fracture or plastic smoothing dominates.

Later, Brochard et al. [118] specifically examined brittle failure in two materials: a simplified 2D toy model and graphene. Using molecular dynamics (MD) simulations, the authors investigate how the stress and toughness criteria contribute to the emergence of a length scale during failure. The toy model, consisting of a regular triangular lattice with harmonic interatomic interactions, allowed for a straightforward theoretical analysis of failure processes. In contrast, graphene, with its more complex atomic structure and realistic mechanical behavior, served as a case study for a real material.

For both materials, the authors use MD simulations to observe failure under different conditions, such as varying temperature, system size, and loading rate. Through these simulations, the study highlighted the emergence of a nonlinear transition length scale at the process zone near the crack tip. This process zone grew larger as the temperature increased, and the material transitions from a stress-based failure mode to one governed by energy dissipation at the crack tip. The results showed that, in graphene, this length scale and the corresponding process zone were much larger compared to the toy model, demonstrating how atomic interactions and material properties influence the scaling of strength and toughness. The simulations provided a deeper understanding of how microscopic bond-breaking processes connect to macroscopic failure behaviors, particularly in materials with varying defect types and sizes.

Chao Correas et al. [80] validated their findings by comparing the FFM approach with both experimental data and atomistic simulations. In terms of atomistic simulations, the study by Ippolito et al. [119] on β-silicon carbide is highlighted. In this work, atomistic simulations were used to create a model free of intrinsic defects by removing atoms from a crystalline lattice to simulate spherical voids. The simulations provided critical material properties, such as fracture toughness and strength, which allowed for the calculation of the Irwin's length (characteristic length scale).

Chao Correas et al. [80] found that the results of the atomistic simulations agreed with the predictions made by FFM, particularly when using the averaged stress variant. This variant provided the most accurate results when compared to the atomistic data, which eliminated scattering from experimental flaws and imperfections. This supported the use of FFM as a robust predictive tool in materials without inherent defects. The study concluded that atomistic simulations are crucial for refining predictions of failure in brittle materials, offering a close match with coupled criteria approaches like FFM in defect-free scenarios.

3.5. *Thick level set*

The underlying idea of the The Thick Level Set (TLS) model is to constrain the norm of the damage gradient to control the evolution of a damage field, introducing a characteristic length which represents the smallest possible distance between a fully damage point and a point where there is no damage. The characteristic length thus represents the extent of the regularization zone

around a sharp crack. Zghal et al. [120] compared the (TLS) approach to the matched asymptotic approach of the CC considering sharp or blunted notches and cavities. TLS and CC resulted in close apparent strengths for all cases provided the assumptions of the matched asymptotic approach were satisfied. However, no comparison between the TLS characteristic length and the CC initiation length was provided.

3.6. *Peridynamics*

Zhang et al. [121] implemented the CC to study crack initiation at circular holes within a peridynamic framework. They showed that similar strain and stress values were obtained using either peridynamics or FE modeling, except locally near the hole edge due to a skin effect arising from the incomplete non-local horizon for nodes around the hole edge. They also demonstrated that peridynamics yielded failure stresses similar to those obtained using Finite Fracture Mechanics [121]. Ultimately, in peridynamics, the characteristic length is defined by the horizon size.

In a subsequent study, Zhang et al. [122] analyzed the stress and IERR for various horizon sizes. The main conclusion was that the skin effect influences both stress and IERR, especially for small crack lengths near a free edge. The stress and IERR values in this region are unreliable, as the local material response near a free edge differs from that in the bulk due to the incomplete horizon. They also observed that the region where stress and IERR deviate from the finite element solution increases with a larger horizon size. Ultimately, the horizon size must be set sufficiently smaller than the initiation length in the CC. Under this condition, similar stress and IERR values are obtained, indicating that peridynamics can predict similar initiation loads as the CC.

3.7. *Gradient elasticity*

The Gradient Elasticity (GE) model and the CC were compared to predict borehole crack initiation under combined pressure and biaxial loading [123]. It was highlighted that the CC is local in its constitutive law but non-local in the failure criterion, as both stress and energy conditions must be met simultaneously at a specific distance from the singular point or stress concentration. Conversely, the GE model is non-local in its constitutive law but local in its failure criterion, treating the governing failure parameter as the local stress concentration factor. The GE model introduces a characteristic length that defines the distance over which non-local effects act, smoothing high variations in the elastic stress field. Similar to TCD, the GE model is inapplicable below a threshold size where the internal length becomes comparable to the specimen's characteristic size. Sapora et al. [123] demonstrated that nearly identical failure stress predictions can be achieved if the internal length in the GE model is calibrated based on Irwin's length.

3.8. *Continuum damage model*

Continuum Damage Mechanics (CDM) [124] provides a framework for understanding how micro-damage, like micro-cracks or voids, impacts material properties at a larger scale. Kachanov [125] introduced the damage variable concept to quantify degradation from micro-defects. CDM uses constitutive models that describe stress–strain relationships and damage evolution equations based on thermodynamics to predict the transition from micro-defects to failure. Although classical CDM models uniform damage well, it faces challenges with discontinuities, prompting the development of gradient damage models [126–130], which include regularization terms to simulate phenomena like brittle fracture [131] and localized damage [132]. Methods for measuring the characteristic length of nonlocal continua have also been proposed [133].

Carrère et al. [134] compared the CC with CDM to investigate failure in adhesively bonded joints. Despite differing definitions of final failure, both models produced similar failure loads under the assumption of small displacements, as crack initiation occurs just before the specimen reaches final failure. A characteristic length emerged in the CDM, corresponding to the extent of the process zone, i.e., the region where the damage variable ranges from 0 (pristine material) to 1 (fully damaged material). At crack initiation, the process zone extent was found to be larger than the initiation length predicted by the CC, yet it followed a similar trend with respect to the material's critical energy release rate.

4. Discussion

The Irwin's length appears in all models that couple a stress and an energy criterion, either directly or indirectly, such as the CC, CZM, and PF models, or as a direct input parameter in models like TCD. This parameter is intrinsic to the material, obtained from a combination of other intrinsic material properties. While linking Irwin's length to the material microstructure is not always straightforward, connections can sometimes be established. For example, in polycrystalline ceramics, the intrinsic tensile strength—determined for specimens with extrinsic defects that are sufficiently small compared to the Irwin's length [23]—is related to grain size [135, 136] as well as the critical energy release rate [22]. This implies that the Irwin's length depends on grain size and other intrinsic defects present within the microstructure.

Beyond its role as an intrinsic material property, Irwin's length is crucial for the numerical implementation of the aforementioned models. It influences computational setups, such as the choice of mesh size in CZM [100, 101] and CC [77], or the selection of the regularization length in PF [74, 137].

If no length scale appears in a fracture model, it is unable to assess configurations related to crack initiation or propagation outside the assumptions of Griffith's model. A first example is Linear Elastic Fracture Mechanics, which predicts infinitely large remote stresses for a crack with vanishing size. This aligns with the assumption of a semi-infinite crack in an infinite medium, which does not hold for finite or diminishing crack lengths. A second example involves applying the TCD to specimens smaller than Irwin's length. Since TCD is based on stress evaluation at a specific distance or over a volume defined by Irwin's length, applying it to small-scale specimens is problematic, as the characteristic length becomes meaningless. A third example concerns TCD's application to energy-driven configurations without stress gradients, such as transverse cracking in laminates with thin plies. In this case, a homogeneous stress field exists within the plies transverse to the loading direction, so the TCD would predict a failure load based solely on the stress within the ply, regardless of ply thickness or the evaluation length or volume. As a result, TCD would miss the observed failure load increase with decreasing ply thickness, which is primarily controlled by energy.

Even for models coupling stress and energy conditions, there exist pathological configurations where the failure description remains incomplete. Certain cases highlight where the CC could be enhanced, specifically when the length effect is effectively "disabled" because the energy criterion predominates, causing the CC to revert to a purely energy-based criterion. Two primary configurations exhibit this behavior.

Firstly, in the presence of strong singularities [138–140], the IERR scales as $K\ell^{2\lambda-1}$ with $\lambda < 1/2$. Here, the IERR approaches infinity as the crack length tends toward zero, which means the stress criterion is always satisfied, causing the CC to revert to an energy-only criterion.

The second configuration involves a semi-infinite crack under remote anti-plane shear loading. An asymptotic approach shows that the stress criterion no longer influences the initiation

generalized stress intensity factor (GSIF), which is predicted solely based on the energy criterion, $K = (\mathcal{G}_c/A)^{1-\lambda}\sigma_c^{2\lambda-1}$, with $\lambda = 1/2$. The IERR reaches its maximum for rectilinear propagation [141–143], whereas experimental observations indicate that facets initiate at an angle inclined with respect to the primary propagation direction of the initial crack front.

In configurations where the CC fails to predict crack initiation due to the absence of a length effect, one potentially missing component could be the description of the process zone prior to initiation. Indeed, the Phase-Field approach can account for the occurrence of facets under antiplane shear [97], as observed experimentally, with the primary distinction from the CC being the presence of a process zone that develops before crack initiation. Previous studies have shown that describing this process zone is essential in PF models to accurately predict other configurations, such as along the two lips of an initial crack [74, 137, 144].

Incorporating this feature into the CC could improve its predictive capability. For example, Dominique Leguillon [145] proposed a model to describe a damage zone ahead of a V-notch prior to initiation. Alternatively, a combination of the crack regularization provided by the PF model with the CC could be implemented, as demonstrated in Ref. [99].

5. Conclusion

In this review, we examined characteristic lengths in fracture mechanics, with a particular focus on the Coupled Criterion framework and its interactions with other advanced fracture models. Our analysis highlighted that the CC, through coupling stress and energy criteria, uniquely clarifies the conditions under which cracks initiate across various configurations, even when dealing with theoretical scenarios that may not manifest in reality. By exploring these boundaries, we gained insights into transition behaviors that occur between configurations and the convergence of stress and energy requirements for crack initiation.

We observed that while the CC provides a comprehensive understanding of crack initiation, it lacks certain advantages of other models, such as autonomous crack path determination or the straightforward handling of multiple cracks initiating and propagating simultaneously. However, it offers valuable insights into other fracture models through the established inter-model dialogue. Our position is that fracture models can mutually benefit by extending this dialogue beyond simple comparisons of predicted failure loads obtained through different approaches.

A promising direction for the CC is to incorporate the regularization provided by the PF model or the process zone (PZ) description available in CZM. Such integration would allow for a detailed process zone description before initiation, addressing limitations in configurations where the length effect vanishes.

The development of such a dialogue between the CC and other fracture models remains an open avenue, as exemplified by the Discrete Elements Method [146, 147], which could offer a way to describe crack initiation in a manner comparable to continuum mechanics and the CC.

Declaration of interests

The authors do not work for, advise, own shares in, or receive funds from any organization that could benefit from this article, and have declared no affiliations other than their research organizations.

Dedication

The manuscript was written through contributions of all authors. All authors have given approval to the final version of the manuscript.

Acknowledgments

The authors express their deep gratitude to Dominique Leguillon for his invaluable advice and inspiration. His unwavering willingness to encourage us will always serve as a guiding example for the community.

References

[1] A. A. Griffith, "The phenomena of rupture and flow in solids", *Philos. Trans. R. Soc. Lond. A* **221** (1921), no. 582-593, p. 163-198.
[2] A. A. Griffith, "The theory of rupture", in *First International Congress on Applied Mechanics*, Waltman, 1924, p. 55-63.
[3] L. da Vinci, *Codex Atlanticus*, Bibilioteca Ambrosiana, 1504, https://en.wikipedia.org/wiki/Codex_Atlanticus.
[4] E. Williams, "Some observations of Leonardo, Galileo, Mariotte and others relative to size effect", *Ann. Sci.* **13** (1957), no. 1, p. 23-29.
[5] G. Galilei, *Discourses and Mathematical Demonstrations Relating to Two New Sciences*, Louis Elsevier, Leida (Leiden), 1638.
[6] D. Kirkaldy, *Results of an Experimental Inquiry into the Tensile Strength and Other Properties of Various Kinds of Wrought-iron and Steel*, Private Publication, London, 1864.
[7] E. Mariotte, *Traité du mouvement des eaux et des autres corps fluides*, Chez Jean Jombert, Paris, 1886.
[8] F. T. Peirce, "Theorems on the strength of long and of composite specimens", *J. Text Inst. Trans.* **17** (1926), no. 7, p. T355-T368.
[9] L. C. H. Tippett, "On the extreme individuals and the range of samples taken from a normal population", *Biometrika* **17** (1925), p. 364-387.
[10] W. Weibull, "Statistical theory of the strength of materials", *Proc. R. Acad. Eng. Sci.* **15** (1939), no. 1, p. 1-45.
[11] W. Weibull, "The phenomenon of rupture in solids", *IVA Handlingar* **153** (1939), p. 1-55.
[12] A. M. Freudenthal, "The statistical aspect of fatigue of materials", *Proc. R. Soc. Lond. Ser. A* **187** (1946), no. 1011, p. 416-429.
[13] P. Kittl, G. Díaz, "Size effect on fracture strength in the probabilistic strength of materials", *Reliab. Eng. Syst. Saf.* **28** (1990), no. 1, p. 9-21.
[14] A. G. Evans, "A general approach for the statistical analysis of multiaxial fracture", *J. Am. Ceram. Soc.* **61** (1978), no. 7-8, p. 302-308.
[15] F. M. Beremin, A. Pineau, F. Mudry, J. C. Devaux, Y. DEscatha, P. Ledermann, "A local criterion for cleavage fracture of a nuclear pressure vessel steel", *Metall. Trans. A* **14** (1983), p. 2277-2287.
[16] Y. Lei, N. P. O'Dowd, E. P. Busso, G. A. Webster, "Weibull stress solutions for 2-D cracks in elastic and elastic-plastic materials", *Int. J. Fract.* **89** (1998), p. 245-268.
[17] G. R. Irwin, *Fracture*, Springer, Berlin, Heidelberg, 1958.
[18] Z. P. Bažant, "Size effect in blunt fracture: concrete, rock, metal", *J. Eng. Mech.* **110** (1984), no. 4, p. 518-535.
[19] Z. P. Bažant, J. Kim, P. Pfeiffer, "Nonlinear fracture properties from size effect tests", *J. Struct. Eng.* **112** (1986), no. 2, p. 289-307.
[20] Z. P. Bažant, "Size effect on structural strength: a review", *Arch. Appl. Mech.* **69** (1999), p. 703-725.
[21] H. Kimoto, S. Usami, H. Miyata, "Flaw size dependence in fracture stress of glass and polycrystalline ceramics", *Trans. Jpn. Soc. Mech. Eng. Ser. A* **51** (1985), no. 471, p. 2482-2488.
[22] S. Usami, H. Kimoto, I. Takahashi, S. Shida, "Strength of ceramic materials containing small flaws", *Eng. Frac. Mech.* **23** (1986), no. 4, p. 745-761.
[23] D. Leguillon, E. Martin, "Prediction of multi-cracking in sub-micron films using the coupled criterion", *Int. J. Frac.* **209** (2018), p. 187-202.
[24] E. Martin, D. Leguillon, O. Sevecek, R. Bermejo, "Understanding the tensile strength of ceramics in the presence of small critical flaws", *Eng. Frac. Mech.* **201** (2018), p. 167-175.
[25] A. Doitrand, A. Sapora, "Nonlinear implementation of finite fracture mechanics: a case study on notched Brazilian disk samples", *Int. J. Non-Linear Mech.* **119** (2020), article no. 103245.
[26] A. Sapora, A. R. Torabi, S. Etesam, P. Cornetti, "Finite fracture mechanics crack initiation from a circular hole", *Fatigue Frac. Eng. Mater. Struct.* **41** (2018), no. 7, p. 1627-1636.
[27] J. Luo, J. Wang, E. Bitzek *et al.*, "Size-dependent brittle-to-ductile transition in silica glass nanofibers", *Nano Lett.* **16** (2016), no. 1, p. 105-113.
[28] Z. P. Bažant, M. T. Kazemi, "Size effect in fracture of ceramics and its use to determine fracture energy and effective process zone length", *J. Am. Ceram. Soc.* **73** (1990), no. 7, p. 1841-1853.

[29] Z. P. Bažant, I. M. Daniel, Z. Li, "Size effect and fracture characteristics of composite laminates", *J. Eng. Mater. Technol.* **118** (1996), no. 3, p. 317-324.
[30] S. Aicher, "Process zone length and fracture energy of spruce wood in mode-I from size effect", *Wood Fiber Sci.* **42** (2010), no. 2, p. 237-247.
[31] S. P. Shah, S. E. Swartz, "Fracture of concrete and rock", in *SEM-RILEM International Conference*, Springer, New York, 1987.
[32] S. Keten, Z. Xu, B. Ihle, M. J. Buehler, "Nanoconfinement controls stiffness, strength and mechanical toughness of β-sheet crystals in silk", *Nat. Mater.* **9** (2010), no. 4, p. 359-367.
[33] J. P. Dempsey, R. M. Adamson, S. V. Mulmule, "Scale effects on the in-situ tensile strength and fracture of ice. Part II: First-year sea ice at Resolute, NWT", *Int. J. Frac.* **95** (1999), no. 1, p. 347-366.
[34] G. R. Irwin, "Fracture dynamics", in *Fracturing of Metals*, American Society for Metals, Cleveland, 1948, p. 147-166.
[35] E. Orowan, "Fracture and strength of solids", *Rep. Prog. Phys.* **12** (1949), p. 185-232.
[36] G. I. Barenblatt, "The formation of equilibrium cracks during brittle fracture. General ideas and hypotheses. Axially-symmetric cracks", *J. Appl. Math. Mech.* **23** (1959), no. 3, p. 622-636.
[37] D. S. Dugdale, "Yielding of steel sheets containing slits", *J. Mech. Phys. Solids* **8** (1960), no. 2, p. 100-104.
[38] J. F. Labuz, S. P. Shah, C. H. Dowding, "Post peak tensile load-displacement response and the fracture process zone in rock", in *The 24th US Symposium on Rock Mechanics (USRMS)*, Association of Engineering Geologists, 1983.
[39] W. Chengyong, L. Peide, H. Rongsheng, S. Xiutang, "Study of the fracture process zone in rock by laser speckle interferometry", *Int. J. Rock Mech. Min. Sci. Geomech. Abstr.* **27** (1990), no. 1, p. 65-69.
[40] E. Denarie, V. E. Saouma, A. Iocco, D. Varelas, "Concrete fracture process zone characterization with fiber optics", *J. Eng. Mech.* **127** (2001), no. 5, p. 494-502.
[41] J. J. Du, A. S. Kobayashi, N. M. Hawkins, "An experimental-numerical analysis of fracture process zone in concrete fracture specimens", *Eng. Frac. Mech.* **35** (1990), no. 1-3, p. 15-27.
[42] Z. K. Guo, A. S. Kobayashi, N. M. Hawkins, "Further studies on fracture process zone for mode I concrete fracture", *Eng. Frac. Mech.* **46** (1993), no. 6, p. 1041-1049.
[43] C.-T. Yu, A.-S. Kobayashi, "Fracture process zone associated with mixed mode fracture of SiCw/Al2O3", *J. Non-Cryst. Solids* **177** (1994), p. 26-35.
[44] A. Zang, F. C. Wagner, S. Stanchits, C. Janssen, G. Dresen, "Fracture process zone in granite", *J. Geophys. Res.: Solid Earth* **105** (2000), no. B10, p. 23651-23661.
[45] K. Otsuka, H. Date, "Fracture process zone in concrete tension specimen", *Eng. Frac. Mech.* **65** (2000), no. 2-3, p. 111-131.
[46] W. K. Zietlow, J. F. Labuz, "Measurement of the intrinsic process zone in rock using acoustic emission", *Int. J. Rock Mech. Min. Sci.* **35** (1998), no. 3, p. 291-299.
[47] J. F. Labuz, S. P. Shah, C. H. Dowding, "The fracture process zone in granite: evidence and effect", *Int. J. Rock Mech. Min. Sci. Geomech. Abstr.* **24** (1987), p. 235-246.
[48] A. Neimitz, E. C. Aifantis, "On the size and shape of the process zone", *Eng. Frac. Mech.* **26** (1987), no. 4, p. 491-503.
[49] L. Cedolin, S. D. Poli, I. Iori, "Experimental determination of the fracture process zone in concrete", *Cem. Concr. Res.* **13** (1983), no. 4, p. 557-567.
[50] J. M. Vermilye, C. H. Scholz, "The process zone: A microstructural view of fault growth", *J. Geophys. Res.: Solid Earth* **103** (1998), no. B6, p. 12223-12237.
[51] Y. Yu, W. Zeng, W. Liu, H. Zhang, X. Wang, "Crack propagation and fracture process zone (FPZ) of wood in the longitudinal direction determined using digital image correlation (DIC) technique", *Remote Sens.* **11** (2019), no. 13, p. 1-13.
[52] K. Haidar, G. Pijaudier-Cabot, J.-F. Dubé, A. Loukili, "Correlation between the internal length, the fracture process zone and size effect in model materials", *Mater. Struct.* **38** (2005), no. 2, p. 201-210.
[53] C. L. Rountree, D. Bonamy, D. Dalmas, S. Prades, R. K. Kalia, C. Guillot, E. Bouchaud, "Fracture in glass via molecular dynamics simulations and atomic force microscopy experiments", *Phys. Chem. Glas.: Eur. J. Glass Sci. Technol. B* **51** (2010), no. 2, p. 127-132.
[54] Z. Brooks, *Fracture process zone: Microstructure and nanomechanics in quasi-brittle materials*, Phd thesis, Massachusetts Institute of Technology, 2013.
[55] J. Réthoré, R. Estevez, "Identification of a cohesive zone model from digital images at the micron-scale", *J. Mech. Phys. Solids* **61** (2013), no. 6, p. 1407-1420.
[56] P.-P. Cortet, S. Santucci, L. Vanel, S. Ciliberto, "Slow crack growth in polycarbonate films", *Europhys. Lett.* **71** (2005), no. 2, p. 242-248.
[57] W. Döll, "Optical interference measurements and fracture mechanics analysis of crack tip craze zones", *Adv. Polym. Sci.* **52-53** (1983), p. 105-168.
[58] W. Döll, L. Könczöl, "Micromechanics of fracture under static and fatigue loading: Optical interferometry of crack tip craze zones", *Adv. Poly. Sci.* **91-92** (1990), p. 137-214.

[59] T. A. Schaedler, A. J. Jacobsen, A. Torrents, A. E. Sorensen, J. Lian, J. R. Greer, L. Valdevit, W. B. Carter, "Ultralight metallic microlattices", *Science* **334** (2011), no. 6058, p. 962-965.
[60] D. Leguillon, "Strength or toughness? A criterion for crack onset at a notch", *Eur. J. Mech.—A/Solids* **21** (2002), no. 1, p. 61-72.
[61] A. Parvizi, K. W. Garrett, J. E. Bailey, "Constrained cracking in glass fibre-reinforced epoxy cross-ply laminates", *J. Mater. Sci.* **13** (1978), p. 195-201.
[62] G. Lamé, B. Clapeyron, "Mémoire sur l'équilibre intérieur des corps solides homogènes", *J. Reine Angew. Math.* **7** (1831), p. 381-413.
[63] H. Neuber, "Theorie der technischen Formzahl", *Forsch. Ingenieurwes. A* **7** (1936), no. 6, p. 271-274.
[64] R. E. Peterson, *Methods of Correlating Data from Fatigue Tests of Stress Concentration Specimens*, Macmillan, New York, 1938, Stephen Timoshenko Anniversary Volume, 179 pages.
[65] J. M. Whitney, R. J. Nuismer, "Stress fracture criteria for laminated composites containing stress concentrations", *J. Compos. Mater.* **8** (1974), no. 3, p. 253-265.
[66] K. Tanaka, "Engineering formulae for fatigue strength reduction due to crack-like notches", *Int. J. Frac.* **22** (1983), no. 2, p. R39-R46.
[67] D. Taylor, *The Theory of Critical Distances*, Elsevier Science Ltd, Oxford, 2007.
[68] J. Aveston, A. Kelly, "Theory of multiple fracture of fibrous composites", *J. Mater. Sci.* **8** (1973), no. 3, p. 352-362.
[69] Z. Hashin, "Finite thermoelastic fracture criterion with application to laminate cracking analysis", *J. Mech. Phys. Solids* **44** (1996), no. 7, p. 1129-1145.
[70] J. A. Nairn, "Fracture mechanics of composites with residual stresses, traction-loaded cracks, and imperfect interfaces", in *Fracture of Polymers, Composites and Adhesives* (J. G. Williams, A. Pavan, eds.), European Structural Integrity Society, vol. 27, Elsevier, Les Diablerets, 2000, p. 111-121.
[71] P. Weißgraeber, D. Leguillon, W. Becker, "A review of finite fracture mechanics: crack initiation at singular and non-singular stress raisers", *Arch. Appl. Mech.* **86** (2016), no. 1-2, p. 375-401.
[72] A. Doitrand, T. Duminy, H. Girard, X. Chen, "A review of the coupled criterion", *J. Theor. Comput. Appl. Mech.* (2024), article no. 11072.
[73] W. J. M. Rankine, "II. On the stability of loose earth", *Philos. Trans. R. Soc. Lond.* **147** (1857), p. 9-27.
[74] G. Molnár, A. Doitrand, R. Estevez, A. Gravouil, "Toughness or strength? Regularization in phase-field fracture explained by the coupled criterion", *Theor. Appl. Frac. Mech.* **109** (2020), article no. 102736.
[75] A. Doitrand, R. Henry, J. Chevalier, S. Meille, "Revisiting the strength of micron-scale ceramic platelets", *J. Am. Ceramic Soc.* **103** (2020), p. 6991-7000.
[76] D. Leguillon, E. Sanchez-Palencia, *Computation of Singular Solutions in Elliptic Problems and Elasticity*, Wiley, USA, 1987.
[77] A. Doitrand, E. Martin, D. Leguillon, "Numerical implementation of the coupled criterion: Matched asymptotic and full finite element approaches", *Finite Element Anal. Des.* **168** (2020), article no. 103344.
[78] D. Leguillon, D. Quesada, C. Putot, E. Martin, "Prediction of crack initiation at blunt notches and cavities—size effects", *Eng. Frac. Mech.* **74** (2007), no. 15, p. 2420-2436.
[79] D. Taylor, P. Cornetti, N. Pugno, "The fracture mechanics of finite crack extension", *Eng. Frac. Mech.* **72** (2005), no. 7, p. 1021-1038.
[80] A. Chao Correas, M. Corrado, A. Sapora, P. Cornetti, "Size-effect on the apparent tensile strength of brittle materials with spherical cavities", *Theor. Appl. Frac. Mech.* **116** (2021), article no. 103120.
[81] Y. Liu, C. Deng, B. Gong, "Discussion on equivalence of the theory of critical distances and the coupled stress and energy criterion for fatigue limit prediction of notched specimens", *Int. J. Fatigue* **131** (2020), article no. 105236.
[82] A. Campagnolo, F. Berto, D. Leguillon, "Fracture assessment of sharp V-notched components under Mode II loading: a comparison among some recent criteria", *Theor. Appl. Frac. Mech.* **85** (2016), p. 217-226.
[83] Z. Yosibash, A. Bussiba, I. Gilad, "Failure criteria for brittle elastic materials", *Int. J. Frac.* **125** (2004), p. 307-333.
[84] B. Gillham, A. Yankin, F. McNamara *et al.*, "Tailoring the theory of critical distances to better assess the combined effect of complex geometries and process-inherent defects during the fatigue assessment of SLM Ti-6Al-4V", *Int. J. Fatigue* **172** (2023), article no. 107602.
[85] A. K. Matpadi Raghavendra, V. Maurel, L. Marcin, H. Proudhon, "Fatigue life prediction at mesoscopic scale of samples containing casting defects: A novel energy based non-local model", *Int. J. Fatigue* **188** (2024), article no. 108485.
[86] A. Doitrand, G. Molnár, D. Leguillon, E. Martin, N. Carrère, "Dynamic crack initiation assessment with the coupled criterion", *Eur. J. Mech.—A/Solids* **93** (2022), article no. 104483.
[87] Z. Hamam, N. Godin, P. Reynaud, C. Fusco, N. Carrére, A. Doitrand, "Transverse cracking induced acoustic emission in carbon fiber-epoxy matrix composite laminates", *Materials* **15** (2022), p. 1-15.
[88] B. Bourdin, G. A. Francfort, J. J. Marigo, "Numerical experiments in revisited brittle fracture", *J. Mech. Phys. Solids* **48** (2000), no. 4, p. 797-826.
[89] B. Bourdin, G. A. Francfort, J.-J. Marigo, *The Variational Approach to Fracture*, Springer, Netherlands, 2008.

[90] J. Reinoso, A. Arteiro, M. Paggi, P. P. Camanho, "Strength prediction of notched thin ply laminates using finite fracture mechanics and the phase field approach", *Compos. Sci. Technol.* **150** (2017), p. 205-216.
[91] J. Bleyer, R. Alessi, "Phase-field modeling of anisotropic brittle fracture including several damage mechanisms", *Comput. Methods Appl. Mech. Eng.* **336** (2018), p. 213-236.
[92] M. Strobl, P. Dowgiallo, T. Seelig, "Analysis of Hertzian indentation fracture in the framework of finite fracture mechanics", *Int. J. Frac.* **206** (2017), p. 67-79.
[93] M. Strobl, T. Seelig, "Phase field modeling of Hertzian indentation fracture", *J. Mech. Phys. Solids* **143** (2020), article no. 104026.
[94] A. Kumar, B. Bourdin, G. A. Francfort, O. Lopez-Pamies, "Revisiting nucleation in the phase-field approach to brittle fracture", *J. Mech. Phys. Solids* **142** (2020), article no. 104027.
[95] A. Abaza, J. Laurencin, A. Nakajo, S. Meille, J. Debayle, D. Leguillon, "Prediction of crack nucleation and propagation in porous ceramics using the phase-field approach", *Theor. Appl. Frac. Mech.* **119** (2022), article no. 103349.
[96] S. Jiménez-Alfaro, J. Reinoso, D. Leguillon, C. Maurini, "Finite fracture mechanics from the macro- to the micro-scale. comparison with the phase field model", *Procedia Struct. Integr.* **42** (2022), p. 553-560, 23 European Conference on Fracture.
[97] G. Molnár, A. Doitrand, V. Lazarus, "Phase-field simulation and coupled criterion link echelon cracks to internal length in antiplane shear", *J. Mech. Phys. Solids* **188** (2024), article no. 105675.
[98] P. K. Kristensen, C. F. Niordson, E. Martinez-Paneda, "An assessment of phase field fracture: crack initiation and growth", *Philos. Trans. R. Soc. A* **379** (2021), no. 2203, article no. 20210021.
[99] A. Doitrand, G. Molnár, "Understanding regularized crack initiation through the lens of finite fracture mechanics", preprint, 2024, https://doi.org/10.21203/rs.3.rs-4583166/v1.
[100] G. Alfano, M. A. Crisfield, "Finite element interface models for the delamination analysis of laminated composites: mechanical and computational issues", *Int. J. Numer. Methods Eng.* **50** (2001), no. 7, p. 1701-1736.
[101] G. Alfano, "On the influence of the shape of the interface law on the application of cohesive-zone models", *Compos. Sci. Technol.* **66** (2006), no. 6, p. 723-730.
[102] P. Cornetti, A. Sapora, A. Carpinteri, "Short cracks and V-notches: finite fracture mechanics vs cohesive crack model", *Eng. Frac. Mech.* **168** (2016), p. 2-12.
[103] P. Cornetti, M. Munoz-Reja, A. Sapora, A. Carpinteri, "Finite fracture mechanics and cohesive crack model: weight functions vs cohesive laws", *Int. J. Solids Struct.* **156-157** (2019), p. 126-136.
[104] E. Martin, T. Vandellos, D. Leguillon, N. Carrère, "Initiation of edge debonding: coupled criterion versus cohesive zone model", *Int. J. Frac.* **199** (2016), p. 157-168.
[105] C. Henninger, D. Leguillon, E. Martin, "Crack initiation at a V-notch—comparison between a brittle fracture criterion and the Dugdale cohesive model", *C. R. Méc.* **335** (2007), no. 7, p. 388-393.
[106] S. Murer, D. Leguillon, "Static and fatigue failure of quasi-brittle materials at a V-notch using a Dugdale model", *Eur. J. Mech.—A/Solids* **29** (2010), no. 2, p. 109-118.
[107] I. G. García, M. Paggi, V. Mantivc, "Fiber-size effects on the onset of fiber–matrix debonding under transverse tension: A comparison between cohesive zone and finite fracture mechanics models", *Eng. Frac. Mech.* **115** (2014), p. 96-110.
[108] P. Cornetti, M. Corrado, L. De Lorenzis, A. Carpinteri, "An analytical cohesive crack modeling approach to the edge debonding failure of FRP-plated beams", *Int. J. Solids Struct.* **53** (2015), p. 92-106.
[109] N. Stein, P. Weissgraeber, W. Becker, "A model for brittle failure in adhesive lap joints of arbitrary joint configuration", *Compos. Struct.* **133** (2015), p. 707-718.
[110] L. Távara, I. G. Garcia, R. Vodicka, C. G. Panagiotopoulos, V. Mantivc, "Revisiting the problem of debond initiation at fibre-matrix interface under transversal biaxial loads - a comparison of several non-classical fracture mechanics approaches", *Trans Tech Publications, Ltd* **713** (2016), p. 232-235.
[111] R. Dimitri, P. Cornetti, V. Mantic, M. Trullo, L. De Lorenzis, "Mode-I debonding of a double cantilever beam: a comparison between cohesive crack modeling and finite fracture mechanics", *Int. J. Solids Struct.* **124** (2017), p. 57-72.
[112] P. L. Rosendahl, P. Weissgraeber, N. Stein, W. Becker, "Asymmetric crack onset at open-holes under tensile and in-plane bending loading", *Int. J. Solids Struct.* **113-114** (2017), p. 10-23.
[113] T. Gentieu, J. Jumel, A. Catapano, J. Broughton, "Size effect in particle debonding: comparisons between finite fracture mechanics and cohesive zone model", *J. Compos. Mater.* **53** (2018), no. 14, p. 1941-1954.
[114] A. Doitrand, R. Estevez, D. Leguillon, "Comparison between cohesive zone and coupled criterion modeling of crack initiation in rhombus hole specimens under quasi-static compression", *Theor. Appl. Frac. Mech.* **99** (2019), p. 51-59.
[115] M. Munoz-Reja, P. Cornetti, L. Távara, V. Mantivc, "Interface crack model using finite fracture mechanics applied to the double pull-push shear test", *Int. J. Solids Struct.* **188-189** (2020), p. 56-73.
[116] R. Aghababaei, D. H. Warner, J.-F. Molinari, "Critical length scale controls adhesive wear mechanisms", *Nat. Commun.* **7** (2016), no. 1, article no. 11816.

[117] R. Aghababaei, D. H. Warner, J.-F. Molinari, "On the debris-level origins of adhesive wear", *Proc. Nat. Acad. Sci.* **114** (2017), no. 30, p. 7935-7940.
[118] L. Brochard, S. Souguir, K. Sab, "Scaling of brittle failure: strength versus toughness", *Int. J. Frac.* **210** (2018), p. 153-166.
[119] M. Ippolito, A. Mattoni, N. Pugno, L. Colombo, "Failure strength of brittle materials containing nanovoids", *Phys. Rev. B* **75** (2007), no. 22, article no. 224110.
[120] J. Zghal, K. Moreau, N. Moës, D. Leguillon, C. Stolz, "Analysis of the failure at notches and cavities in quasi-brittle media using the Thick Level Set damage model and comparison with the coupled criterion", *Int. J. Frac.* **211** (2018), p. 253-280.
[121] H. Zhang, P. Qiao, "A coupled peridynamic strength and fracture criterion for openhole failure analysis of plates under tensile load", *Eng. Frac. Mech.* **204** (2018), p. 103-118.
[122] H. Zhang, P. Qiao, L. Lu, "Failure analysis of plates with singular and non-singular stress raisers by a coupled peridynamic model", *Int. J. Mech. Sci.* **157-158** (2019), p. 446-456.
[123] A. Sapora, G. Efremidis, P. Cornetti, "Comparison between two nonlocal criteria: a case study on pressurized holes", *Procedia Struct. Integr.* **33** (2021), p. 456-464.
[124] J. Lemaitre, "How to use damage mechanics", *Nucl. Eng. Design* **80** (1984), no. 2, p. 233-245.
[125] L. M. Kachanov, "Rupture time under creep conditions", *Izvestia Akademii Nauk SSSR, Otdelenie tekhnicheskich nauk* (1958), no. 8, p. 26-31, Leningrad University (translated) (in Russian) reprint: https://doi.org/10.1023/A:1018671022008.
[126] G. Pijaudier-Cabot, Z. P. Bažant, "Nonlocal damage theory", *J. Eng. Mech.* **113** (1987), no. 10, p. 1512-1533.
[127] A. Benallal, R. Billardon, J. Lemaitre, "Continuum damage mechanics and local approach to fracture: numerical procedures", *Comput. Methods Appl. Mech. Eng.* **92** (1991), no. 2, p. 141-155.
[128] R. de Borst, A. Benallal, O. M. Heeres, "A gradient-enhanced damage approach to fracture", *J. Phys. IV* **6** (1996), no. C6, p. 491-502.
[129] R. H. J. Peerlings, R. de Borst, W. A. M. Brekelmans, J. H. P. de Vree, "Gradient enhanced damage for quasi-brittle materials", *Int. J. Numer. Methods Eng.* **39** (1996), no. 19, p. 3391-3403.
[130] R. H. J. Peerlings, R. de Borst, W. A. M. Brekelmans, M. G. D. Geers, "Gradient-enhanced damage modelling of concrete fracture", *Mech. Cohesive-frict. Mater. Int. J. Exp. Model. Comput. Mater. Structures* **3** (1998), no. 4, p. 323-342.
[131] R. de Borst, "Fracture in quasi-brittle materials: a review of continuum damage-based approaches", *Eng. Frac. Mech.* **69** (2002), no. 2, p. 95-112.
[132] M. G. D. Geers, R. de Borst, W. A. M. Brekelmans, R. H. J. Peerlings, "Strain-based transient-gradient damage model for failure analyses", *Comput. Methods Appl. Mech. Eng.* **160** (1998), no. 1-2, p. 133-153.
[133] Z. P. Bažant, G. Pijaudier-Cabot, "Measurement of characteristic length of nonlocal continuum", *J. Eng. Mech.* **115** (1989), no. 4, p. 755-767.
[134] N. Carrère, E. Martin, D. Leguillon, "Comparison between models based on a coupled criterion for the prediction of the failure of adhesively bonded joints", *Eng. Frac. Mech.* **138** (2015), p. 185-201.
[135] E. O. Hall, "The deformation and ageing of mild steel: III discussion of results", *Proc. Phys. Soc. Section B* **64** (1951), no. 9, p. 747-753.
[136] N. J. Petch, "The cleavage strength of polycrystals", *J. Iron Steel Inst.* **174** (1953), p. 25-28.
[137] G. Molnár, A. Doitrand, A. Jaccon, B. Prabel, A. Gravouil, "Thermodynamically consistent linear-gradient damage model in Abaqus", *Eng. Frac. Mech.* **266** (2022), article no. 108390.
[138] D. Leguillon, C. Lacroix, E. Martin, "Interface debonding ahead of a primary crack", *J. Mech. Phys. Solids* **48** (2000), no. 10, p. 2137-2161.
[139] D. Leguillon, S. Murer, "Fatigue crack nucleation at a stress concentration point", in *CP2012 Conference Proceedings*, vol. 46, ESIS Publishing House, 2012, https://www.gruppofrattura.it/ocs/index.php/esis/CP2012/paper/viewFile/9235/5996.
[140] M. T. Aranda, D. Leguillon, "Prediction of failure of hybrid composites with ultra-thin carbon/epoxy layers using the Coupled Criterion", *Eng. Frac. Mech.* **281** (2023), article no. 109053.
[141] B. Mittelman, Z. Yosibash, "Asymptotic analysis of the potential energy difference because of a crack at a V-notch edge in a 3D domain", *Eng. Frac. Mech.* **131** (2014), p. 232-256.
[142] B. Mittelman, Z. Yosibash, "Energy release rate cannot predict crack initiation orientation in domains with a sharp V-notch under mode III loading", *Eng. Frac. Mech.* **141** (2015), p. 230-241.
[143] A. Doitrand, D. Leguillon, G. Molnár, V. Lazarus, "Revisiting facet nucleation under mixed mode I+III loading with T-stress and mode-dependent fracture properties", *Int. J. Frac.* **242** (2023), p. 85-106.
[144] M. Klinsmann, D. Rosato, M. Kamlah, R. M. McMeeking, "An assessment of the phase field formulation for crack growth", *Comput. Methods Appl. Mech. Eng.* **294** (2015), p. 313-330.
[145] D. Leguillon, Z. Yosibash, "Failure initiation at V-notch tips in quasi-brittle materials", *Int. J. Solids Struct.* **122-123** (2017), p. 1-13.

[146] D. André, J. Girardot, C. Hubert, "A novel DEM approach for modeling brittle elastic media based on distinct lattice spring model", *Comput. Methods Appl. Mech. Eng.* **350** (2019), p. 100-122.

[147] M. Voisin-Leprince, J. Garcia-Suarez, G. Anciaux, J.-F. Molinari, "Two-scale concurrent simulations for crack propagation using FEM–DEM bridging coupling", *Comput. Part. Mech.* **11** (2024), no. 5, p. 2235-2243.

ACADÉMIE DES SCIENCES
INSTITUT DE FRANCE

Comptes Rendus. Mécanique
2026, Vol. 354, p. 25-33
https://doi.org/10.5802/crmeca.311

Research article

A simple model for estimating the crack kinking angles of pure shear fracture of 3D printing polymers

Luoyu Roy Xu [*,a] **and Yuelong Jiang** [a]

[a] School of Mechanical Engineering and Mechanics, Ningbo University, Zhejiang, China

E-mail: l.roy.xu@alumni.caltech.edu (L. R. Xu)

Abstract. Shear fracture studies of three-dimensional (3D) printing polymers with interfaces were rarely reported due to their complicated mechanics and material issues. In this study, a short-beam shear fracture approach was employed to characterize the mode-II shear fracture toughness of polyamide specimens of three printing surface angles made with selective laser sintering (SLS). Results show that a pure shear crack only existed if the initial crack propagated along the printing interface. In other cases, initial cracks kinked right after crack initiation, so no valid shear fracture toughness was measured. A simple model based on linear elastic fracture mechanics including anisotropic fracture toughnesses was proposed to predict the crack kinking angles. The prediction agreed with the measurements well and was more reasonable than the prediction based on the maximum tensile stress criterion.

Keywords. Shear fracture, Fracture toughness, 3D printing, Polymer, Interfaces.

Note. Article submitted by invitation.

Manuscript received 24 January 2025, revised and accepted 18 June 2025, online since 16 January 2026.

1. Introduction

The mode-II fracture toughness has long been a difficult property to quantify for isotropic materials, because a mode-II crack tends to kink away from the original crack path [1], and thereby makes the measured fracture toughness the mode-I fracture toughness. However, a pure mode-II crack may exist in some special materials with preferred interfaces like layered materials, or composite materials [2]. Indeed, layered 3D printing materials have numerous interfaces between the printing layers as the weak paths for potential crack propagation. With the growing applications of 3D printing materials, it is important to develop new approaches to measure their mode-II shear fracture toughnesses because of their anisotropic strengths and fracture toughnesses [3,4]. 3D printing materials based on single-material printing can be treated as isotropic and homogenous materials in terms of stiffness because no second material (only defects such as voids) exists in the printed materials. However, their strengths and fracture toughnesses were slightly anisotropic due to the printing interfaces and the intrinsic build direction that led to initial defects in different directions [5–7]. It should be noted that their anisotropic degree was much lower than the layered composite materials [8].

* Corresponding author

There were a few shear fracture experiments of 3D printing polymers in the open literature. But two major issues were found, (1) a pure shear stress field ahead of a shear crack was not shown, and (2) the initial shear crack might kink right away. For example, Khan et al. [9] employed 3D printing polymer specimens for the mode-I, II and mixed-mode fracture toughness tests, but the above critical fracture mechanics issues were not addressed. Therefore, whether their measured values can be treated as valid fracture toughnesses or not is still a big question. Hence, to measure the valid mode-II fracture toughnesses of 3D printing polymers, a short-beam shear fracture (SBSF) approach initially proposed by Krishnan and Xu [10] was modified to eliminate the friction between the cracked surfaces, and ensure a pure shear stress field, thereby offering a more reasonable value of the mode-II fracture toughness. Another advantage of the SBSF approach was that the shear crack propagated along the initial crack path if the initial crack path was along the interface, not immediately kinked from the initial crack. If the initial crack path was not along the interface, the initial crack might kink right after the crack initiation. Crack kinking is a special fracture problem, and it has been received long-term attention since it can occur during static and dynamic loading processes [11–14]. Hence, in this paper, a simple model using linear elastic fracture mechanics (LEFM) was employed to analyze the crack kinking during a pure shear fracture experiment. The purpose of this study was to predict the crack kinking angles if the initial crack kinked.

2. Theory

2.1. *Stress intensity factors of a kinked crack including the T-stress*

As shown in Figure 1, based on LEFM, the two-dimensional full-field stress of a main crack can be expressed in a polar coordinate system [15]:

$$\sigma_{ij}(r,\theta) = \frac{K_{\mathrm{I}}}{\sqrt{2\pi r}} \sum_{ij}^{\mathrm{I}}(\theta) + T\delta_{i1}\delta_{j1} + \frac{K_{\mathrm{II}}}{\sqrt{2\pi r}} \sum_{ij}^{\mathrm{II}}(\theta) + O(r^{\frac{1}{2}}) \qquad (i,j=1,2) \tag{1}$$

where K_{I} and K_{II} are the mode-I and mode-II stress intensity factors, T is a nonsingular stress term, $O(r^{\frac{1}{2}})$ represents the higher-order terms of the length scale r and will be dropped if the kinked crack length "l" is very small; and the known functions $\Sigma_{ij}^{\mathrm{I}}(\theta), \Sigma_{ij}^{\mathrm{II}}(\theta)$ represent the angular variations of the 2-D stress components. Previous research on crack kinking was mainly focused on the relation between the stress intensity factors before and after crack kinking [16]. If the T-stress is considered during crack kinking, the two stress intensity factors of the kinked crack k_{I} and k_{II} became [11,17]:

$$k_1 = C_{11}K_{\mathrm{I}} + C_{12}K_{\mathrm{II}} + 2T\sqrt{\frac{2l}{\pi}}\sin^2\beta \tag{2}$$

$$k_2 = C_{21}K_{\mathrm{I}} + C_{22}K_{\mathrm{II}} - 2T\sqrt{\frac{2l}{\pi}}\sin\beta\cos\beta \tag{3}$$

where β is the kinking angle, i.e., the angle between the main crack and the kinked crack as seen in Figure 2. The coefficients C_{ij} $(i,j=1,2)$ were initially reported by Contrell and Rice [16]:

$$C_{11} = \left(\frac{3}{4}\cos\frac{\beta}{2} + \frac{1}{4}\cos\frac{3\beta}{2}\right) \qquad C_{12} = -\frac{3}{4}\left(\sin\frac{\beta}{2} + \sin\frac{3\beta}{2}\right) \tag{4}$$

$$C_{21} = \left(\frac{1}{4}\sin\frac{\beta}{2} + \frac{1}{4}\sin\frac{3\beta}{2}\right) \qquad C_{22} = \left(\frac{1}{4}\cos\frac{\beta}{2} + \frac{3}{4}\cos\frac{3\beta}{2}\right). \tag{5}$$

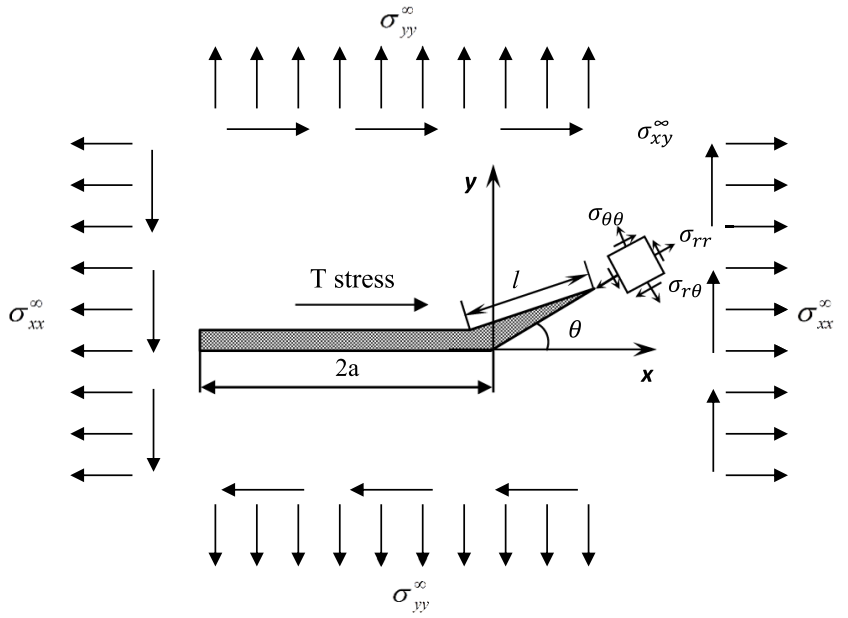

Figure 1. Schematic of a kinked crack (with a very small length l) initiating from a main crack (length 2a) subjected to remote 2-D mixed-mode loading. The local stress field at the kinked crack tip is shown in a polar coordinate system.

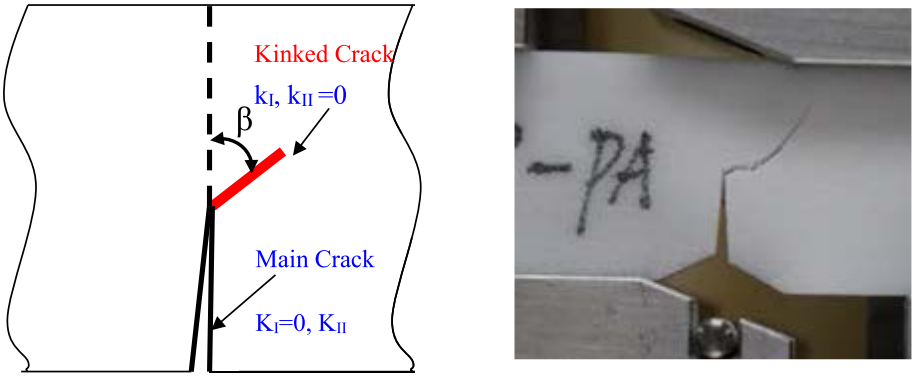

Figure 2. Schematic diagram of a kinked crack (left), and a photo of the actual crack kinking of a shear fracture 3D printed specimen under loading (right).

Now we consider a shear main crack with $K_{\mathrm{I}} = 0$, and assume the kinked crack is a mode-I crack ($k_2 = 0$), Equations (2) and (3) yield:

$$k_1 = C_{12} K_{\mathrm{II}} + 2T\sqrt{\frac{2l}{\pi}}\sin^2\beta \tag{6}$$

$$k_2 = C_{22} K_{\mathrm{II}} - 2T\sqrt{\frac{2l}{\pi}}\sin\beta\cos\beta = 0. \tag{7}$$

Substitute Equation (7) into (6) to eliminate T and l, the mode-I stress intensity factor of the kinked crack becomes,

$$k_1 = (C_{12} + C_{22}\tan\beta)K_{\mathrm{II}}. \tag{8}$$

The kinked crack is often a mode-I crack because this conclusion was verified by the authors' dynamic fracture experiments using high-speed photography [14,18]. If $T = 0$,

$$k_2 = C_{22}(\beta)K_{\mathrm{II}} = 0, \quad \text{then } \beta \approx 70.5°. \tag{9}$$

Erdogan and Sih [19] proposed the maximum tensile stress (MTS) criterion (no T-stress was involved) and assumed that the kinked mode-I crack initiated in the direction corresponding to where the circumferential tensile stress around the crack tip reaches its maximum value. For a pure shear crack, the crack kinking angle predicted by the MTS criterion is around 70.5°, i.e., the same outcome.

2.2. *Energy-based fracture criterion for crack kinking from the interface*

As shown in Figure 3, a modified short-beam shear fracture specimen was proposed, and it was subjected to an asymmetric four-point bending load. Indeed, this was not a typical asymmetric four-point bending test because this experiment was conducted using an Iosipescu shear fixture as seen in Figure 4. The load acting on the specimen was distributed load, not point load as shown in Figure 3 for illustration purposes. The printing surface (interface) angles were 0°, 45°, and 90°. If the printing surface angle is 90°, the printed initial crack is along the interface (a weak path). For a mode-II main crack of an interfacial shear fracture toughness measurement, $K_{\mathrm{I}} = 0$. Therefore, a valid shear fracture experiment requires that continuous crack propagation along the original crack path occurs when the mode-II energy release rate, G_{II} exceeds the fracture toughness of the printing interface $\Gamma^{IT}_{\mathrm{II}C}$, i.e.,

$$G_{\mathrm{II}} = \frac{K^2_{\mathrm{II}}}{E^*} \geq \Gamma^{IT}_{\mathrm{II}C} \tag{10}$$

where $E^* = E$ for plane stress and $E^* = E/(1-\nu^2)$ for plane strain, and E is the Young's modulus of the material and ν is the Poisson's ratio. On the other hand, the initial crack will kink if the mode-I energy release rate of the kinked crack tip, g_{I}, exceeds the mode-I fracture toughness of the bulk printing material next to the printing interface, $\Gamma^{\mathrm{BM}}_{\mathrm{I}C}$, i.e.,

$$g_{\mathrm{I}} = \frac{k^2_{\mathrm{I}}}{E^*} \geq \Gamma^{\mathrm{BM}}_{\mathrm{I}C}. \tag{11}$$

Hence, crack kinking is only possible if this inequality holds:

$$\frac{g_{\mathrm{I}}}{G_{\mathrm{II}}} = [C_{12} + C_{22}\tan\beta]^2 > \frac{\Gamma^{\mathrm{BM}}_{\mathrm{I}C}}{\Gamma^{IT}_{\mathrm{II}C}} = \left(\frac{k^{\mathrm{BM}}_{\mathrm{I}C}}{K^{IT}_{\mathrm{II}C}}\right)^2 = \lambda. \tag{12}$$

Therefore, only the ratio of two independent fracture toughnesses λ determines the crack kinking angle. Indeed, the outcome of this paper will be applicable to more material systems with weak interfaces rather than 3D printing materials only.

3. Methods and materials

As shown in Figure 2, the printed notch had a variable width to conveniently cut a sharp notch using a fresh razor blade. At the bottom of the specimen, the notch had a sudden wide opening to avoid specimen/loading block contact when the applied load/displacement was large for the soft polymer specimens. For each printing surface angle, at least eight identical specimens were made and tested. It should be noted that for the 90° specimen, the printing surface/interface was along

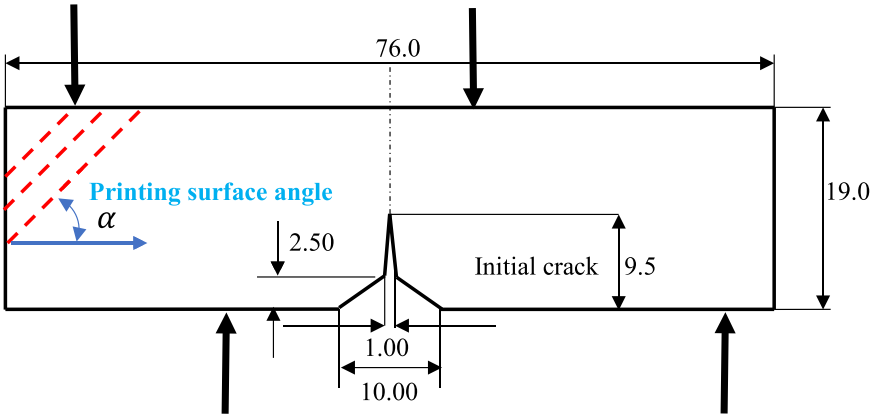

Figure 3. Size and applied load of a short-beam shear fracture specimen (All dimensions are in mm. The thickness was 4 mm). The printing surface angles α were 0°, 45°, and 90°.

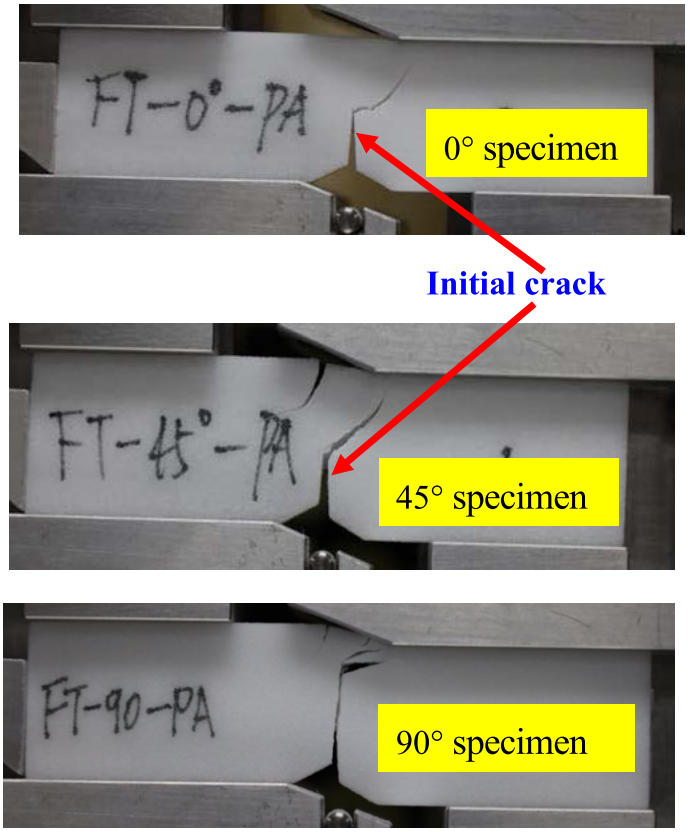

Figure 4. Failure modes of PA specimens with different printing surface angles.

the initial crack direction to measure the mode-II interlayer shear fracture toughness. To create polyamide (PA) specimens, PA powder (FS3300PA) with a spherical shape and a mean particle size of 120 μm was used, and the apparent density was 0.48 g/cm^3. A selective laser sintering apparatus (HT252P) was employed to make these specimens. The apparatus was equipped with

a 60 W carbon dioxide laser with a focal laser beam diameter of ≤0.5 mm. The processing parameters were set as follows: a laser power of 45 W, a laser scanning speed of 10 m/s, and a layer thickness of 0.1 mm. A heater was equipped to preheat the raw powder material, capable of reaching a maximum temperature of up to 225 °C. During the printing process, the chamber was filled with high-purity nitrogen to protect the specimens from oxidation. All fracture specimens were tested on an Instron 5966 test frame equipped with a 10 kN load cell using an Iosipescu shear fixture. The displacement rate for all tests was set at 1 mm/min, and the maximum loadings of the specimens were recorded. Photos were taken from some specimens to record the final crack pattern before they were removed from the test machine. More experimental details will be reported by Wang et al. [20].

4. Results and discussion

4.1. *Crack kinking in different specimens with different printing surface angles*

Figure 4 shows two different fracture modes of three types of shear fracture specimens. For the specimens with the printing surface angles of 0° and 45°, the crack kinked from the initial crack right after its initiation and formed a mode-I crack as seen in almost all homogenous materials subjected to a pure shear load. For the specimens with the printing surface angle of 90°, the initial shear crack propagated along the initial crack path. Based on the energy release rate definition, a crack creates the fracture surface in an in-plane shear pattern after crack initiation. Hence, it is concluded that the mode-II shear fracture toughness for the 90° specimens is valid. It is important to note that this crack finally kinked but it was caused by the mixed load (not pure shear load) because of the large specimen deformation and the close distance of the crack tip and the load block. The propagation of an interfacial crack is a more complicated case [11,21], therefore, it is not considered in this simple study. However, for the 0° and 45° specimens, the crack created the fracture surface in an opening mode, so a valid shear fracture toughness was not obtained for these two specimens.

Therefore, the measured shear fracture toughness of 90° specimens was the interlayer shear fracture toughness because a shear crack only existed in the weak printing interfaces between different layers. The measured mode-II fracture toughness based on LEFM of the printing interface $K_{\mathrm{IIC}}^{\mathrm{I}T}$ (2.57 MPa·m$^{1/2}$) was slightly more than the mode-I fracture toughness of the printing interface $K_{\mathrm{I}C}^{\mathrm{I}T}$ (2.30 MPa·m$^{1/2}$) for the same material interface/same specimen thickness [22]. The $K_{\mathrm{II}C}$ of the printing interface was obtained as

$$K_{\mathrm{IIC}}^{\mathrm{I}T} = \frac{P_{\mathrm{C}}}{Wt}\sqrt{\pi a}F_{\mathrm{II}}^{\mathrm{SBSF}}\left(\frac{a}{W}\right) \tag{13}$$

where $F_{\mathrm{II}}^{\mathrm{SBSF}}$ is a dimensionless parameter [10], and P_{C} is the critical load at crack initiation, W is the specimen width, t is the specimen thickness, and a is the crack length. This fracture toughness indicated that there was little friction between the cracked faces, because friction led to significant energy dissipation and inaccurately contributed to the fracture toughness.

4.2. *Crack kinking analysis based on the proposed model*

The measured crack kinking angles are listed in Table 1. The predicted kinking angle according to the MTS criterion was 70°, i.e., between the kinking angles of the 0° specimen and the 45° specimen. This inaccuracy is probably caused by the two disadvantages of the MTS criterion: (1) the crack kinking angle is independent of the material properties (e.g., fracture toughness), and (2) the T-stress is neglected.

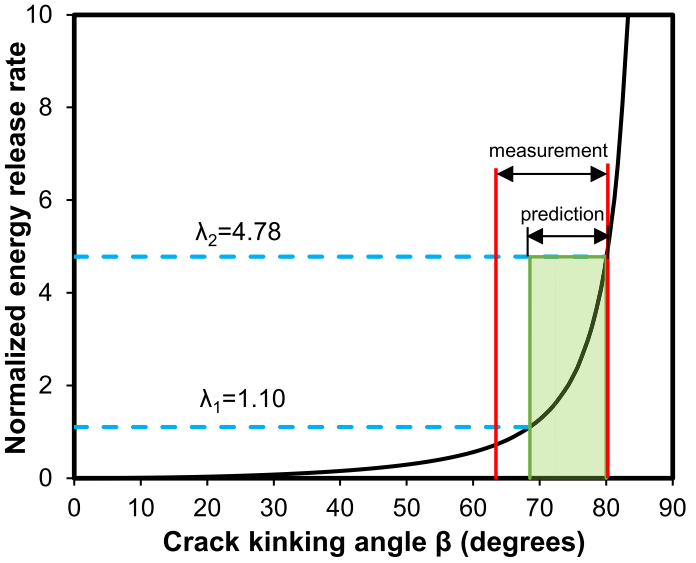

Figure 5. Normalized energy release rate g_I/G_{II} as a function of the crack kinking angle. The predicted crack kinking angles were 68° to 80°, while the actual crack kinking angles were 64° to 80°.

Table 1. Crack kinking angles of the specimen with different printing surface angles

	0° specimens	45° specimens
Crack kinking angle Ω	79.92 ± 7.07	64.13 ± 12.31

The proposed model does not have these disadvantages and clearly shows the dependence of the crack kinking angles on the fracture toughness as seen in the Equation (12). About the potential range of the ratio of two independent fracture toughnesses λ, it is difficult to measure the fracture toughness of the printing layer. However, the mode-I intralayer fracture toughness of the 3D printing layer is always lower than the mode-I fracture toughness of the traditional polymers (e.g., inject-molding) due to fewer initial defects. Therefore, the mode-I intralayer fracture toughness of the bulk PA is around 2.70 to 5.62 MPa·m$^{1/2}$ based on previous measurements [23], or $\lambda_1 = 1.10$ and $\lambda_2 = 4.78$. Their corresponding crack kinking angles are 68° to 80°, while the actual crack kinking angles are 64° to 80° as shown in Figure 5. Obviously, our prediction is better than the MTS criterion.

However, our simple model cannot predict the different crack kinking angles for the 0° and the 45° specimens individually, although they are indeed different as shown in Table 1. Because our model assumes that the interface/printing surface has no thickness like numerous traditional interface mechanics models. If we assume that the interface/printing surface has a thickness, its thickness becomes a variable for different materials and might become a fitting parameter rather than a material constant. However, for a specific 3D printing technique, the interface thickness should be treated as a material constant, and it should be less than 1% of the thickness of a printing layer although there are no direct measurements. For example, for the current PA specimen made with SLS, its layer thickness is 0.1 mm, so the thickness of the printing interface should be below 100 μm. Also, the PA powder had a mean diameter of 120 μm before the SLS process, therefore, an upper limit of 100 μm is a reasonable assumption for the thickness of the SLS printing interfaces. Anyway, the anisotropic feature of the interfaces should be considered

for future sophisticated models. Also, the material properties of the finite interfaces could be assumed to be different from the properties of the printing layers.

5. Conclusions

A simple model based on linear elastic fracture mechanics including anisotropic fracture toughnesses was proposed to predict the crack kinking angles. The prediction agreed with the measurements well and was more reasonable than the prediction based on the maximum tensile stress criterion. Future new models should consider the anisotropic features/thickness of the interfaces in order to predict the crack kinking more reasonably.

Declaration of interests

The authors do not work for, advise, own shares in, or receive funds from any organization that could benefit from this article, and have declared no affiliations other than their research organizations.

References

[1] T. L. Anderson, *Fracture Mechanics: Fundamentals and Applications*, 3rd edition, CRC Press: Boca Raton, 2004.
[2] D. Coker and A. J. Rosakis, "Experimental observations of intersonic crack growth in asymmetrically loaded unidirectional composite plates", *Philos. Mag. A* **81** (2001), pp. 571–595.
[3] T. Brugo, R. Palazzetti, S. Ciric-Kostic, X. T. Yan, G. Minak and A. Zucchelli, "Fracture mechanics of laser sintered cracked polyamide for a new method to induce cracks by additive manufacturing", *Polym. Test.* **50** (2016), pp. 301–308.
[4] E. Monaldo, M. Ricci and S. Marfia, "Mechanical properties of 3D printed polylactic acid elements: experimental and numerical insights", *Mech. Mater.* **177** (2023), article no. 104551.
[5] L. R. Xu and D. Leguillon, "Dual-notch defect model to understand the anisotropic strengths of 3d printed polymers", *ASME J. Eng. Mater. Technol.* **142** (2020), no. 2020, article no. 14501.
[6] Q. Wang, G. Zhang, X. Zheng, Y. Ni, F. Liu, Y. Liu and L. R. Xu, "Efficient characterization on the interlayer shear strengths of 3D printing polymers", *J. Mater. Res. Technol.* **22** (2023), pp. 2768–2780.
[7] G. Zhang, Q. Wang, Y. Ni, P. Liu, F. Liu, D. Leguillon and L. R. Xu, "A systematic investigation on the minimum tensile strengths and size effects of 3D printing polymers", *Polym. Test.* **117** (2023), article no. 107845.
[8] I. M. Daniel and O. Ishai, *Engineering Mechanics of Composite Materials*, Oxford University Press: New York, 2005.
[9] A. S. Khan, A. Ali, G. Hussain and M. Ilyas, "An experimental study on interfacial fracture toughness of 3-D printed ABS/CF-PLA composite under mode I, II, and mixed-mode loading", *J. Thermoplast. Compos. Mater.* **34** (2019), pp. 1599–1622.
[10] A. Krishnan and L. R. Xu, "A short-beam shear fracture approach to measure the mode II fracture toughness of materials with preferred interfaces", *Int. J. Fract.* **169** (2011), pp. 15–25.
[11] J. W. Hutchinson and Z. Suo, "Mixed mode cracking in layered materials", *Adv. Appl. Mech.* **29** (1992), pp. 63–191.
[12] J.-B. Leblond and J. Frelat, "Crack kinking from an initially closed crack", *Int. J. Solids Struct.* **37** (2000), no. 11, pp. 1595–1614.
[13] J.-B. Leblond and J. Frelat, "Crack kinking from an interface crack with initial contact between the crack lips", *Eur. J. Mech.—A/Solids* **20** (2001), no. 6, pp. 937–951.
[14] L. R. Xu, Y. Y. Huang and A. J. Rosakis, "Dynamic crack deflection and penetration at interfaces in homogeneous materials: experimental studies and model predictions", *J. Mech. Phys. Solids* **51** (2003), pp. 461–486.
[15] A. T. Zehnder, *Fracture Mechanics*, Springer: New York, 2012.
[16] B. Cotterell and J. R. Rice, "Slightly curved or kinked cracks", *Int. J. Fract.* **16** (1980), no. 1980, pp. 155–169.
[17] X.-F. Li and L. R. Xu, "T-stresses across static crack kinking", *J. Appl. Mech.* **74** (2007), pp. 181–190.
[18] L. R. Xu and A. J. Rosakis, "An experimental study on dynamic failure events in homogeneous layered materials using dynamic photoelasticity and high-speed photography", *Opt. Laser Eng.* **40** (2002), no. 2003, pp. 263–288.
[19] F. Erdogan and G. C. Sih, "On the crack extension in plates under plane loading and transverse shear", *J. Basic Eng.* **85** (1963), pp. 519–525.
[20] Q. Wang, G. Zhang, X. Zheng and L. R. Xu, "Experimental study on the shear fracture toughness of 3D printing polyamide", 2025. under review.

[21] V.-X. Tran, D. Leguillon, A. Krishnan and L. R. Xu, "Interface crack initiation at V-notches along adhesive bonding in weakly bonded polymers subjected to mixed-mode loading", *Int. J. Fract.* **176** (2012), pp. 65–79.

[22] G. Zhang, J. Ghorbani, X. Zheng, et al., "Anisotropic and elastoplastic mode-I fracture toughnesses of three additively manufactured polymers fabricated via material extrusion and powder bed fusion", *Fatigue Fract. Eng. Mater. Struct.* **46** (2023), pp. 4776–4782.

[23] *Materials Databook*, University of Cambridge Engineering Department, 2003.

Comptes Rendus
Mécanique

Objet de la revue

Les *Comptes Rendus Mécanique* sont une revue électronique évaluée par les pairs de niveau international, qui couvre l'ensemble des domaines des sciences mécaniques.
Ils publient des articles originaux de recherche, des articles de synthèse, des mises en perspective historiques, des textes à visée pédagogique, ou encore des actes de colloque, en anglais ou en français, sans limite de longueur et dans un format aussi souple que possible (figures, données associées, etc.).
Depuis 2020, les *Comptes Rendus Mécanique* sont publiés avec le centre Mersenne pour l'édition scientifique ouverte, selon une politique vertueuse de libre accès diamant, gratuit pour les auteurs (pas de frais de publication) comme pour les lecteurs (accès libre, immédiat et pérenne).

À propos de la revue

Toutes les informations concernant la revue, y compris le texte des articles publiés qui est en accès libre intégral, figurent sur le site https://comptes-rendus.academie-sciences.fr/mecanique/.

Informations à l'attention des auteurs

Pour toute question relative à la soumission des articles, les auteurs peuvent consulter le site https://comptes-rendus.academie-sciences.fr/mecanique/.

Contact

Académie des sciences
23, quai de Conti, 75006 Paris, France
Tel: (+33) (0)1 44 41 43 72
cr-mecanique@academie-sciences.fr

Pour citer ce numéro :
Leblond Jean-Baptiste (ed). Advances in finite fracture mechanics : a tribute to Dominique Leguillon's scientific achievements. Comptes Rendus Mécanique, 2025. https://doi.org/10.5802/crmeca.sp.2.

COMPTES RENDUS
DE L'ACADÉMIE DES SCIENCES

Mécanique

Advances in finite fracture mechanics : a tribute to Dominique Leguillon's scientific achievements / *Progrès récents en mécanique finie de la rupture : un hommage à l'œuvre scientifique de Dominique Leguillon*

Contents

Please note that the page numbers indicated are those of the electronic file of the issue. Each article also has its own pagination, linked to its publication date.

Cover illustration: Portrait of Dominique Leguillon, from his personal webpage .

1873-7234 (electronic)

Académie des sciences - Paris